



*„BioTechNan - the programme of interdisciplinary cross-institutional post gradual studies KNOW
in the field of Biotechnology and Nanotechnology”*

Institute of Advanced Materials
Faculty of Chemistry
Wrocław University of Science and Technology

DOCTORAL DISSERTATION

*Gold Nanoparticles as Components of Advanced Hybrid
Materials Employing Light to Control the Course of
Chemical Processes*

mgr inż. Nina Tarnowicz-Staniak

Supervisor: prof. dr hab. inż. Katarzyna Matczyszyn
Institute of Advanced Materials, Faculty of Chemistry,
Wrocław University of Science and Technology

Co-Supervisor: dr Marek Grzelczak, Centro de Física de Materiales
(CSIC-UPV/EHU), San Sebastian, Spain

Wrocław, June 2024



Wrocław University
of Science and Technology



Uniwersytet
Wrocławski



WROCLAW UNIVERSITY
OF ENVIRONMENTAL
AND LIFE SCIENCES

Acknowledgements

I would like to express my sincere gratitude to my Supervisors, Prof. Katarzyna Matczyszyn and Dr Marek Grzelczak. I am very grateful for your mentoring, support, kindness, and your help throughout my PhD studies. Thank you.

I would also like to thank my colleagues and co-workers from Wrocław University of Science and Technology, particularly from the Institute of Advanced Materials. I very much appreciate your help and support. I also thank my colleagues from San Sebastian for making me feel welcome in Spain and for creating a positive working environment.

Last but not least, I sincerely thank my Family – my husband, my parents, and my in-laws. Thank you for being by my side.

TABLE OF CONTENTS

Abbreviation List	3
Summary	5
Streszczenie (Summary in Polish).....	7
I Introduction	11
Chapter 1. <i>Motivation and Objectives</i>	12
Chapter 2. <i>General Literature Review</i>	16
2.1. Plasmonic nanoparticles – properties and synthesis.....	16
2.1.1. Properties of plasmonic nanoparticles	19
2.1.2. Synthesis of gold nanorods.....	23
2.2. Plasmon-related effects as important catalytic tools	30
2.2.1. Local Electromagnetic Field Enhancement	33
2.2.2. Highly energetic charge carriers	36
2.2.3. Thermal effects	41
2.2.4. Interband transitions	46
2.3. Cellulose as component of advanced materials.....	48
2.3.1. Nanocellulose	49
2.3.2. Hybrid materials based on cellulose and gold nanoparticles	53
2.3.3. Hybrid materials based on cellulose and dyes	61
2.4. Hybrid materials based on azobenzenes and gold nanoparticles.....	66
2.4.1. Azobenzene type photochromes	67
2.4.2. Azo-AuNPs hybrids.....	71
II Results, discussion, and methodology.....	79
Chapter 3. <i>Cellulose as a Robust Scaffold for the Stabilization of Gold Nanorods in the Photocatalytic Regeneration of Cofactor Molecules</i>	80
3.1. Motivation	80
3.2. Materials and methods.....	83
3.2.1. Materials and techniques	83
3.2.2. Nanoparticles synthesis.....	84
3.2.3. Nanoparticles-CNFs composites preparation	86
3.2.4. One-pot plasmon-assisted photoregeneration of cofactor molecules	87
3.3. Results and discussion.....	88
3.3.1. Preparation and properties of AuNRs-CNFs and AuPdNRs-CNFs composites....	88
3.3.2. Plasmon-assisted regeneration of cofactor molecules using AuPdNRs-CNFs photocatalyst	96
3.4. Conclusions	103
Chapter 4. <i>Plasmonic-Photochromic Hybrid Materials Exhibiting Water-Functionality</i>	105
4.1. Motivation	106

4.2.	Materials and methods	111
4.2.1.	Materials and techniques	111
4.2.2.	Nanoparticles synthesis	112
4.2.3.	Azo derivative synthesis	113
4.2.4.	Hybrid materials	117
4.3.	Results and discussion	118
4.3.1.	Composites prepared with AuNSs and thiolated Azo ligand	119
4.3.2.	AzoGly and CNFs interactions leading to formation of hybrid materials	124
4.3.3.	Composites prepared with AuNRs and new Azo ligand – the final formulation..	130
4.4.	Conclusions	144
Chapter 5. <i>Catalytic Influence of Gold Nanorods on Azobenzene Isomerization</i>		146
5.1.	Motivation	147
5.2.	Materials and methods	150
5.2.1.	Materials and techniques	150
5.2.2.	Hybrid materials preparation	151
5.2.3.	Isomerization of photochromic component in hybrid materials	154
5.3.	Results and discussion	155
5.3.1.	UV-Vis-induced direct Azo photoswitching in hybrid materials	155
5.3.2.	Thermal relaxation of hybrid materials in the dark	164
5.4.	Conclusions	174
Chapter 6. <i>Plasmon-Assisted Isomerization of Azobenzene and Its Control via Plasmon-Related Effects</i>		176
6.1.	Motivation	177
6.2.	Materials and methods	181
6.2.1.	Materials and techniques	181
6.2.2.	Hybrid materials preparation	181
6.2.3.	Plasmon assisted isomerization of AzoGly	183
6.3.	Results and discussion	185
6.3.1.	Plasmon-assisted Z-E isomerization of free AzoGly in ethanol solution	187
6.3.2.	Plasmon-assisted Z-E isomerization of AzoGly in the hybrid material	191
6.4.	Conclusions	200
6.5.	Appendix	201
III Summary		203
Chapter 7. <i>Conclusions and Perspectives</i>		204
Scientific Curriculum		208
Bibliography		214

ABBREVIATION LIST

AA – ascorbic acid

AMI2030 – Advanced Materials 2030 Initiative

AR – aspect ratio

ARIMA – Autoregressive Integrated Moving Average

AuNPs – gold nanoparticles

 NPs - nanoparticles

AuNRs – gold nanorods

AuNSs – gold nanospheres

Azo – azobenzene/azobenzene derivative

BC – bacterial cellulose

CMC – critical micelle concentration

CNCs – cellulose nanocrystals

CNFs – cellulose nanofibres

CTAB – cetyltrimethylammonium bromide

CTAC – cetyltrimethylammonium chloride

CW – continuous wave

DE - diarylethenes

eT – electron transfer

EtOH – ethanol

HQ – hydroquinone

IBs – interband transitions

KETs – Key Enabling Technologies

LISA – Light Induced Self-Assembly

LSPR – Localized Surface Plasmon Resonance

 l-LSPR – longitudinal LSPR

 t-LSPR – transverse LSPR

LUMO – Lowest Unoccupied Molecular Orbital

OBA – optical brightening agents

NAD⁺ – oxidized form of nicotinamide adenine dinucleotide

 NADH – reduced form of nicotinamide adenine dinucleotide

NIR – Near Infrared

PSS/PSSs – Photostationary State/Photostationary States

PSS_E – Photostationary state of E-isomer

PSS_Z – Photostationary state of Z-isomer

SAMs – Self-Assembled Monolayers

SERS – Surface Enhanced Raman Spectroscopy

SPP – Surface Plasmon-Polaritons

SPR – Surface Plasmon Resonance

TEM – Transmission Electron Microscopy

TFA – trifluoroacetic acid

THF – tetrahydrofuran

SUMMARY

Scientific research on advanced materials is required for the overall development of humankind. New material designs enable exploration of previously unattainable experimental scenarios and phenomena. Thus, the overall understanding of the world is broadened and new things become possible.

The presented dissertation is interdisciplinary and combines fields of chemical sciences and materials science. This work aims at the preparation of advanced materials able to employ light to control the course of chemical processes. Light is one of the best stimuli to control the behaviour of materials, because it is ultrafast, fully tunable, and can trigger phenomena with high spatio-temporal resolution. Since plasmonic nanostructures, such as gold nanoparticles (AuNPs), provide both catalytical surfaces and strong interactions with light, they became a central component of the materials proposed in this dissertation. Moreover, to investigate influence of optical properties of nanostructures, anisotropic nanoparticles of a rod-like geometry (AuNRs) were employed. The second important component of the proposed hybrid materials is cellulose in a form of nanofibres (CNFs). Due to rich surface chemistry CNFs enable immobilization of gold nanorods and stabilization of their optical properties.

First section of the dissertation (Introduction) consists of two chapters. Chapter 1 presents motivation for undertaking this research project and sets four rational criteria for the hybrid materials. Moreover, objectives and hypotheses of the dissertation are presented. Chapter 2 constitutes a review of general literature knowledge in four crucial areas, namely plasmonic nanoparticles (their properties and synthesis are discussed), plasmon-related effects as important catalytic tools (here different phenomena, such as local field enhancement, hot charge carriers generation, and thermoplasmonic effect are presented), cellulose as component of advanced materials (special emphasis is put on nanocellulose composites with gold nanoparticles and organic dyes), and hybrid materials based on azobenzenes (Azo) and gold nanostructures.

Second section of the dissertation (Results, discussion, and methodology) consists of four chapters focused on the presentation of the experimental results and their discussion.

Chapter 3 establishes general protocol for the preparation of AuNRs-CNFs materials. Immobilization of nanostructures on cellulose nanofibers grants great stability of nanocrystals' plasmonic properties under intense illumination, elevated temperatures, and in a wide range of pH. This chapter presents also functionality of the proposed formulation as a photocatalyst and introduces a conceptually new plasmon-assisted photochemical process of simultaneously coupled dehydrogenation of sodium formate and regeneration of cofactor molecules in the presence of plasmonic hybrid material under visible light irradiation.

Chapter 4 addresses current challenges in the field of plasmonic-photochromic hybrid systems by establishing general protocol for the preparation of multifunctional, water-based, CNFs-stabilized plasmonic-photochromic hybrid material. In this chapter mutual interactions between CNFs and AuNRs, as well as CNFs and the chosen Azo photochrome are analysed. The proposed formulation enables efficient transfer of Azo to water, a solvent in which it is not normally soluble. Moreover, the exceptional stability of AuNRs-CNFs in ethanol is investigated and the comparative analysis of the IR spectra confirms role of CTAB on the surface of AuNRs in maintaining material's structural integrity. Notably, both functional components maintain

their functionality and optical properties. Results presented in this chapter constitute an important step forward in the field of Azo-AuNPs hybrids, since the incorporation of big, anisotropic nanostructures enables beneficial spectral separation of Azo and AuNRs.

Chapter 5 focuses on the influence of AuNRs on the isomerization of the photochromic component in the hybrid Azo-AuNRs-CNFs formulation. Presence of AuNRs grants catalytic enhancement of both, photoinduced and thermal Azo isomerization. Based on the observed coherent and reversible changes in the position of 1-LSPR band of AuNPs (about 2-4 nm) the electron transfer mechanism of the catalytic influence is proposed. The results obtained for samples containing AuNRs of different sizes indicate that catalytic enhancement increases with the decreasing aspect ratio of AuNRs, however, the postulated size effect is presumably a convolution of more than one descriptor of samples' composition. Moreover, this chapter presents a complete sets of thermodynamic parameters describing thermal back-isomerization of Azo component in the hybrid materials. For all Au-containing samples, thermal relaxations in the dark were characterized by activation energy lower by 20 kJ/mol compared to hybrid sample without Au.

Chapter 6 presents plasmon-assisted *Z-E* isomerization of the photochrome in two forms, as free Azo molecules in solution and as a component of the hybrid formulation. Upon red-NIR irradiation (650-1100 nm), photochrome exhibits dramatic increase of the *Z-E* isomerization rate in the presence of AuNRs. Based on the exponential correlation between isomerization rate constants in hybrid materials and irradiation intensity, the predominant influence of thermoplasmonic effect is proposed. The observed kinetic changes of Azo can be recalculated to estimate the extent of the thermoplasmonic effect, and hence value of 21°C is obtained. Hence, the dissertation introduces application of Azo type photochromes as molecular thermometers. Chapter 6 proposes also specific experimental design in which hybrid Azo-AuNRs-CNFs material is subjected to the interval dark and light irradiation conditions. Novel, at least from chemical point of view, statistical modelling tools are also proposed to analyse the obtained data. The statistical modelling based on the Autoregressive Integrated Moving Average approach enables conclusion on the statistical significance of the observed kinetic changes in the Azo isomerization in the presence of AuNRs. Hence, indirect photocontrol over the *Z-E* isomerization of Azo in the ON-OFF manner is possible. Statistical modelling also enabled final conclusion on the predominant contribution of the thermoplasmonic effect triggered upon irradiation.

Third section of the dissertation (Summary) consists of three parts. Chapter 7 presents general conclusions of the research and summarizes its key aspects and findings. Moreover, further research directions for each experimental chapter are proposed. Second part showcases scientific activities and achievements of the author. Bibliography is the final, third part of the last section.

In summary, this dissertation provides important insight into the preparation and operation of hybrid plasmonic and plasmonic-photochromic CNFs-based materials. AuNRs incorporated in the proposed systems enable control over the course of the chemical process via light-induced plasmon-related effects. Presented work is at the intersection of chemical sciences and material science and contributes to both fields.

STRESZCZENIE (SUMMARY IN POLISH)

Badania naukowe skupione na materiałach zaawansowanych są konieczne dla ogólnego rozwoju ludzkości. Nowoprojektowane materiały umożliwiają zbadanie niemożliwych do wcześniejszego zrealizowania scenariuszy eksperymentalnych i trudnych do obserwacji zjawisk. Można więc powiedzieć, że ogólne rozumienie świata poszerza się dzięki temu, że to, co nowe, staje się możliwe.

Niniejsza rozprawa jest pracą interdyscyplinarną i łączy w sobie zagadnienia z dwóch obszarów: nauk chemicznych i inżynierii materiałowej. Praca ta ma na celu przygotowanie materiałów zaawansowanych zdolnych do wykorzystania światła do kontroli przebiegu procesów chemicznych. Światło jest jednym z najlepszych bodźców do kontroli działania materiałów, ponieważ jest ultraszybkie, w pełni przestrajalne i umożliwia wywoływanie zjawisk z wysoką rozdzielczością czasowo-przestrzenną. Nanostruktury plazmoneczne, takie jak nanocząstki złota (AuNPs), zapewniają zarówno powierzchnię katalityczną, jak i silne oddziaływanie ze światłem. Wobec tego zostały wybrane na kluczowy komponent materiałów zaproponowanych w niniejszej rozprawie. Ponadto, aby zbadać wpływ właściwości optycznych nanostruktur, wykorzystano nanocząstki o prętopodobnej geometrii (AuNRs). Drugim ważnym komponentem zaproponowanych materiałów hybrydowych jest celuloza w formie nanowłókien (CNFs). Wobec bogatej chemii powierzchni, nanowłókna celulozowe umożliwiają efektywną immobilizację AuNRs oraz stabilizację ich właściwości optycznych.

Pierwsza sekcja rozprawy (*Introduction*) składa się z dwóch rozdziałów. Rozdział nr 1 prezentuje motywację, jaka leży u podstaw podjęcia się tego projektu badawczego oraz cztery kryteria dla przygotowywanych materiałów hybrydowych. Ponadto, zaprezentowano cele pracy i hipotezy badawcze. Rozdział nr 2 stanowi przegląd wiedzy literaturowej w czterech kluczowych obszarach, mianowicie nanocząstek plazmonecznych (ich właściwości i syntezy), efektów wynikających z właściwości plazmonecznych jako istotnych narzędzi katalitycznych (omówiono zjawiska takie jak lokalne wzmocnienie pola elektrycznego, generacja wysokoenergetycznych nośników ładunku oraz efekt termoplazmoneczny), celulozy jako komponentu materiałów zaawansowanych (specjalny nacisk położono na kompozyty nanocelulozy z nanocząstkami plazmonecznymi oraz barwnikami organicznymi), a także materiałów hybrydowych bazujących na pochodnych azobenzenu (Azo) oraz nanocząstkach złota.

Druga sekcja rozprawy (*Results, discussion, and methodology*) składa się z czterech rozdziałów, które przedstawiają wyniki eksperymentalne oraz ich dyskusję.

W rozdziale nr 3 przedstawiono ustalony w toku badań protokół przygotowania materiału AuNRs-CNFs. Immobilizacja nanostruktur na nanowłóknach celulozowych zapewnia dużą stabilność właściwości plazmonecznych nanokryształów w warunkach intensywnego naświetlania, podwyższonych temperaturach, a także w szerokim zakresie pH. Rozdział ten przedstawia również wykorzystanie zaproponowanej formułacji jako fotokatalizatora i wprowadza koncepcyjnie nowy proces fotochemiczny wspomagany plazmonem, mianowicie jednoczesną dehydrogenację mrówczanu sodu oraz regenerację cząsteczek kofaktora w obecności plazmonecznego materiału hybrydowego i w czasie naświetlania światłem widzialnym.

Rozdział nr 4 odnosi się do obecnych wyzwań w obszarze hybrydowych układów plazmoneczno-fotokromowych poprzez przedstawienie ogólnego protokołu przygotowania

wielofunkcyjnego, rozdyspergowanego w wodzie, stabilizowanego na celulozie hybrydowego materiału plazmionczno-fotochromowego. Ponadto, w tym rozdziale badane są wzajemne interakcje między CNFs a AuNRs oraz CNFs a wybraną pochodną fotochromową Azo. Zaproponowana formuacja umożliwia efektywny transfer Azo do wody, pomimo iż związek nie jest rozpuszczalny w tym rozpuszczalniku. Ponadto, zbadana została wyjątkowa stabilność AuNRs-CNFs w etanolu, a porównawcza analiza widm IR potwierdziła istotną rolę CTAB, znajdującego się na powierzchni AuNRs, w zapewnieniu integralności strukturalnej materiału. Co ważne, oba komponenty funkcjonalne zachowują swoje właściwości, w tym właściwości optyczne. Wyniki zaprezentowane w tym rozdziale stanowią istotny wkład w obszar hybryd Azo-AuNPs, ze względu na inkorporację dużych, anizotropowych nanostruktur, które umożliwiają korzystną separację spektralną obu komponentów.

Rozdział 5 skupia się na zbadaniu wpływu AuNRs na proces izomeryzacji komponentu fotochromowego w hybrydowej formuacji Azo-AuNRs-CNFs. Obecność AuNRs zapewnia katalityczne wzmocnienie zarówno fotoindukowanej jak i termicznej izomeryzacji Azo. Na podstawie zaobserwowanych spójnych i odwracalnych zmian w pozycji pasma 1-LSPR nanocząstek (ok. 2-4 nm) jako mechanizm wzmocnienia katalitycznego zaproponowano transfer elektronu. Wyniki uzyskane dla próbek zawierających AuNRs o różnych rozmiarach wskazują, że efekt katalityczny nanocząstek wzrasta wraz z malejącym parametrem kształtu AuNRs. Jednakże postulowany wpływ rozmiaru jest najprawdopodobniej splotem więcej niż jednego parametru opisującego skład próbki. Ponadto, rozdział prezentuje kompletny zestaw parametrów termodynamicznych opisujących izomeryzację termiczną Azo w materiałach hybrydowych. Dla wszystkich próbek zawierających Au, relaksacje termiczne w ciemności charakteryzują się energiami aktywacji niższymi o 20 kJ/mol w porównaniu z próbką hybrydową, która nie zawiera Au.

Rozdział 6 przedstawia wspomaganą plazmonem izomeryzację *Z-E* fotochromu w dwóch formach, jako swobodnych cząsteczek Azo w roztworze oraz jako składnika formuacji hybrydowej. Pod wpływem naświetlania światłem czerwonym i podczerwonym (650-1100 nm) fotochrom wykazuje dramatyczny wzrost szybkości reakcji izomeryzacji w obecności AuNRs. Dzięki wykładniczej zależności między stałymi szybkości izomeryzacji *Z-E* w materiałach hybrydowych a intensywnością naświetlania, zaproponowano dominujący wpływ efektu termoplazmioncznego. Zaobserwowane zmiany kinetyki Azo można wykorzystać do oszacowania zakresu tego efektu, dzięki czemu uzyskano wartość 21°C. Wobec tego niniejsza rozprawa wprowadza koncepcję zastosowania fotochromów typu azobenzenu jako cząsteczkowych termometrów. Rozdział 6 proponuje również szczególny rodzaj eksperymentu, w którym materiał hybrydowy Azo-AuNRs-CNFs jest poddawany naprzemiennym warunkom ciemnym i naświetlaniu. W analizie wyników wykorzystano nowe, z chemicznego punktu widzenia, narzędzia statystyczne. Modelowanie statystyczne w oparciu o autoregresyjny zintegrowany model średniej ruchomej (Autoregressive Integrated Moving Average) umożliwiło wnioskowanie na temat statystycznej istotności zaobserwowanych zmian kinetyki izomeryzacji Azo w obecności AuNRs. Zaprezentowana została więc możliwość niebezpośredniej, przełączalnej (on-off) fotokontroli procesu izomeryzacji *Z-E* Azo. Modelowanie statystyczne umożliwiło również sformułowanie ostatecznych wniosków o dominującym wpływie efektu termoplazmioncznego wywoływanego w czasie naświetlania.

Trzecia sekcja rozprawy (*Summary*) składa się z trzech części. Rozdział 7 przedstawia ogólne wnioski badań i podsumowuje ich kluczowe aspekty i odkrycia. Ponadto, dla każdego rozdziału eksperymentalnego, zarysowane zostały również dalsze kierunki badawcze. Druga

część przedstawia aktywność i osiągnięcia naukowe autorki, natomiast bibliografia stanowi trzecią, ostatnią część tej sekcji.

Podsumowując, niniejsza rozprawa dostarcza istotnego wglądu w przygotowanie i działanie materiałów hybrydowych, plazmonicznych i plazmoniczno-fotochromowych, bazujących na nanowłóknach celulozowych. Nanopręty złota zawarte w przedstawionych układach zapewniają kontrolę nad przebiegiem procesów chemicznych dzięki indukowanemu światłem efektom plazmonicznym. Niniejsza rozprawa jest na granicy nauk chemicznych oraz inżynierii materiałowej i wnosi swój wkład w obie te dyscypliny.

I INTRODUCTION

C Chapter 1. Motivation and Objectives

European Commission considers Research and Innovation policy as "*an engine of the green and digital transitions on the continent*".¹ Within this policy, the Industrial Research and Innovation area, with its six Key Enabling Technologies (KETs), has a special priority supported by Horizon Europe.² One of the KETs, particularly important for this dissertation, is the field of advanced materials. European Commission defines advanced materials as "*engineered materials with innovative properties and functionalities*"³ and lists as key examples materials containing, e.g. metallic nanoparticles, nanocrystals, and thermochromic components. The policy also emphasizes the importance of nanomaterials in micro- and nanoelectronics and photonics.

On 27 February 2024, the European Union adopted a series of actions to maintain Europe's leadership in advanced materials, emphasizing this research field's crucial role for Europe's society, environment, and economy.³ The Advanced Materials 2030 Initiative (AMI2030) further lists essential aspects, such as a rapid need for increasingly complex materials (Main Challenge 1), utilization of reusable components that may circulate in the economy (part of AMI2030 Principles), discovery, design, and development of frontier materials, including customized materials and materials with novel functionalities (first segment of the Circular Value Chain and one of the named Cross-Cutting Needs).⁴

Scientific research on advanced materials is required for the overall development of humankind. Depending on the intended application, research might be even considered to be urging, such as for health-related issues and development of new theranostic platforms.⁵ However, design and investigation of advanced materials are also justifiable from the point of fundamental science. New material designs and new compositions sometimes enable exploration of previously unattainable experimental scenarios and phenomena.⁶ Thus, the overall understanding of the world is broadened and new things become possible by harnessing new phenomena. Moreover, since work of scientists very often relies on their creativity, simple curiosity also constitutes a very important motivation. Many scientific discoveries started with the question *What if...?* One can also ask: what if we mix component A and component B to obtain material C?

These aspects were, to some extent, motivation for undertaking the research project summarized in this thesis, entitled *Gold Nanoparticles as Components of Advanced Hybrid Materials Employing Light to Control the Course of Chemical Processes*. Gold nanoparticles (AuNPs)

constituted a central component of the designed and investigated materials due to their several advantages, such as chemical stability, tunability of optical properties, and abundance of synthesis protocols resulting in various morphologies of the structures. These characteristics predestine AuNPs as components of advanced materials, especially the stimuli-responsive functional structures.⁷ Stimuli-responsiveness is a crucial property of natural systems and constitutes the basis for their autonomous, intelligent, and adaptive behaviour. Mimicking these characteristics in synthetic materials became an important objective in the fields of chemical sciences and materials engineering.⁸

Out of all possible chemical and physical stimuli, light is certainly one of the best to control the behaviour of materials and the course of chemical processes. Light is ultrafast, fully tunable, and can trigger phenomena with high spatio-temporal resolution. Since plasmonic nanostructures provide both catalytical surfaces and strong interactions with light, they became crucial for the design of materials translating light-matter coupling to the control of chemical reactions.⁹ This is why an important part of the research presented within this dissertation is dedicated to stabilization of optical properties of AuNPs (Chapter 3), design and preparation of multifunctional light-responsive materials (Chapter 4), investigation and description of their properties and behaviour (Chapter 5), and harnessing the light-induced (mostly plasmon-related) phenomena to gain control over chosen chemical processes (Chapters 3 and 6).

The whole research project relied on a framework built upon a set of four rational criteria defined specifically within this dissertation for the designed advanced materials in question.

- (1) Advanced materials consist of **functional components**, meaning components with unique physical or chemical properties. Scientific novelty of constituents is not required, however, novel materials should combine or utilize well-known components in new systems and scenarios.
- (2) Properties of advanced materials should be **designed for specific applications** and should also be **stable over time** and **under various conditions**.
- (3) The rapid need for advanced materials in different industrial sectors requires facile design adaptation from the research laboratory to the production stage. Hence, **ease of preparation and processing** are realistic requirements. Tailor-made materials that can be obtained in one specific laboratory are of no particular benefit to society. Procedures and protocols need to be **easily reproducible and reliable**.
- (4) Advanced materials should exhibit **multifunctionality**, namely more than one specific feature, stemming from the presence of the advanced units within the composition. This requires a rationally **increasing level of materials' complexity**.

To meet requirement (1) in all crucial experiments described within the dissertation gold nanorods (AuNRs) were used as recognized advanced and functional components. Most of the applications utilize the optical properties of AuNRs, as they can be precisely designed at the synthesis stage, which is in agreement with aspect (2). The optical responsiveness of AuNRs was the underlying reason for selecting light-controlled processes for the materials' functionality validation. In order to ensure the stability of plasmonic properties upon irradiation, cellulose nanofibres (CNFs) were proposed as an immobilization matrix. Cellulose is a material of natural origin, abundantly available, and biodegradable. CNFs increased material processability (3) and enabled the introduction of multifunctionality postulated in requirement (4). Namely, due to the functional CNFs scaffold available for impregnation with dye molecules, a novel hybrid formulation was designed containing AuNRs and azobenzene-type photochromic components (Azo). Azobenzenes are well-known and robust photochromes that have already been used to prepare plasmonic-photochromic hybrids.⁷ Hence, there is a broad scope of advanced systems that can be used as a reference for the proposed formulation.

The suggested requirements for the advanced materials presented within this dissertation are verified by stating proper research objectives and hypotheses.

Objective 1: To stabilize optical properties of AuNRs for applications in processes or phenomena requiring intense illumination, high temperatures, or wide pH range (**Chapter 3**).

Hypothesis 1: Cellulose may serve as an inert scaffold for AuNRs and does not alter the optical properties of nanocrystals.

Hypothesis 2: Cellulose-stabilized AuNRs can serve as a reusable catalyst for model photocatalytic reactions.

Objective 2: To prepare multifunctional, hybrid plasmonic-photochromic material based on cellulose-stabilized AuNRs and model azobenzene-type photochrome and, simultaneously, to address current challenges in the field of plasmonic-photochromic hybrids, such as structures' water-functionality, use of non-thiolated Azo ligands, preparation of hybrids operating without aggregation (**Chapter 4**).

Hypothesis 3: Cellulose can serve as a scaffold for AuNRs and a photochromic dye of choice.

Hypothesis 4: Both functional components (AuNPs and Azo) preserve the entirety of their optical properties and functionality.

Objective 3: To investigate the mutual interactions of plasmonic and photochromic components and the kinetics of azobenzene photoswitching in the dark and upon UV-Vis irradiation in the presence of AuNRs (**Chapter 5**).

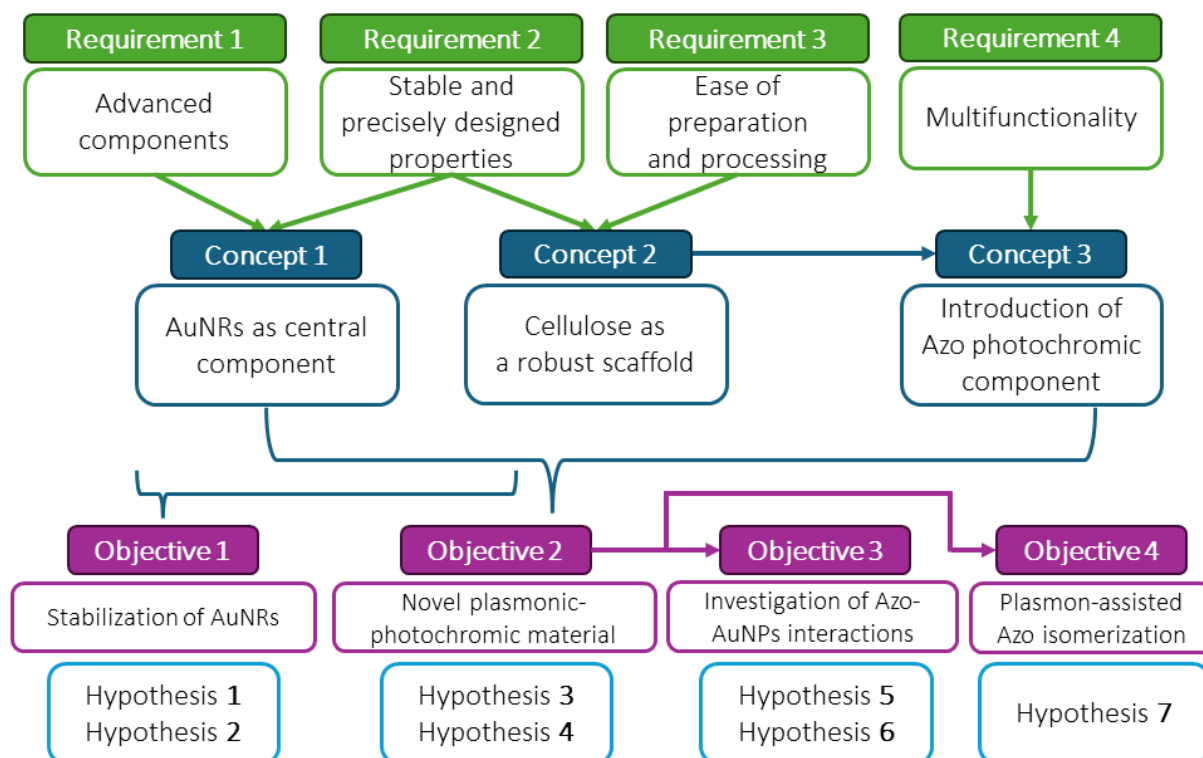
Hypothesis 5: AuNRs catalyse Azo photoswitching via the electron transfer mechanism, both in the dark and under illumination.

Hypothesis 6: The catalytic effect of AuNRs is size-dependent.

Objective 4: To investigate the possibility of plasmon-assisted Azo isomerization and reaction control via plasmon-related effects (**Chapter 6**).

Hypothesis 7: Kinetics of the Azo isomerization can be controlled via red-NIR irradiation (at wavelengths not absorbed by a photochrome) due to the thermoplasmonic effect of AuNRs.

Hypotheses 1, 3, and 4 concern materials science-related part of the project and correlate to tackling specific material challenges. Hypotheses 2, 5, 6, and 7 link to the topics of catalysis and reaction mechanisms by concerning light control of the chemical reactions. Framework of the project, representing relationships between all of the aspects, is presented in the **Scheme 1**.



Scheme 1. Schematic representation of the project's framework.

Chapter 2. *General Literature Review*

This chapter constitutes a review of general literature knowledge regarding four chosen aspects at the intersection of chemical sciences and materials engineering. The following topics, central for the dissertation, are discussed:

- **Plasmonic nanoparticles – properties and synthesis** – their basic properties in the context of nanoplasmonics (mainly the optical properties) and most crucial aspects of their chemical synthesis (focus on the gold nanorods as a chosen geometry of nanostructures central for the dissertation);
- **Plasmon-related effects as important catalytic tools** – this section discusses important catalytic tools derived from plasmonic properties of nanoparticles that can be employed in chemical sciences, namely local field enhancement, hot (highly energetic) charge carriers, and thermoplasmonic effect;
- **Cellulose as a component of advanced materials** – here, the properties of cellulose and its advanced applications in materials engineering are presented, including different types of cellulose nanomaterials and its composites, especially cellulose-AuNPs and cellulose-dyes;
- **Plasmonic-photochromic hybrids** – this subsection presents hybrid materials and nanostructures obtained via coupling of azobenzene derivatives and gold nanoparticles (special emphasis is put on the most popular designs, novel types of hybrid materials, and current challenges in the field).

Each section constitutes an important starting point for the results and discussions presented within the dissertation. To provide more clarity to the reader, specific aspects presented in this chapter are also followed-up and broadened at the beginning of each experimental chapter. This assures a more detailed look into the topics crucial for the dissertation.

2.1. Plasmonic nanoparticles – properties and synthesis

Nanotechnology is a field of science concerning design, preparation, investigation, and application of structures, materials, and systems with nanometer (10^{-9} m) dimensions and/or operating at a nanometer scale.¹⁰⁻¹² Material is classified as a nanomaterial if any of its external dimensions is in the 1-100 nm range or if its internal (inner or surface) structure is in the

nanoscale.¹² Hence, nanomaterials can be classified either as individual nanoobjects (e.g. nanoparticles) or as nanostructured materials (e.g. nanoporous systems). Nanomaterials may appear naturally in the environment,^{13,14} for example in a form of minerals (e.g. fibrous clay minerals, such as sepiolites¹⁵), as nanostructured surfaces of plants (e.g. lotus¹⁶), or as products of microbial activity (e.g. bacterial cellulose¹⁷). They have also been generated by various anthropogenic activities, both intentionally and accidentally.^{13,14} People have been using nanomaterials unknowingly for millennia, like in case of ancient Egypt hair dyes¹⁸ or stained glass windows (**Figure 1**).¹⁹ Nowadays, nanomaterials are used in a conscious way in various advanced applications, such as medical treatments^{20–22} and aerospace technologies²³ or as components of sensors²⁴, quantum computers²⁵, and solar cells.²⁶

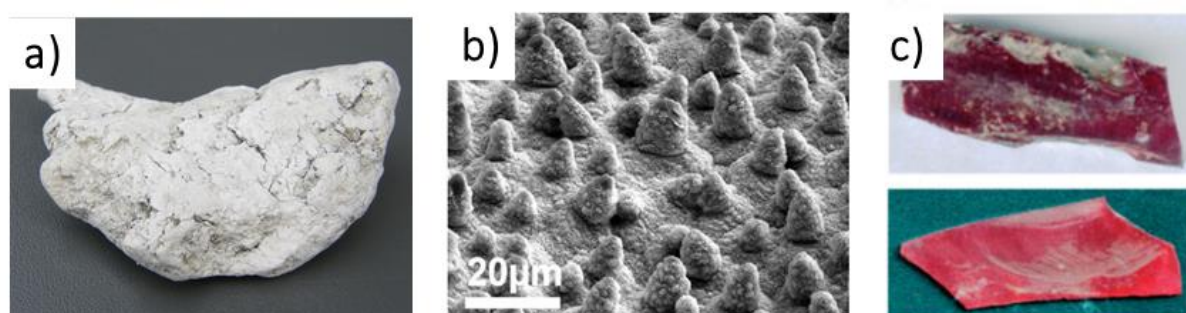


Figure 1. **a)** Picture of sepiolite, a natural mineral. Reprinted from ²⁷. **b)** Scanning Electron Microscope image of the lotus leaf surface. Reprinted from ¹⁶. **c)** Comparison of the medieval red flashed (top) and 19th century red coated (bottom) glass pieces from the Amiens Cathedral and Sèvres National Factory in France, respectively. Reprinted from ¹⁹.

Plasmonic nanoparticles are a type of inorganic nanoobjects, belonging to the class of one-dimensional (1D) nanomaterials. They are made of metals which contain free conduction band electrons such as, e.g. Au, Ag, or Cu. Properties of plasmonic nanoparticles are strongly dependent on their geometry and size. Since the very first systematic study on the preparation and properties of colloidal gold published by Michael Faraday in 1857,²⁸ plasmonic nanoparticles have gained a great scientific attention. As of May 2024, there are about 38 500 scientific publications registered in the Web of Science Core Collection database (searched by publication date: 1900–2024) that contain at least one of the following key words (searched by topic): *plasmonic nanoparticles*, *localized surface plasmon resonance*, *LSPR*, or *nanoplasmonics*. If the search is broadened with two additional keywords, referring to presumably the most popular representatives of the plasmonic nanoparticles, namely *gold nanoparticles* or *gold nanostructures*, the number of records rises to more than 180 000 (**Figure 2**).

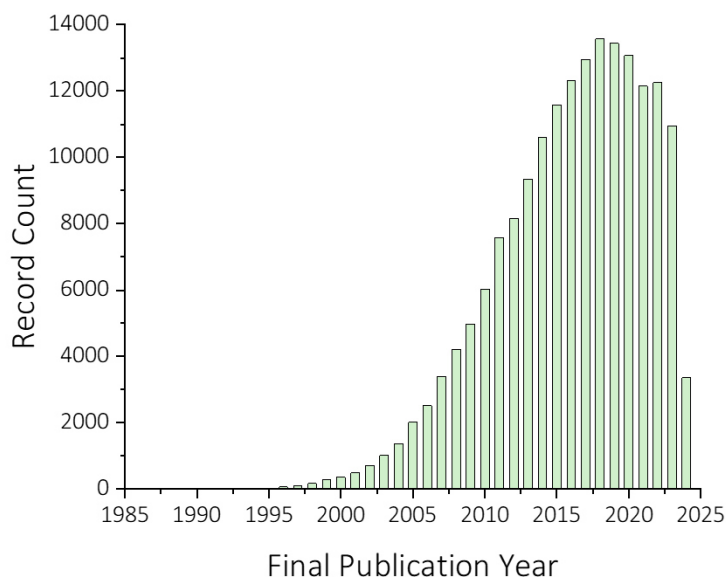


Figure 2. Number of publications per year registered in the Web of Science Core Collection database (www.webofscience.com) containing at least one of the following key words (searched by topic): *plasmonic nanoparticles, localized surface plasmon resonance, LSPR, nanoplasmonics, gold nanoparticles, or gold nanostructures*. Plot was based on the data acquired in May 2024.

Starting from the 1990s interest in the topic of plasmonic nanoparticles has been significantly growing, reaching almost 13 500 scientific publications solely in 2019. Saturation in the number of publications per year can be observed for years 2020-2022, most probably due to the slowdown of scientific research during the pandemic of SARS-CoV-2. 2024 and the following few years will show whether the scientific interest in plasmonic nanoparticles will further grow or rather stagnate. Over the years, both synthesis and properties of plasmonic nanostructures were investigated and characterized in-depth. Therefore, nowadays, the focus of the scientific community is shifted more towards advanced applications of these nanostructures and systems utilizing them,²⁹⁻³¹ which may result in a fewer number of publications. Spotlight might have also shifted towards other topics due to the new types of nanostructures and nanomaterials that emerged in recent years. Nevertheless, research related to plasmonic nanoparticles remains highly relevant and important.³²⁻³⁶

The following subsections of this chapter describe properties (mainly optical) of plasmonic nanoparticles and most popular approaches to their synthesis. For the sake of clarity and to assure it corresponds well with the topic of dissertation, most of the information or examples concern gold nanoparticles, with particular emphasis on gold nanorods, since these nanostructures constitute the central geometry utilized during the experimental part of the PhD project.

2.1.1. Properties of plasmonic nanoparticles

The sole definition of nanotechnology³⁷ indicates the fact that certain properties and/or phenomena can be manifested only at a specific size scale, namely at the nanoscale. Properties of nanomaterials are – in some cases – even drastically different from bulk materials of the same composition. For instance, macroscopic, bulk Au is golden yellow in colour due to the pronounced relativistic effect (**Figure 3a**). Meanwhile, the most recognizable colour of the nanostructured gold is red (for gold nanospheres – AuNSs), which is a direct result of light-Au interactions unique to the nanoscale (vide infra).

At the nanoscale, the surface of nanomaterial or nanostructure becomes highly relevant.³⁸ Higher reactivity and different chemistry of the surface atoms is a direct result of their different steric environment in comparison to bulk (or inner) atoms. This impacts, e.g. lattice parameters^{39,40} or melting points^{41,42} of nanoparticles. For instance, for 2.59 nm Au nanoclusters surface atoms constitute about 50% of the total number of atoms in the cluster,⁴³ Au-Au bond length drops to about 0.283 nm⁴⁴ (from 0.288 nm for bulk gold), and the melting temperature decreases to about 775-800 K⁴⁵ (comparing to 1337 K for bulk gold; **Figure 3b**).

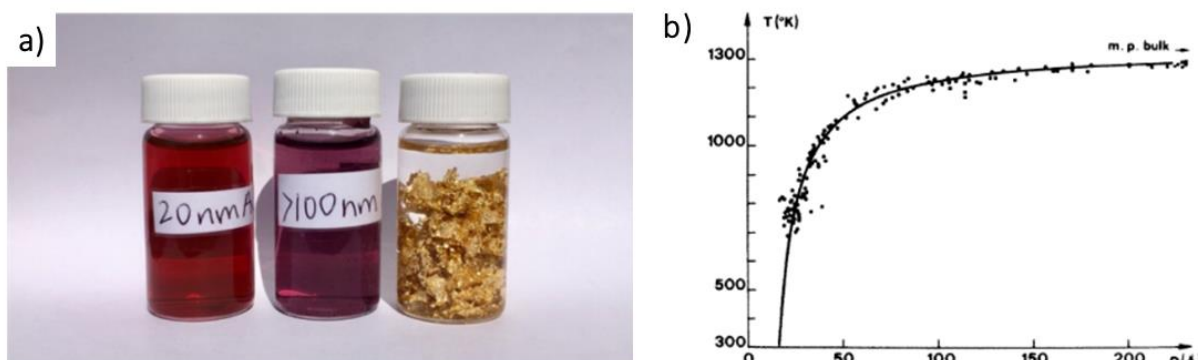


Figure 3. Illustrative depiction of size effect for plasmonic nanoparticles and differences between nano and bulk Au. **a)** Physical appearance of water dispersions of AuNSs (diameters: left – 20 nm, middle – above 100 nm) differs from bulk Au (right). Reprinted from⁴⁶. **b)** Melting point of Au nanostructures (Y axis [K]) as a function of their size (X axis [Å]). Reprinted from⁴⁵.

In addition to this, nanomaterials exhibit also a size effect,⁴⁷ which means that their properties are size-dependent within the considered size scale (nanoscale). For different classes of nanostructures different size effects are manifested. For instance, semiconductor nanoparticles, also commonly known as quantum dots,⁴⁸ exhibit size-dependent fluorescence.^{49,50} Silica nanostructures of different sizes aggregate at different pH.⁵¹ And the ability of nanostructures build of ferro- and ferrimagnetic materials, including Co, Fe, and Ni⁵² to heat up the local

environment upon exposure to the alternating magnetic field also changes with size.⁵³ Moreover, the nanoscale gives rise to the unique features of nanoobjects. For plasmonic nanostructures such unique and most important characteristics are their optical properties and the resulting phenomena, such as heat generation, local field enhancement, and generation of highly energetic (hot) charge carriers (which will be discussed in section 2.2. of this chapter).

The most characteristic feature of plasmonic materials (and hence also their name), stems from the interactions of free metal electrons with the incident electromagnetic waves at the metal-dielectric interface. Electromagnetic excitations that mediate these interactions are called *surface plasmons* and are collective and coherent oscillations of free conduction band electrons (electron cloud, not bound to any atom) of the metal, in response to the oscillating electric field of the incident wave. *Localized surface plasmons* are defined for materials and structures smaller than the wavelength of the incident irradiation and under this condition the entirety of an electron cloud oscillates with respect to the positive-ion background (**Figure 4**). Under the quasi-static regime, when uniform oscillation in phase of all charges in the nanostructure along with the inner electric field is assumed, the oscillations are described by unique resonant frequency:

$$\text{Equation 1. } \omega_{LSPR} = \sqrt{\frac{e^2}{m_e 4\pi \epsilon_0 r_s^3}} ,$$

where e is electron charge, m_e is mass of an electron, ϵ_0 is vacuum permittivity, and r_s is the Wigner-Seitz radius, defined as radius of a sphere whose volume is equal to the volume per conduction electron in the bulk.⁵⁴

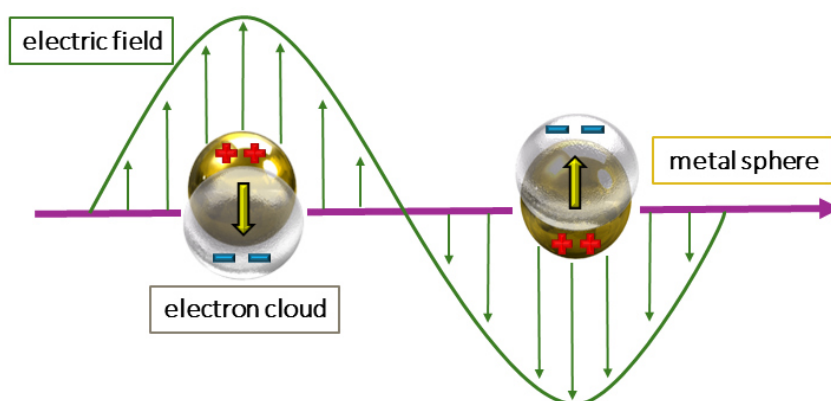


Figure 4. Localized Surface Plasmon – schematic depiction of the collective and coherent oscillation of the electron cloud of metallic nanoparticle upon interaction with the incident electromagnetic wave.

Optical properties are typically described in relation to the intensity loss (extinction) of the incident light beam as a result of light absorption and scattering. Hence, optical properties of

the colloidal dispersion of small plasmonic nanoparticles are described using extinction cross section σ_{ext} . For spherical nanostructures with radius R , σ_{ext} can be predicted using Mie theory^{54,55}:

$$\text{Equation 2. } \sigma_{ext} = \frac{24\pi^2 R^3 \varepsilon_m^{3/2}}{\lambda} \frac{\varepsilon_2(\omega)}{(\varepsilon_1(\omega) + 2\varepsilon_m)^2 + \varepsilon_2(\omega)^2} ,$$

where ε_m is a dielectric constant of the surrounding medium and $\varepsilon(\omega)$ is a complex frequency-dependent dielectric constant of the nanostructure, $\varepsilon(\omega) = \varepsilon_1(\omega) + i\varepsilon_2(\omega)$. The real part $\varepsilon_1(\omega)$ describes strength of material polarization and the imaginary part $\varepsilon_2(\omega)$ represents LSPR damping due to the losses caused by e.g. electron-phonon collisions. For spherical nanostructures with relatively small diameter $2R \ll \lambda$ (λ – wavelength of the incident light, $2R$ up to 30-40 nm), absorption is the dominant effect.^{56,57}

The optical properties of plasmonic nanostructures are, however, shape dependent and the extinction cross-section for the elongated plasmonic nanostructures, such as AuNRs, were derived by Gans⁵⁸:

$$\text{Equation 3. } \sigma_{ext} = \frac{8\pi^2 R^3 \varepsilon_m^{3/2}}{3\lambda} \sum_j \frac{(1/P_j^2)\varepsilon_2(\omega)}{\left(\varepsilon_1(\omega) + \frac{1-P_j}{P_j}\varepsilon_m\right)^2 + \varepsilon_2(\omega)^2} ,$$

where P_j stands for the depolarization factors ($j = a, b, c$) for nanorod axes (a – length, b, c – width, $a > b = c$). Depolarization factors can be described as follows:

$$\text{Equation 4. } P_a = \frac{1-r^2}{r^2} \left[\frac{1}{2r} \ln \left(\frac{1+r}{1-r} \right) - 1 \right] \quad \text{and}$$

$$\text{Equation 5. } P_b = P_c = \frac{1-P_a}{2} .$$

r is referred to as ellipticity of the rod and is related to the aspect ratio ($AR = \frac{b}{a}$) of the nanostructure:

$$\text{Equation 6. } r = \sqrt{1 - (b/a)^2} .$$

Spectra of the AuNRs are hence, characterized by two bands, called transverse Localized Surface Plasmon Resonance (t-LSPR) and longitudinal LSPR (l-LSPR). t-LSPR is caused by the oscillation of free electrons perpendicular to the main axis, while l-LSPR originates from oscillations parallel to the main axis. Hence, l-LSPR is red-shifted with respect to t-LSPR and the spectral separation is affected by the AR of the nanostructure (the red-shift increases with the increasing AR; **Figure 5**). Moreover, according to the equations presented above, optical properties of nanostructures are also dependent on the dielectric properties of the surrounding

medium, meaning solvent or even shell layer.⁵⁷ For noble metal nanoparticles LSPR bands typically appear in the UV-Vis and Near Infrared (NIR) range. The LSPR for AuNSs usually appears around 520 nm and can be hardly shifted above 600 nm by increasing size of the nanostructure. Structures with different AR,⁵⁹ additional dielectric coating,⁶⁰ or dimer structures⁶¹ exhibit significantly different resonances.

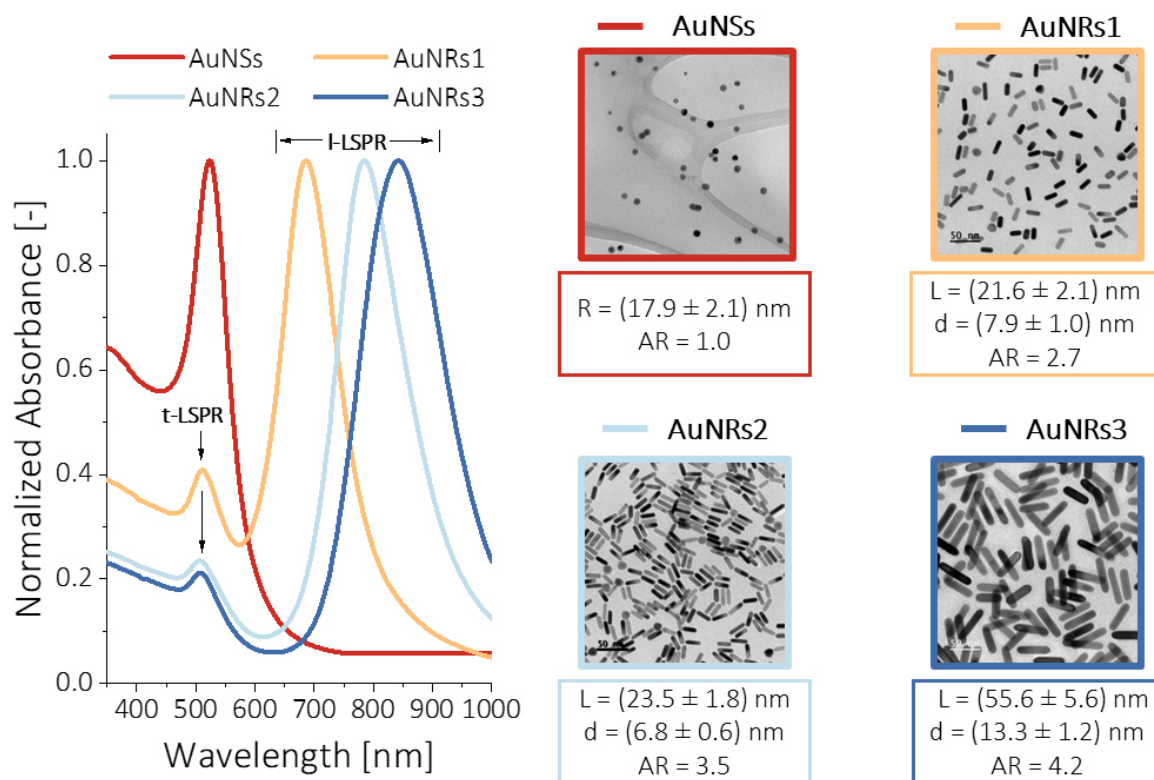


Figure 5. Differences in optical properties of plasmonic Au nanoparticles stemming from their shape (AuNSs vs. AuNRs) and size – own results.

Huge popularity of gold nanostructures among other plasmonic nanoparticles is undeniable and originates from few important properties of gold, such as low cytotoxicity⁶² and chemical inertia, which also leads to the good agreement between optical simulations and experimental results. Moreover, the possibility of shifting AuNPs LSPR to the NIR spectral range (and hence also towards therapeutic optical window⁶³) and easy molecular functionalization through gold-sulphur covalent bond, make AuNPs especially appealing for various fields.

2.1.2. Synthesis of gold nanorods

Typically nanostructures are prepared according to one of two approaches: top-down or bottom-up.⁶⁴ Top-down approach, such as milling or lithography, concerns breaking down macroscopic, bulk materials into smaller pieces. The bottom-up methods enable assembly of nanostructures from smaller building blocks (e.g. atom by atom), which usually provides better control over the morphology and size of the resulting nanomaterials. In case of plasmonic nanoparticles, the most popular synthetic approach is bottom-up assembly based on wet chemical synthesis, which can be performed according to two main mechanisms.⁶⁵ The first one, called nucleation and growth, relies on the fast reduction of metal ions by a strong reducing agent and subsequent overgrowth of the nanostructure around such nucleation centre (**Figure 6**). Monodisperse nanoparticles are obtained by increasing the nucleation rate through the increase of the metal precursor's concentration. This method, however, produces only isotropic AuNPs. The second mechanism, the so-called seeded-growth method, requires formation of small nanostructures – seeds. The following autocatalytic reduction of metal ions takes place on the surface of seeds, leading to the formation of the final nanostructures (**Figure 6**). Their size is directly related to the number of seeds and amount of metal precursor in the growth solution. One of the most popular AuNPs synthesis protocols was published in 1951 by Turkevich *et al.*⁶⁶ This method enables preparation of 13 nm spherical nanostructures by using sodium citrate as both mild reducing agent and surface stabilizer. Over the years the original procedure evolved, including protocols proposed by Frens⁶⁷ and Bastús.⁶⁸ By extending the number of steps, regulating synthesis parameters such as temperature, and performing overgrowth of initial AuNSs, bigger spherical nanoparticles can be obtained.

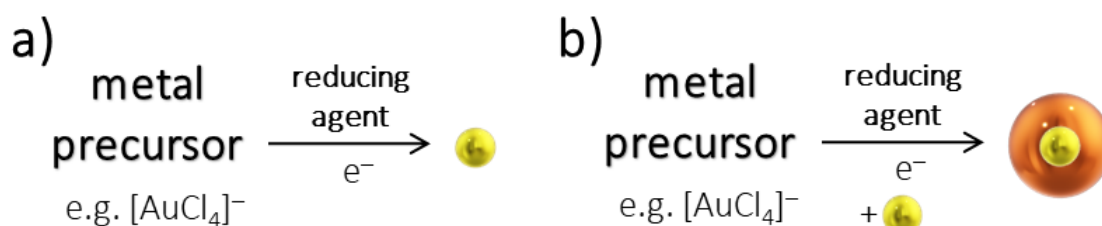


Figure 6. Schematic depiction of two mechanisms of AuNPs synthesis: **a)** nucleation and growth and **b)** seeded-growth approach. Inspired by ⁶⁵.

Spherical nanostructures can be used to synthesise anisotropic shapes, such as nanorods. And although there are wet chemistry techniques such as template⁶⁹ and electrochemical⁷⁰ methods that might be applied, seeded-growth approach remains the most popular and reliable. The most important reason for that is the extensive research attention the method received over the years.^{71,72} Plenty of scientific effort has been put to increase synthesis yields and

monodispersity of the structures, to optimize synthesis conditions or to gain control over the synthesis steps and understand their mechanistic aspects. Seeded-growth technique is very versatile – even faint changes to the synthesis protocol (conditions, additives, ratio between reagents) lead to a vast variety of anisotropic shapes that can be obtained. However, in order for anisotropic nanoparticles to be formed out of the isotropic seeds, a symmetry-breaking event must first take place. Various mechanisms have been proposed,⁷³ including surfactant template effects,⁷⁴ selective inhibition of the growth process of certain crystallographic facets,⁷² or LSPR excitation effects.⁷⁵ The most favoured mechanism, especially in the field of materials science, is the crystallographic one, mostly due to the strong affinity of certain additives towards the adsorption on the metallic surface of nanoparticles.⁷⁵

AuNRs are most commonly obtained as one of two types, namely five-fold twinned pentagonal (elongated in the $\langle 110 \rangle$ direction) or single crystal octagonal (elongated in the $\langle 001 \rangle$ direction). Formation of the specific product is dictated by the composition of the growth solution (**Figure 7**). Pentatwinned AuNRs are obtained upon overgrowth of citrate-stabilized seeds in the growth solution that does not contain Ag^+ .⁷⁶ Their first synthesis yielded only 4% of rod-like nanostructures,⁷⁷ however after careful optimization (mostly of pH and surfactant and reducing agent concentrations) the yield was substantially increased. Pentatwinned nanorods exhibit not only different geometry, but also larger dimensions and higher ARs compared to single crystal AuNRs.

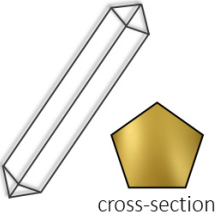
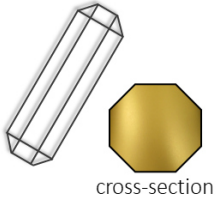
AuNRs	growth solution	structure	size	yield
pentatwinned	Contains Ag^+ ? NO addition: citrate-capped seeds	 cross-section	AR: 6-20	< 30%
single crystal	Contains Ag^+ ? YES addition: CTAB-capped seeds	 cross-section	AR: 1.5-5	~90%

Figure 7. Differences between pentatwinned (top) and single crystal (bottom) AuNRs.

Since all of the AuNRs used for the research part of this dissertation were prepared based on the protocols of single crystal AuNRs synthesis, the following part of the introduction is devoted to this specific synthetic approach. Both theoretical and practical aspects are included, since both are crucial for the understanding of the topic.

Single crystal AuNRs are typically synthesised according to one of two protocols, by Jana *et al.*⁷⁸ or Nikoobakht *et al.*⁷⁹ Both protocols rely on use of surfactant, cetyltrimethylammonium bromide (CTAB) and silver nitrate as key reagents.⁸⁰ In the first step seeds (~2 nm) are obtained upon reduction with strong reducing agent, such as sodium borohydride, NaBH₄, which causes reduction of Au(III) to Au(0). Reducing agent needs to be added quickly and under vigorous stirring in order to induce nucleation homogeneously in the whole solution volume. This produces highly monodisperse seeds. To assure that NaBH₄ is not decomposed before the start of the synthesis, the solution should be prepared using water that has been cooled down in the ice bath beforehand. Moreover, to decrease the decomposition rate, NaBH₄ solution should be prepared directly before reagent addition. The resulting seed solution is brownish in colour and does not exhibit any LSPR band. The as-obtained seeds (which are single crystalline) are transferred to the growth solution where they are subjected to the overgrowth process in the presence of silver ions, Ag⁺. Use of mild reducing agent (such as hydroquinone, HQ or ascorbic acid, AA) in the overgrowth step helps to avoid creation of more nucleation centres,^{71–73} and hence, contributes to the increased monodispersity of AuNRs. Upon addition of AA the reduction of Au(III) to Au(I) occurs, turning the growth solution colourless. Upon addition of seeds, the comproportionation reaction starts and the reduction of Au(I) to Au(0) occurs. Reaction conditions need to be adjusted to acidic pH, since the reduction potential of AA is pH-dependent. This assures that the reduction of Au(I) occurs solely upon the addition of seeds.

Seeds formation and overgrowth are performed in the presence of surfactant, CTAB. Role of the surfactant is crucial, since at high concentrations micelles and bilayers of CTAB stabilize nanoparticles in solution.⁸¹ However, the initial choice of CTAB for the synthesis of AuNRs is an excellent example of a true scientific serendipity. First, CTAB was assumed to serve as a soft template for AuNRs formation, since it creates cylindrical micelles in the presence of Ag⁺.⁷³ Second assumption proposed preferential CTAB binding to the longitudinal facets of AuNRs which directed the Au(III) reduction on the geometric tips of the nanorods.⁷⁶ Currently, scientific discussion points towards crucial role of CTAB as a supply of bromide ions, Br⁻. Nowadays, the role of the counterion seems to be significantly more important and complex than the role of the organic tail, which will be also mentioned a little further in the context of halides as possible synthesis additives. Nevertheless, the exact role of CTAB remains under scientific debate. One of the hypotheses postulates formation of CTA⁺[AuBr₄]⁻ complexes, which increases Au redox potential and enables control over the rate of the gold reduction. The other theory proposes that Br⁻ supplied by CTAB forms insoluble AgBr in the presence of

Ag^+ .⁸² It is presumed that salt blocks high surface energy facets of gold, thus preventing their overgrowth.

Considerations dedicated to the role of CTAB inevitably lead to the question about the role of silver ions, which are the second key component for the synthesis of single crystal AuNRs. Exactly as it is for the surfactant, different roles of silver have been proposed over the years and its true function is still under debate. The most popular hypotheses include: Ag^+ as a nanorods capping agent in a form of specific complex, $\text{Ag}[\text{BrCTA}]_2$;⁸⁰ induction of the soft template effect by modifying CTAB micelle formation;⁷³ underpotential deposition (UPD) of $\text{Ag}(0)$ atoms.⁸³ Importantly, presence of Ag^+ seems to be influencing the selectivity of gold reduction – in the presence of Ag^+ synthesis of pentatwinned AuNRs is hindered, while single crystal AuNRs are elongating with the increasing silver concentration. Growth process of the latter is relatively slow and needs several hours to be completed. In contrast to pentatwinned AuNRs, for which steady redshift of 1-LSPR and hence also constant increase of the AR can be observed, single crystal AuNRs grow in two distinct stages. In the first stage the rapid redshift occurs, thus indicating quick formation and elongation of the rod-like structures. Xia *et al.*⁸⁴ identified two key aspects of this symmetry-breaking event – transformation of isotropic seeds towards anisotropic rods (under kinetic control) and stabilization of crystallographic facets (under thermodynamic control). In the second stage a blueshift of the 1-LSPR band can be observed, which is mainly related either to the growth of nanostructures in the isotropic manner or to the reshaping of the tips.

Although the composition of the growth solution in the seed-mediated synthesis of AuNRs may be perceived as complicated, each reagent plays a specific and important role and cannot be omitted. There are many comprehensive publications focused on unravelling the interplay between synthesis parameters in order to better understand AuNRs formation mechanism and possible optimization pathways.^{85–88} One of the commonly used mechanistic investigation techniques is introduction of additives. And so, the introduction of different halides has been linked to the formation of specific shapes in otherwise the same experimental conditions. DuChene *et al.*⁸⁹ proposed AuNRs' growth from citrate-capped seeds in the facet-selective manner based on the adsorption of different halides (**Figure 8**). By introducing potassium iodide or replacing CTAB with CTAC (cetyltrimethylammonium chloride) it has been found that another morphologies of AuNPs can be formed, such as nanoplates⁷² or nanoprisms.^{90,91} This emphasises that the shape control is relying on use of appropriate halides and ratio between them and Ag^+ .⁹² This is how it has been realized that the presence of Br^- is crucial to the AuNRs formation. Pivotal role of bromide is emphasised from the very start of the synthesis by Br^- interactions with HAuCl_4 , tetrachloroauric acid, the most widely used

source of Au(III). Au(III) forms square planar complexes and Br^- affinity to Au(III) is stronger than the one of Cl^- . Hence, the complexation of Au(III) with Br^- occurs in the presence of CTAB. From the practical point of view it means that the experimenter needs to wait for the formation of $[\text{AuBr}_4]^-$ complex (which is manifested as a solution colour change from bright yellow, to orange) before any other reagent is added.

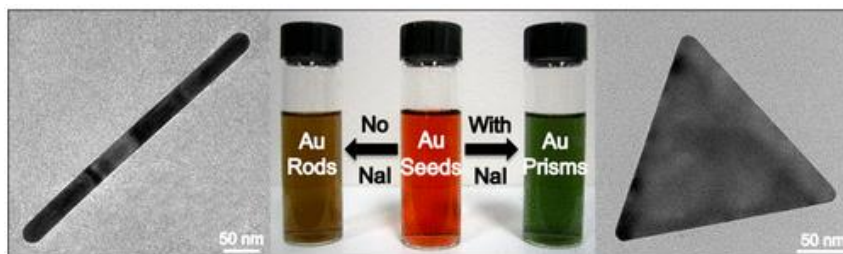


Figure 8. Shape of the nanoparticles can be drastically changed even upon minor changes in the composition of the growth solution, such as introduction of trace amounts of iodide. Reprinted from ⁸⁹.

Upon mechanistic investigations also other additives were used, including e.g. sodium oleate or the salicylic acid. The first one led to the formation of binary surfactant mixture with CTAB and, as a result, longer AuNRs were obtained.⁹³ On the other hand, salicylic acid and its salts were able to intercalate to the CTAB bilayer (via hydrophobic interactions) which led to better product quality due to the better control over symmetry breaking event.⁹⁴ Scarabelli *et al.* undertook the synthesis in the presence of 5-bromosalicylic acid acting as both co-factor and reducing agent (for Au(III) to Au(I) reduction).⁸⁶ They observed that through this modification the improved yield of Au reduction and better AR tuning can be achieved.

The more advanced mechanistic investigations focus on variation of experimental parameters beyond synthesis reagents. Sanchez-Iglesias *et al.* have found that thermal treatment of Au seeds may lead to seeds twinning and, as a result, to yield improvement.⁸⁷ Authors have also slightly modified seeds by addition of second metal – palladium – which allowed them for seed localization in the final nanostructures (**Figure 9**). In case of AuNRs, seeds were mostly localized off the centre of the rod-like geometry, leading to new questions regarding the symmetry-breaking event.

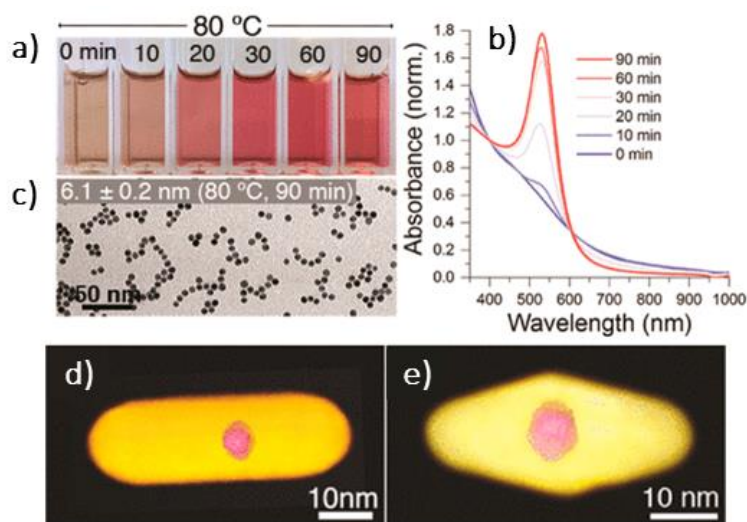


Figure 9. Influencing the synthesis of AuNPs by thermal treatment of seeds (80°C). **a)** Visual appearance and **b)** matching UV-Vis absorption spectra of the seed solutions after thermal treatment for different times. **c)** TEM image of the seed batch treated for 90 min. **d)** 3D visualisation of the individual gold nanorod and **e)** gold bipyramid with the Pd-coated gold seed, deepening the understanding of the anisotropic growth mechanism. All panels reprinted from⁸⁷ and rearranged for presentation.

Taking into account all possible modifications that can be introduced for a single process is there still some room for a step further? Or maybe after so many years of scientific focus we have utilized all possible tools? Certainly not, since, for instance, new technologies can be harnessed to understand the synthesis of AuNRs better. Grzelczak *et al.* employed Bayesian optimization, a black-box optimization protocol,⁹⁵ and machine learning to unravel more information on the AuNRs synthesis and find new connections between synthesis conditions.⁸⁸ Authors used Gryffin⁹⁶ experimental planner, an especially effective tool for the synthesis of AuNPs. Such methods showcase how the scientific toolbox available for researchers evolved through time. Authors varied temperature and concentrations of Ag^+ , AA, HCl, and seed to find which conditions produce AuNRs with similar optical properties (**Figure 10**). New synthesis parameters have been identified, enabling almost 5 times faster synthesis. Also new synergy between reagent and physical parameter, namely AA concentration and temperature was found. It was revealed that these two parameters can balance respective undesirable influences, such as shortening of AR at higher temperature and possible secondary nucleation occurring upon AA addition.

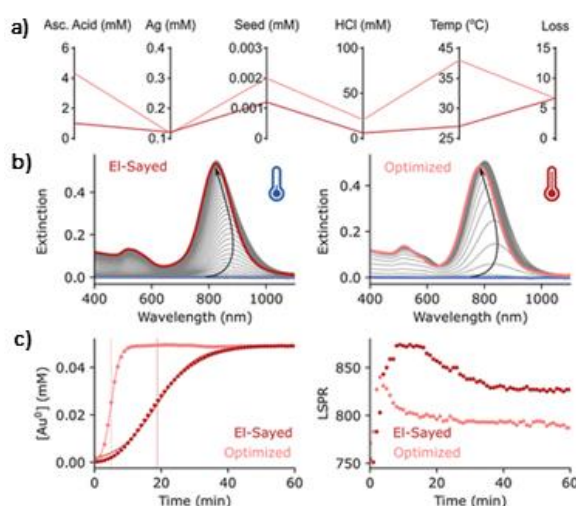


Figure 10. Comparison of the most popular protocol for the synthesis of AuNRs (El-Sayed⁷⁹) and the same synthetic protocol optimized by Bayesian optimization protocol. **a)** Parallel coordinate graph comparing experimental conditions resulting in the AuNRs exhibiting the same optical properties. **b)** Evolution of the AuNRs UV-Vis-NIR absorption spectra over time, monitored during synthesis performed according to base (left) and optimized (right) protocol. **c)** Evolution of the Au(0) concentration (left) and l-LSPR position over time, showcasing that optimized parameters lead to the faster formation of the desired product. Reprinted from ⁸⁸ and relabelled.

Finally, some practical aspects of the AuNRs synthesis conclude this subchapter, for all of the considerations presented above are verified in the real laboratory conditions. There are several key aspects that need to be taken into account while adapting literature protocols or, otherwise, the products will not exhibit desired characteristics. Such practical aspects are also an important topic of literature reports. Here, only a chosen few, crucial for AuNRs and AuNPs synthesis in general, are listed following work by Scarabelli and co-workers⁸⁰:

- (1) **Water quality** – to efficiently synthesise nanostructures Milli-Q grade water (meaning deionized and filtered, however not distilled) is required. Since protocols rely on specific pH conditions, pH of the water can be in some cases decisive. Moreover, water is one of the main sources of impurities in the synthesis, and these can strongly influence e.g. the AR of the AuNRs.
- (2) **Glassware** – besides the good laboratory practice that requires use of clean glassware, for the synthesis of AuNPs each glass piece must be also washed with *aqua regia*. This step removes any metal residues, which is key if the equipment is repeatedly used for the synthesis of Au nanostructures. Remaining metal residues may act as unintended nucleation centres leading to not only the disruption of the synthesis, but in many cases, total aggregation of metallic Au.

- (3) **Supplier and purity of chemicals** – sole example of CTAB may illustrate that differences in the reagent purity (very often being a result of different reagent suppliers) can drastically affect the morphology of nanostructures. Typically BioXtra quality CTAB or CTAB for molecular biology are used, because they are specifically purified to remove redundant halides, especially Γ^- . It has to be emphasised, that even iodide content below 3.0 ppm may compromise the synthesis of AuNRs.
- (4) **Proper handling of stock solutions** – some of the stock solutions for the synthesis may be stored for months (e.g. CTAB), however some of them should be prepared freshly for each synthesis, like solutions of Ag^+ and AA. HAuCl_4 stock solution can be kept for over a year if properly stored, meaning kept in the fridge and away from any light source.

By applying these and other important rules and upon individual optimization of the synthesis protocols (which very often requires multiple parameters to be varied, since synthesis depends not on the singular reagent concentration, but ratios between chemicals⁹⁷) desired results in terms of structural and also optical properties can be successfully obtained.

2.2. Plasmon-related effects as important catalytic tools

Chemical transformations triggered by light have been scientifically appealing for a very long time. Photocatalysis finds its use e.g. in organic synthesis,⁹⁸ hazardous waste remediation,⁹⁹ or wastewater treatment.¹⁰⁰ Alongside transition metal complexes,¹⁰¹ metal oxide semiconductors,¹⁰² and metal-free organic dyes¹⁰³ serving as photocatalysts, plasmonic nanoparticles¹⁰⁴ are especially interesting candidates for many reasons. Firstly, their properties are entirely tunable through the control over the size, shape, and composition. This enables preparation of systems precisely designed for specific applications. Secondly, due to the available surface-functionalization approaches, plasmonic nanoparticles can be immobilized on different types of substrates and are very attractive as heterogeneous catalysts. Thirdly, the recyclability of the nanostructures is usually higher than the recyclability of molecular catalysts. Finally, their unique interactions with light upon irradiation at resonant frequency are the foundation of chemically useful phenomena, such as local electromagnetic field enhancement, generation of highly energetic (hot) charge carriers, or photothermal effect. Hence, strong interactions between light and plasmonic nanoparticles enable very precise spatial control over the triggered photocatalytic processes. Their resolution is even smaller than the wavelength of the incident light, because plasmon effect confines light's energy to a nanometer-scale area of effect, which allows the photocatalysis to be performed under lower irradiation intensity. Of course, there are some drawbacks of plasmonic nanostructures, such as not efficient catalytic

use of the inner atoms or the hindering effect of the capping ligands. These, however, do not surpass the undeniable advantages of plasmonic nanoparticles that manifest during photocatalytic processes.

Since catalytic properties of plasmonic nanoparticles stem from the interactions between nanostructures and light, it is essential to describe what phenomena follow the photoexcitation of these nanostructures.

Absorption of a photon by a metallic nanoparticle can be enhanced by exciting LSPR (**Figure 11a**). Typically, within the first 1–100 fs after excitation, surface plasmons dephasing occurs and the highly energetic electron-hole pairs are produced via Landau damping and other photon-electron interactions (**Figure 11b**).¹⁰⁵ Excited electrons have energies in a range from the Fermi level E_f up to $E_f + \hbar\omega_0$ (where the frequency of the incident light is represented by ω_0) and the energies of the holes range from $E_f - \hbar\omega_0$ up to E_f .¹⁰⁶ Within this time, the excited plasmon resonances are relaxed either radiatively (by re-emission of a photon, however with low probability) or through non-radiative paths (via electron-electron interactions resulting in the carrier multiplication). The following redistribution of the energy of the highly energetic carriers ensues mostly through electron-electron scattering within a 100 fs–1 ps timeframe (**Figure 11c**).^{105,107} Subsequently, on a scale of 1–5 ps, transfer of the generated heat inside of the nanostructure takes place by electron-phonon scattering, followed up by the phonon-phonon and phonon-surrounding scattering (even up to 10 ns from the excitation, **Figure 11d**).¹⁰⁷ All of the abovementioned relaxation mechanisms overlap over time.¹⁰⁸ Timescales of these processes depend on the external temperature, beam intensity, properties of the environment, and particle size.^{105,109}

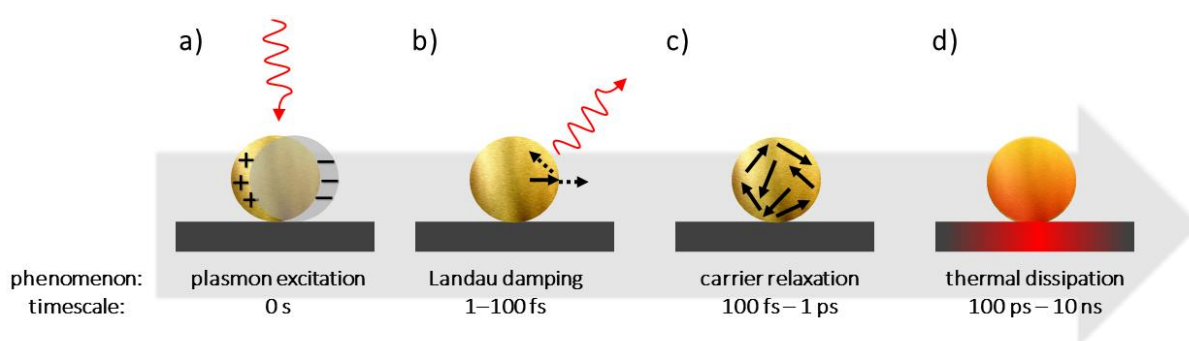


Figure 11. Relaxation processes occurring after **a)** photoexcitation of a single plasmonic nanoparticle. **b)** Decay of the athermal distribution of highly energetic electron-hole pairs through re-emission or carrier multiplication. **c)** Hot carriers energy redistribution via electron-electron scattering. **d)** Heat transfer from a metallic nanoparticle to its surroundings. Figure based on ¹⁰⁵.

These phenomena reflect in the spectral parameters of the LSPR, namely the bandwidth, which is proportional to the total relaxation rate Γ .¹¹⁰ Γ is proportional to both the non-radiative electronic relaxation processes Γ_{nr} and the radiative decay rate Γ_r ¹¹¹:

$$\text{Equation 7. } \Gamma = \Gamma_{nr} + \omega^2 \Gamma_r \text{ ,}$$

where ω^2 factor indicates that the influence of the radiative term decreases with the decreasing SPR frequency. According to the classic electrodynamic theory, the Γ_r term is related to the emission of far-field radiation of the accelerating and decelerating charged particles. The non-radiative term Γ_{nr} is related to the dephasing mechanisms described above, namely: electron-electron (e-e) scattering, electron-phonon (e-ph) scattering, electron-defects scattering (e-d), and damping caused by surface effects (s), which can be expressed according to the Matthiessen law¹⁰⁷:

$$\text{Equation 8. } \Gamma_{nr} = \frac{1}{t_{e-e}} + \frac{1}{t_{e-ph}} + \frac{1}{t_{e-d}} + \frac{1}{t_s} \text{ .}$$

Therefore, dumping frequency increases for polycrystalline or defective nanostructures, and hence, for such nanostructures, larger LSPR band is produced.¹¹²

Regarding radiative relaxation of plasmons, typical photoluminescence efficiency of plasmonic nanostructures is below 10^{-3} – 10^{-5} ,¹¹¹ however, it is still five or even seven orders of magnitude higher than for the bulk Au.¹⁰⁷ The strongest contribution to the photoluminescence mechanism is often attributed to the surface impurities.¹¹³

In order to efficiently boost chemical reactions by means of plasmonic photocatalysis, different aspects need to be taken into account, in particular¹¹⁴:

- 1) **All factors influencing surface plasmons.** Here, especially size, composition, and morphology of the nanoparticles need to be considered, since these features control light harvesting properties of the plasmonic system. Typically nanoparticles in a 10–180 nm size range are used and the bigger nanostructures are applied in the scenarios where enhancement of the electromagnetic field is required. Size of the nanostructure also influences lifetime of the highly energetic carriers, as well as their production rates.¹¹⁵
- 2) **All factors influencing the course of the chemical reactions in question.** Here, surface activity should be scrutinized, including use of reaction mediators. First type of mediator, such as small size platinum nanostructures that can be attached to bigger Au or Ag nanostructures, assures catalytically active sites. Second type, such as semiconductor, mediates charge transfer and compensates for short lifetimes of highly energetic charge carriers. Moreover, adsorption of the reactant, formation of the

intermediate, and desorption of the product should also be considered, however these are usually more complex to analyse.

- 3) All factors related to the coupling between adsorbed molecules (reactants or mediators) and surface plasmons.** Here, surface and interface play the most important role. Especially for the charge transfer process the nature of the contact at the heterojunction is significant. For metal-semiconductor contacts there are two type of contacts: Ohmic and Schottky. Both can permit or filter specific charge transfers. Moreover, in case of nanostructures synthesised in the presence of surfactants forming the stabilizing layer on the surface of nanocrystals, hindering effect of the surfactant layer may be observed. Especially for the reactions requiring short distance between reactant and plasmonic nanostructure.

The following subsections focus on the catalytically useful plasmon-related phenomena, namely: local field enhancement, hot charge carriers generation, and photothermal effect. For each phenomenon a few exemplary photocatalytic processes are presented. The last subsection emphasises the difference between intra- and interband transitions.

2.2.1. Local Electromagnetic Field Enhancement

At resonance, the collective oscillation of the conduction band electrons in the metallic nanostructure causes near-field electromagnetic enhancement.¹¹¹ At resonance conditions, the depolarization and polarization fields are in phase, hence, the amplitude of the electric field increases in a close vicinity to the accumulating charges, namely at the surface of the nanostructure. The enhancement can be observed at a distance of a few nanometers around the nanoparticle. The local field enhancement factor (EF) can be expressed as:

$$\text{Equation 9. } EF(\vec{r}) = \frac{E_{loc}(\vec{r})}{E_0} ,$$

where \vec{r} is the position vector of any point, E_{loc} is local electric field, and E_0 is the incident electric field.¹¹⁶

Local field enhancement is limited to the so-called near-field zone and for an individual nanosphere in the quasistatic regime local field is inversely proportional to the third power of the distance from the surface of nanostructure, r^{-3} . If the localized surface plasmons in the Au nanosphere are approximated to oscillating dipole (described by dipole moment \vec{p}), the local electric field can be described as:

$$\text{Equation 10. } \vec{E}_{loc}(r) = \vec{E}_0 + \frac{3\vec{n}(\vec{n}\cdot\vec{p})-\vec{p}}{4\pi\epsilon_0\epsilon_m} \frac{1}{r^3} ,$$

where \vec{n} is the unit vector pointing to the direction of interest and normal to the surface of the nanostructure.¹¹⁶

Excited nanoparticles are called “nanoantennae”, since they act as both light controllers and guides. In case of single, isolated nanostructure, electromagnetic field can be enhanced by three orders of magnitude in a 10-50 nm range around the surface (depending on the morphology of nanostructure and type of the dielectric medium).¹¹⁷ For nanostructures with tips (such as nanorods) and edges (such as nanoplates), the local field enhancement is especially pronounced.¹¹¹ These specific morphological features are called ‘hot spots’,¹¹⁸ (**Figure 12**) and can be also observed between two nanostructures oriented close to each other.¹¹⁹

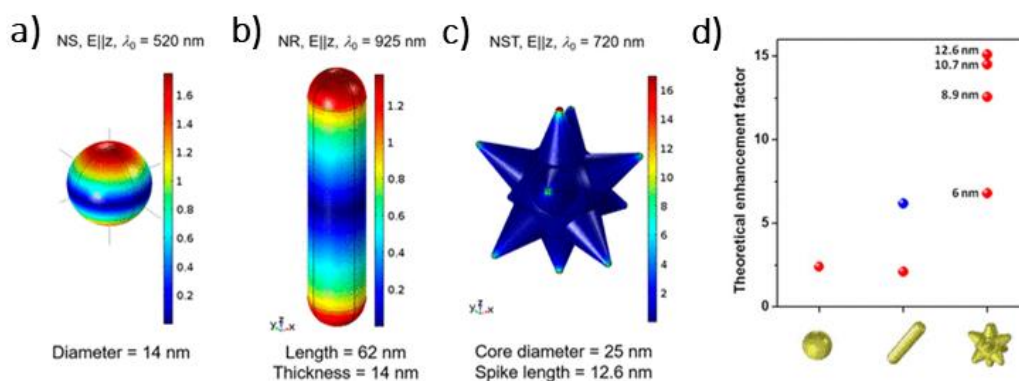


Figure 12. Visualisation of the morphological hot spots. Normal-to-surface field maps (for the LSPR peaks) calculated for different morphologies of nanostructures – **a)** nanospheres, **b)** nanorods, and **c)** nanostars. **d)** Theoretical enhancement factors determined for the morphologies presented in a-c. Results for nanostars include morphologies with the same core size but different spike lengths. For nanorod the enhancement factor represented by the blue dot refers to the parallel orientation of the rod with respect to the incident electric field vector. Reprinted from ¹²⁰. Rearranged for presentation.

At the junction of two nearby nanostructures, the enhancement by a factor of even 10^6 can be observed¹¹⁷ (**Figure 13**). Concept of plasmon hybridization¹²¹ (an analogy to the molecular orbital hybridization) enables design of specific structures providing precise field enhancement at exact nanoscale-located spots.

The phenomenon is particularly useful in sensing,¹¹⁹ plasmon enhanced fluorescence,^{122,123} near field microscopy,¹²⁴ and has been a foundation of surface enhanced Raman spectroscopy¹²³ (SERS). SERS is one of the crucial modern technologies and enables, e.g. single-molecule detection.¹²⁵

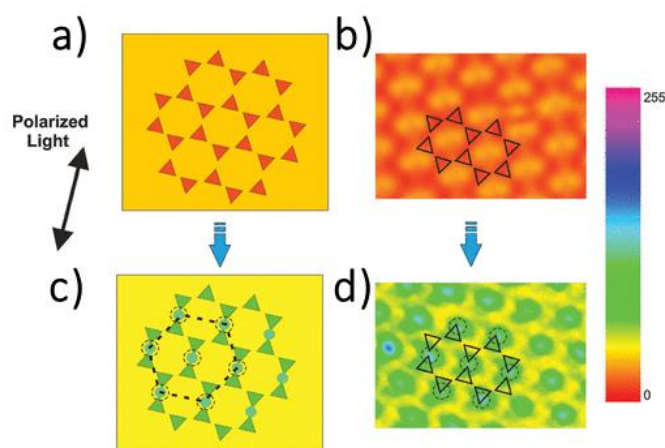


Figure 13. Visualisation of hot spots in the arrays ($0.65 \mu\text{m}$) of gold nanotriangles with 25 nm silica layer on top. **a)** Model and **b)** optical transmission image before addition of dye. **c)** Model and **d)** optical transmission image after addition of dye (same area as panel b). Reprinted from ¹²⁶ and relabelled for clarity.

Photochemistry mediated by local field enhancement is correlated to the excitation of the reacting molecules. To assure efficient resonant energy transfer the energy overlap between the HOMO-LUMO gap of the molecule and the plasmonic field is required.¹²⁷ The enhanced near-field enables¹¹⁴:

- 1) **increase of the light absorption** due to the extended light pathway or/and increase in the light intensity;
- 2) **control** over the reaction **on the nanometer scale**;
- 3) performing reactions under **low-intensity illumination**.

Local electromagnetic field enhancement has not been as central to the plasmon-mediated catalysis as photothermal effect or employment of highly energetic charge carriers. Nevertheless, there are examples of its efficient catalytic use. For instance, Scaiano *et al.* showed the cross-linking of trimethylolpropane triacrylate initiated by the enhancement of the electromagnetic field in the vicinity of the AgNPs.¹²⁸ Authors postulated amplified photodegradation of the reaction initiator, 2,2'-azo-bis-isobutyronitrile, due to the catalytic effect of Ag nanostructures, which was manifested by the formation of polymer shell (6 nm thick) around the AgNPs. Another example is work of Christopher *et al.*, focused on the use of heterometallic Ag@SiO₂/Pt nanostructures in the photocatalytic CO oxidation.¹²⁹ Size of the nanocatalyst was determined to be crucial for the efficiency of the reaction. Too large Ag cores were leading to substantial efficiency decrease due to light scattering beyond the photocatalyst bed. Only for the appropriate size range of the plasmonic cores the field enhancement at the Pt interface translated into efficient catalytic reaction. These results

emphasize the importance of different aspects and their interplay that need to be considered upon designing the plasmonic system for the photocatalytic purposes (**Figure 14**).

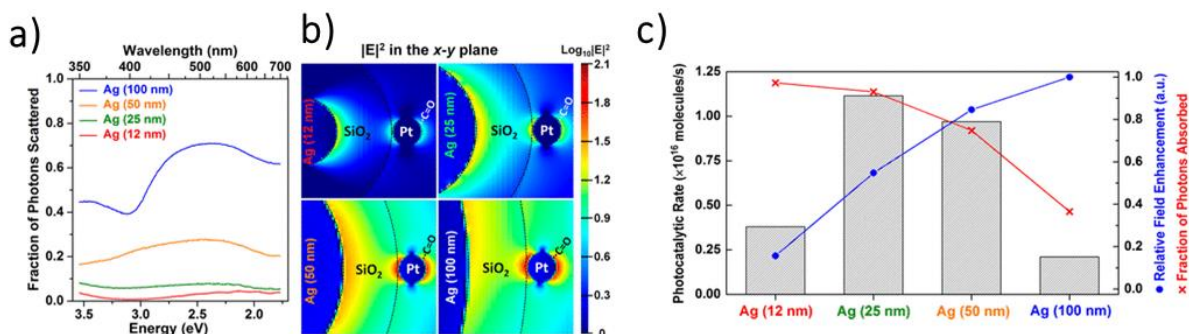


Figure 14. *Ag@SiO₂/Pt heterostructures - investigation of the influence of different Ag plasmonic core sizes. a) Monte Carlo simulation of the wavelength-dependent scattering on the catalyst bed. b) FDTD simulations of x-y plane electromagnetic field distributions at the surface of Pt component at 500 nm. c) Comparison of the fraction of the absorbed photons – red crosses, relative field enhancements at the surface of a Pt component – blue dots, and measured photocatalytic rates (white light, 600 mW/cm²) – column bars. Reprinted from ¹²⁹ and rearranged for presentation.*

In another example, Cronin *et al.* presented that addition of Au nanostructures (5 nm-thick nanoislands of Au) to the TiO₂ (exhibiting strong catalytic properties) leads to the enhancement of the photocatalytic water splitting under visible illumination by a factor of 66.¹³⁰ The 5-fold increase in the photocurrent under visible light irradiation was attributed to the local field enhancement. Watanabe *et al.* relied on similar photocatalyst design and presented 7 times enhanced decomposition of methylene blue under near UV illumination of the photocatalyst consisting of 50 nm spherical AgNPs coated with 50 nm-thick SiO₂ shell and covered with 90 nm-thick TiO₂ film.¹³¹

2.2.2. Highly energetic charge carriers

Relaxation pathways of plasmon excitations are described in the introductory part of **Section 2.2**. However, from the photocatalytic point of view, it is more important to harness the highly energetic charge carriers, generated upon plasmon excitation, in order to accelerate chemical reactions. Plasmon-mediated mechanisms open new pathways of chemical processes, just as in work of Schlücker *et al.*¹³² where photocatalytic reduction of 4-nitrothiophenol to 4-aminothiophenol in the presence of AgNPs and without conventional chemical reductants was reported. On the other hand, awareness of the plasmon-mediated photocatalytic phenomena may help to rule out misinterpretation of some crucial results, as presented by Tian *et al.*¹³³ who

described highly undesirable effect of selective oxidation of p-aminothiophenol (an important probe molecule in SERS) to 4,4'-dimercaptoazobenzene on Ag nanoparticles at room temperature and under measurement conditions.

Upon excitation of plasmonic nanoparticles at resonant conditions the energy distribution of the charge carriers population broadens. Some of the electrons are called 'hot' because their energies are above those corresponding to a Fermi-Dirac distribution at room temperature.¹⁰⁵ Hot carriers (electrons or holes) can be injected from the plasmonic metal to a reactant molecule (through the transient electronic exchange) or to the mediator remaining in contact with plasmonic structure, such as semiconductor exhibiting suitable energy levels.¹³⁴ Generally, there are five major pathways for hot carriers harvesting. The first one concerns **indirect hot electron injection into the adsorbate**. In this pathway the deposition of the kinetic energy of transferred electrons activates the reactant, leading to its vibrational excitation, which may further result in breaking of chemical bonds. The lowest unoccupied molecular orbital (LUMO) of the adsorbate serves as a transient energy reservoir for hot electrons. Halas *et al.* presented dissociation of H₂ according to this mechanism.¹³⁵ Photocatalytic activity of AuNPs was presented at room temperature, despite the large activation barrier of this reaction. Authors postulated existence of shortly lived H₂^{δ-} transition negative ion, which accumulated vibrational energy necessary to induce stretching of the H – H bond. Another example is work of Linic *et al.*, who presented that Ag nanostructures can drive catalytic ethylene, CO, and NH₃ oxidation under low-intensity irradiation, via formation of transient negative ion state out of oxygen, O₂.¹³⁶ Reactions were carried out under visible light source of the intensity equal to 2-3 times solar irradiation intensity. The UV irradiation was almost entirely removed to minimise the possibility of interband transitions. The pathway of indirect hot electron injection into the adsorbate can be even further advanced by the development of bimetallic plasmonic core-shell designs, which may facilitate coupling of hot carriers with vibrational modes of the adsorbate, according to Norris *et al.*¹³⁷

Hot **electron transfer** can also occur **directly into the adsorbate** for reactants exhibiting strong interactions with metal surface.¹³⁸ In such case, direct promotion of the excited electron to the hybridized adsorbate-metal states occurs upon plasmon decay. Such a mechanism, without mediation of the hot electron states, is not very common. One of the examples is work of Christopher *et al.*, in which authors reported CO oxidation on the surface of Pt nanostructures (below 5 nm) in H₂ rich streams.¹³⁹ By using nanostructures bigger than 2 nm authors avoided formation of bulk Pt oxide. At the same time, by imposing the 5 nm size limit of the structures, they increased the surface to volume ratio in order to maximize light absorption. Postulate of the adsorbate-specific resonant photon induced activation was confirmed in the preferential

oxidation experiments. Hence, the results confirmed that selectivity in plasmon-driven catalysis can be rationally controlled. Especially useful for the investigation of this catalytic pathway seems to be SERS, which has been utilized in the investigation of the dimerization reactions leading to the formation of 4,4'-dimercaptoazobenzene as the model molecule. Reactions were carried out on various plasmonic structures, including Au, Ag, and Cu films,¹⁴⁰ and silver nanoflowers resembling peonies.¹⁴¹

Differences between indirect and direct hot electron transfer are depicted in **Figure 15**.

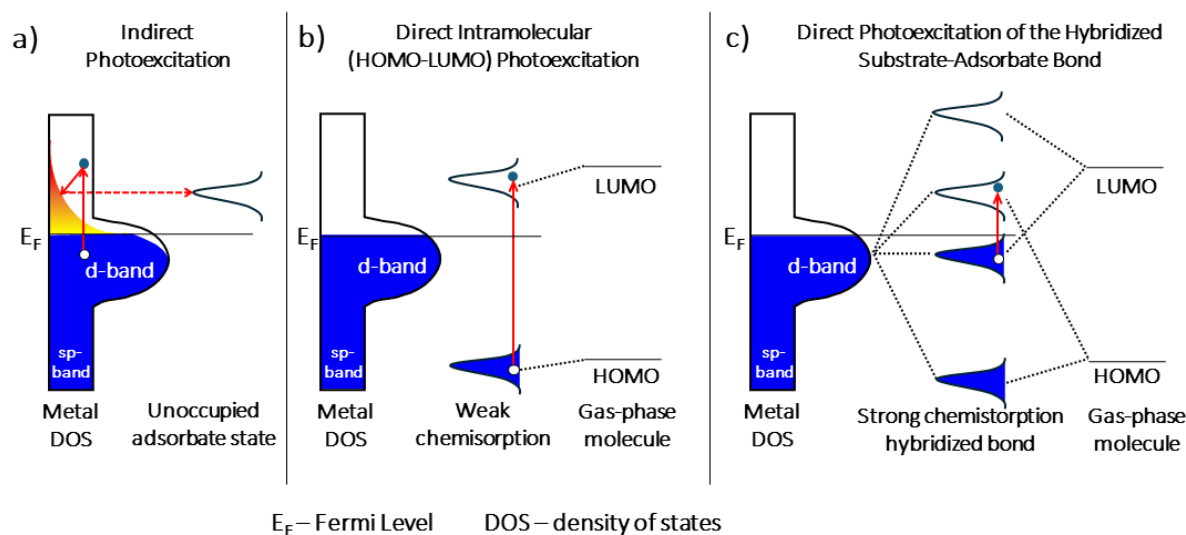


Figure 15. Schematic depiction of the photoexcitation pathways on the metal surfaces. **a)** Photon absorption in the bulk transition metal creates distribution of hot charge carriers which may undergo transient transfer into the unoccupied adsorbate states (indirect photoexcitation). **b)** For the weakly chemisorbed adsorbates their photoexcitation is similar to the one occurring for the molecules in the gas phase. The only difference lies in the broadened and stabilized electronic states, due to the presence of the metal substrate (direct intramolecular photoexcitation). **c)** For the strongly chemisorbed adsorbates hybridization between *d*-states of the metal and molecular states of the adsorbate occurs. In such case resonant electronic transitions take place between the hybridized states (direct photoexcitation of the hybridized substrate-adsorbate bond). Figure based on ¹³⁹.

Certainly hot electrons are much more commonly mentioned in the context of plasmon-mediated catalysis, however **hot holes** mediate the third important photocatalytic pathway. Hot holes can accept electrons transferred from the highest occupied molecular orbital (HOMO) of the adsorbate to the plasmonic nanostructure. For instance, Jia *et al.* presented oxidation of benzyl alcohol at the surface of CuPt@TiO₂.¹⁴² Authors postulated, that although the generated hot electrons are injected in the TiO₂, they do not interact with the substrate and the whole

reaction is carried out due to hot holes. Hot holes stabilize the substrate and lead to the breaking of the $O - H$ bond in the benzyl alcohol molecule. Again, size of the catalyst was emphasized to be one of the crucial aspects, since the mean free paths of hot holes are relatively short (below 1 nm). Hence, the size of the metal nanostructures needed to be limited. Role of hot holes was also discussed by Brus *et al.* in their work focused on the hot holes-induced oxidation of the surface stabilizing agent of Ag nanostructures.¹⁴³ Upon low-intensity 514 nm irradiation of silver nanoparticles adsorbed on ITO, citrate ions were oxidized and, as a result, degradation of plasmonic nanostructures ensued.

The fourth important type of hot carriers harvesting is another indirect pathway involving **hot electron injection into the semiconductor**. In such cases, plasmonic nanoparticles do not necessarily provide catalytically active sites (although they can), but mostly act as light absorbers. This scenario is one of the most commonly reported ones, mainly because it broadens application of the semiconducting nanostructures, which typically require high energy excitations, since they exhibit absorption in the UV region of the spectrum. Typically most commonly used semiconductors are TiO_2 and ZnO_2 . By coupling of plasmonic nanoparticles and semiconductors, the spatial separation of the excited electron-hole pairs can be achieved, thus increasing carriers' lifetime. However, the contact between metal surface and semiconductor results in the alignment of their Fermi energies. Due to the transformation of the surface states of both materials, bending of the valence and conduction bands ensues, resulting in the formation of a Schottky barrier (its typical magnitude is 0.5-1.5 eV¹⁴⁴). Hot electrons injection in the semiconductor may occur only if carriers can surpass this threshold¹⁴⁵ (see **Figure 16**). Wei *et al.* presented that Au/ TiO_2 heterostructures might be used for the visible-light-driven (irradiation above 515 nm) hydrogen evolution from water.¹⁴⁶ Authors also reported, that the lifetimes of hot electrons injected from plasmonic component are two orders of magnitude longer than those of electrons photogenerated upon UV excitation in the semiconducting unit. After the injection electrons diffuse within the conduction band. One fraction of the hot carriers population participates in the catalytic transformation on the semiconductor's surface, while the other fraction might be trapped in the states inside the bandgap. This, however, does not limit their ability to promote the occurrence of chemical reactions. Surface properties of the heterogeneous plasmonic-semiconducting catalysts, particularly the oxygen vacancies, were investigated by Zhang *et al.*¹⁴⁷ Authors focused on the aerobic alcohol oxidation on Au-BiOCl photocatalyst. The investigated reaction typically exhibits low efficiency due to weak interactions between O_2 and the surface of the photocatalyst. Moreover, the overoxidation or mineralization may occur due to the strong oxidizing power of the holes photogenerated in the semiconductor. Hence, proper photocatalyst

design is necessary to successfully perform the process. One of the most typical defects in BiOCl are oxygen vacancies, which enable enhanced O₂ adsorption and may serve as trapping sites for hot plasmon-generated electrons in the plasmonic-semiconducting heterostructure. Such material design, relying on two components, also enables separation of hot carriers from Au, and thus strongly oxidative holes are not participating in the process.

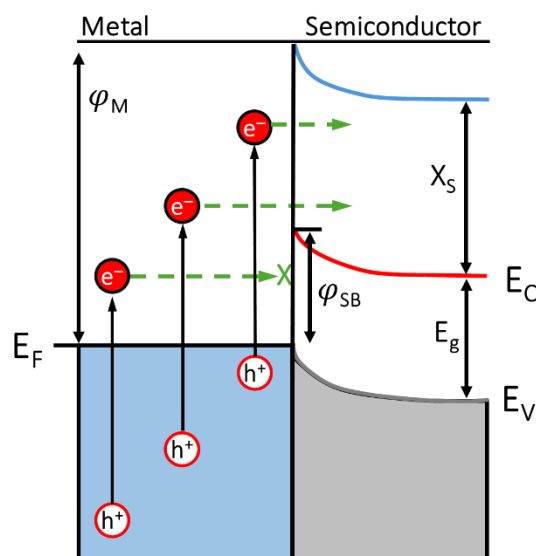


Figure 16. Schematic depiction of the Schottky barrier at the metal-semiconductor junction. Hot electrons (energies above Fermi level – E_F) with proper energies can overcome the barrier (ϕ_{SB}) and be injected into the conduction band of the semiconductor (E_C). Other abbreviations: ϕ_M – metal workfunction, X_S – semiconductor electron affinity, E_g – semiconductor bandgap, E_V – semiconductor valence band. Figure based on ¹⁴⁸.

Finally, the last possible pathway is **direct hot electron injection into a semiconductor**. In contrast to the fourth process, this is a one-step hot electron transfer in which electrons from metal equilibrium states are directly promoted to the semiconductor conduction band. Hence, the energy losses due to electron-electron and electron-phonon scattering can be avoided, increasing the overall efficiency of the process. Lian *et al.* prepared Au-tipped CdSe nanorods (dumbbell morphology) and observed >24% quantum efficiency of the charge separation.¹⁴⁹ Process was also polarization dependent and more efficient upon excitation along the nanorod axis. Moreover, Sönnichsen *et al.* linked the direct plasmon decay with the bandgap of the semiconductor.¹⁵⁰ Authors investigated AuNRs covered with three different semiconductors, namely Al₂O₃, HfO₂, and TiO₂. They observed faster decays for the heterostructures with semiconductors exhibiting smaller bandgaps.

To summarize, transfer of highly energetic charge carriers constitutes an important and diversified photocatalytic mechanism. Catalysts relying on the heterogeneous

plasmon-semiconductor nanostructures seem to be the most popular and reliable ones, due to the significant scientific attention they received. However, as it is often emphasised, this field still requires a lot of exploration and many aspects remain unexplained.¹⁵¹

2.2.3. Thermal effects

One of the most important nonradiative plasmon damping phenomena is transformation of the energy absorbed by the nanoparticle into heat. Generated heat dissipates locally at the surface of the plasmonic nanostructures¹⁵² and can be used e.g. in targeted photothermal cancer therapies.^{153,154} Moreover, since the reaction rates of chemical processes are affected by temperature according to the Arrhenius law, triggering of the thermoplasmonic effect is one of the very efficient approaches to the plasmonic photocatalysis.¹⁵⁵ Plasmonic nanoparticles can be used as nanoheaters, namely to increase the rates of chemical reactions by providing energy necessary to overcome the energy barriers. Plasmonic nanostructures are better light to heat converters than other materials,¹⁵⁵ mostly due to their large absorption cross sections and low probability of the radiative relaxations of excited electrons. Moreover, the employment of heat at the nanoscale is especially effective because of the confinement effect.¹⁵⁶ Hence, the processes can be very precisely addressed and the heating dynamics is improved.

By assuming steady-state, the temperature increase ΔT for a single nanoparticle can be obtained from heat transfer equation,¹⁵⁷ and equals:

$$\text{Equation 11. } \Delta T(r) = \frac{V_{NP}Q}{4\pi k_0 r} ,$$

where r is the distance from the centre of the nanostructure, V_{NP} is the volume of a single nanoparticle, Q is the rate of heat dissipation, and thermal conductivity of the surrounding medium is described by k_0 . For the small spherical plasmonic nanostructures heat generation Q (or total heat power in other words¹⁵⁸) under incident light of a wavelength much longer than the radius of the nanoparticle is given by¹⁵⁷:

$$\text{Equation 12. } Q = \frac{\omega}{8\pi} E_0^2 \left| \frac{3\varepsilon_0}{2\varepsilon_0 + \varepsilon_{NP}} \right| \text{Im}\varepsilon_{NP} ,$$

where angular frequency of irradiation is denoted by ω , E_0 represents amplitude of the applied radiation, ε_0 is the dielectric constant of the medium, and ε_{NP} is the dielectric constant of the nanostructure. Upon further derivation¹⁵⁹ thermal enhancement of the spherical nanoparticle (described as maximum temperature increase at the distance r equal to the radius of a nanosphere R_{NP}) can be described as:

$$\text{Equation 13. } \Delta T_{max}(I_0) = \frac{R_{NP}^2}{3k_0} \frac{\omega}{8\pi} \left| \frac{3\varepsilon_0}{2\varepsilon_0 + \varepsilon_{NP}} \right|^2 \text{Im}\varepsilon_{NP} \frac{8\pi I_0}{c\sqrt{\varepsilon_0}},$$

where I_0 describes light intensity inside of the surrounding medium.

Generally, the observed temperature increase is proportional to the second power of the size of the nanostructure, which is governed by the heat transfer (proportional to the nanoparticle's surface area) and total heat generation rate (proportional to the volume of the nanoparticle).¹⁵⁷ Hence, the bigger the nanostructures the bigger the extent of the thermoplasmonic effect (see **Figure 17**). Also, in contrary to the hot electrons-driven photocatalysis, relationship between the reaction rate under the photothermal enhancement and illumination intensity is exponential.¹⁶⁰

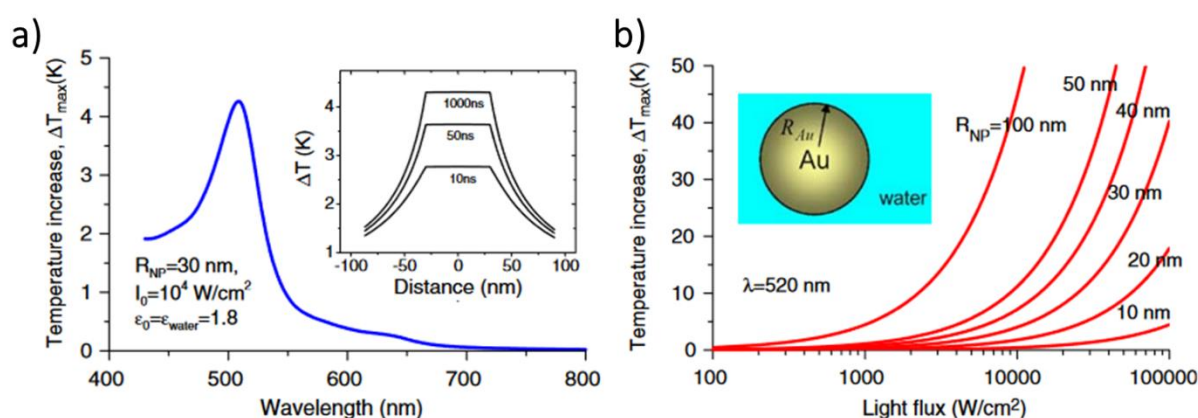


Figure 17. Influence of different parameters on temperature increase ΔT observed for gold nanoparticle placed in water as a surrounding medium, upon triggering thermoplasmonic effect. Calculated ΔT at the surface of the nanostructure **a)** as a function of irradiation wavelength (inset presents ΔT evolution as a function of distance from the center of nanostructure at different times) and **b)** as a function of the illumination power for spherical nanoparticles of different radii. Reprinted from¹⁵⁹ and reorganized for clarity.

Exchange of the heat generated within plasmonic nanostructure with the environment can be described in terms of transient evolution of the temperature in the environment, given as¹⁵⁸:

$$\text{Equation 14. } T(r, t) = \frac{Q_0}{4\pi k_0 r} \left(1 - \text{erf} \left(\frac{r}{\sqrt{4D_s t}} \right) \right)$$

for switching light on at $t = 0$ and, hence, for constant heat power $Q(t) = Q_0$ for $t \geq 0$ and $Q(t) = 0$ for $t < 0$.

For stopping the illumination at $t = 0$, and hence for constant heat power $Q(t) = Q_0$ for $t < 0$ and $Q(t) = 0$ for $t \geq 0$, the transient temperature evolution is given by¹⁵⁸:

$$\text{Equation 15. } T(r, t) = \frac{Q_0}{4\pi k_0 r} \operatorname{erf}\left(\frac{r}{\sqrt{4D_s t}}\right),$$

where t is time, erf is error function, and D_s is thermal diffusivity (other parameters as defined above for **Equation 11**).

Hence, the timescale of the system's temperature evolution is given by the error function. For $\operatorname{erf}(1) \approx 0.84$ (which translates to the temperature increase equal to 84% of the final temperature increase) we can introduce new parameter, τ to rewrite the error function $\operatorname{erf}(1)$ as $\operatorname{erf}\left(\sqrt{\frac{\tau}{t}}\right)$. Thus, the following equation:

$$\text{Equation 16. } \tau = \frac{r^2}{4D_s},$$

represents timescale of the temperature evolution and manifests clear advantage of using plasmonic nanoparticles as heat sources, namely fast dynamics due to weak thermal inertia.¹⁵⁸ To give an example, for a nanoparticle placed in water (D_s equal $1.46 \text{ m}^2\text{s}^{-1}$) at 100 nm from a heat source the timescale of temperature evolution is $\tau \approx 17 \text{ ns}$.

In order to enhance heating, collective effects can be employed. For the collection of nanostructures heat fluxes from different nanoparticles can be added and strong enhancement due to the collective plasmon resonances can be observed.¹⁵⁷ Hence, the temperature increase experienced by single nanoparticle located in between N identical spherical nanostructures of radius R_{NP} , and each nanostructure delivers power Q_i and is located at position \mathbf{r}_i , $i \in \llbracket 1; N \rrbracket$ is given by¹⁵⁸:

$$\text{Equation 17. } \delta T_j = \frac{Q_j}{4\pi k_0 R_{NP}} + \sum_{\substack{k=1 \\ k \neq j}}^N \frac{Q_k}{4\pi k_0 |\mathbf{r}_j - \mathbf{r}_k|}.$$

Hence, δT_j results from self contribution δT_j^{self} and the contribution of the $N - 1$ nanostructures surrounding the considered nanoparticle δT_j^{ext} . If δT_j^{self} dominates, the system is considered to be in the temperature confinement regime. In such case, the observed temperature increase occurs only in a close vicinity to the nanostructure. If δT_j^{ext} dominates, so-called thermal collective effects occur and the temperature distribution is homogenous on a macro scale. Prediction of the regimes relies on a dimensionless parameter proposed by Baffou¹⁵⁸:

$$\text{Equation 18. } \zeta_m = \frac{p}{R_{NP}N^{(m-1)/m}} \quad \text{for } m \geq 2 \quad ,$$

where p is the average interparticle distance, R_{NP} represents radius of spherical nanostructures or typical size of the non-spherical nanoparticle, N stands for number of nanostructures, and m for system dimensionality, namely $m = 1$ represents linear chain of nanostructures, $m = 2$ two-dimensional array, and $m = 3$ nanoparticles in solution. For $m = 1$ **Equation 18** reads

$$\zeta_1 = \frac{p}{R_{NP} \ln N}$$

$\zeta_m \gg 1$ describes system in the temperature confinement regime (**Figure 18**), where nanoparticles do not influence each other. For $\zeta_m \leq 1$, system exhibits collective heating, and hence the overall temperature offset can be observed (**Figure 18**). For systems described by $\zeta_m \ll 1$ temperature homogenization occurs and temperature distribution becomes smooth. The interparticle distance sufficient to observe dominant collective effects is in a microscale, e.g. for separated 10 nm nanoparticles the average sufficient distance of 10 μm was reported.¹⁶¹

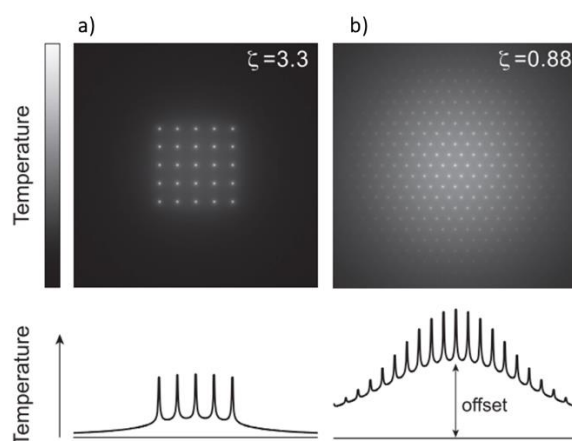


Figure 18. Temperature distribution in the surroundings of arrays of gold nanostructures. **a)** Localized regime (temperature rise around individual sources of heat). **b)** Regime of collective effects, as a result an overall temperature offset arises. Reprinted from ¹⁵⁸.

To benefit from collective effects, one also needs to consider the timescale of irradiation and how this parameter influences heat propagation. Temperature envelope $T_{max}(\mathbf{r})$ is a concept defined as the maximum temperature achieved in the surrounding medium at any location and over time. Temperature envelope differs for continuous wave (CW) and pulsed irradiations, as well as for point and spherical sources of heat. For a spherical source of heat under CW irradiation, the envelope profile scales as $\frac{1}{r}$, while for femtosecond pulsed laser irradiation the envelope profile scales as $\frac{1}{r^3}$ (see **Figure 19**).¹⁵⁸ On the other hand, the average temperature

$\bar{T}(\mathbf{r})$ under pulsed illumination scales as $\frac{1}{r}$. Thus, under pulsed illumination the enhanced spatial confinement typically concerns only the $T_{max}(\mathbf{r})$.

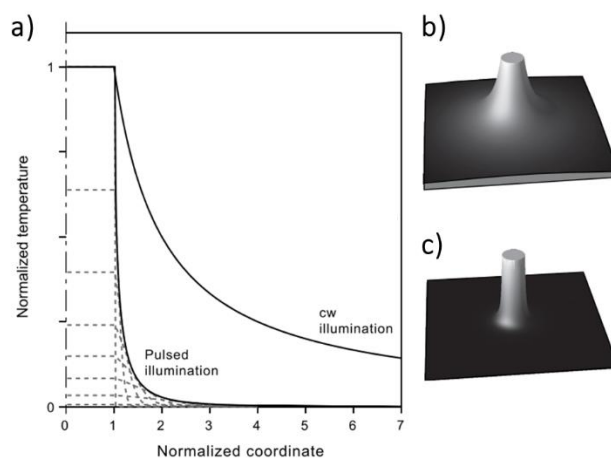


Figure 19. **a)** Temperature profiles around a sphere heated by a pulse source (dashed lines) at different times and the envelope of the temperature evolution compared with the profile under illumination with CW source. **b)** Three-dimensional representation of the steady state temperature profile under CW illumination. **c)** Three-dimensional representation of the temperature envelope under pulsed illumination. Reprinted from ¹⁶².

As a summary of this subsection a few examples of the employment of the thermoplasmonic effect in the photocatalytic enhancement of chemical reactions will be presented.

Branda *et al.* presented photothermal enhancement of the retro-Diels-Alder reaction, leading to the controlled release of a fluorescein dye.¹⁶³ Authors presented the possibility of controlling the chemical reaction of molecular systems anchored to the surface of nanoparticles. Core-shell nanostructures (silica core ~200 nm in diameter and Au shell ~10 nm thick) exhibited two LSPR bands at 700 and 1000 nm. Within the bicyclic system anchored to the nanoparticles' surface a fluorescein dye was attached to the furan component. And as long as the molecule remained attached by a maleimide component to the surface of nanostructures, the emission of the dye was quenched. Upon irradiation at 800 nm (pulsed laser, 700 mW, 1kHz, 100 fs) release of the dye was observed, which confirmed successful reaction upon triggering the thermoplasmonic effect, although no measurable temperature change was observed.

Scaiano *et al.* worked on the employment of the thermoplasmonic effect to the decomposition of dicumyl peroxide (DCP).¹⁶⁴ Usually this reaction requires a high temperature of about 140°C (activation energy equals 34.3 kcal/mol). Authors reported that upon pulsed laser irradiation (532 nm, 8 ns pulse duration, irradiation for 1 min) the temperature inside of the liquid drop containing gold nanospheres (12.7 nm in diameter) and DCP rose locally to about 500°C for

submicrosecond times. The same group presented also the follow-up work in which the Friedel-Crafts alkylation of anisole by benzyl chloride was performed.¹⁶⁵ Authors were able to carry out the reaction at 80°C in contrast to the normally required temperature of 120°C (or even higher). In this research, the 4.4 nm and 6.2 nm spherical AuNPs were used on the Nb₂O₅ support.

Xiong *et al.* presented the applicability of Pd nanostructures, synthesised in the presence of Ru³⁺.¹⁶⁶ For these structures authors were able to control the contribution of two important photocatalytic effects – hot electrons generation and thermoplasmonic effect. Influence of nanostructures of different morphologies on the styrene hydrogenation was investigated, including nanocubes, octahedrons, and concave morphology of nanoparticles. Catalytic efficiency of the reaction performed under 100 mW/cm², Xe-lamp full spectrum irradiation, and in the presence of Pd concave nanostructures was comparable to the fully thermal reaction performed without a catalyst at 70°C.

The final example is work focused on bimetallic nanostructures presented by Scott *et al.* and focused on use of Au-Pd triangular nanoparticles (average edge length of 43 nm, irregular polycrystalline Pd shells).¹⁶⁷ The thermoplasmonic enhancement of the Suzuki-Miyaura cross-coupling and hydrogenation reactions were investigated. In this case an array of green LEDs was used as a light source (~500 mW, 360° illumination). Even for the low power and unfocused light source the photocatalytic effect of the thermoplasmonic effect was apparent.

2.2.4. Interband transitions

In the context of plasmon-mediated photocatalysis it is important to distinguish between intraband and interband electron transitions in plasmonic nanoparticles. If electrons are excited through the LSPR, the change in their energy distribution occurs within the conduction band. Such excitations are called “intraband transitions” and occur between two states (characterized by different momenta) within the same sp-bands (**Figure 20a**). These transitions become allowable due to the assistance of defects, electron-electron scattering, or phonons.¹⁶⁸ On the other hand there are also interband transitions (IBs), which are the allowed transitions from d- to sp-bands determined by band structures (**Figure 20b**). Typically they can be addressed in such a spectral region that does not overlap with the LSPR part of the spectrum and hence are considered to be a nonplasmonic phenomenon. Nevertheless, IBs can be used to affect the chemical reactions catalytically.^{169,170} IBs occur for AuNPs around 400 nm (**Figure 20c**), since the energy gap between the highest occupied 5d band and lowest unoccupied 6sp band is 2.4 eV.¹⁷¹ Their contribution is particularly strong e.g. for nanoparticles made of Pd or Pt (**Figure 20d**). IBs grant the intrinsic absorption properties of the nanostructure and are not

strongly affected by the geometry of the nanoparticle.¹⁷² Due to the spectral overlapping between LSPR and interband transitions in some cases the determination of the exact photocatalytic mechanism might be complicated, since the coupling between both regimes can be strong¹⁷³ and the decay of LSPR to IBs can occur.¹⁷⁴ One of the most common techniques used to correlate photocatalytic effect to the particular transition type is investigation of wavelength-dependent catalytic activity.

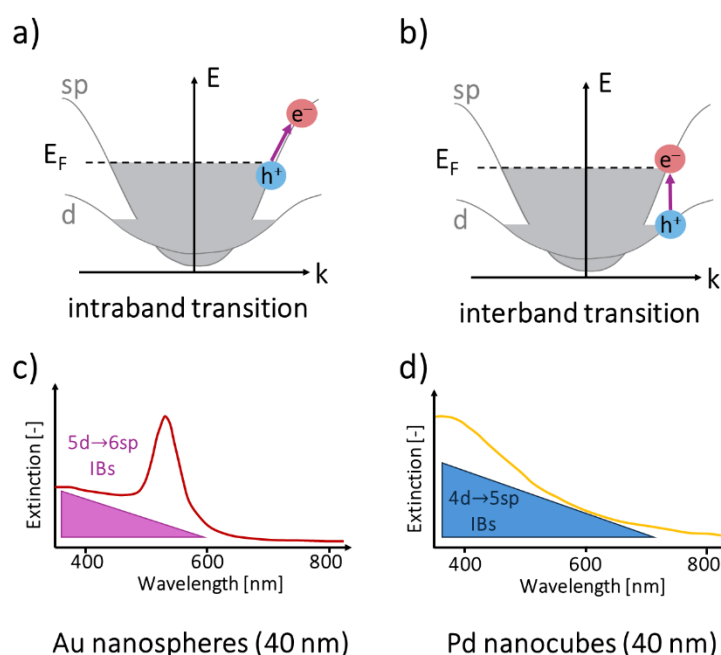


Figure 20. Schematic depiction of **a)** intraband and **b)** interband transitions. Schematic depictions of the positions of interband transitions on the UV-Vis spectra of **c)** spherical AuNPs and **d)** Pd nanocubes. Figure based on ¹⁷².

When photon absorption leads to the direct promotion of the d -band electrons to the sp -bands, the direct IBs take place. According to calculations of Atwater *et al.*, the energy distribution of the generated energetic carriers is dependent on the position of the d -bands.¹⁷⁵ Electrons excited upon IBs have energies very close to the Fermi level and are not considered to be hot electrons (e.g. they would not overcome Schottky barrier). On the other hand, the corresponding holes generated upon IBs have a large potential below E_F , and thus are very reactive.¹⁷⁶ Interband carriers exhibit much shorter electron-electron scattering time,¹⁶⁸ but the electron-phonon and phonon-phonon scattering are comparable to those occurring after intraband transition. Comparison of the general properties of carriers generated upon inter- and intraband transitions are presented in **Figure 21**.

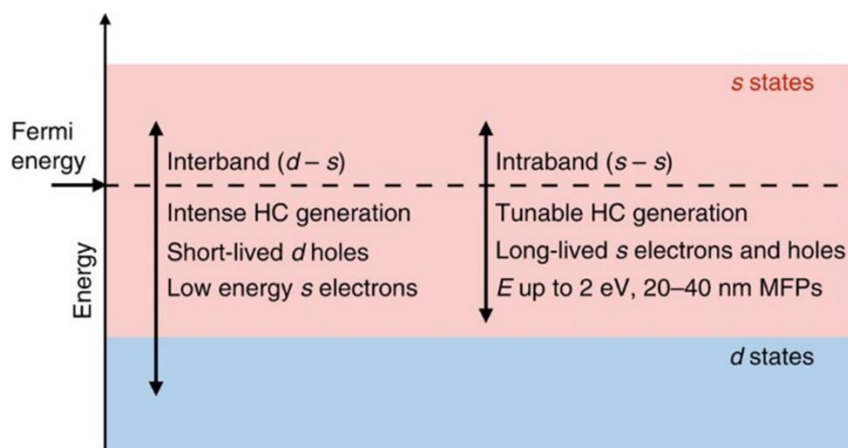


Figure 21. Comparison of the properties of hot carriers generated upon interband and intraband transitions in AuNPs. Reprinted from ¹⁷⁷.

To present the extent of the IBs applicability in the field of photocatalysis a few examples are presented to conclude this subsection. Nguyen *et al.* presented special photocatalyst design enabling elimination of mechanistic unambiguities and used mesoporous PdNPs with LSPR shifted to the near-infrared region.¹⁷⁸ Hence, authors focused solely on the photocatalytic properties of d-band holes during investigation of aryl halide oxidation addition. This reaction is an important step that determines the rate of the Suzuki-Miyaura reaction as a whole. The deeper holes in the d-band were found to catalyse the process and hot electrons were determined to not participate in it.

Landes *et al.* presented oxidative dissolution of individual AuNRs and compared the rates of the process under both IBs and LSPR.¹⁷⁹ It was possible to distinguish contribution of holes generated from IBs and hot holes around Fermi level by performing wavelength-dependent experiments. Research indicated towards better catalytic efficiency of IBs and d-band holes.

Toste *et al.*¹⁸⁰ investigated photocatalytic reduction of Fe^{3+} under IBs, which led to oxidative etching of the AuNPs used as the photocatalyst. Reaction was coupled with the cyclization of alkynylphenols in which the photogenerated Au^+ holes were employed. As a result of such experimental design, the catalytically active gold nanoclusters were formed, which constitutes an entirely new route for the preparation of novel catalytically active species.

2.3. Cellulose as component of advanced materials

This subchapter focuses on cellulose, since this biopolymer in a form of nanofibres was used as a robust and functional scaffold of the materials presented in the experimental part of the dissertation. Section 2.3.1. focuses on cellulose as a biopolymer and its different forms at

the nanoscale called also ‘nanocellulose’. Section 2.3.2. presents composite materials containing both cellulose and gold nanoparticles. Since combination of both constituents can provide new functional systems, the most relevant literature examples are presented as an important context for the experimental part of the dissertation. Finally, section 2.3.3. discusses different approaches to cellulose impregnation with dye molecules. Such procedures are not only industrially relevant, but also lead to new formulations beneficial for the development of advanced materials.

2.3.1. Nanocellulose

Cellulose is a biopolymer, an unbranched homopolysaccharide consisting of β -1,4-linked D-glucopyranosyl units (**Figure 22**)¹⁸¹ exhibiting flat ribbon-like conformation. Typical number of monomers in the polymer chain is between 10 000 and 15 000, depending on the source of cellulose. As important structural component of plants, produced also by some animals, fungi, or bacteria, it is probably the most abundant polymer in Nature.¹⁸² Although the monomeric unit of cellulose is soluble in water, cellulose itself is not, which is often attributed to hydrogen bonds preserving structural integrity of the polymer.¹⁸³ This argument is however strongly contested.¹⁸¹ Nevertheless, topic of hydrogen bonds in the context of cellulose and its inter- and intramolecular interactions is very important, although in recent years it has been postulated that other nonbonded interactions might be just as crucial.¹⁸⁴ Due to high number of hydroxyl groups within the structure of polymeric chain of the unmodified cellulose, this polymer is able to interact with water, which leads to swelling of materials composed of cellulose.

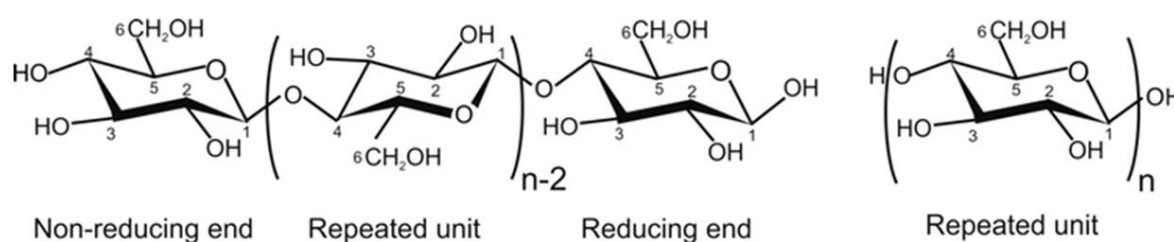


Figure 22. Chemical structure of cellulose. Right-hand panel presents typical notation, while the left-hand panel presents notation with both ends of the chain indicated. Reprinted from ¹⁸¹.

Cellulose is one of the components of primary and secondary walls of plant cells. Walls help to maintain structural integrity of the cells and contain also lignin, pectin, soluble proteins, and other components.¹⁸⁵ Cellulose is biosynthesised within plasma membrane of the plant cells due to the activity of enzyme complex called cellulose synthase complex.¹⁸⁵ Biosynthesised chains are organised into more complex structures composed of 18-24 chains and called

cellulose microfibrils (or elementary fibrils).¹⁸⁶ Microfibrils formation is promoted due to the parallel stacking of cellulose chains. Microfibrils may aggregate even further to form larger fibrils (diameter of 5-50 nm and length up to several micrometres, see **Figure 23**). Within primary cell walls bundles of cellulose microfibrils might be bound spontaneously to hemicellulose, a branched polymer of different sugar units.¹⁸⁷ Such binding serves as a glue for the microfibrils within the cell walls. Natural fibres containing cellulose come from various plant sources and are vital for the economics of different countries, e.g. India where most of the world production of plant fibres is based.¹⁸⁸ Natural cellulose-based materials, such as wood, cotton, and linen, have been vital for humankind throughout the history. Natural fibres remain important today and are crucial for production of e.g. paper or ropes.

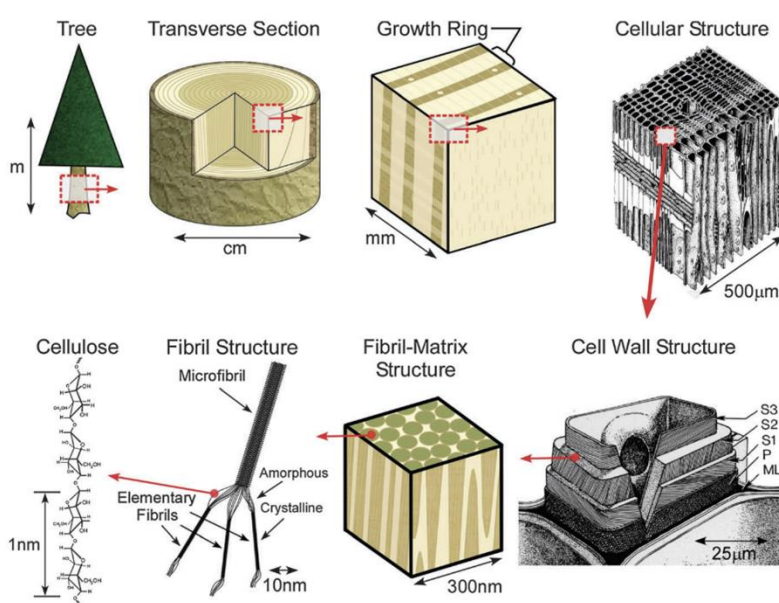


Figure 23. Hierarchical structure from cellulose to the tree as a whole. Abbreviations: S – secondary cell wall, P – primary cell wall, ML – middle lamellae between tracheids. Reprinted from ¹⁸⁹.

Surface of cellulose is rather chemically inactive, however, it does not prevent adsorption of chemical species.¹⁹⁰ In order to induce better chemical reactivity structural modifications of cellulose need to be performed. Moreover, cellulose is a semicrystalline material (on fibrillar level typical degree of crystallinity is 50-85%¹⁹¹) in which both crystalline and amorphous regions coexist. Crystalline cellulose exhibits polymorphs I, II, III, and IV.¹⁸² Cellulose I, or natural cellulose, is produced e.g. by plants and bacteria. It is a thermodynamically metastable structure, which may convert to cellulose II or III. Cellulose I itself has two polymorphic structures, namely triclinic (I α , provided mostly by algae¹⁹² and bacteria¹⁹³) and monoclinic (I β , derived from higher-plant cell walls¹⁹⁴). For I α and I β unit cells, polymeric chains of cellulose are arranged in the ‘parallel up’ configuration.¹⁹⁵ This means that

the 1→4 linkages of the stacked chains are oriented in the same direction ('parallel') and their direction points towards the positive c-axis direction of the unit cell ('up'). Cellulose II is monoclinic and the most stable cellulose structure obtained typically via regeneration and mercerization.¹⁹⁶ It was used for the production of cellophane or synthetic textile fibres. Cellulose III can be obtained from cellulose I and II by heat treatment and can be used to produce cellulose IV. To describe the overall fibrillar structure of cellulose two models have been proposed. One of them is the amorphous domain model¹⁹⁷ which makes the analogy with semicrystalline polymers and presents cellulose as the chain of the crystalline domains separated by amorphous segments. The second, fringe model¹⁹⁸ proposes that amorphous chains are distributed over crystalline domains constituting the core of the fibril.

In the context of materials engineering it is important to mention that cellulose can be extracted from source materials in a form of structures called 'nanocellulose' or 'cellulose (nano)particles'. There is a huge diversity of cellulose nanostructures, mostly due to the vast number of cellulose sources, which dictate morphology, crystallinity, and aspect ratio of the microfibrils. Moreover, different extraction processes can be employed to extract cellulose particles from cellulose microfibrils. Finally, there is a great number of protocols enabling surface modification, which further broadens the collection of possible nanomaterials. In general, the isolation of particles is performed in a two-stage procedure. Firstly, pretreatment in a form of purification and homogenisation of the source material is carried out.¹⁹⁹ Secondly, separation of the components into (micro)fibrillar and crystalline fractions is performed.²⁰⁰ The most common isolation protocols are acid hydrolysis²⁰¹ and mechanical treatment (the latter can be performed e.g. in high-pressure homogenizers²⁰² and followed up by filtration). Upon the top-down processing of cellulose fibrils different types of nanostructures can be obtained. The number of possible nanocellulose morphologies is relatively big, mostly due to the fact that the nomenclature has not been standardized yet.¹⁹¹ Youngblood *et al.* proposed nine main types: wood fibre (WF) and plant fibre (PF) particles, microcrystalline and microfibrillated cellulose (MCC and MFC respectively), nanofibrillated cellulose (often called cellulose nanofibres, CNFs), cellulose nanocrystals (CNCs), tunicate cellulose nanocrystals (t-CNCs), algae cellulose (AC), and bacterial cellulose (BC).¹⁹¹ Out of them CNCs, CNFs, and BC are presumably the most popular types of nanocellulose (**Figure 24**). CNCs are relatively short and rod-like. They are 3-5 nm wide and 50-500 nm long, which makes them high aspect ratio structures.^{191,203} CNCs are highly crystalline (54-88%) and mostly consist of I β fraction (68-94%).¹⁹¹ On the other hand, CNFs are long (up to several microns) and very narrow fibrils (diameters in a nanometer range), exhibiting square cross-section and both crystalline and amorphous nature.^{203,204} CNFs are the only type of nanocellulose used in all of the experiments

described within this dissertation. There are different types of cellulose treatments resulting in CNFs, one of them, presumably the most common, is TEMPO (2,2,6,6-tetramethylpiperidinyl-1-oxyl) oxidation. This procedure results in the generation of carboxyl groups, which also ensures faster fibrillation.^{204,205} CNFs exhibit tendency to form robust networks, mostly due to the formation of hydrogen bonds and entanglement of the fibres. Finally, BC particles are microfibrils produced by bacteria. They are microns in length and exhibit $AR > 50$.¹⁹¹ Their morphology is strongly dependent on the bacteria used and the culturing conditions. Upon changing temperature or providing additives, the $I\alpha/I\beta$ ratio or width of the fibrils can be changed.¹⁹³

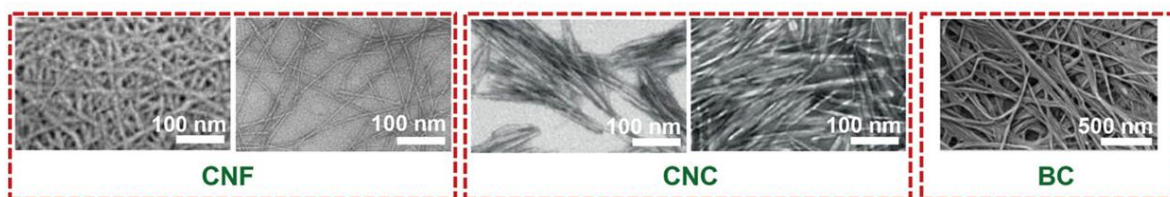


Figure 24. Morphologies of the most common types of nanocellulose, namely CNF – cellulose nanofibres CNC – cellulose nanocrystals, and BC – bacterial cellulose. Reprinted from ²⁰⁶.

Properties of cellulose nanoparticles are strongly dependent on their surface chemistry, which is a direct result of the fabrication process²⁰⁷ (**Figure 25**). Typically, CNCs are prepared either upon degradation by the sulfuric acid, which results in the formation of sulphate ester groups,²⁰¹ or upon degradation with hydrochloric acid, providing hydroxylated surfaces.²⁰⁸ On the other hand, CNFs are usually prepared by applying mechanical methods or TEMPO-mediated oxidation. In addition, surface chemistry of nanocellulose may stem from properties of adsorbed species (e.g. CTAB²⁰⁹ or stearic acid²¹⁰), and derivatization of the surface (e.g. covalent attachment of polyolefins²¹¹, isocyanates²¹², or silanes²¹³).

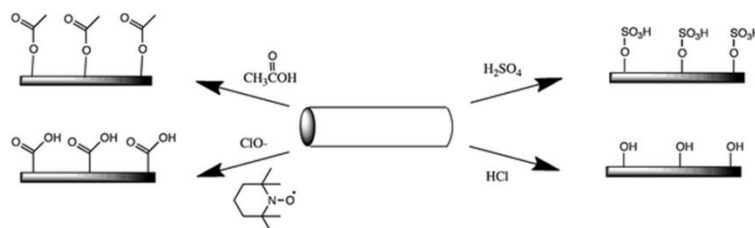


Figure 25. Most popular surface chemistries of cellulose nanoparticles, resulting from specific processing of initial cellulose fibrils. Top left – acetyl groups, a result of acetic acid treatment. Top right – sulphate esters, a result of sulfuric acid treatment. Bottom left – carboxyl groups, a result of TEMPO oxidation. Bottom right – hydroxyl groups, a result of hydrochloric acid treatment. Reprinted from ¹⁹¹.

Nanocellulose might be used to prepare engineered composite materials for applications requiring transparent films²¹⁴, thermal or mechanical reinforcements²¹⁵, or barrier films.²¹⁴

Cellulose nanoparticles may be either added to various types of polymers or pure cellulose nanomaterials can be modified in order to obtain desired parameters of the final formulation. Different types of materials based on nanocellulose or incorporating it as a component can be prepared, including cellulose-reinforced polymer matrix composites^{216,217} and modified nanocellulose films (e.g. composites with silk,²¹⁸ polyvinyl alcohol,²¹⁹ or glycerol²²⁰). From the perspective of this dissertation, however, cellulose-gold nanoparticles and cellulose-dye composite materials are the most interesting and the two following subsections will be specifically devoted to them.

2.3.2. Hybrid materials based on cellulose and gold nanoparticles

Nanocellulose can be used as a template or scaffold for advanced materials. It possesses several advantages over other typically used structures. First and foremost, in contrary to many polymers, sol-gel matrices, or carbon nanotubes, cellulose is biocompatible and biodegradable.²⁰⁴ Notably, nanocellulose has been joined with gold nanoparticles to form advanced composites exhibiting new properties. First example of such material was reported by Chanzy *et al.* in the 1980s.²²¹ Authors used 4-6 nm gold nanoparticles to label cellulose microfibrils and microcrystals obtained from algae and bacteria. After preparation of Au-enzyme complex, cellulose digestion by enzymes could have been investigated using electron microscopy. Au-enzyme complex exhibited very strong affinity towards cellulose, however the formation of the composite material was rather a side effect, not a goal on its own. Since then the field of cellulose-AuNPs composites has grown. This subchapter presents the most popular approaches to the preparation of cellulose-AuNPs hybrid materials and their applications.

Mixing approach. One of the most commonly used approaches is simple mixing of AuNPs and nanocellulose suspensions. This path requires precise material design in terms of the surface chemistry of both components, as emphasised by Majoinen *et al.*, who mixed positively charged spherical AuNPs (capped with ligand containing quaternary ammonium groups) with negatively charged CNCs (containing sulphate groups).²²² Authors employed electrostatic interactions between components in the formation of the composite (**Figure 26**), which constitutes an important starting point for materials designed within this dissertation. Upon addition of CNCs to the water dispersion of Au nanostructures, precipitation of the resulting composite occurred, hence facilitating the separation of the final material.

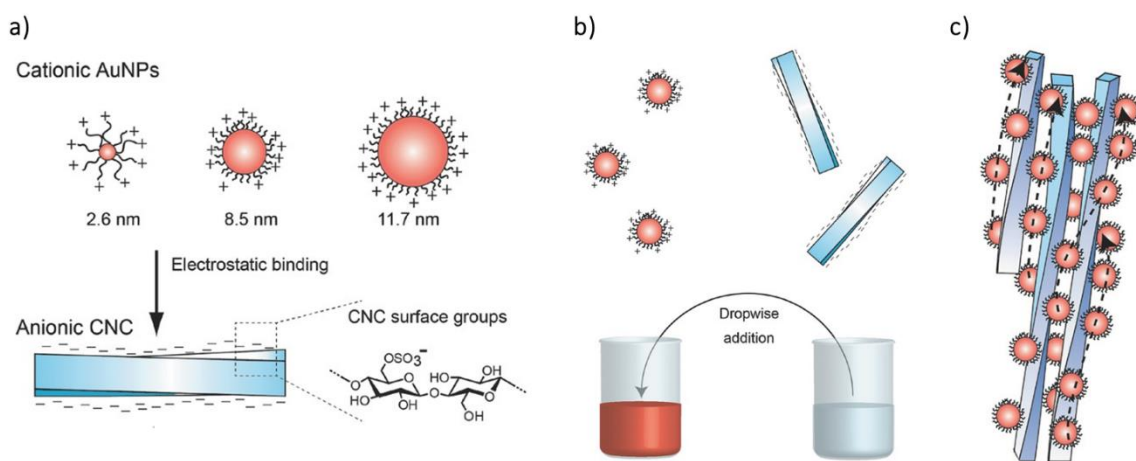


Figure 26. Schematic representation of the employment of electrostatic interactions in the formation of AuNPs-decorated CNCs. **a)** Proper design of components' surface chemistry ensures mutual interactions. **b)** Hybrid material can be prepared upon simple addition of CNCs dispersion to AuNPs dispersion. **c)** Scheme of CNC/AuNP superstructures formed upon electrostatic binding. Reprinted from ²²². Assembled from different figures and organized for presentation.

If surface chemistry of the components is not matching, proper functionalization might be required as presented by Lam *et al.*, who performed deposition of carbonate-coated AuNPs (spherical, 3.1 nm diameter) on the surface of CNCs which were modified with poly(diallyldimethyl ammonium chloride) (PDDA).²²³ Initial CNCs were negatively charged, due to the $-\text{COOH}$ groups on their surface. To render nanocrystals compatible with also negatively charged Au nanostructures, CNCs were coated with polyelectrolyte, PDDA. Due to the electrostatic interactions between components, uniform coating of nanocellulose occurred (**Figure 27**). Nevertheless, the repulsion forces between components exhibiting the same surface charge can also be employed to drive the ordering of the composite, just as in work of Qu *et al.*²²⁴ who used sulphonated-CNCs and bovine albumin-coated Au nanoclusters (composed of 25 Au atoms). Both components exhibited negatively charged surface, which excluded flocculation and enabled preparation of uniform self-standing films. Iridescent colours, optical, and chiroptical properties were dependent on the content of Au nanoclusters.

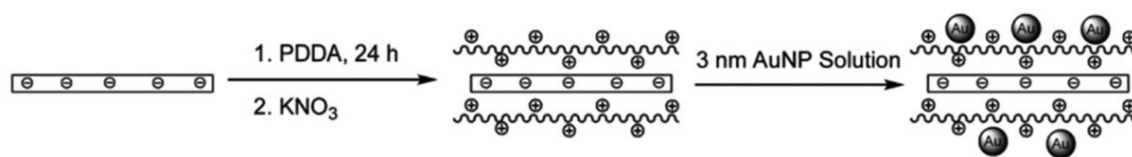


Figure 27. Schematic depiction of the CNCs' surface modification leading to the preparation of AuNP-decorated cellulose nanocrystals. Reprinted from ²²³.

Formation of cellulose-AuNPs composites via mixing is not limited to CNC morphology. Guo *et al.* used two surface-modified CNFs, one with quaternary ammonium groups and one with amine groups, to electrostatically bind citrate-capped AuNPs.²²⁵ Eskilson *et al.*, on the other hand, presented homogenous electrostatic adsorption of CTAB-coated AuNRs and cationic thiols-coated AuNSs on bacterial cellulose membranes.²²⁶

One of the most important properties of cellulose is its chirality occurring at a molecular level as well as at other scales, for instance, CNCs can form liquid crystalline cholesteric (chiral nematic) phase.¹⁹⁶ In such molecular organization, rod-like CNCs form a left-handed helix. The effect occurs for dispersions of CNCs in different solvents, which classifies cellulose as lyotropic liquid crystal (**Figure 28**).

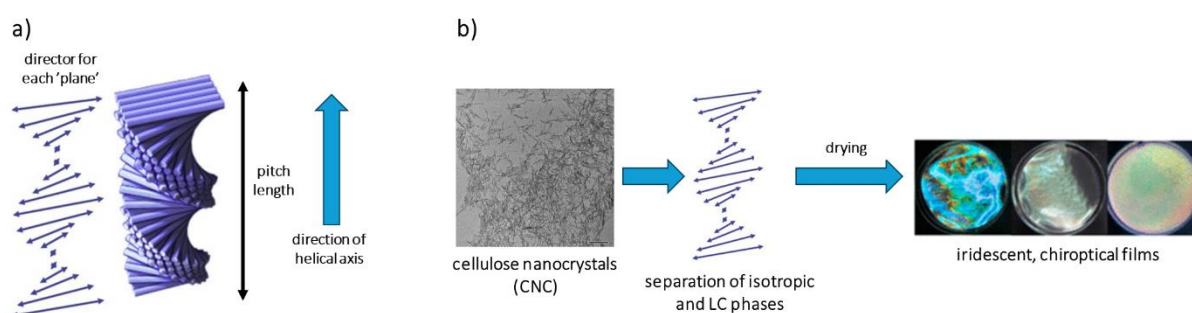


Figure 28. a) Schematic depiction of the liquid crystal chiral nematic ordering. Changes in the orientation of the long axis of molecule for each layer is presented next to the schematic 3D structure with direction of the helical axis indicated. Pitch length corresponds to the 360° turn of the director. Reprinted from ²²⁷ and relabelled for clarity. b) Evolution of CNCs from individual nanocrystals, through liquid crystal (LC) ordering, to iridescent, solid films. Inspired by ²²⁷. TEM image of CNCs reprinted from ²²⁸ and image of solid CNC films reprinted from ²²⁹.

The ability of nanocellulose to form liquid crystalline ordering was one of most employed for the preparation of chiroptical plasmonic materials. Lukach *et al.* investigated influence of four types of AuNPs dispersed with negatively charged CNCs (216 nm in length and 13 nm diameter) on the formation of chiral solid films.²³⁰ Such films can be obtained by evaporating nanocellulose suspensions at room temperature for several days using even simple Petri dish as a casting mould. Authors utilized positively and negatively charged spherical AuNPs (capped with benzyldimethylhexadecylammonium chloride, BCAD and 1-mercapto-3,6,9,12-tetraoxapentadecan-15-oic acid, respectively) of two sizes, 9 and 43 nm. Size and charge of AuNPs did not have influence on the properties of the resulting films. The decisive parameter was found to be concentration of plasmonic nanoparticles, which influenced global chiral nematic order. At higher AuNPs concentrations, more disordered regions were observed which

led to the decrease of the circular dichroism signal. Resulting composites combined optical properties of AuNPs and chiroptical activity of CNCs. Similar results were presented by Querejeta-Fernández for sulphate-functionalized CNCs mixed with AuNRs (14 nm diameter and 41 nm length).²³¹ Due to the elongated shape, AuNRs followed the liquid crystalline ordering of CNCs (**Figure 29**). Dry films of such suspensions exhibited strong circular dichroism signal and chiral nematic order distorted at higher Au concentrations. Importantly, authors presented how the plasmonic chiroptical activity of the films can be controlled by dimensions of AuNRs, and presence of additives such as salt. These factors were found to regulate the pitch of the chiral nematic ordering of the CNC matrix.

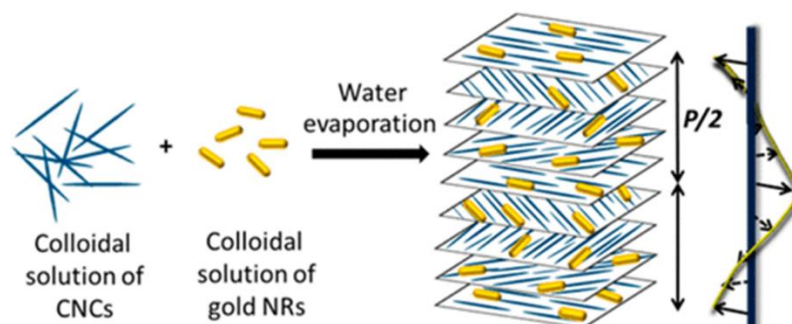


Figure 29. Preparation of the composite chiroptical plasmonic film via mixing approach. Slow evaporation of solvent results in the formation of a left-handed liquid crystalline chiral nematic phase and, subsequently, a solid film. AuNRs follow the ordering of cellulose nanocrystals. Reprinted from ²³¹.

Chu *et al.* presented how to prepare free-standing chiral plasmonic films based on CNCs and citrate-capped AuNPs.²³² Despite random distribution of Au nanospheres, nanoparticles did not aggregate and CNC matrix maintained its chiral nematic ordering. Using polarized light microscopy, a common technique in the investigation of liquid crystal materials, fingerprint texture of the matrix was confirmed. Composites exhibited also tunable and switchable plasmonic properties and angle-dependent position of the SPR band.

The incorporation of AuNPs in the cellulose matrix might be also facilitated by cross-linking. Garavand *et al.* proposed a very interesting approach in which AuNRs (9 nm in diameter and 30 nm in length) served as a cross-linking agent between cellulose nanocrystal xanthate and *S* – *H* functionalized polypseudorotaxane.²³³ As a result, a hybrid, organic-inorganic gel was obtained. In another work, Guo *et al.* used surface-modified propargyl-CNFs to induce click reaction with azido-terminated AuNPs in the presence of AA and CuSO₄·5H₂O.²²⁵

Nanocellulose does not need to serve only as a matrix for Au nanocrystals, it might also be used as a ligand and upon mixing of both components various morphologies of cellulose-AuNP systems can be obtained. Ohlendorf *et al.* were able to prepare hybrids exhibiting three different

organizations, namely, stable cellulose-Au cluster suspensions, instable cluster suspensions quickly undergoing aggregation, and single cellulose-stabilized AuNPs.²³⁴ Authors used hydroxypropyl cellululose-3-methyltiopropionyl chloride (HPC-MTP) and 11.9 nm diameter, spherical, citrate-stabilized AuNPs. Morphologies were controlled by concentration of HPC-MTP used during ligand exchange as depicted in **Figure 30**.

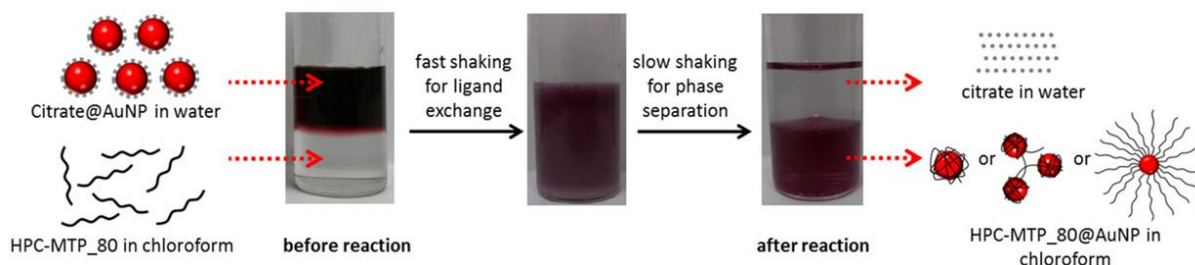


Figure 30. Cellulose as a ligand for AuNPs. Ligand exchange process can result in different organisations of AuNPs. Reprinted from ²³⁴.

***In situ* gold reduction in the presence of cellulose.** Second important approach to the preparation of hybrid cellulose-AuNPs materials relies on the *in situ* fabrication of AuNPs in the presence of cellulose. Usually this process is performed in two steps. In the first step, gold precursor is adsorbed on the cellulose of a chosen morphology. In the second step, reducing agent is added and the generated metallic gold forms AuNPs. In a slightly different approach, chemical groups on the surface of the modified cellulose can serve as reductants. Despite the approach applied, cellulose also acts as either matrix or surface stabilizing agent. Generally, however, the *in situ* method results in less uniform hybrid materials in terms of the homogeneity of AuNPs deposition, as emphasised by Lam *et al.*,²²³ who compared the results of the *in situ* Au(III) reduction with mixing approach. Compared to the *in situ* reduction, mixing method resulted in the more uniform AuNPs deposition on the surface of CNCs.

In order to promote adsorption of tetrachloroauric acid, Dong *et al.* modified cellulose that initially contained $-OH$ groups by immersing it in the solution of cationic epoxide.²³⁵ Upon the reaction of hydroxyl groups and epoxide, quaternary ammonium ions were introduced and cellulose became cationic itself, which further promoted adsorption of $[AuCl_4]^-$ ions. Formation of AuNPs was initiated by addition of $NaBH_4$ and, as a result, polydisperse, irregular nanoparticles in a 8-10 nm size range grew directly on the surface of cellulose substrate. Nanocellulose may also be modified in such a way to promote very strong and direct bonding to the metallic gold. For instance, Yokota *et al.* prepared thiolabelled cellulose, thus enabling instant S-Au bonding upon AuNPs formation.²³⁶ Presence of the bond was confirmed by XPS spectroscopy. The as-synthesised nanoparticles were rather uniform (6.8 nm in size) and not aggregated (**Figure 31**).

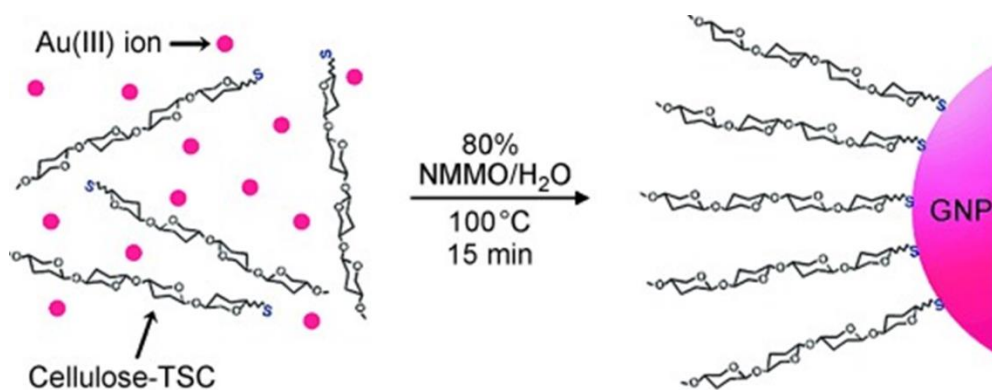


Figure 31. Reaction conditions for the *in situ* synthesis of AuNPs in the presence of sulphur-containing cellulose acting as a ligand for the as-prepared Au nanostructures. Reprinted from ²³⁶.

Dispersity of AuNPs can be controlled by asserting proper reaction conditions. For example, He *et al.* used porous cellulose fibres, hence providing specific nanoreactors for the reduction of gold precursor.²³⁷ Resulting AuNPs were smaller than 10 nm and their size distribution could have been controlled due to the ion-dipole interactions between metal precursor and hydroxyl groups of cellulose, as postulated by authors. Formation of other noble metal nanostructures, namely Ag, Pd, and Pt nanoparticles was also explored. A thorough investigation by Ashraf *et al.* provided more information on the effect of the reducing agent.²³⁸ Both sodium hydroxide and sodium borohydride were used to reduce Au precursor in the presence of lecithin treated and thiol-modified CNFs. Chemical modification of cellulose helped to form almost spherical nanostructures, although sodium borohydride led to higher polydispersity and lower loading (~22 wt%) of AuNPs. Nevertheless, materials could have been successfully employed as catalyst in the reduction of 4-nitrophenol.

Another types of cellulose surface modifications that can be made to assure stabilization of the *in situ* synthesised AuNPs are the introduction of carboxyl²³⁹ and amino²⁴⁰ functional groups. Chen *et al.* grafted polyamidoamine dendrimers onto TEMPO-oxidized CNCs.²⁴¹ Dendrimers-modified CNCs not only provided stabilization for the *in situ* formed AuNPs, but were also able to induce gold reduction, and no other reducing agent was needed. The size distribution of the resulting Au nanocrystals was broader than in case of NaBH₄-reduced AuNPs, however this aspect could have been influenced through the control of the CNC-dendrimers concentration.

The another example for the approach discussed in this section is work of Yan *et al.*, where one-pot synthesis of AuNPs on CNCs was proposed at elevated temperatures and in the presence of polyethylene glycol (PEG).²⁴² PEG served as a reducing agent at 80°C, yet the controlled temperature changes were found to control the size of nanostructures. BC can also

be used in such synthetic approach, just as in the work of Zhang *et al.*, who prepared Au-BC hybrids by using poly(ethyleneimine) as both reductor and linking agent.²⁴³ Great separation of individual AuNPs formed at 60°C was obtained and relatively uniform size (about 9 nm) and surface coverage (~80% of the BC surface area) were observed as well. In a similar work, Li *et al.* presented that the BC-AuNPs composites can exhibit 3D network structures with interconnected pores.²⁴⁴

Although literature proposes various protocols of the *in situ* AuNPs formation in the presence or on the surface of nanocellulose of different morphologies,²⁰⁴ this approach usually does not provide the precise control over the optical properties of the resulting hybrids. The main reason for that is relatively low control over the process of Au nanocrystals synthesis. As it has been presented in the section 2.1.2 of this dissertation, synthesis of AuNPs of desired morphologies (and hence also exhibiting defined optical properties) is a complicated task influenced by various nuanced factors. By incorporating cellulose in the reaction mixture, another variable is introduced, which significantly changes process conditions. Moreover, due to the huge variety of cellulose sources and morphologies, each process is essentially different. As a result, there is only a poor control over the morphology and size of the synthesised nanostructures. Hence, preparation of composites containing anisotropic nanoparticles with well-defined optical properties with this approach is very improbable.

Other approaches. Mixing and the *in situ* synthesis are not the only methods of cellulose-AuNPs composites preparation. One can also distinguish alternative approaches, such as dip coating,²⁴⁵ solid grinding,²⁴⁶ layer-by-layer assembly,²⁴⁷ seeded-growth,²⁴⁸ inkjet printing,²⁴⁹ and micro-patterning.²⁵⁰ An example of a dip coating approach can be found in the work of Ngo *et al.*, where ordinary paper was used as an adsorbent for AuNSs synthesised by Turkevich method.²⁵¹ Au content was controlled by the concentration of the dipping dispersion, which enabled control over the aggregation state of nanostructures (**Figure 32**). Such composite plasmonic papers were used to amplify the SERS signal of the investigated dyes. An example of the seeded-growth approach is work of Gruber *et al.*, who presented a facile way for the tuning of the composites' plasmonic properties.²⁴⁸ Authors introduced silica coating on CNCs, which not only increased the stability of the template, but also – through control over the thickness of silica layer – enabled control over the plasmonic properties of Au deposited in the next step. After reduction, preformed silica nanowires were coated with gold, and the thickness of the coating was controlled by increasing gold-silica ratio. Changes to dimensions of both gold shell and silica core, provided tuning of the SPR.

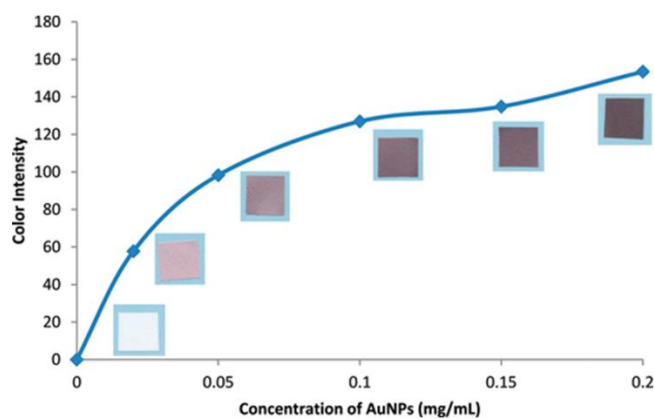


Figure 32. Colours of the hybrid papers dip-coated with AuNPs were a direct result of using solutions of different AuNPs' concentrations. Hence, not only the total deposition, but also the aggregation state of nanostructures were controlled. Reprinted from ²⁵¹.

Applications. To summarize this subsection, a short paragraph concerning applications of the cellulose-AuNPs composites is presented.

Due to the huge variety of the hybrid materials consisting of nanocellulose and Au nanostructures, such formulations can find applications in various fields. For instance, Bothra *et al.* presented that cellulose modified with bovine serum albumin-decorated Au nanoclusters can be used for the detection of Hg^{2+} in a 1nM–1mM concentration range.²⁵² Detection relied on the colour change of the observed fluorescence coming from nanoclusters. Changes could have been observed even with a naked eye. Limit of the detection was relatively low and met the detection requirements for drinking water provided by the European Union. BC-based hybrid materials are often used for the preparation of biosensors, e.g. for sensing of enzymes²⁴⁴ or hydrogen peroxide.²⁴³

Another important application is preparation of SERS substrates. Zhang *et al.* presented a reproducible SERS substrate based on Au-decorated CNFs.²⁴⁵ Substrate was tested using 4-aminothiophenol, a model molecule. Use of CNFs instead of other possible morphologies of nanocellulose increased substrate reproducibility comparing to paper or cotton. Wei *et al.*²⁵³ as well as Park *et al.*²⁵⁴ demonstrated preparation of AuNPs-decorated BC hydrogels and creation of SERS hot spots upon drying of the hydrogel structures. Upon drying spatial deformation was imposed on the hydrogels, which resulted in the SERS signal enhancement.

Au-decorated nanocellulose can also exhibit antioxidant²⁵⁵ and antimicrobial²⁵⁶ activity or be utilized for protein separation²⁵⁷ or enzyme immobilization.²⁵⁸ From the perspective of this dissertation, however, one of the most important applications of such hybrid materials is in the field of catalysis. In this field various nanocellulose morphologies are utilized, including CNFs,²³⁹ CNCs,²⁴² or BC.²⁵⁹ One of the most common reactions evaluating catalytic efficiency of the composites is reduction of 4-nitrophenol to 4-aminophenol with NaBH_4 (**Figure 33**). The

turnover frequency (namely number of moles of the reacting molecule per mole of Au per hour) in the presence of cellulose-AuNPs materials can be even up to 4 orders of magnitude higher comparing to plasmonic catalysis performed using polymer-supported AuNPs.²³⁹ Columns filled with BC-AuNPs were able to operate even for several months without losses in the catalytic activity²⁵⁹ and the very intuitive relation was observed, namely the smaller the AuNPs used, the higher the catalytic activity of the composites, due to the higher surface area of the plasmonic metal.²⁶⁰

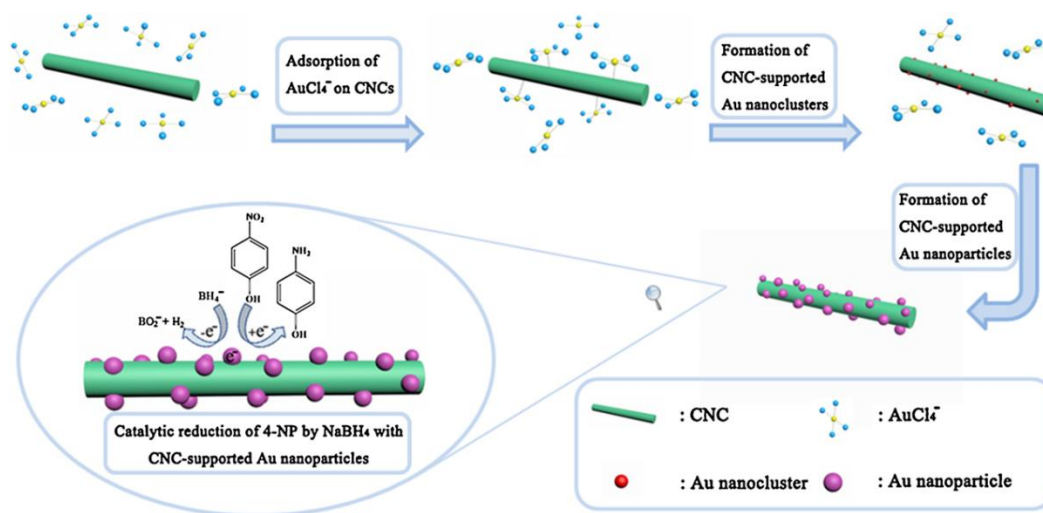


Figure 33. Nanocellulose-AuNPs composites can be utilized in various fields, including field of photocatalysis. One of the reactions commonly used for the evaluation of the catalytic activity of composites is reduction of 4-nitrophenol (4-NP) with NaBH_4 . Reprinted from ²⁴².

2.3.3. Hybrid materials based on cellulose and dyes

The final subsection of this subchapter concerns formulation of hybrid materials consisting of nanocellulose and dyes. In contrast to AuNPs, dyes are molecular species. For the formation of cellulose-dye materials in this subchapter the term ‘impregnation’ is used. First, the possible interactions at the foundation of the impregnation process are discussed and further, important aspects and parameters influencing the process are presented with examples.

Main properties of cellulose stem from its molecular interactions (adsorption and adhesion) with various chemical species on the surface of the fibrils. Essentially, reactivity of cellulose towards various reagents comes from the reactivity of the oxygen atoms of **O2**, **O3**, and **O6** hydroxyl groups (**Figure 34**), depending on the degree of cellulose organization.²⁶¹

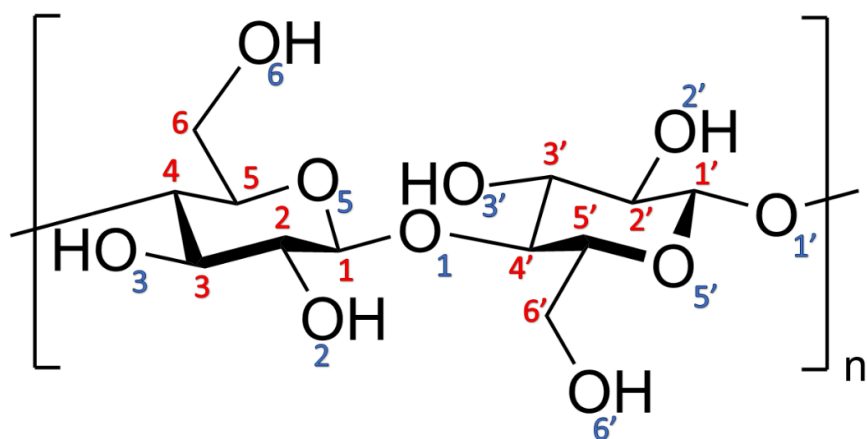


Figure 34. Cellulose – two repeated units presenting atom numbering.

Generally, for the ordered cellulose, the oxygen atoms in **O3'** hydroxyl groups are forming hydrogen bonds with **O5** oxygen atoms in the neighbouring glucose units. Hence, the **O3'** hydroxyls are not reactive. On the contrary, in the amorphous structures, oxygen atoms **O2**, **O3**, and **O6**, should be equally reactive, however, depending on the crystallinity, the **O3** oxygen atoms can be more or less accessible. For bacterial cellulose (which exhibits high crystallinity) the **O3** hydroxyls are almost non-reactive, yet in less ordered cotton fibres the same groups can be much more accessible.²⁶¹ However, the intra-chain hydrogen bond between **O5** acting as hydrogen acceptor and **O3H3** acting as hydrogen donor is in most cases very stable, and as a result there are only 3.6 OH groups/nm² accessible for hydrogen bonds formed with other fibrils, solvent, molecules, or macromolecules.¹⁸⁴ Hence, cellulose can clearly form both inter- and intramolecular hydrogen bonds, which is one of the primary interactions binding small molecules, such as dyes.^{261,262}

In case of TEMPO-oxidized CNFs (which were used in the experimental part of this dissertation) the carboxyl group appears on the **C6** and **C6'** atoms. They are responsible for increasing the stability of cellulose nanofibres in aqueous solution – their dissociation in water helps to avoid sedimentation and aggregation, due to the electrostatic repulsion. Their negative charge is not formal and delocalized between two oxygen atoms in the $-COO^-$ group. Thus, CNFs may potentially form both hydrogen bonds and ionic bonds.

Interactions between dyes and cellulose are basic for a field which is very common and vital for the humankind, such as dyeing of fabrics,²⁶³ but also for water depollution^{264,265} or for the development of optical brightening agents (OBA)^{266–268} applied to improve visual properties of paper and pulp products. Cellulose dyeing is dependent on pH, temperature, chemical structure of a dyeing molecule, its concentration, as well as diffusion process.²⁶³ For some of the dyes the fixation procedure is needed, which results in necessity for harsh basic and high temperature conditions. This is why cellulose-dye molecules interactions are of scientific

interest on both macroscopic and molecular level. There are many different aspects that need to be taken into account when preparing cellulose-dye hybrid materials and there are plenty of approaches to the process. Some of them, particularly important for the context of this dissertation, are presented and discussed below.

Spatial accessibility of cellulose chains. In order for the interactions between two species to occur, both of them need to be accessible for each other. Dye molecules may be entrapped within the cellulose macroscopic structure when enough free volume is created for the interactions to occur. Kim *et al.* have proposed dyeing of cellulose acetate fibres, prepared via electrospinning technique, with curcumin dissolved in the NaOH/ethanol solution.²⁶⁹ Electrospinning yielded material with high roughness and surface area, which resulted in the superb coloration. Curcumin entrapment within material's structure happened during the deacetylation of cellulose. The resulting dye-impregnated material exhibited chromatic responsiveness when exposed to HCl or NH₃ vapours (**Figure 35**).

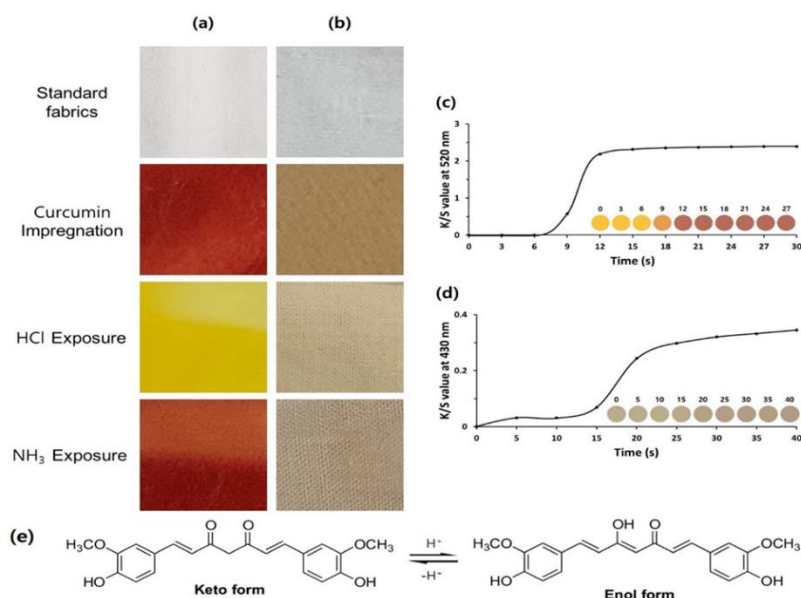


Figure 35. Impregnation of two different cellulose-containing materials with curcumin. Images representing colour changes of the curcumin-impregnated **a)** cellulose acetate fibres and **b)** cotton under different conditions. Colour depth of the samples expressed as *K/S* value (ratio of absorption coefficient, *K* and scattering coefficient, *S*) determined for 520 nm as a function of time for **c)** cellulose acetate fibres and **d)** cotton. **e)** Chemical reaction responsible for the colour change of the samples. Reprinted from ²⁶⁹.

Strength of interactions and promoting adsorption. Cellulose can interact with both anionic and cationic dyes, the only difference being its surface preparation and modification. In order to increase the strength of interactions and promote adsorption, cellulose processing needs to include steps leading to the increase in the number of proper functional groups. Zhou *et al.* have

modified cellulose with glycidyl methacrylate (GMA) to obtain epoxy cellulose, which was further modified with diethylenetriamine pentaacetic acid (DTPA), and thus more $-COOH$ groups have been introduced.²⁷⁰ This enabled efficient adsorption of malachite green and basic fuchsine. Additional chemical modification of cellulose is, however, not necessary to promote interactions with other species. Wang *et al.* used carboxylated CNFs to reinforce collagen film via inter- and intramolecular electrostatic interactions between negatively charged CNFs and positively charged collagen (due to the protonation of its amine groups in acidic conditions, $-NH_3^+$).²⁷¹ Besides the ionic bonds, the hydrogen bonds between $-NH_2$, $-COOH$, and $-OH$ of CNFs and collagen have also been observed (**Figure 36**). Such composite cellulose-collagen materials can be further used for the adsorption of dyes, e.g. tannin, and further serve as bioadsorbents for the removal of metal ions from water.²⁷²

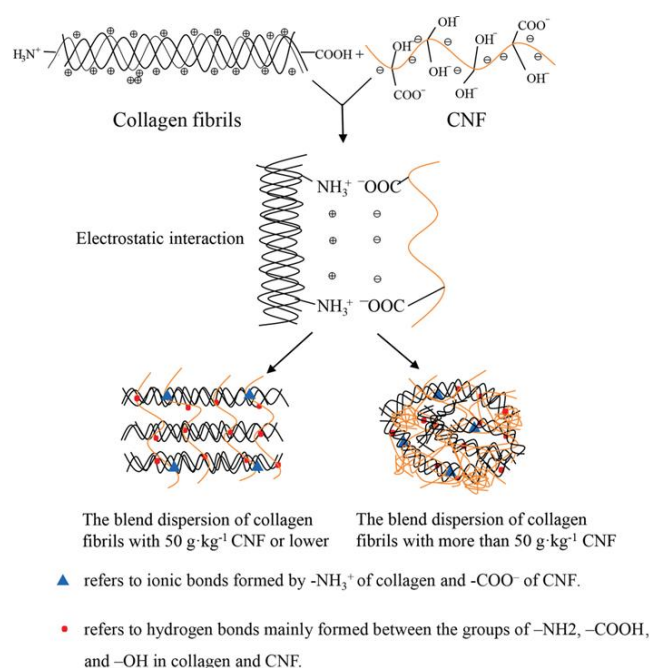


Figure 36. CNF and collagen interactions – electrostatic interactions and hydrogen bonds – as an underlying reason for the formation of an interpenetrating network. Reprinted from²⁷¹.

Cellulose-dye interactions can be mediated. Low molecular weight compounds, such as surfactants²⁶⁷ or salts²⁶⁸ can be used to mediate cellulose-dyes interactions or assist the sorption process.²⁷³ Liu and co-workers presented how to adsorb negatively charged stilbene on the surface of negatively charged cellulose.²⁶⁸ Adsorption was carried out due to the introduction of divalent salts, such as $CaCl_2$. Ca^{2+} cations reduced electrostatic repulsion between stilbene and CNFs, helped to form more extended conformation of the fibres, and finally created bridges between the two components.

Importance of electrostatic interactions. Iamazaki and Atvars have investigated possibility of sorption of an OBA, 4,4'-distyrylbiphenyl sodium sulfonate (Tinopal CBS), on cellulose

fibres in the presence of surfactants: anionic sodium dodecyl sulphate (SDS) and cationic dodecyltrimethylammonium chloride (DTAC).²⁶⁶ This work emphasises the importance of electrostatic interactions in the sorption of dyes on cellulose by focusing on the competing dye-surfactant and cellulose-surfactant interactions. Authors observed that both surfactants, despite different charges, interact with cellulose and cause phase separation of the fibres, leading to the turbidity of the solution. Since Tinopal CBS is negatively charged, it does not interact with SDS and the competition in their sorption on cellulose was observed. For the cationic surfactant, DTAC, interactions with dye molecules were possible, however, in the presence of cellulose and below critical micelle concentration (CMC) of DTAC, dye adsorption on cellulose occurred. Authors emphasise complexity of the whole process, involvement of several different interactions, such as hydrogen bonds, lateral hydrophobic association, van der Waals, and electrostatic interactions and note, that dyes can be adsorbed either inside the amorphous regions of cellulose fibres, or on their interface with its crystalline regions.

Ionic strength needs to be considered. As presented for the sorption of dyes in the presence of surfactants, addition of salts might influence their CMC and, hence, also their interactions with dyes and cellulose.²⁶⁶ Additionally, CNFs need to be considered as a polyelectrolyte surface. Thus, CNFs' surface charge and conformation might be influenced by ionic strength.

Cellulose can increase water-dispersibility of hydrophobic dyes. Very often use of various dyes is limited due to their solubility. In such case cellulose can be used as a platform to transfer dye molecules to the desired solvents and systems. Sun *et al.* have presented CNCs used without any surface modification as a platform for spirooxazine (SO) derivative.²⁷⁴ Hydrophobic SO dye was adsorbed on the surface of hydrophilic cellulose in a form of a nanometer scale aggregates, attached to the spindle-shaped cellulose nanocrystals (**Figure 37**). Photochromic paper strips prepared with CNCs-dispersed SO dye exhibited higher values of differential light absorption coefficients. Hence, the amount of dye that needed to be used to observe the desired photochromic effect could have been limited and the related costs were decreased.

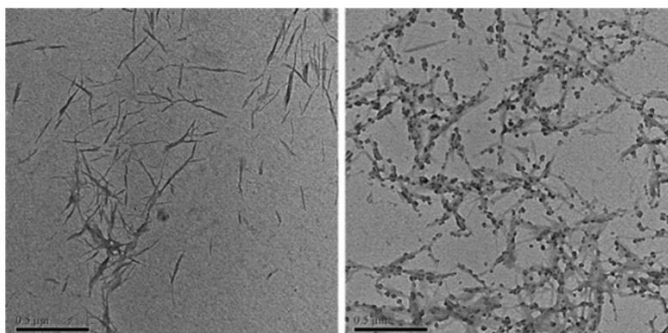


Figure 37. Cellulose as a platform for solvent transfer of water-insoluble dye. Comparison of (left) bare CNCs and (right) CNCs with adsorbed aggregates of hydrophobic spirooxazine derivative. Reprinted from ²⁷⁴.

If the dye is chosen to match the surface chemistry of cellulose, no special treatment is necessary. As presented by Araki, adsorption of cationic dyes on nanocellulose can be not only qualitative but also quantitative and can be used to assess number of cellulose acidic surface groups.²⁷⁵ Proposed protocol is very rapid, employs uncomplicated cellulose-dye interactions, and does not require any additional steps or cellulose functionalization. In the experiment of Araki, toluidine blue O (TBO) was used to assess sulphate and carboxyl groups on the surface of cellulose nanowiskers (CNWs). CNWs were chosen due to their surface chemistry. TBO, a cationic dye, formed ionic bonds with carboxyl groups on the surface of nanocellulose, which was used for the quantification of their number based on the spectrophotometric measurements.

As clearly presented above, there are various routes to prepare dye-impregnated cellulose. Despite all different factors that need to be considered, huge variety of dyes and different cellulose morphologies, combined with cellulose rich surface chemistry, constitute a strong and convenient starting point for the design of plethora of interesting systems. Linking this type of hybrid materials with the ones presented in the **Section 2.3.2** of this introduction opens new possibilities and makes new material designs possible. Such hybrid materials might be used in the previously unattainable experimental scenarios.

2.4. Hybrid materials based on azobenzenes and gold nanoparticles

The final subchapter of the introduction discusses hybrid materials composed of AuNPs and azobenzene type photochromes (Azo). Such material design corresponds really well with the requirements for the smart materials, which are able to convert the action of the external stimuli in the microscale to the desired material behaviour in the macroscale. Design and preparation of such materials is presumably one of the more interesting challenges at the intersection of chemical sciences and materials engineering. One of the best stimuli that enables control over smart materials is light. Light is fully tunable in terms of its wavelength (energy), exposition time, and intensity. Moreover, light is ultrafast, efficient, ecological, and can be controlled with high spatiotemporal resolution.^{276,277} Out of many light responsive systems the nanostructured or supramolecular ones are particularly noteworthy, due to the potential ease of modification, low costs, and high economic and societal impact.²⁷⁶ Such systems are typically based on photochromic molecules and nanoparticles. Especially popular designs are Azo-AuNPs hybrids, which exhibit dual functionality, namely plasmonic and photochromic properties at the same time. Firstly, this subchapter describes azobenzene type photochromes.

Subsequently, the most popular Azo-AuNPs hybrids designs are presented and their functionality is discussed.

2.4.1. Azobenzene type photochromes

Azobenzenes are a family of molecules that exhibit photochromism. A word ‘photochromism’ comes from two Greek words, photos (light) and chroma (colour), hence, the simplest definition of this phenomenon is the ability of a molecule to undergo reversible light-induced change of colour due to the occurrence of chemical reaction.²⁷⁸ This definition is related to the first observation of the phenomenon in 1867 by Fritzsche, who observed that orange naphthalene solution becomes colourless in the daylight, yet it recovers its colour in the dark or upon heating.²⁷⁹ The most common model describing photochromism is a two-way reaction between species A and B, which are forms of the same chemical compound, separated by a potential barrier (ΔE ; **Figure 38a**). Reaction $A \rightarrow B$ occurs upon irradiation and usually A absorbs in the UV or near-UV (**Figure 38b**). Reaction $B \rightarrow A$ may also occur solely upon light absorption, for bistable systems with high ΔE barrier, which is called P-type photochromism. However, for some of the molecules with thermodynamically unstable form B (low potential barrier), the back-reaction may occur spontaneously. Such compounds are called T-type photochromes, which refers to the thermally induced reaction $B \rightarrow A$ (**Figure 38c**).^{280,281}

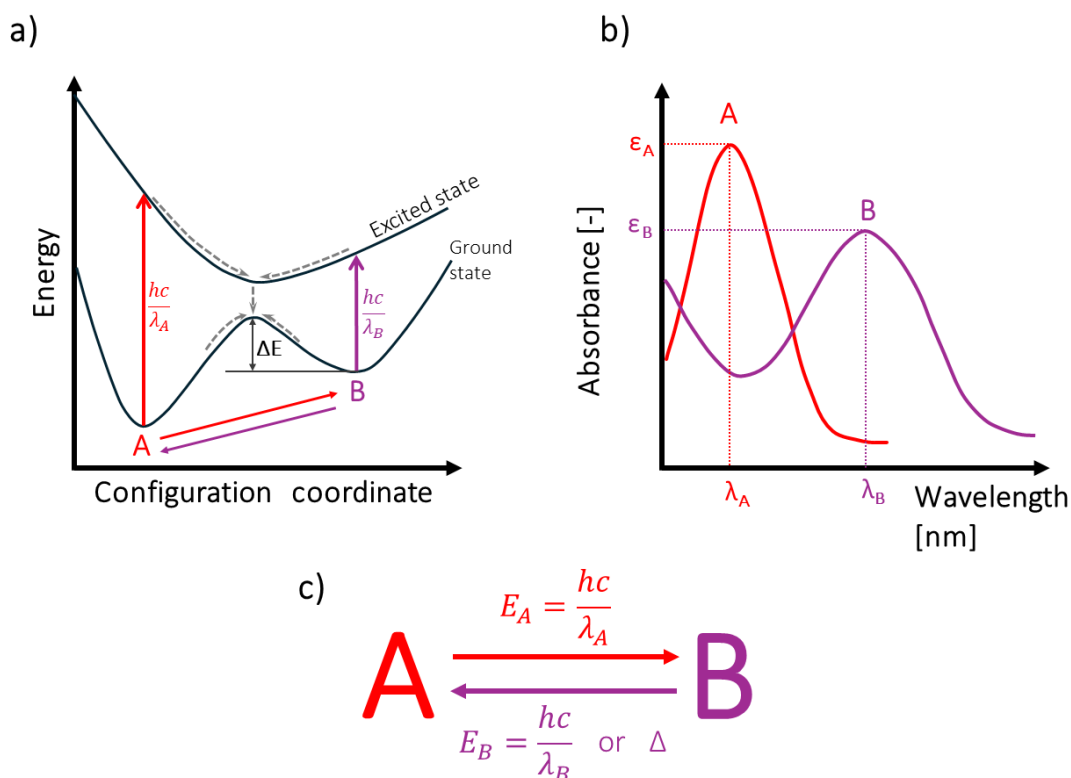


Figure 38. Photochromism depiction. **a)** Potential energy diagram. **b)** Schematic absorption spectra of species A and B. **c)** Photochromic reaction between species A and B. Inspired by ^{278,280,281}.

Upon irradiation, photochromic molecules change their geometrical conformation as well as chemical and physical properties, such as light absorption or emission profiles, conductivity, catalytic or magnetic properties. There are different types of photochromic molecules, including azobenzenes,²⁸² diarylethenes,²⁸³ stilbenes,²⁸⁴ and spiropyrans²⁸⁵ (**Figure 39**). Photochromes find applications e.g. in electronics,²⁸⁶ teranostics,²⁸⁷ or as functional coatings²⁸⁸ and in order to efficiently utilize them, especially in advanced applications, some of their characteristics need to be researched and improved. First, photochromes need to be characterized by high fatigue resistance, namely, they should exhibit as many switching cycles as possible. Second, to improve switching speed and switching extent, quantum yield of the photochromic reactions should be high. Third, for P-type photochromes, molecules should exhibit complete bistability, while for the T-type photochromes, back-reaction should occur with precisely defined rate (usually very quickly, although this aspect is strongly application-dependent). Finally, distinct spectral shifts between both forms are required, which also translates to significant changes in other properties of the molecular photoswitch.

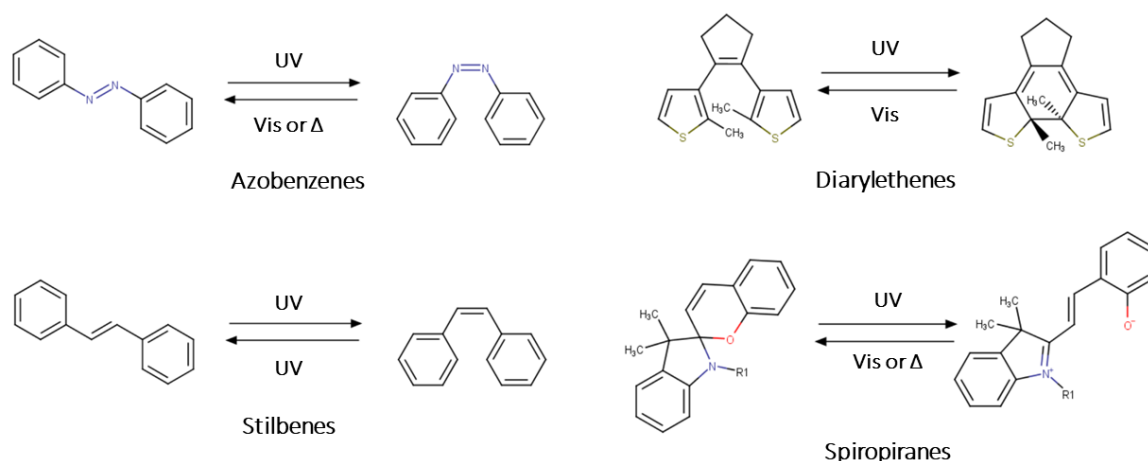


Figure 39. Photoswitching of different types of photochromes. Figure based on²⁸⁹.

Azobenzene is an organic azo compound, a derivative of diazene, in which both hydrogen atoms were replaced by phenyl rings. Such molecular structure was discovered in the 19th century, but the photochemistry of the molecule was not described until 1937.²⁹⁰ Azobenzene and its derivatives, due to the presence of double bond between nitrogen atoms, may occur in a form of two isomers: *cis* and *trans* or *Z* (from German ‘zusammen’ – together) and *E* (from German ‘entgegen’ – opposite), respectively. *E* isomers are more thermodynamically stable, mostly due to the steric effects, hence the *Z–E* isomerization may occur spontaneously, meaning that azobenzenes are T-type photochromes. Presence of substituents can drastically influence photochemical and physicochemical properties of Azo, as well as the stability of *Z* isomer.²⁹¹ Typically, however, Azo are characterized by two distinct bands, $\pi\text{-}\pi^*$ more pronounced and intense appearing in the UV part of the spectrum (usually

around 320–365 nm) and $n\text{-}\pi^*$ appearing in the visible spectral region (above 400 nm). Presence and type of substituents may substantially influence position and intensity of the bands. The effects may be even further influenced by type of the solvent.²⁹¹

Upon isomerization geometry of Azo molecule undergoes a distinct change centred around a movement of one of the phenyl rings with respect to the other (**Figure 40**). Upon such structural change, the distance between groups or atoms directly at the positions 4 and 4' changes from about 9.0 Å in a *trans*-Azo to about 5.5 Å in a *cis*-Azo.²⁹² For the terminal atoms in the chemical groups in the 4,4'-substituted azobenzenes the changes are even bigger. Such considerable geometrical change might be translated into properties and macroscopic behaviour of the Azo-doped materials, such as Azo-incorporating polymers²⁹³ and molecular crystals.²⁹⁴

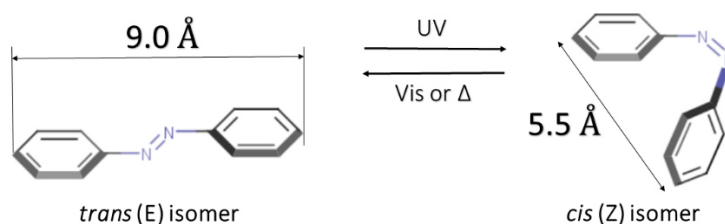


Figure 40. Geometrical change occurring upon Azo isomerization.

Isomerization of Azo also results in the change of molecule's polarity. In the *E* form lone electron pairs of both nitrogen atoms are oriented in the opposite directions, which is reflected in the low dipole moment of the molecule, typically 0.0–1.2 D, while for the *Z* form of Azo dipole moment increases to 3.1–4.4 D, depending on the substitution of the Azo core^{295,296} (**Figure 41**). Such effect can be successfully used e.g. to tune the polarity of the Azo-decorated cavities.²⁹⁷ Both effects can induce motion in supramolecular switches, as it has been presented for cyclophanes²⁹⁸ or cyclodextrins²⁹⁹ where *E*–*Z* Azo isomerization was used to release molecular ‘cargo’ from cavities of macrocyclic hosts.

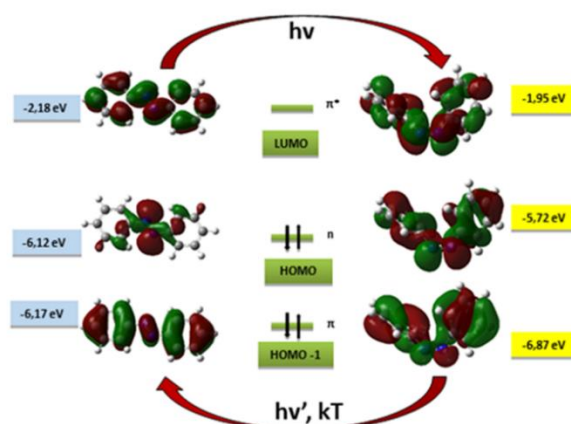


Figure 41. Molecular orbitals for *E* and *Z* isomers of unsubstituted Azo with corresponding energies [eV]. Reprinted from³⁰⁰.

Azo molecules are especially popular photochromes used for the design of advanced materials exhibiting photoswitching properties, mostly due to their relatively simple synthesis (their molecular structure can be easily modified) and high photostability even after prolonged irradiation.²⁹¹ Azo are also characterized by a good fatigue resistance, quick photoswitching (both $E-Z$ and $Z-E$ reactions can be completed within picoseconds³⁰¹) and low reactivity.³⁰² The usually indicated limiting factors are variable stability of the Z -Azo isomer and the fact that the positions of $\pi-\pi^*$ and $n-\pi^*$ bands are not that easily influenced, which is problematic for bio-related applications, since $\pi-\pi^*$ band of Azo occurs in the UV. However, the stability of Z isomer can be tuned by both internal and external factors, namely by the structure³⁰³ and surroundings³⁰⁴ respectively, and hence, can be adjusted to the desired applications. Moreover, there are multiple new Azo synthesis protocols enabling shifting of the absorption bands more into the Vis region of the spectrum. One of the synthetic approaches is the decrease of HOMO-LUMO gap, which redshifts Azo absorption bands. To effectively execute that approach π conjugation needs to be extended or electron-withdrawing groups (EWGs) and/or electron-donating groups (EDGs) at *ortho* or *para* positions need to be introduced.³⁰⁵ However, this strategy influences also thermal half-life of the Z isomer, usually by decreasing it.²⁹¹ Therefore, another strategy is often applied and involves separation of the $n \rightarrow \pi^*$ transition. To achieve that Woolley *et al.* introduced methoxy group at the *ortho* position (**Figure 42a**).³⁰⁶ The another example is work of Bleger *et al.* who proposed *ortho* substitution with fluorine³⁰⁷ (**Figure 42b**). This synthetic approaches result in Azo molecules exhibiting more bistable character, which further predestines them for the bio-related applications.³⁰⁸

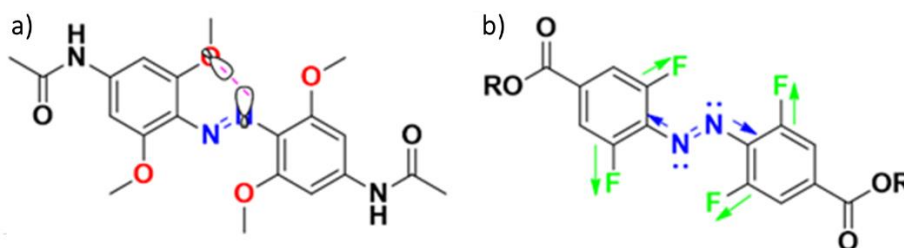


Figure 42. Azo molecules can be modified by substitution in the *ortho* position to affect the energy of the $n \rightarrow \pi^*$ transition. **a)** Upon substitution with four methoxy groups in all *ortho* position the *trans-cis* isomerization can be induced with green light (530-560 nm).³⁰⁶ **b)** Upon substitution with fluorine in all *ortho* positions the *trans-cis* isomerization can be induced with light above 500 nm light.³⁰⁷ Reprinted from ³⁰⁰.

2.4.2. Azo-AuNPs hybrids

To summarize this chapter, which is focused on the introduction of the most essential topics from the perspective of the dissertation, a short discussion regarding the most popular designs of Azo-AuNPs plasmonic-photochromic hybrids is presented.

Due to high affinity towards thiol- and amine-terminated molecules^{309,310} gold can be used as a surface for efficiently deposition of properly designed azobenzene derivatives. Such photochromic ligands need to include in their structure functional groups terminated with $-SH$ or $-NH_2$ moieties. Initially research attention was placed on the self-assembled monolayers (SAMs) of Azo ligands on planar gold surfaces (**Figure 43a**).^{295,311–314} Such material design was relatively uncomplicated and enabled macroscopic control over the surface properties. As presented by Lim *et al.*, due to the changes in the dipole moment of the Azo ligand upon isomerization, such hybrid materials exhibited switchable wettability.³¹⁵ On the other hand, Liu *et al.* presented reversible cell adsorption on the Au planar surface decorated with mSAMs of protein-terminated Azo-thiol and background alkanethiol.³¹⁶

However, the dense packing of Azo SAMs typically results in the constrained photoswitching.^{312,313,317,318} The estimated volume required for *trans-cis* isomerization of a single Azo unit is about 127 \AA^3 ³¹⁹ and the minimal planar surface is 0.40 nm^2 .³²⁰ Studies showed, that the average surface area occupied by a single Azo molecule in SAM on planar Au is about 0.187 nm^2 ,³¹⁷ which is lower than for a single alkyl thiol (0.215 nm^2),³²¹ and lower than necessary for efficient isomerization. It was confirmed, that such dense packing of Azo ligands is a direct result of interactions between the neighbouring molecules (especially between their $-N = N -$ motifs).³²² Because photoswitching is the most crucial property of any material containing photochromic component, maintaining the photoswitchability of Azo on planar Au surfaces became an important challenge in the field. The remedy for the steric hindrance experienced by ligand molecules was found in a few approaches. One of them is preparation of mixed SAMs (mSAMs), where non-photochromic, shorter background ligands are introduced, mostly alkanethiols.^{311,323–326} Hence, the necessary space is created through background molecules acting as spacers between the neighbouring Azo. Another approach relies on the modification of the ligand's structure through introduction of bulky spacers or elongated linkers near to $-N = N -$ motif.^{327–330} For instance, Ito *et al.* presented that p-carborane (carboranes³³¹ are a class of non-classically bonded boron, hydrogen, and carbon clusters, adapting a 3D geometry) can be used as bulky spacers to provide necessary free volume for Azo isomerization within SAMs.³²⁷ The another pathway involves use of unsymmetrically substituted disulfides as linkers anchoring Azo unit to the surface of gold.^{332–334} Such linker provides two anchoring

points and hence one dialkyl disulfide molecule occupies the average area of 0.43 nm^2 , similarly to the surface necessary for Azo molecule to freely isomerize.³³⁵ In order to avoid phase separation upon ligand adsorption on Au, which usually occurs due to the disulfide cleavage into a pair of thiolates, unsymmetrical disulfides are used.

Nevertheless, from the perspective of materials science the most favourable approach to the elimination of the Azo ligands' steric hindrance was introduction of new material design in which photochromes are bound to the positively curved surfaces, such as nanoparticles. Because of this, efficient weakening of intermolecular interactions between Azo molecules ensues, which results in the increased free volume.³³⁶ Such novel formulation enabled observation of new phenomena and started an undeniable boom for Azo-nanoparticles hybrids.^{7,337–339} Especially systems relying on plasmonic Au nanocores^{340–343} became popular (**Figure 43b**), because the presence of a metallic core exhibiting one-of-a-kind optical properties stemming from surface plasmons granted new functionalities and possibilities.¹¹⁴

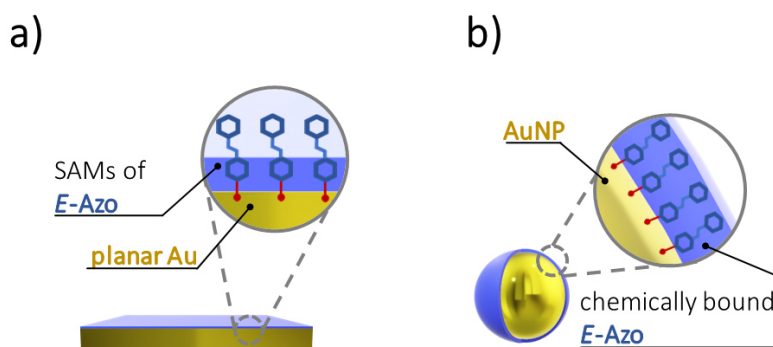


Figure 43. The most typical Azo-Au hybrid materials **a)** SAMs on the surface of planar Au and **b)** Azo-decorated Au nanoparticles.

Preparation of Azo-AuNPs as a new type of interfaces resulted in the enlarged surface area of the materials and facilitated ligand exchange processes. Nowadays, the majority of studies focuses on hybrids prepared via direct interactions between the plasmonic nanostructures and the photochromic ligand. Usually the modifications to the nanomaterial properties, such as optical response or aggregation state, are central to the literature reports.^{339–342,344–347} Particularly the Light-Induced (Reversible) Self-Assembly^{337,340,346,348} of nanostructures (**Figure 44**) equipped with Azo ligands has evoked a great interest.

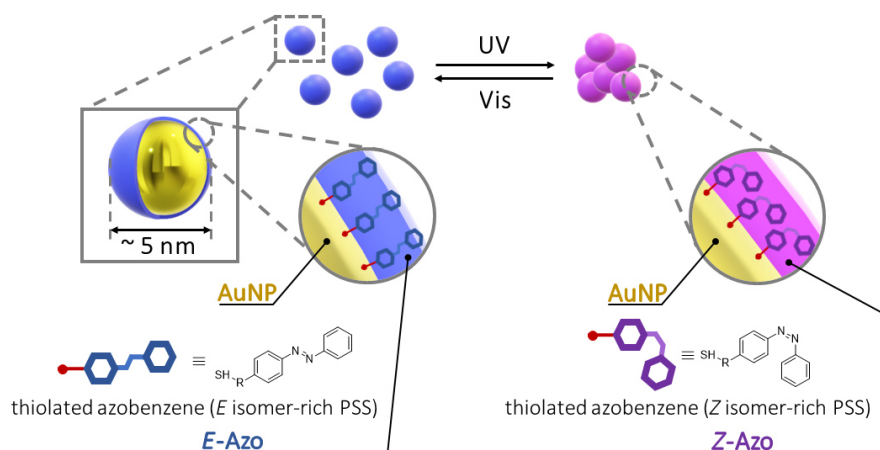


Figure 44. Schematic depiction of the Light-Induced Self-Assembly phenomenon observed for the Azo-AuNPs hybrid structures upon irradiation inducing isomerization of the photochromic ligand.

One of the best known examples of Azo-AuNPs and LISA applications are self-erasing inks. Klajn *et al.* described reversible aggregation of photoactive 5.6 nm Au and 5.3 nm Ag nanostructures embedded into the PMMA films (150 μm).³⁴⁰ After UV irradiation through a photomask patterns with different levels of complication could have been imprinted in the film, due to Azo-AuNPs aggregation (**Figure 45a**). Depending on the Azo ligands concentration on the surface of nanostructures pattern self-erasure times in the daylight could have been modified. Writing times and irradiation intensities were about 0.8-10 s and 10 mW/cm^2 respectively. It was possible to create multicolour regions by varying irradiation times. After pattern erasure films could be re-written multiple times.

Typically, aggregates of nanoparticles are associated with disordered structures. However, contrary to what would be intuitively expected, LISA may also lead to the formation of ordered aggregates. As presented by Klajn *et al.* proper hybrid's design may lead to the formation of crystalline assemblies (**Figure 45b**).³⁴⁸ By utilizing dithiol azobenzene ligand, able to create covalent bonds between two neighbouring nanoparticles, and by controlling the number of ligands adsorbed on the surface of spherical AuNPs, one may obtain both light-reversible and irreversible crystals next to amorphous precipitate and unaggregated nanostructures. Covalent bonding of nanoparticles is mediated by light-induced dipoles of *cis*-Azo. Zhao *et al.* presented, that such Azo-AuNPs crystals created via LISA may be used as nanoreactors (called by authors 'nanoflasks', **Figure 45c**).³⁴⁹ By creating confined volumes, comparable to the dimensions of molecules, local changes of e.g. polarity may occur and lead to chemical processes with high stereoselectivity. Sizes of the nanoflasks might be controlled by size of the Au core and length of Azo ligands. Creation of mSAMs may help to improve selectivity towards trapped reagents.

As clearly presented, LISA can be advantageous for certain applications. Nevertheless, it may pose considerable challenges for other purposes, mainly due to the fact, that optical properties of AuNPs are drastically changed upon aggregation. From the point of view of this dissertation LISA phenomenon is considered to be undesirable.

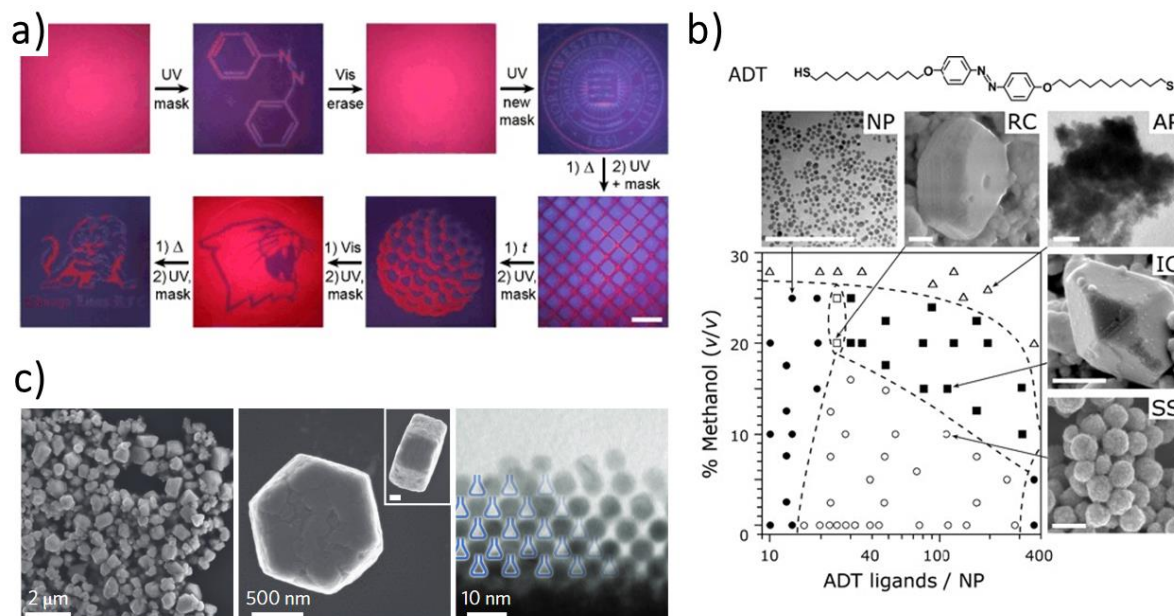


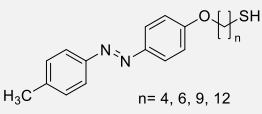
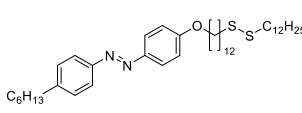
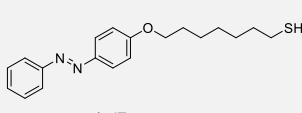
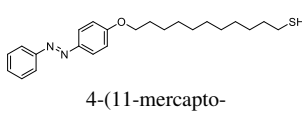
Figure 45. **a)** Azo-AuNPs rewritable, flexible PMMA films. Sequential writing (2 s, 10 mW/cm² UV irradiation, except for array of squares where exposure time was 5 s) and erasing ('t' indicates long-time daylight exposure, 'Vis' refers to short visible light exposure, and 'Δ' indicates heating to 50 °C for 20 s) for the same film sample. Scale bar equals 5 mm. Reprinted from ³⁴⁰. **b)** Crystalline Azo-AuNPs assemblies. (Top) Structure of the Azo ligand (ADT) mediating LISA phenomenon. (Bottom) Phase diagram and related suprastructures obtained via LISA: NP – unaggregated AuNPs, AP – amorphous precipitate, RC – light-reversible crystals, IC – irreversible crystals, and SS – supraspheres. Scale bars equal 100 nm. Reprinted from ³⁴⁸. **c)** Formation of nanoflasks upon Azo-AuNPs aggregation (6 nm AuNPs decorated with 4-(11-mercapto-undecanoxy)azobenzene). Electron micrographs of colloidal crystals obtained after exposure to UV irradiation. Inset scale bar equals 200 nm. As-formed nanocavities (also named 'nanoflasks') are indicated with blue lines in the picture on the right. Reprinted from ³⁴⁹.

The influence of AuNPs on the properties and photoswitching behaviour of the Azo ligands, although not as much researched as LISA, remains an important topic as well. In particular, since plasmonic cores are a source of powerful light-induced catalytic tools (as described in the section 2.2. of the dissertation), it can be stated that plasmon-related phenomena can be potentially used to affect the isomerization of azobenzenes (both *trans*–*cis*

and *cis*–*trans* reactions) by influencing mechanisms, rate constants (k), and half-times (τ) of the reactions.

The summary of the selected research attempts focused on the investigation of AuNPs influence on the isomerization of Azo as one of the goals is presented in **Table 1** to form more comprehensive picture of the phenomenon. This also presents scope of challenges crucial to this work and remaining to be addressed in the field.

Table 1. Summary of the selected literature reports focused on the influence of AuNPs (solvent of the process indicated in the brackets) on the isomerization of azobenzenes (including kinetic parameters – reaction rate constant, k and reaction half-time, τ). Change in the kinetic parameters is given in relation to free Azo molecules (solvent for the comparative Azo solution indicated in brackets).

Authors (year)	Azo derivative	AuNPs type (solvent)	Azo-AuNPs interactions	Catalysed reaction (irradiation conditions)	Observed effect, proposed mechanism
J. Zhang <i>et al.</i> (2001) ³⁵⁰	 4-methyl-4'-(mercaptoalkoxy)azobenzenes with varying alkyl chain lengths	~2.5 nm Au ₅₀₀ cluster (toluene → DCM or chloroform)	direct Azo attachment	UV-induced <i>trans</i> – <i>cis</i> isomerization (350 nm, Rayonet Photochemical Reactor)	slower isomerization than free Azo (DCM); chain length-dependent quenching by metal cluster; no detailed comment on the kinetics
A. Manna <i>et al.</i> (2003) ³⁵¹	 4-hexyl-4'-(12-(dodecyl-dithio)-dodecyloxy)azobenzene	~5.2 nm spherical (toluene)	direct Azo attachment	UV-induced <i>trans</i> – <i>cis</i> isomerization (364 nm; 1.5 mW/cm ² and 0.1 mW/cm ²) Vis-induced <i>cis</i> – <i>trans</i> isomerization (440 nm; 1.5 mW/cm ²)	no influence; first order kinetics k - slight increase (toluene), first order kinetics (negligible steric effect)
K. Shin <i>et al.</i> (2008) ³³⁶	 4-(7-mercaptoheptyloxy)azobenzene	2-3 nm spherical (toluene → DCM)	direct Azo attachment	UV-induced <i>trans</i> – <i>cis</i> isomerization (350 nm, Rayonet Photochemical Reactor) thermal (dark) <i>cis</i> – <i>trans</i> isomerization	k ~2.9-times increase (DCM), first order kinetics k ~2.3-times increase (DCM), first order kinetics
R. Klajn <i>et al.</i> (2009) ³⁴⁰	 4-(11-mercapto-undecanoxo)azobenzene mSAMs with dodecylamine	~5.6 nm spherical (toluene → sPMMA matrix)	direct Azo attachment	UV-induced <i>trans</i> – <i>cis</i> isomerization (365 nm; I _{UV} =0.7-10 mW/cm ²) in the sPMMA matrix	faster isomerization with increasing I _{UV} ; k value dependent on the surface concentration of Azo (χ); first order kinetics; reversible aggregation

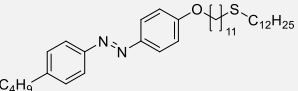
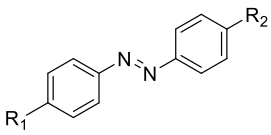
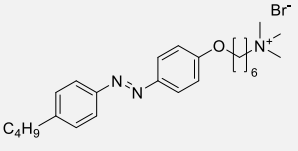
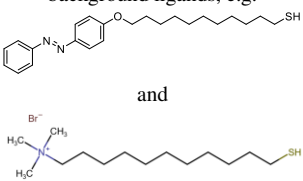
J. H. Yoon <i>et al.</i> (2011) ³⁴⁷	 <p>4-butyl-4'-(11-dodecylthio-undecyloxy)azobenzene</p>	33 nm spherical, <u>aggregated</u> (water:ethanol, 1:1, v/v)	Azo chemisorption on the surface; formation of aggregates and confinement of Azo	UV-induced <i>trans-cis</i> isomerization (365 nm, 51 mW/cm ² , Hg-Xe lamp, 10x microscope objective)	further aggregation; no comment on the kinetics 15-times increase of k (DCM), first order kinetics (reduced N=N bond order)
G. Hallett-Tapley <i>et al.</i> (2013) ³⁵²	 <p>1 2 3 4 R₁: H, H, Cl, CH₃ R₂: H, OCH₃, Cl, CH₃ 4 different derivatives</p>	~12 nm spherical pseudo-naked (water)	no attachment, free Azo and AuNPs in solution; AuNPs added to max- <i>cis</i> water-MeCN Azo solution	thermal (dark) <i>cis-trans</i> isomerization	no comparison with pristine Azo; varying k values (AuNPs batch- and Azo-dependent); Azo-AuNPs electron transfer (eT) → formation of radical cation intermediate → rotation about N=N bond → AuNPs-Azo eT
Lysyakova <i>et al.</i> (2015) ³⁴³	 <p>[6-[4-(4-hexylphenylazo)-phenoxy]-hexyl]-trimethylammonium bromide surfactant-type molecule</p>	~10 nm spherical, pseudo-naked (water)	electrostatic interactions (formation of complexes with morphology dependent on surfactant loading)	thermal (dark) <i>cis-trans</i> isomerization	three modes of relaxation, τ equal 2.3, 9.2, and 442 min – each for different fraction of Azo surfactant vs. 60 h for free Azo (water)
Z. Chu <i>et al.</i> (2019) ³³⁹	<p>various 4-(mercapto-alkyloxy)azobenzenes and 4-(mercapto-oligo(ethylene) glycol)azobenzenes mSAMs with charged and polar background ligands, e.g.</p>  <p>and</p>	~2.5 nm spherical (water and different water-solvent mixtures) or 5.5 nm spherical (9:1 water-methanol) and	direct Azo attachment	both UV- and Vis-induced isomerizations thermal (dark) <i>cis-trans</i> isomerizations	no comment on the kinetics first-order kinetics; k typically not dependent on the Azo surface concentration (χ); faster isomerization for smaller AuNPs for the same χ ; k comparable or one/two orders of magnitude larger than for free Azo (organic solvent) depending on the background ligand

Table 1 summarizes the most representative examples of Azo-AuNPs hybrids that have been investigated for the last 25 years. The timescale was selected to present evolution of the field. The last row of the table should include an example of current year's studies (2024) and

this dissertation, with results presented in Chapter 5 and 6, aims to fill in the blanks and continue research directions set up in the quoted works.

What is important in the analysis of the research papers summarized in **Table 1** is the fact that at the very beginning there were only qualitative reports on the AuNPs influence on the kinetics of Azo isomerization. Gradually, the quantitative parameters appeared, however except of a few selected works the investigations were not carried out systematically. Moreover, most of the works is focused on one type of isomerization. Initially, mostly irradiation-induced reactions were investigated. Over the years first reports regarding thermal relaxation of Azo ligands in Azo-AuNPs hybrids have started to appear. Nowadays thermal relaxations seem to be the main focus of any kinetic investigations and there seems to be a universal consensus on the first-order kinetics of the reaction in the presence of Au. Moreover, virtually all of the research attempts are limited to covalently bound hybrids operating mostly in organic solvents and small, spherical nanostructures which hinders harnessing of the potentially catalytic plasmon-assisted phenomena.

Based on the information presented in this chapter, as well as in **Table 1**, list of the current challenges in the field can be proposed: **(1)** comprehensive investigation of the influence of AuNPs on Azo isomerization in hybrid systems in all possible reaction scenarios, namely upon irradiation and in the dark (thermal process); **(2)** investigation of the Azo isomerization mechanism in the presence of Au; **(3)** utilization of bigger and anisotropic AuNPs in order to affect Azo isomerization reactions through plasmonic effect (currently due to small size and spectral overlapping of AuNSs and Azo this aspect is too complicated, if not impossible, to be reliably investigated); **(4)** preparation of Azo-AuNPs hybrids without covalent bonding of the components to provide more hybrid formulations for advanced applications; **(5)** transfer of the Azo-AuNPs functionality from organic solvents to water to broaden their potential applications (e.g. in bio-related research).

This dissertation addresses challenges presented here.

II RESULTS, DISCUSSION, AND METHODOLOGY

Chapter 3. *Cellulose as a Robust Scaffold for the Stabilization of Gold Nanorods in the Photocatalytic Regeneration of Cofactor Molecules*

This chapter focuses on cellulose nanofibres as a robust scaffold for plasmonic nanoparticles, enabling stabilization of their optical properties under various conditions. The preparation of cellulose nanofibres decorated with AuNRs is described and the proposed material is characterised in terms of its stability and optical properties. The proposed design is utilized to prepare CNFs decorated with bimetallic AuPdNRs. Such catalytically active composite is evaluated as a potential photocatalyst. The photocatalytic efficiency is determined in the model reaction of the cofactor (oxidized form of nicotinamide adenine dinucleotide, NAD⁺) regeneration. Hence, the results presented here challenge Objective 1 and verify hypotheses 1 and 2 of the dissertation.

Objective 1: To stabilize the optical properties of AuNRs for applications in processes or phenomena requiring intense illumination, high temperatures, or wide pH range.

Hypothesis 1: Cellulose may serve as an inert scaffold for AuNRs and does not alter the optical properties of nanocrystals.

Hypothesis 2: Cellulose-stabilized AuNRs can serve as a reusable catalyst for model photocatalytic reactions.

Results presented within this chapter were published in *ACS Applied Materials & Interfaces*:³⁵³ [N. Tarnowicz-Staniak, S. Vázquez-Díaz, V. Pavlov, K. Matczyszyn, M. Grzelczak, *Cellulose as an Inert Scaffold in Plasmon-Assisted Photoregeneration of Cofactor Molecules*, ACS Appl. Mater. Interfaces **2020**, 12, 17, 19377–19383, <https://doi.org/10.1021/acsami.9b21556>.](https://doi.org/10.1021/acsami.9b21556)

3.1. Motivation

Plasmonic nanoparticles, due to their unique properties described in the subsection 2.2. of this dissertation, find applications e.g. in plasmonic catalysis.^{104,114,127} In order to efficiently

trigger plasmon-related phenomena optical properties of plasmonic nanostructures need to be precisely controlled, which is usually achieved via wet chemistry synthetic methods. Such protocols typically rely on use of surfactants as surface stabilizers, especially for big and anisotropic nanoparticles. Surfactants contain long alkyl chains and thus, plasmonic nanocrystals are covered with an insulating shell hampering their catalytic activity.^{354,355} Removal of the shell may lead to the aggregation of nanostructures, which alters their optical characteristics and makes them unsuitable for further use. Hence, before surface stabilizers can be removed, nanocrystals should be first immobilized on a proper substrate. Supports such as oxides (e.g. TiO₂,³⁵⁴ SiO₂,¹⁶¹ and Al₂O₃¹³⁶), graphene,³⁵⁶ glass,^{357,358} or MoS₂³⁵⁹ can be used, however, they are usually not inert and the ensuing obstacles include altering of the electronic properties of plasmonic nanocrystals and changes in the dynamics of carriers flow. As a result, autonomous plasmonic catalysis cannot be performed.

Necessary supports exhibiting chemical and physical inertia can be potentially found in a group of natural organic materials such as cellulose. Cellulose is a polymer of natural origin and appears abundantly in Nature. Upon proper processing it yields nanocellulose, namely nanostructured cellulose exhibiting high surface area. So far cellulose has been combined with semiconducting nanoparticles to efficiently produce photocatalysts.^{360–362} Because of rich surface chemistry it can be potentially used to stabilize surfactant-coated plasmonic nanostructures (**Objective 1**) and act as a support in the process of surface ligand removal. Hence, theoretically, optical properties of nanoparticles should be maintained (**Hypothesis 1**).

Novel photocatalysts formulations require proper evaluation of their catalytic efficiency. There are many photocatalytic reactions that can be employed for this purpose, including e.g. regeneration of cofactor molecules.

Cofactors are electron donors or acceptors required in the reactions of oxidoreductases, which are enzymes participating in the redox processes requiring electron transfer.³⁶³ Cofactors serve as active sites for the charge transfer³⁶⁴ and one of their most common species are nicotinamides, such as nicotinamide adenine dinucleotide (NAD⁺ and NADH, oxidized and reduced form, respectively). NAD⁺/NADH mediate many two-electron redox reactions,³⁶⁵ including anabolic reactions of cellular respiration. NAD⁺/NADH is a niacin derivative³⁶⁴ and is composed of two dinucleotides, namely nicotinamide and adenosine 5'-monophosphate, connected through their phosphate groups (**Figure 46a**). The NAD⁺/NADH system provides two highly energetic electrons and a proton and its reversible reduction is presented in **Figure 46b**.

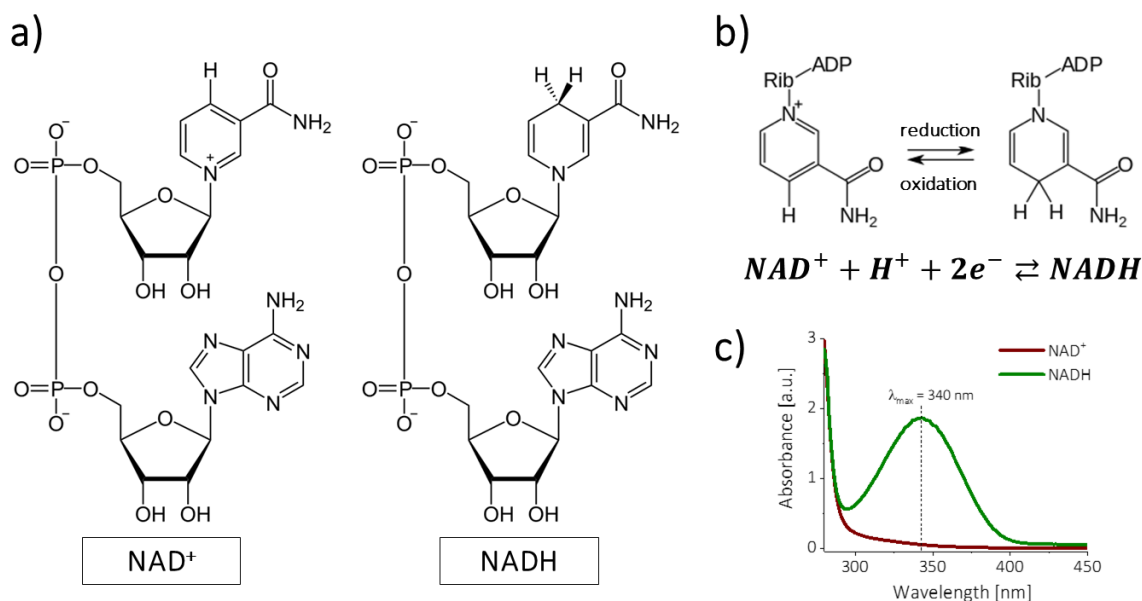


Figure 46. a) Chemical structures of cofactor nicotinamide adenine dinucleotide in its oxidized (NAD^+) and reduced ($NADH$) form. b) Reversible reduction of NAD^+ to $NADH$. c) Both forms of cofactor exhibit band at 260 nm, however only $NADH$ exhibits a pronounced band at 340 nm. Own results presenting difference in the optical properties of aqueous solutions of NAD^+ and $NADH$.

NAD^+ is typically derived from yeast³⁶⁶ and appears as white, amorphous, and hygroscopic powder. This cofactor is also well soluble in water, however not stable in the solution outside of neutral pH condition. NAD^+ easily decomposes at high pH, while $NADH$ in acidic conditions.³⁶⁶ Both forms also differ in optical properties – although both exhibit absorption band at 260 nm ($\epsilon_{NAD^+}(260) = 16900 \text{ M}^{-1}\text{cm}^{-1}$), $NADH$ exhibits also another band at 340 nm ($\epsilon_{NADH}(340) = 6220 \text{ M}^{-1}\text{cm}^{-1}$)³⁶⁷ as presented in **Figure 46c**. The industrial scale $NADH$ regeneration is always carried out enzymatically,³⁶³ however the non-enzymatic approaches have been developed over the last few decades and can be divided into three categories, namely chemical,^{368,369} electrochemical,³⁷⁰ and photocatalytic^{371,372} methods. Hence, it is justifiable to test new photocatalyst, proposed within this dissertation, on the reaction of $NADH$ regeneration.

So far many different hydride donors for the cofactor regeneration have been proposed, including glucose, propanol, or molecular hydrogen.³⁷³ $HCOOH$ is considered a liquid hydrogen carrier, due to its high volumetric and gravimetric H_2 capacity.³⁷⁴ Moreover, it is easy to handle and not very toxic and hence can be used in such processes as well. Typically, to perform $HCOOH$ dehydrogenation, elevated temperatures and noble metal catalysts (e.g. Pd, Pt) are required. Some photocatalytic methods also have been proposed, including use of carbon nitride,³⁷⁵ quantum dots,³⁷⁶ and plasmonic nanoparticles.³⁷⁷ Plasmonic nanostructures,

however, need to be supported by a co-catalyst, such as palladium, which can be deposited on their surface to facilitate the process. Moskovits *et al.* proposed hot carriers-driven mechanism of formic acid dehydrogenation in the presence of plasmonic catalyst.³⁷⁸

To facilitate the process of NAD^+ reduction, this dissertation proposes coupling of the reaction with sodium formate as hydride donor (**Figure 47**). Such process is mimicking the naturally occurring HCOOH dehydrogenation by an enzyme formate dehydrogenase, in which hydride (proton and two electrons) is transferred to NAD^+ .³⁷⁹ Here, Pd-coated AuNRs supported on nanocellulose scaffold are used as an efficient and reusable photocatalyst under visible light irradiation (**Hypothesis 2**).

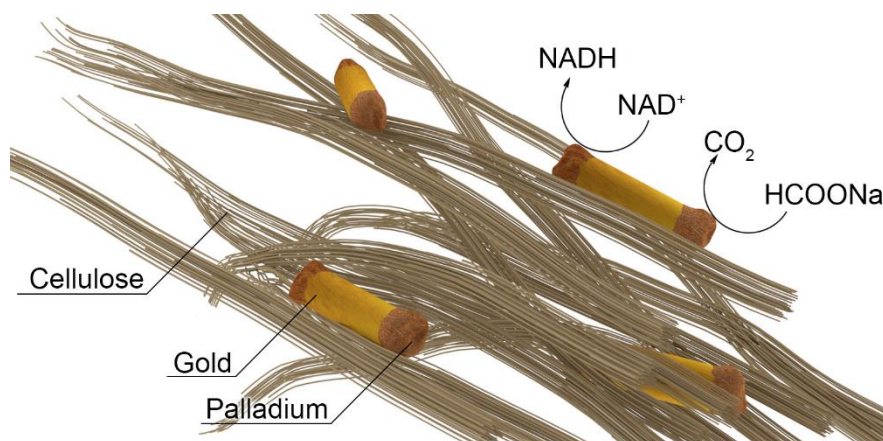


Figure 47. Schematic depiction of hybrid AuPdNRs-CNFs photocatalyst. Upon visible light irradiation, plasmonic nanoparticles catalyse the dehydrogenation of sodium formate (HCOONa) and, hence, reduction of cofactor molecules (NAD^+) occurs simultaneously. Figure reprinted from own source publication³⁵³.

3.2. Materials and methods

3.2.1. Materials and techniques

Materials

Chemicals used for the experiments were commercially available and did not require purification. In all experiments deionized water with the resistivity of $18.2 \text{ M}\Omega \cdot \text{cm}$ (Millipore Milli-Q grade) was used. If not indicated otherwise, chemicals were purchased from Sigma-Aldrich. For the synthesis of AuNRs and AuPdNRs the following reagents were used:

- metallic precursors: gold(III) chloride trihydrate ($\text{HAuCl}_4 \cdot 3\text{H}_2\text{O}$) and potassium tetrachloropalladate(II) (K_2PdCl_4),
- surface stabilizing agent: cetyltrimethylammonium bromide (CTAB),

- reducing agents: sodium borohydride (NaBH_4) and L-ascorbic acid (AA),
- other additives: silver nitrate (AgNO_3), and hydrochloric acid (HCl, 37%, Scharlab).

Support for nanoparticles: TEMPO-oxidized cellulose nanofibres (CNFs) supplied by CelluForce (Canada).

Moreover, for the cofactor regeneration experiments β -nicotinamide adenine dinucleotide (NAD^+) and sodium formate (HCOONa) were used.

Other chemicals: sodium hydroxide (NaOH).

Techniques

UV-Vis-NIR extinction spectra of all samples were measured using JASCO V-770 UV-Vis spectrophotometer. Transmission Electron Microscopy (TEM) images were taken using JEOL JEM-1400PLUS. Scanning TEM were performed using JEOL JEM-F200. X-ray photoelectron spectroscopy (XPS) measurements were performed using SPECS Sage HR100 spectrometer equipped with a non-monochromatic X-ray source (Aluminum $\text{K}\alpha$ line of 1486.6 eV, 300 W).

3.2.2. Nanoparticles synthesis

AuNRs synthesis

Gold nanorods were prepared according to silver-assisted seeded growth approach, using the most popular synthesis protocols by Nikoobakht *et al.*⁷⁹ and Liu *et al.*⁸³

In the first step seeds were prepared by reducing gold precursor, HAuCl_4 (0.025 mL, 0.05 M) in aqueous solution of CTAB (4.7 mL, 0.1 M) with ice-cold NaBH_4 (0.3 mL, 0.01 M) added under vigorous stirring. The mixture was left for 30 min to assure seed formation and reducing agent decomposition. Mixture was mildly stirred during that time.

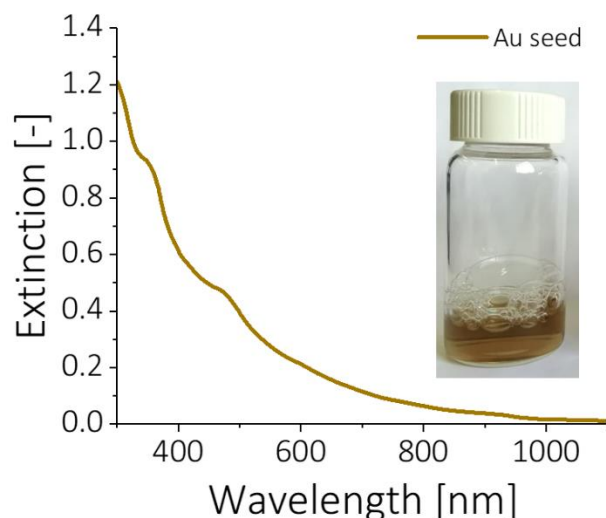


Figure 48. UV-Vis spectrum of the seed solution. The inset presents the visual appearance of the sample. Seed absorption spectra are typically sufficient to assess seed quality (based on the overall profile and absorbance value at 400 nm) and hence, TEM imaging is not necessary.

These results present standard features of the seed solution and are representative of all performed AuNRs syntheses. Thus, seed spectra will not be presented in the further parts of the dissertation.

In the second step, Ag-assisted seeds overgrowth was performed in the solution containing HAuCl_4 (0.1 mL, 0.05 M), CTAB (10 mL, 0.1 M), HCl (0.19 mL, 1 M), AgNO_3 (0.12 mL of 0.01 M), and AA (0.08 mL, 0.1 M) upon the addition of Au seed solution (0.024 mL). AuNRs were formed at room temperature and growth solution was left undisturbed for at least 2 h. The final concentration of metallic gold was 0.0005 M as determined by AuNRs absorbance at 400 nm.^{380,381} The as-synthesised AuNRs were used to (1) prepare bimetallic AuPdNRs and (2) to investigate interactions between AuNRs and CNFs and formation of composite AuNRs-CNFs materials.

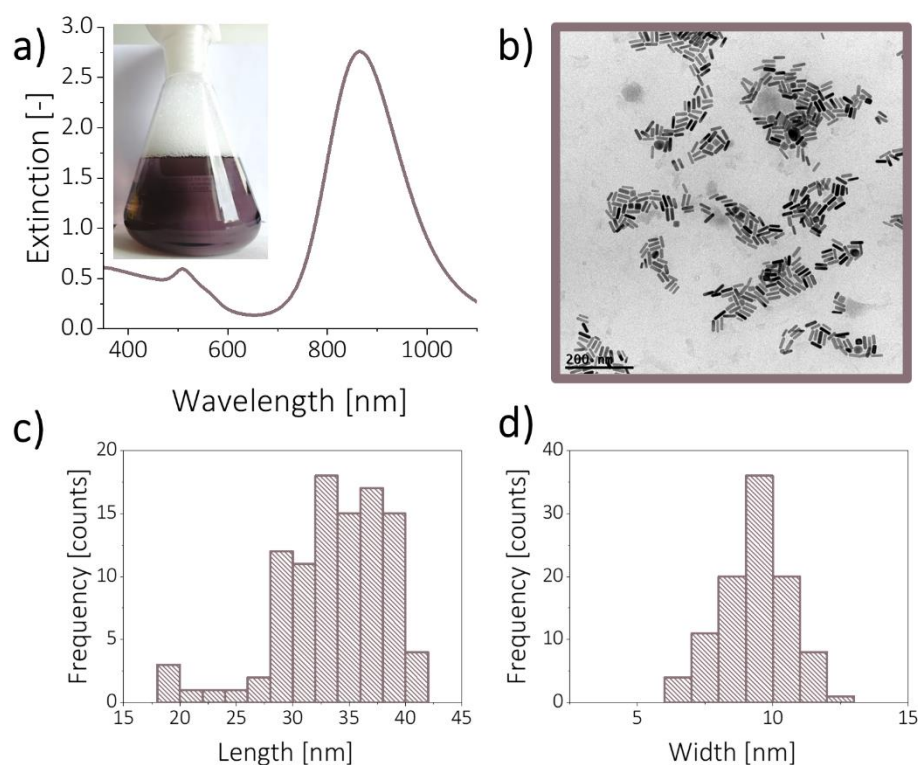


Figure 49. a) UV-Vis-NIR extinction spectra of the as-synthesized AuNRs. The position of the *l*-LSPR band is 864 nm. The inset presents visual appearance of the sample. Appropriate b) TEM image and histograms presenting c) length and d) width distributions of the nanostructures. Average length: 33.6 ± 4.8 nm, average width: 9.3 ± 1.3 nm, number of nanoparticles measured $N = 100$, aspect ratio $AR = 3.61$. Panels b)-d) adapted from own source publication³⁵³.

AuPdNRs synthesis

Palladium overgrowth over the as-synthesised AuNRs was performed according to the silver-assisted protocol by Zheng *et al.*³⁷⁷ This protocol enables preferential Pd reduction over tips of the initial AuNRs at low Pd mol%.

First, AA (1.136 mL, 0.1 M) was added to the dispersion of AuNRs (10 mL, 0.0005 M). AuNRs were not washed after their synthesis, hence Ag^+ ions added during silver-assisted AuNRs growth remained in the solution and could participate in the Pd overgrowth. Subsequently, given amount of K_2PdCl_4 (0.01M) was added to obtain the desired Pd mol% in relation to Au molar content. The chosen Pd mol% were 10, 25, and 41. In the end, HCl (80 μL of 0.1 M) was added and the solution was left for 12 hours at 40°C in order to assure complete reduction of the second metal. The as-synthesised AuPdNRs were used to prepare plasmonic photocatalyst.

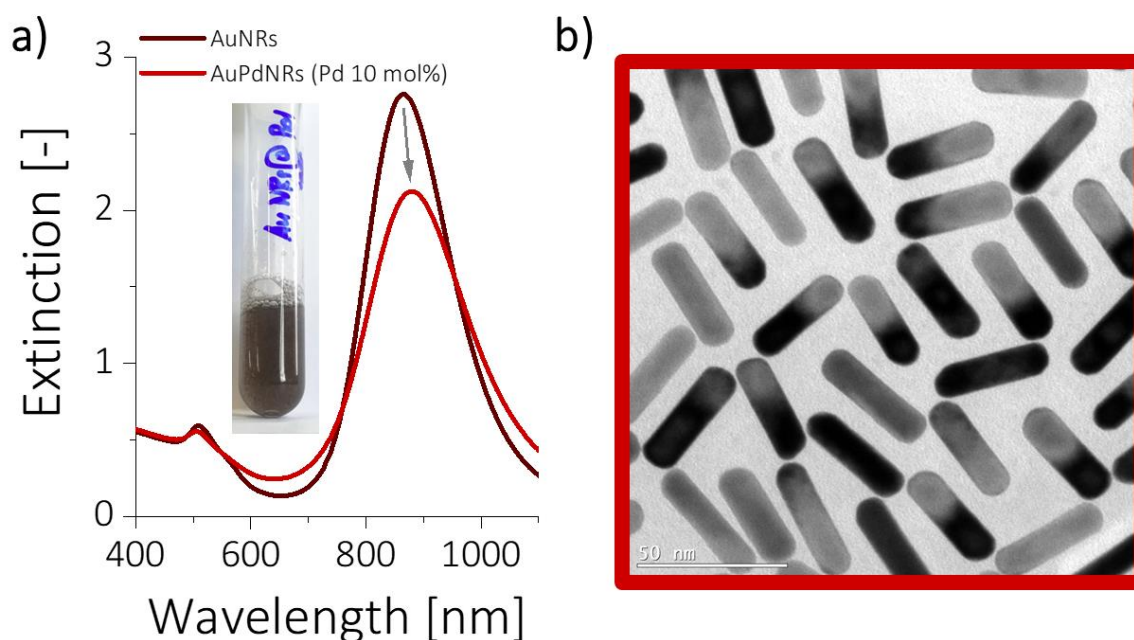


Figure 50. a) UV-Vis-NIR extinction spectra of AuNRs coated with Pd in the overgrowth process performed at 10 mol% of Pd with respect to the molar content of Au. Inset presents visual appearance of the sample. b) TEM image of AuPdNRs (Pd 10 mol%). Average length: 37.1 ± 2.3 nm, average width: 10.0 ± 0.8 nm, number of nanoparticles measured $N = 100$, aspect ratio $AR = 3.71$.

3.2.3. Nanoparticles-CNFs composites preparation

AuNRs-CNFs composites

First, bare AuNRs (10 mL, 0.0005 M) were washed twice with water by centrifugation (8950g, 15 min). After washing, nanoparticles were redispersed in CTAB solutions of varying concentrations, namely 1 mM, 5 mM, 10 mM, or 15 mM. The volume of CTAB was adjusted

to control the wt% of Au with respect to CNFs added in the next step (from 7.5 to 35 wt% of Au with respect to dry mass of CNFs depending on the intended use of the composite).

In order to promote interactions between AuNRs and CNFs, each nanoparticles dispersion was titrated with the aqueous CNFs dispersions of varying concentration (0.5, 1.0, 2.5, 4.0, and 5.0 wt%) under vigorous stirring. Composites preparation was performed at room temperature and the AuNRs:CNFs volume ratio of 2:1 was kept the whole time. The as-prepared composites were used to investigate interactions between AuNRs and CNFs and to optimize the preparation of the final photocatalyst.

AuPdNRs-CNFs photocatalyst preparation

Aqueous AuPdNRs dispersion (2.5 mL, [Au] = 0.00225 M, [CTAB] = 1 mM) was titrated with an aqueous CNFs dispersion (1.25 mL, 0.5 wt%) under vigorous stirring. After phase separation of AuPdNRs-decorated CNFs, the mixture was centrifuged three consecutive times to remove the excess of surfactant. The resulting composite was dispersed in water (2.5 mL) and contained ~18 wt% of Au.

3.2.4. One-pot plasmon-assisted photoregeneration of cofactor molecules

The reaction mixture (total volume of 2.5 mL) consisted of HCOONa (1 M) and NAD⁺ (1 mM) prepared in phosphate buffer (0.1 M, pH 5.96 or 7.91). To the reaction mixture AuPdNRs-CNFs photocatalyst was added in such amount to obtain desired absorption level of its 1-LSPR band (0.5, 1.0, and 2.0). The whole mixture was irradiated for 2 h using MI-150TM light source (Dolan-Jenner Industries). The applied light power density was 200 mW/cm² and it was determined that the irradiation led to the increase of the mixture's temperature up to 40°C.

To detect regenerated NADH, an aliquot was collected every 30 min and put directly to the 1 mm quartz cuvette in order to measure the UV-Vis absorption spectra. NADH concentration was determined based on the peak intensity at 340 nm (**Figure 51**). After 2 h sample was centrifuged (1000g, 15 min). Photocatalyst, remaining as a pellet, was separated for washing and potential subsequent use in further reactions and the supernatant was collected to determine the absolute amount of the regenerated NADH.

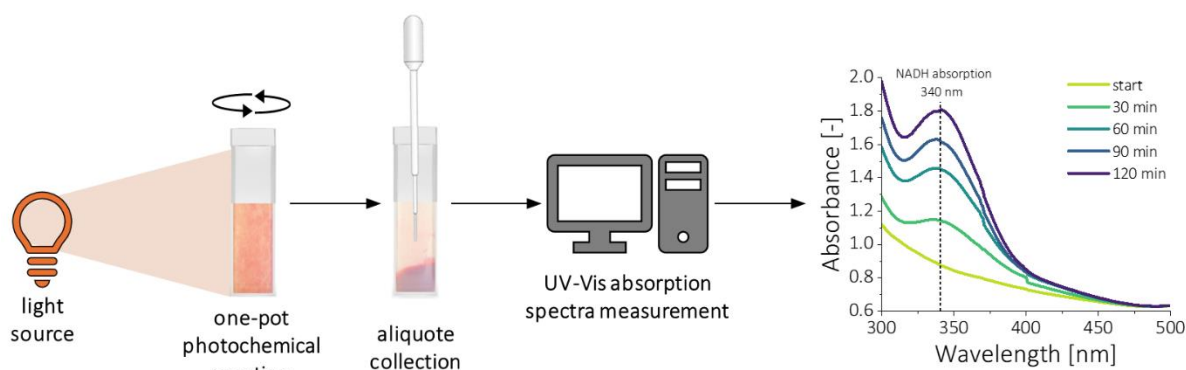


Figure 51. Schematic depiction of the cofactor regeneration process workflow. At certain times irradiation of reaction mixture was stopped and aliquot was collected to measure the UV-Vis absorption spectra and determine NADH concentration based on the intensity of the absorption peak at 340 nm.

Photoelectrochemical measurements

The photocurrent measurements were conducted on DRP-110 (DropSens) at -0.4 V (vs. Ag) by potentiostat (Autolab Electrochemical Workstation, PGSTAT302N). Ag and carbon were used as pseudo-reference and counter electrode, respectively. The working electrodes were functionalized with bare CNFs, AuNRs-CNFs, and AuPdNRs by drop-casting (15 μ l of each dispersion was used) followed by overnight evaporation at room temperature. For all photoelectrochemical experiments, sodium formate (20 μ l, 1 M) was deposited on the electrode surface and followed by current stabilization for 60 s. Measurements were performed at room temperature. A halogen illuminator (Fiber-Lite MI-150, Dolan-Jenner Industries) with a spectral range of 400-1200 nm and a power density of 87 mW/cm² on the sample was used for the irradiation.

3.3. Results and discussion

3.3.1. Preparation and properties of AuNRs-CNFs and AuPdNRs-CNFs composites

As presented in the subsection 2.3.2. *Hybrid materials based on cellulose and gold nanoparticles* of the Introduction, interactions between nanocellulose and components such as AuNPs are driven by both constituents' surface chemistry. Hence, CNFs and AuNRs exhibiting opposite surface charges were selected to induce electrostatic interactions as a basis for the formation of composite material. CTAB molecules, due their role of surface stabilizers, are intrinsically present after the synthesis of AuNRs according to the chosen protocol and grant

positive charge of the nanostructures. At concentrations higher than CTAB critical micelle concentration (1 mM), AuNRs dispersion also contains positively charged CTAB micelles. On the other hand, the chosen TEMPO-oxidized CNFs are rich in $-COO^-$ groups and hence exhibit negative surface charge. Thus, upon mixing of both components, conditions for mutual electrostatic interactions between CNFs and AuNRs were created (**Figure 52**).

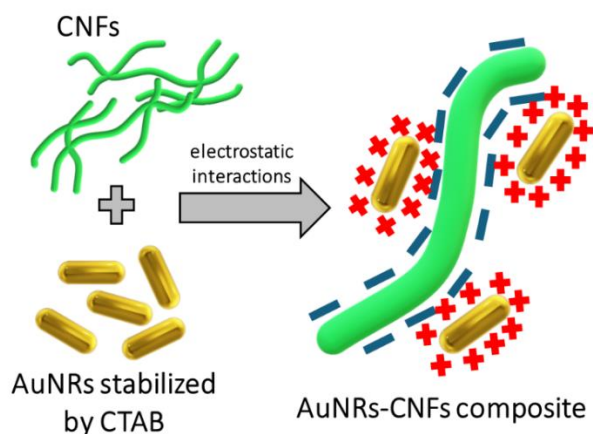


Figure 52. Electrostatic interactions between AuNRs and CNFs can lead to the formation of AuNRs-CNFs composite and stabilization of Au nanostructures in the solution.

For the nanocellulose-surfactant systems concentrations of both components are crucial, since they dictate phase forms of the system as a whole. By varying CTAB and nanocellulose concentrations e.g. suspensions or gels can be formed, as presented by Tardy *et al.*³⁸² This is why AuNRs were dispersed in CTAB solutions of different concentrations (1-15 mM) before mixing with CNFs, although the overall AuNRs content was kept constant in all samples. Concentration of the aqueous nanocellulose dispersions titrating plasmonic nanocrystals was also varied in the 0.5-5.0 wt% range. As a result, the quasi-phase diagram of AuNRs-CNFs system was obtained (**Figure 53**).

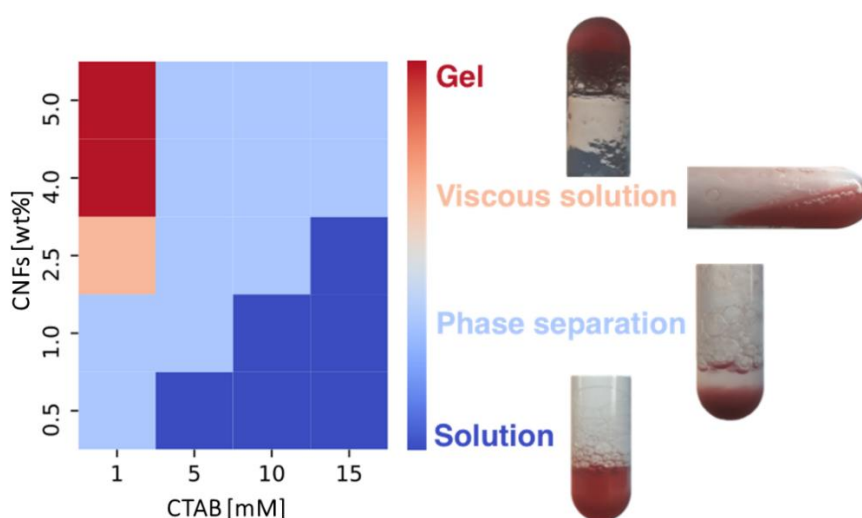


Figure 53. Quasi-phase diagram of the AuNRs-CNFs system (2:1 volume ratio, constant AuNRs loading), presenting dependency between identified phases and concentrations of CTAB

and CNFs. Solution, two-phase system, viscous solution, and gel phases were identified. Figure reprinted from own source publication ³⁵³.

Stable gel and viscous solution were formed at high CNFs and low (1 mM) CTAB concentrations (Figure 53, red and pink regions), which indicates cross-linking of CNFs fibres solely by AuNRs. On the other hand, for the decreasing CNFs concentration and the increasing CTAB concentration (Figure 53, dark blue region) stable colloidal solution was formed. It can be assumed, that free surfactant molecules and micelles replace AuNRs in the interactions with CNFs. Thus, surface of CNFs (or rather CTAB-CNFs) becomes positively charged and electrostatic repulsion with AuNRs instead of electrostatic attraction occurs, similarly to the mechanism of nanoparticles stabilization by CTAB micelles after the synthesis of nanocrystals. However, for the broad range of concentrations, the precipitation of AuNRs-decorated CNFs ensued (Figure 53, pale blue region). As presented in the accompanying image (Figure 53, on the right-hand side to the colour scale), phase separation resulted in the clear supernatant, which indicates complete anchoring of nanostructures on cellulose nanofibres. For the further preparation of plasmonic photocatalyst the ensuing phase separation was found to be very beneficial, because such material can be easily handled, washed, and separated from reaction mixture, for instance by centrifugation. Hence, this phase form of the system was selected for the preparation of photocatalyst in the further steps.

To characterize prepared composites quantitative spectroscopy analysis of the samples was performed. CNFs did not exhibit any absorption in the UV-Vis-NIR spectral range. The slight slope observed in the extinction spectra for the two-phase control sample prepared upon mixing of 0.5 wt% CNFs with 1 mM CTAB (**Figure 54a**) comes from the scattering of the fibres building up below 600 nm. Hence, the overall optical properties of hybrid AuNRs-CNFs (**Figure 54b**) stem from the presence of gold. Upon AuNRs immobilization on CNFs the global optical features of nanostructures were not changed (**Figure 54b**) – both t-LSPR and l-LSPR bands were clearly visible. Slight blueshift of l-LSPR band (9 nm) originates most probably from two effects, namely change in the local environment (introduction of nanocellulose) and plasmon coupling between immobilized nanoparticles. Conclusion on the latter might be justified by the simultaneously observed slight broadening of the l-LSPR. Moreover, below 600 nm the contribution of CNFs scattering was clearly visible. Hybrid material exhibited structural integrity and the deposition of AuNRs on the CNFs was also confirmed by TEM (**Figure 54c**). To further determine the optimal conditions (CNFs and CTAB concentrations) for the formation of two-phase systems exhibiting the most pronounced and not distorted optical properties, for each phase separated system represented in Figure 53 UV-Vis-NIR spectrum of

the dispersion was measured in 1 mm cuvette (**Figure 54d**) and, subsequently, ratio between l-LSPR and t-LSPR was calculated (**Figure 54e**).

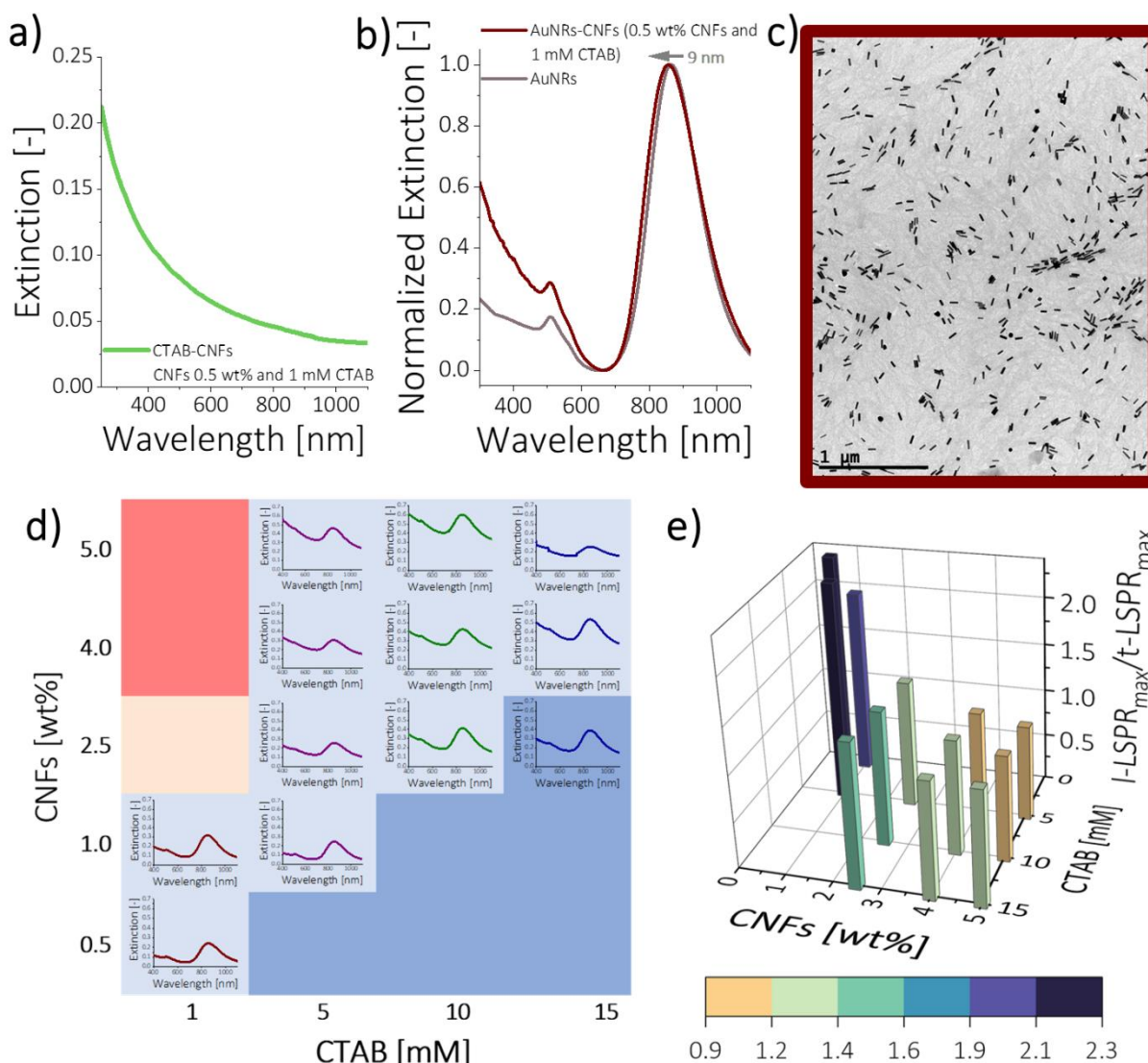


Figure 54. UV-Vis-NIR extinction spectra of **a)** CTAB-CNFs control precipitate without AuNRs and **b)** AuNRs-CNFs composite prepared at low CNFs (0.5 wt%) and CTAB (1mM) concentrations compared with spectrum of pristine AuNRs. **c)** TEM image of AuNRs-CNFs composite presented in **b)**. **d)** Systematic screening of the optical properties of two-phase systems. **e)** Quantitative optical analysis of two-phase systems reflecting contribution of plasmon band to the overall optical characteristics of the composite. Particularly pronounced plasmon contribution (reflected as high ratio between maxima of l-LSPR and t-LSPR bands) can be observed at low CTAB and CNFs concentrations. Panels **d)** and **e)** are based on own source publication ³⁵³.

Upon changing CTAB and CNFs concentrations the optical properties of AuNRs immobilized on CNFs were not drastically altered. Both LSPR bands were visible, although for higher CNFs

content the t-LSPR band became less pronounced, mostly due to the increased scattering of the scaffold overlapping with the plasmon band. Moreover, as presented in **Figure 54d**, upon increasing CNFs concentration an offset to the overall spectral profile of the composites appeared, shifting profiles along the Y axis. With the increasing CNFs and CTAB concentrations ratio between maxima of l-LSPR and t-LSPR bands decreased from about 2.3 to about 0.9. These observations clearly indicate the increasing scattering contribution of the CNFs scaffold to the optical properties of the composites in place of the plasmonic contribution. Hence, to maintain pronounced plasmonic properties of the AuNRs-CNFs, optimal nanocellulose and surfactant concentrations were determined to be 0.5 wt% and 1 mM, respectively.

To further enhance plasmonic properties, the number of AuNRs immobilized on cellulose scaffold was increased by using concentrated AuNRs dispersions and maintaining other optimized conditions, namely constant AuNRs:CNFs volume ratio (2:1), CTAB (1mM), and cellulose (0.5 wt%) concentrations (**Figure 55a**). Up to 18 wt% of Au with respect to the dry mass of cellulose, intensity of the l-LSPR band was beneficially increasing. For Au content over 18 wt% the spectra became distorted, namely l-LSPR band became damped and broadened, presumably due to the plasmon coupling, a result of decreased distance between nanostructures immobilized on CNFs.³⁸³ To exclude effect of plasmon coupling during the further planned photocatalytic process, the 18 wt% Au content was set as the upper limit for material preparation.

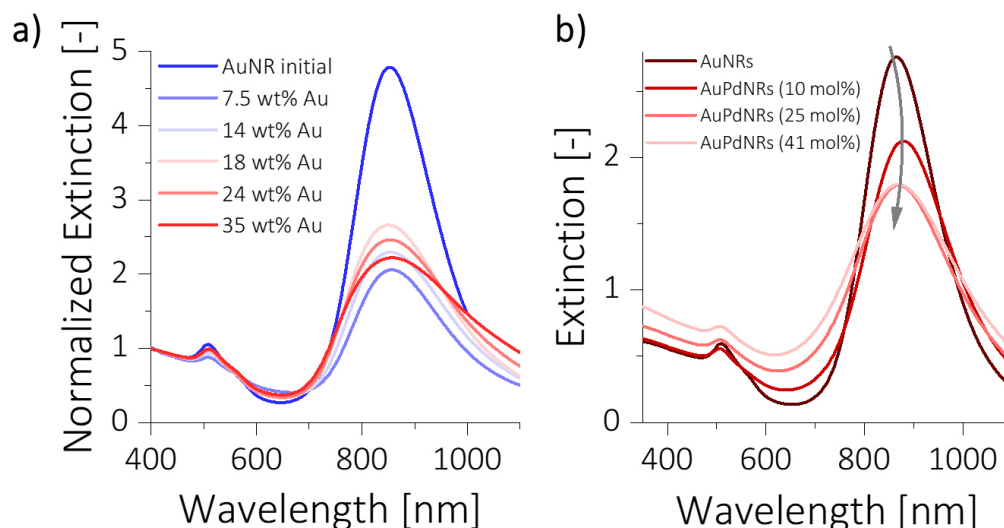


Figure 55. **a)** UV-Vis-NIR spectra of the AuNRs-CNFs two-phase systems as a function of Au mass content. The broadening of the l-LSPR band above 18 wt% of Au due to the plasmon coupling can be observed. **b)** UV-Vis-NIR spectra of bimetallic AuPdNRs prepared upon coating of pristine AuNRs with different Pd content (molar content with respect to Au indicated in brackets). Panels reprinted from own source publication³⁵³ and rescaled for presentation.

The determined optimal conditions were subsequently extended to the preparation of plasmonic photocatalyst containing bimetallic AuPd nanorods in place of bare Au nanostructures. Palladium was introduced as a potential co-catalyst of the planned photochemical process. Presence of second metal in the final formulation was confirmed and both its role and influence were investigated as described below.

For low Pd content (10 mol%) the thickness of the resulting coating was relatively low. Hence, the change in the overall geometrical structure of the nanorods was not distinguishable based on the TEM image (**Figure 50**). There was only 7% change in width and 10.5% change in length of AuPdNRs comparing to pristine AuNRs, accompanied by AR increase from 3.61 to 3.71. Even if random error resulting from manual size measurement (performed in the ImageJ computer programme) is taken into account, these changes clearly indicate towards more preferential Pd deposition on the tips of nanorods. Nevertheless, Pd deposition was well reflected and evident in the spectral profile of the sample (**Figure 55b**). Due to the slight elongation of nanoparticles and general increase of their AR, slight redshift of the L-SPR band occurred. Upon further increase in Pd content, plasmon band was progressively broadened, damped, and blueshifted. These effects are related to the interband transitions of palladium and relative changes in the shape and AR of nanostructures upon Pd deposition.³⁸⁴ UV-Vis-NIR extinction spectra presented in **Figure 55b** confirmed formation of AuPdNRs, however other experimental techniques were used to support this conclusion and further characterise the sample. The most important confirmation of Pd presence on nanoparticles surface is presented in **Figure 56**, where scanning transmission electron microscopy (STEM) and energy dispersive X-ray spectroscopy (EDS) elemental maps of single AuPd nanorod (coated with 41 mol% of Pd) are compiled.

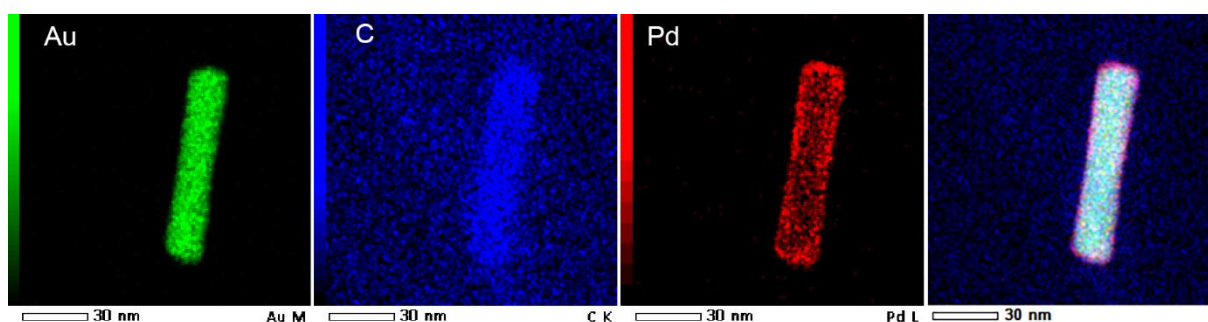


Figure 56. Scanning transmission electron microscopy and energy dispersive X-ray spectroscopy results. Elemental map of gold, carbon, and palladium from individual AuPd nanorod (coated with 41 mol% of Pd) compiled in the final panel to present whole bimetallic nanostructure. Figure reprinted from own source publication³⁵³.

Presence of crucial components, namely Au, Pd, and cellulose in both types of composites (AuNRs-CNFs and AuPdNRs-CNFs), was also confirmed by X-ray photoelectron spectroscopy

(XPS), as presented in **Figure 57**. Gold is present for both types of composites, while presence of palladium was confirmed only for composite containing AuPd nanorods (**Figure 57a**). Presence of chemical groups, such as $-COOH$, $C=O$, and $C-O$ (**Figure 57b, left column**) confirms abundance of anchor points enabling immobilization of metallic nanoparticles on the surface of CNFs. Although most of CTAB is removed upon composites washing, since no Br 3d peaks at 68.7 eV were observed (**Figure 57b, right column**), it can be assumed that some residual surfactant, mediating interactions between NRs and CNFs by involvement in the electrostatic binding of components, remains within composites. **Figure 57b, middle column** presents some residual signals that might be assigned to the polar head of CTAB molecule. Nevertheless, it can be stated that most of the native surfactant is effectively removed from the surface of nanoparticles, thus making the surface accessible for photochemical processes.

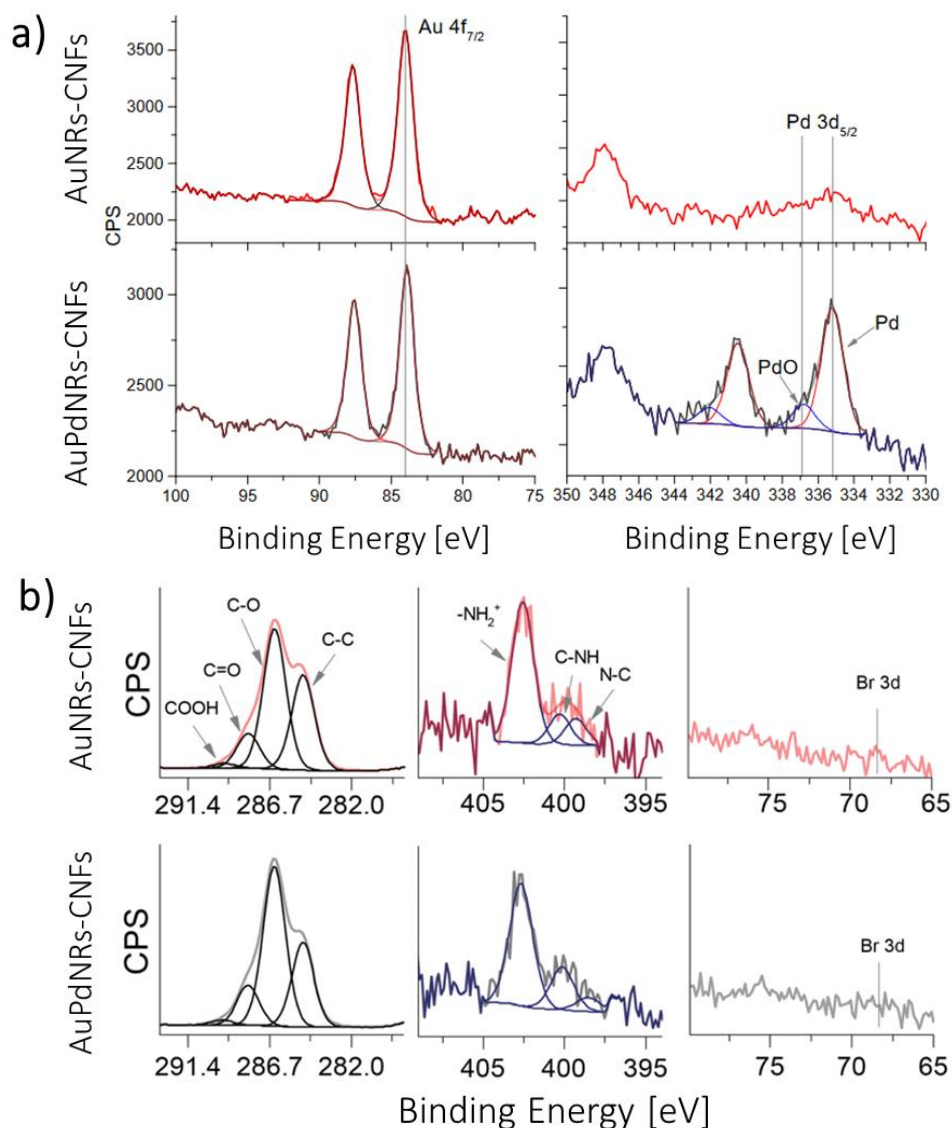


Figure 57. XPS analysis of AuNRs-CNFs and AuPdNRs-CNFs (Pd 41 mol%). **a)** Presence of proper metallic components is confirmed in the respective composites. **b)** Photoemission

spectra and fits of CIs (left column) and NIs (middle column). No Br was detected (right column). Figure reprinted from own source publication ³⁵³.

Attachment of AuPd nanoparticles to the cellulose nanofibres was confirmed by low-resolution TEM and STEM analysis as presented in **Figure 58**. There were no free AuPdNRs found apart from the CNFs scaffold. As presented in **Figure 58a** nanorods follow the direction of the nanofibres (visible as light grey wavy areas) on the TEM grid. These observations, combined with the visual appearance of the two-phase systems, where clear supernatant remains above intensely coloured AuPdNRs-CNFs precipitate (**Figure 58c**), indicate efficient immobilization of nanostructures.

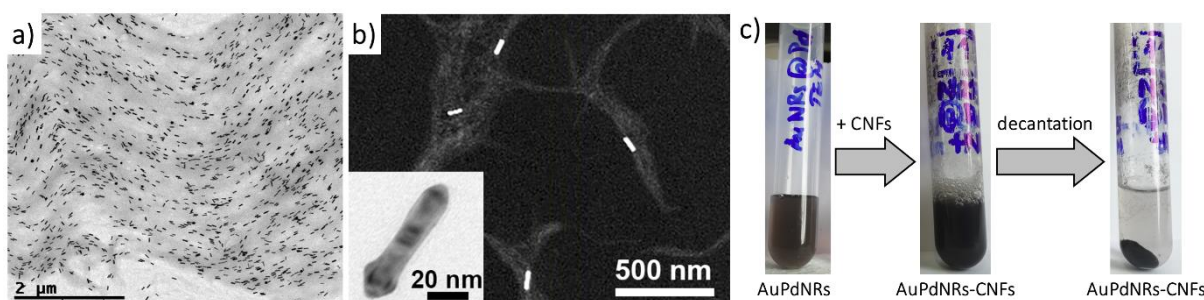


Figure 58. AuPdNRs-decorated CNFs. **a)** TEM image of the composite. **b)** STEM image (dark mode) depicting how nanostructures are embedded within cellulose nanofibres. Inset presents TEM image of the individual AuPd nanostructure (Pd 41 mol %). **c)** Images depicting visual macroscopic appearance of the composite, starting from dispersion of free AuPdNRs (left), through AuPdNRs-CNFs right after immobilization (middle), and after decantation of the composite with transparent supernatant above the precipitate (right). Panels a) and b) reprinted from own source publication ³⁵³.

Final aspect included in the investigation of the composite properties was its stability in the broad pH range. As indicated in the introductory section of this chapter the photocatalytic reaction of NADH regeneration, which was selected to evaluate the efficiency of the catalyst, is pH-sensitive. Hence, the stability of the composite should also be investigated under different conditions. As presented in **Figure 59**, AuPdNRs-CNFs material exhibited great stability in a broad pH range starting from pH 2.2 up to 9.7. Positions of the LSPR bands are maintained and the FWHM (full width at half maximum) values are oscillating around 180 nm.

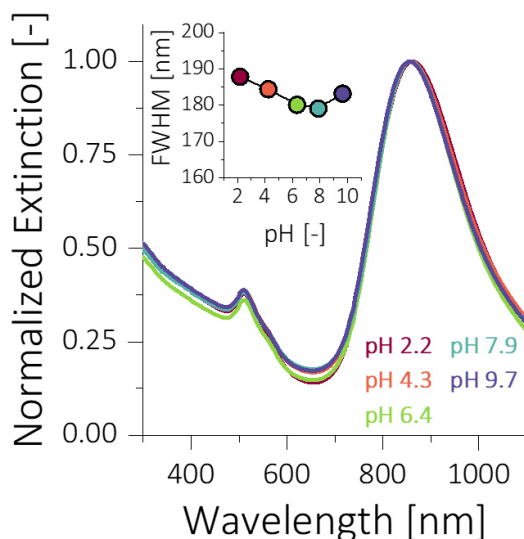


Figure 59. UV-Vis-NIR spectra of the composites dispersed at different pH. The inset presents FWHM values of the *l*-LSPR band on the corresponding spectra as a function of pH. Figure adapted from own source publication ³⁵³.

To conclude this subchapter, the stated **objective 1** and **hypothesis 1** should be verified. Part of **objective 1** was successfully achieved, since cellulose was effectively used as a scaffold for AuNRs and the resulting AuNRs-CNFs composite exhibited stable properties, also under different pH conditions. The following subsection demonstrates whether optical properties of nanoparticles in such hybrid material are stabilized also under illumination and at elevated temperatures. The **hypothesis 1** was corroborated, since optical properties of AuNRs (and AuPdNRs as well) were stable and not altered upon immobilization on cellulose nanofibres.

3.3.2. Plasmon-assisted regeneration of cofactor molecules using AuPdNRs-CNFs photocatalyst

To verify photocatalytic efficiency of AuPdNRs-CNFs composite process of sodium formate dehydrogenation coupled with simultaneous NADH regeneration is proposed. The hypothesis is introduced that NAD^+ can be used to capture molecular hydrogen (product of formate dehydrogenation) and the total efficiency of the process is represented by the amount of the NADH formed.

Hence, material was exposed to white light (400-1200 nm, 200 mW/cm²) in the presence of NAD^+ (1 mM) and HCOONa (1 M) at pH 7.91 (setup and the photocatalyst macroscopic appearance are presented in **Figure 60**). Temperature of the reaction and mixing of reagents were ensured by heating plate. It was established by using the Pt1000 sensor that for 25°C set on the heating plate temperature of the sample was in fact 40°C due to intense irradiation.



Figure 60. *AuPdNRs-CNFs photocatalyst in a 1 mm cuvette and representative photograph of the photocatalytic setup.*

Gradual conversion of the oxidized cofactor into its reduced form, NADH, was observed based on the absorbance changes at 340 nm (**Figure 61a-c**). Role of Pd was found to be critical, because no NADH regeneration was observed for the bare AuNRs-CNFs composite material (**Figure 61d**). Both Pd content and photocatalyst content were related to the rate and total efficiency of NADH formation. Upon increasing coverage of the Au plasmonic cores' surface with Pd, NADH conversion rate was also increasing (**Figure 61a**). For AuPdNRs prepared using 10 mol% of Pd almost no regeneration of NADH occurred, while for the highest Pd loading (41 mol%) 15% of NADH was regenerated in 2 h. Similar tendency was observed for the increasing amount of the composite (for constant Pd loading of 41 mol%), represented by the absorbance value at the maximum of 1-LSPR band of AuPdNRs (**Figure 61b**). At low photocatalyst content, namely absorbance of 0.5, no NADH was formed, while for the increased photocatalyst content (absorbance 2.0) almost 40% of NAD^+ was reduced to NADH in 2 h. As discussed in the introductory part of this chapter, the stability of the regenerated NADH is pH dependent, and reduced cofactor is more stable above pH 7.0.³⁸⁵ However, on the other hand, HCOONa dehydrogenation to H_2 on electrodes made of Pd is clearly more efficient at pH 4.0.³⁸⁶ Hence, photocatalytic process was also investigated for Pd 41 mol% and $\text{Abs}_{\text{1-LSPR}} = 1.0$ at pH 5.96. As presented in **Figure 61c** almost 5 times more NADH was formed at higher pH after 2 h of irradiation. Hence, it can be stated that stability of the regenerated NADH is the limiting factor in the investigated process. At lower pH the unfavoured back oxidation of NADH occurs and significantly weakens total efficiency of the reaction.

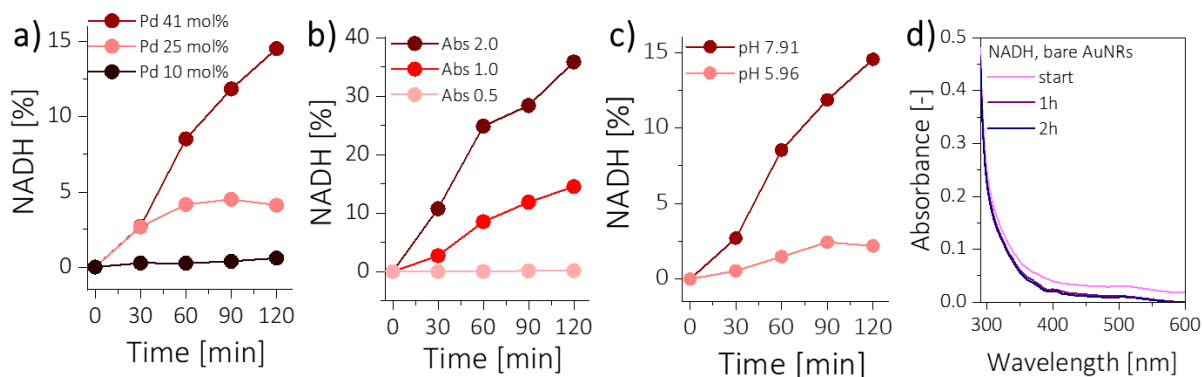


Figure 61. NADH photoregeneration under visible light irradiation. **a)** Effect of Pd content (for material $Abs_{SI-LSPR} = 1.0$, pH 7.91) and **b)** composite content (for Pd 41 mol%, pH 7.91) on the efficiency of NADH formation. **c)** Influence of pH on the NADH regeneration efficiency (Pd 41 mol%, material $Abs_{SI-LSPR} = 1.0$). **d)** No NADH was regenerated for composite without Pd (material $Abs_{SI-LSPR} = 1.0$, pH 7.91). Panels a)-d) reprinted from own source publication³⁵³.

To investigate the proposed photocatalytic process thoroughly, three questions were asked: **(1)** Is CNFs scaffold truly inert or does it participate in the reaction? **(2)** What form of hydrogen is responsible for NAD^+ reduction – molecular hydrogen or rather some surface-related species? **(3)** How the photocatalytic process compares to thermal $HCOONa$ dehydrogenation?

Regarding question **(1)**, one-pot photochemical regeneration of NADH was performed at the most optimal conditions defined above, however without sodium formate in the reaction mixture. As presented in **Figure 62a** no NADH was formed after standard reaction time (2 h). This excludes CNFs dehydrogenation under reaction conditions. Moreover, under visible light irradiation, in contrary to AuPdNRs-CNFs photocatalyst, the bare CNFs scaffold does not exhibit any photocurrent density at -0.4 V vs. Ag electrode (**Figure 62b**). This excludes electron-donating character of CNFs. To sum up, it can be stated that CNFs constitutes an entirely inert scaffold that does not participate in the photocatalytic process.

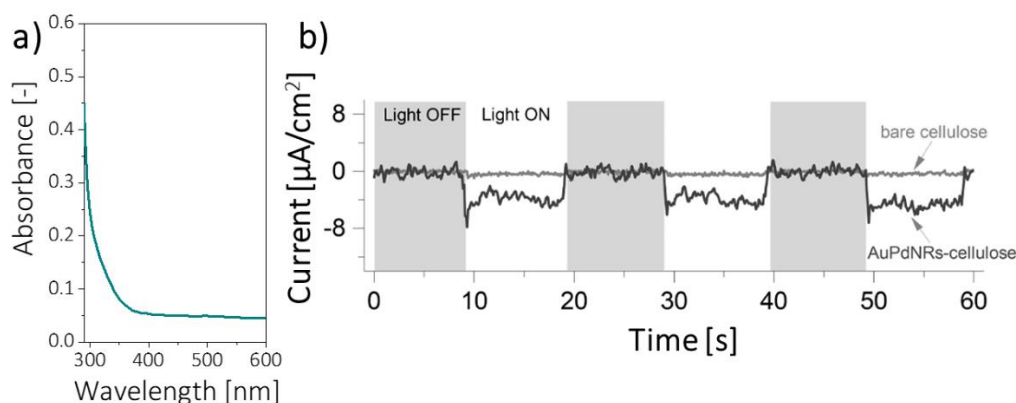


Figure 62. **a)** No NADH was regenerated under optimal reaction conditions in the absence of sodium formate. **b)** Bare CNFs and AuPdNRs-CNFs photocurrent response at -0.4 V vs. Ag electrode (1 M HCOONa, periodic ON/OFF visible light irradiation, $\lambda > 400$ nm). Panels reprinted from own source publication³⁵³ and adjusted for presentation.

Question (2) comes from two aspects. Firstly, NAD^+ reduction may occur in the presence of molecular hydrogen.³⁸⁷ Secondly, dehydrogenation of HCOONa to molecular hydrogen on Pd catalyst may result in formation of palladium hydride.³⁷⁸ Hence, there is a need to determine which species are responsible for the NAD^+ reduction by investigating whether the performed photocatalytic process is surface-dependent. In order to examine this aspect three different experimental scenarios for one-pot cofactor regeneration at optimal conditions, namely 1 M HCOONa, 1 mM NAD^+ , pH 7.91, Pd 41 mol%, and $\text{Abd}_{\text{I-LSPR}} = 1.5$, were performed.

In the first experiment, whole reaction mixture was irradiated for 1 hour and then evolution of NADH regeneration was investigated in the dark. As presented in **Figure 63a** gradual increase of the signal at 340 nm was observed, which indicates that irradiation induces formation of reactive species able to reduce NAD^+ even in the dark. Second experimental scenario relied on the pre-irradiation of the reaction mixture without NAD^+ . After 1 hour of pre-irradiation the oxidized form of the cofactor was added and the evolution of the band at 340 nm in the dark ensued (**Figure 63b**), further indicating towards accumulation of reductive species in the system. Third experimental scenario enabled to distinguish whether the reduction ensued due to molecular hydrogen or rather on the surface of the photocatalyst. After 1 hour irradiation of the complete reaction mixture, AuPdNRs-CNFs photocatalyst was removed by centrifugation and the light was switched off. In this case no 340 nm band build up was observed (**Figure 63b**) and hence, contribution of molecular hydrogen was excluded. These three experiments suggest, that simultaneous dehydrogenation of HCOONa and reduction of NAD^+ are related to the formation of surface-related reductive species, such as palladium hydride or reduced functional groups of CNFs.

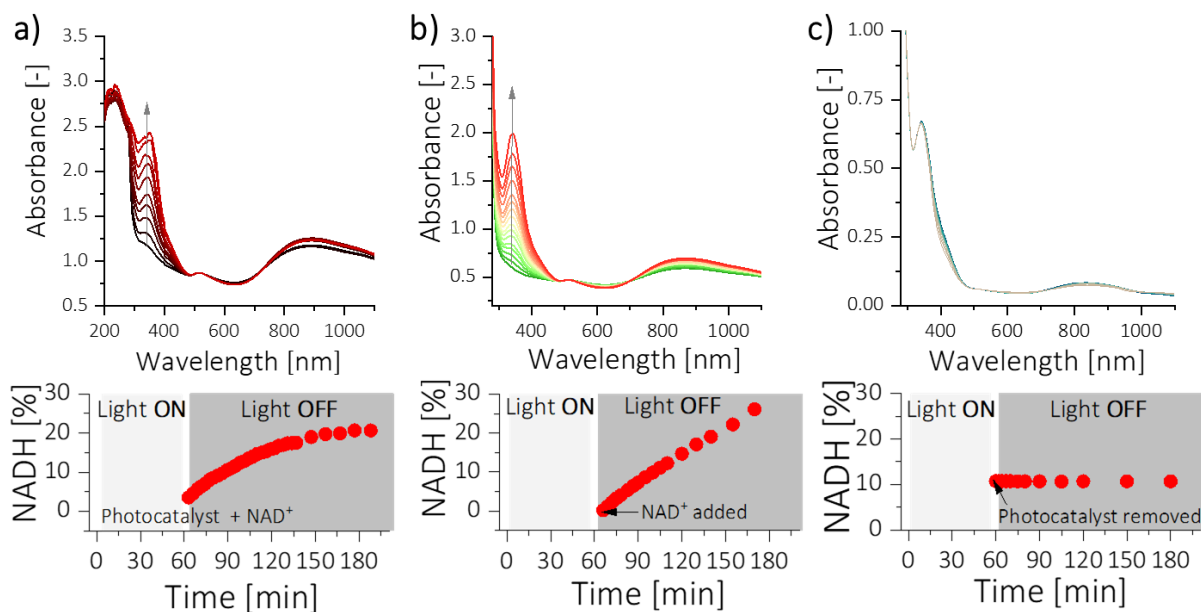


Figure 63. NADH regeneration **a)** after 1 h irradiation and switching light off, **b)** after 1 h pre-irradiation followed by NAD⁺ addition, and **c)** after 1 h irradiation followed by photocatalyst removal. Top panels present evolution of the spectra (340 nm band) and bottom panels present evolution of the %NADH regenerated. Panels adapted from own source publication³⁵³.

Question (3) is relevant due to the fact, that catalytic dehydrogenation of HCOONa occurs at elevated temperatures. Thus, the investigated process was repeated several times under both dark and light conditions, in the presence of AuPdNRs-CNFs photocatalyst, and at different temperatures. For light conditions, due to intense irradiation, the lowest available temperature was 40°C and higher temperatures were achieved by proper settings adjustment of the heating plate to account for thermal contribution of the irradiating beam. For both dark and light conditions the efficiency of the NADH formation was increasing with the increasing temperature. In the dark, at 30°C the efficiency was 0%, however at 60°C it was almost 12% (**Figure 64**). Upon irradiation the efficiencies were even higher (almost 7% for 40°C and 16% for 60°C). However, the overall ratio of NADH regenerated under irradiation to NADH regenerated in the dark decreased from 3.7 to 1.2 as the temperature increased from 40°C to 60°C. These results suggest both inherent contribution of the plasmonic effect of AuPdNRs-CNFs photocatalyst to the investigated process and decrease of this contribution with the increasing temperature. These conclusions are in a good agreement with results presented by Majima *et al.* who related generation of hydrogen from HCOOH on Pd-coated AuNRs to the transfer of carriers between Au core and Pd shell.³⁷⁷

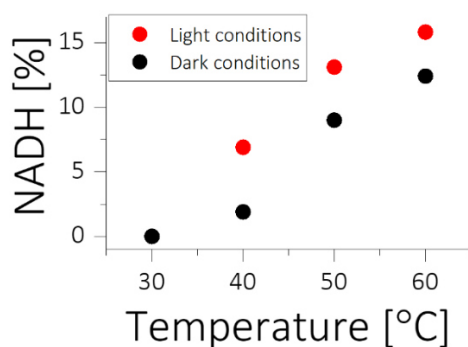


Figure 64. Influence of the temperature on NADH formation under dark and light conditions. Figure reprinted from own source publication ³⁵³.

One of the aspects emphasized in the dissertation as a motivation for using CNFs in the photocatalyst formulation was stabilization of optical properties of plasmonic nanoparticles. This is why UV-Vis-NIR absorption spectra of the AuPdNRs-CNFs composite were evaluated after its separation from the one-pot process. However, this point was broadened to simultaneously assess motivation for using two-phase separated system, which was facile material handling e.g. by centrifugation. To evaluate whether composite can be easily separated and repeatedly used without significant loss of the catalytic efficiency, four consecutive process runs were performed and material was evaluated after each of them. As presented in **Figure 65a,b** the efficiency of the photocatalyst was gradually decreasing and after four repetitions of the process a 45% drop in the total efficiency was observed (in relation to the initial efficiency of NADH regenerated after the first cycle). The relative efficiency accounted for I-LSPR band intensity changes (**Figure 65c**) due to both slight material losses after each cycle and changes in material structure. Visual appearance of the material was changing in such a way that photocatalyst clumps formed after consecutive cycles were observed. Hence, it can be assumed that AuPdNRs are gradually embedding within CNFs scaffold upon the exposure to intense irradiation, vigorous mixing, and elevated temperatures. The underlying reasons for that are most probably the chemically-rich surface of the fibres and the overall dynamic structure of CNFs. Moreover, as derived from spectra presented in **Figure 65c**, the overall optical properties of AuPdNRs were not drastically changed after 4 intense irradiations at elevated temperature (40°C). A 25 nm blueshift of I-LSPR band and 37 nm FWHM increase (from 278 nm to 315 nm) were observed. This further confirms gradual embedment of nanorods within CNFs scaffold and passivation of their surface with the fibres, which both changes local environment (and hence I-LSPR band position) as well as distance between nanorods (and thus I-LSPR band broadening occurs). Nevertheless, AuPdNRs maintain their characteristic optical features after prolonged and repeated exposure to harsh conditions due to the presence of CNFs scaffold.

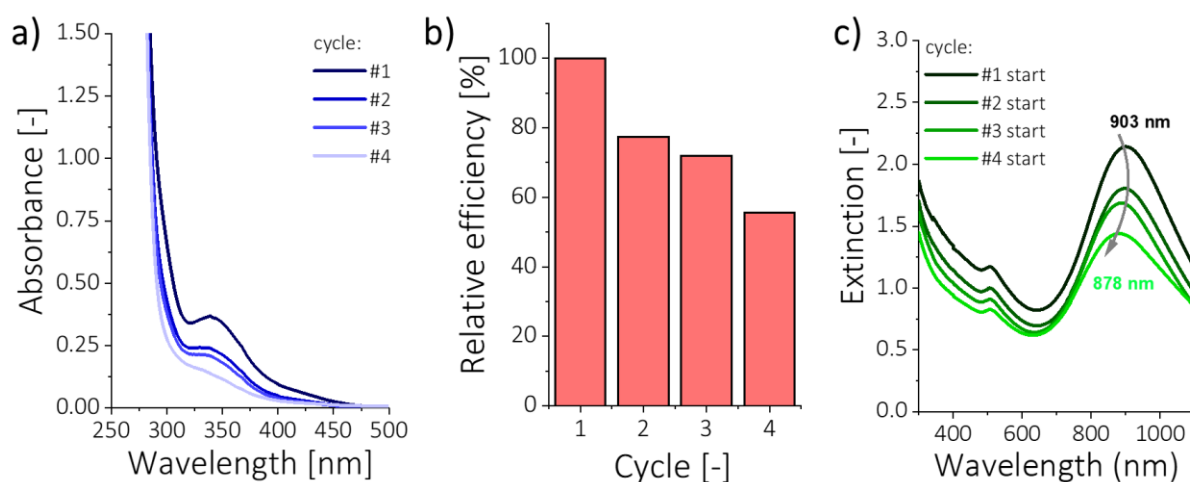


Figure 65. **a)** Intensity changes at 340 nm (NADH identification spectral range). **b)** Changes in the relative efficiency of the photocatalyst after its recycling and use in many process cycles. **c)** Changes in the UV-Vis-NIR extinction spectra of the recycled AuPdNRs-CNFs photocatalyst in between subsequent cycles of NADH regeneration. Panels reprinted from own source publication³⁵³.

Final results presented in this subchapter are focused on emphasising one more time the importance of CNFs as a scaffold for plasmonic photocatalyst. As it was presented in the sections above, presence of CNFs enables effective CTAB removal from the surface of nanocrystals, which is important for the efficiency of the photocatalytic process. Insulating CTAB shell can drastically hinder activity of the plasmonic nanocrystals. As presented in **Figure 66a** although optical properties of AuPdNRs were very similar to AuPdNRs-CNFs composite, there was no NADH regeneration observed when free CTAB-coated AuPd nanostructures were used (**Figure 66b**). Similarly, if AuPdNRs-CNFs photocatalyst was utilized but extra surfactant was added (20 mM CTAB), reaction was also hindered. Hence, important role of CNFs scaffold is entirely manifested, since its use for stabilization nanocrystals enables elimination of surfactant during material post-synthetic treatment while beneficial optical properties of plasmonic nanoparticles are maintained.

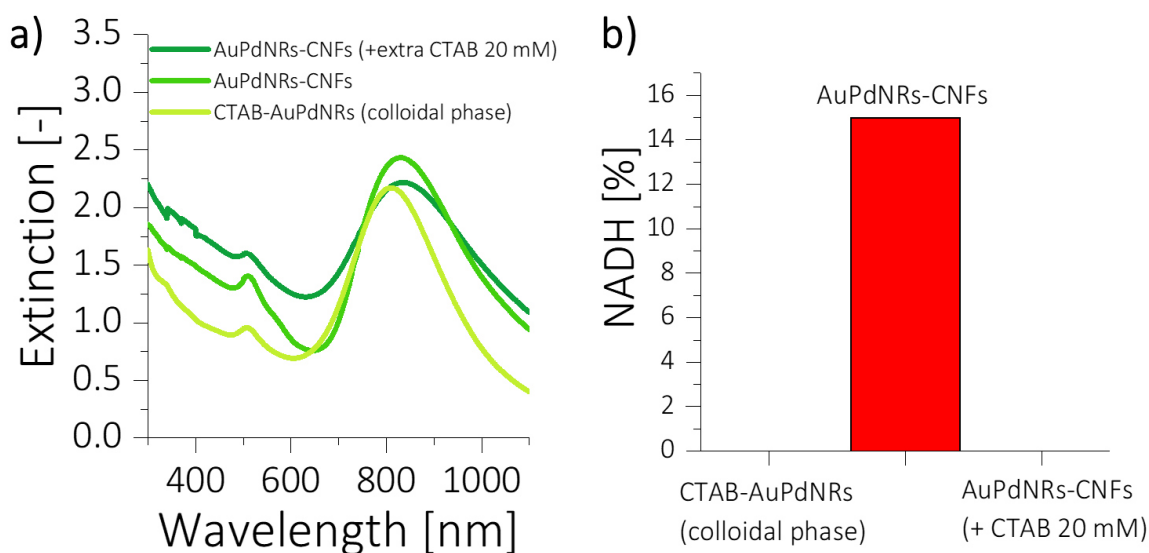


Figure 66. Influence of CTAB on NADH regeneration investigated using three different materials: free CTAB-stabilized AuPdNRs (colloidal phase), AuPdNRs-CNFs (proposed photocatalyst), and AuPdNRs-CNFs in the presence of extra CTAB (20 mM). **a)** UV-Vis-NIR extinction spectra of the materials. **b)** NADH formation efficiency showing inhibiting influence of surfactant. Panels reprinted from own source publication ³⁵³.

To conclude this subchapter, the stated **objective 1** and **hypothesis 2** should be verified. The remaining part of **objective 1** was successfully achieved, since stabilizing role of CNFs was manifested for harsh process conditions, including intense illumination and high temperatures. The **hypothesis 2** was also corroborated, since Pd-decorated AuNRs immobilized on CNFs scaffold were successfully used in a novel photocatalytic process coupling two model photochemical reactions, namely sodium formate dehydrogenation and cofactor (NADH) regeneration.

3.4. Conclusions

This chapter establishes general protocol for the preparation of plasmonic nanoparticles-cellulose nanofibres hybrid materials in which CNFs are primarily used as a scaffold enabling stabilization of AuNRs optical properties under various conditions (**objective 1**). Systematic screening of components concentration, including CTAB, surfactant inherently present after synthesis of AuNRs, enabled preparation of composites exhibiting different phases, such as stable colloidal solution, two-phase system, viscous solution, and gel. The phase separated system constituted a central formulation investigated within this chapter, although other phase forms can certainly find applications as advanced materials as well. Prepared composites exhibited great stability of plasmonic properties under intense illumination,

elevated temperatures, and at wide pH range. Hence, the role of CNFs as an inert scaffold preserving optical properties of plasmonic nanocrystals was confirmed (**hypothesis 1**). Proposed formulation relies on electrostatic interactions between components and does not require covalent bonding, which makes this protocol easily replicable using other surfactant-stabilized nanoparticles. In this chapter protocol was easily extended to bimetallic AuPd nanostructures. The demonstrated functionality of AuNRs-CNFs and AuPdNRs-CNFs composites can constitute an interesting starting point for further development of macroscopic, processable materials exhibiting hierarchical structures, e.g. by employing 3D printing. This chapter also presents a conceptually new plasmon-assisted photochemical process in which dehydrogenation of sodium formate is simultaneously coupled with regeneration of NADH cofactor molecules. Influence of several parameters including Pd content, material content, and pH was investigated. Results emphasised role of Pd as a co-catalyst of the process and limitations stemming from NADH back-oxidation at low pH. At optimal conditions this plasmon resonance-driven process reaches up to 40% conversion efficiency within 2 hours without use of additional reaction mediators (**hypothesis 2**). A set of control experiments enabled establishing that process is surface-dependent and possible due to use of CNFs scaffold, which facilitates efficient CTAB removal and excludes its hindering effect.

Chapter 4. *Plasmonic-Photochromic Hybrid Materials Exhibiting Water-Functionality*

This chapter describes the process of establishing the protocol for preparation of plasmonic-photochromic hybrid materials. Simultaneously, the following three challenges for such systems out of the five outlined in subsection 2.4.2. of Chapter 2 are addressed, namely: (1) inclusion of big, anisotropic AuNPs in the formulation, (2) preparation of Azo-AuNPs hybrids without covalent bonding of the components, and (3) preparation of water-functional hybrid systems. Relying on the experience stemming from Chapter 3, CNFs were chosen again as a scaffold for the stabilization of AuNPs. The first experimental attempts focus on CNFs-stabilized Au nanospheres and well-known thiolated Azo ligands. Subsequently, protocol modification towards using positively charged Azo molecule, able to interact with CNFs scaffold instead of the surface of AuNPs, is discussed. Finally, the protocol is modified to include bigger, anisotropic AuNRs and charged Azo molecules. The procedure is optimized in such a way as to yield materials with pronounced plasmonic and photochromic optical features at the same time. Hence, the results presented here challenge Objective 2 and verify hypotheses 3 and 4 of the dissertation.

Objective 2: To prepare multifunctional, hybrid plasmonic-photochromic material based on cellulose-stabilized AuNRs and model azobenzene-type photochrome and, simultaneously, to address current challenges in the field of plasmonic-photochromic hybrids, such as structures' water-functionality, use of non-thiolated Azo ligands, preparation of hybrids operating without aggregation.

Hypothesis 3: Cellulose can serve as a scaffold for AuNRs and a photochromic dye of choice.

Hypothesis 4: Both functional components (AuNPs and Azo) preserve the entirety of their optical properties and functionality.

Part of the results presented within this chapter is available as a preprint:
³⁸⁸ N. Tarnowicz-Staniak, M. Staniak, M. Dudek, M. Grzelczak, K. Matczyszyn, *Gold Nanorods Grant an ON-OFF Control over the Kinetics of the Z-E Isomerization of Azobenzene-Based Photoswitch via Thermoplasmonic Effect*, preprint ChemRxiv **2024**, <https://doi.org/10.26434/chemrxiv-2024-vnj32>.

4.1. Motivation

As presented in Chapter 2, currently, the most popular formulations of plasmonic-photochromic materials rely on small, spherical AuNPs and thiolated Azo ligands covalently bound to the surface of nanostructures.^{335,389} Such systems are mainly investigated in terms of their reversible aggregation (LISA phenomenon^{340,348}). However, the aggregation of nanoparticles leads to the decline of the plasmonic properties of such systems. On the other hand, some of the hybrids also exhibit limited photoswitching, as described in subsection 2.4.2. of the dissertation. Thus, it can be concluded that in case of many approaches, the critical features of the components are restricted or even lost in the final formulation. New material designs should address this aspect to become appealing for applications where stable photoswitching or stable plasmonic properties or both are necessary. In order to further develop the field, novel plasmonic-photochromic materials need to go beyond what has been presented so far.

The use of small, spherical nanoparticles is mainly rooted in their easier stabilization upon ligand exchange compared to bigger, anisotropic nanostructures. Moreover, anisotropic nanoparticles are usually stabilized by bilayers and micelles of surfactant molecules (e.g. CTAB or CTAC) that disintegrate in organic solvents, leading to the immediate aggregation of AuNPs. Hence, the surfactant exchange on the surface of nanostructures is not trivial.^{390,391} However, there are reports presenting Azo-decorated nanostructures such as AuNRs. One of the first literature examples is the work of Khoury *et al.*³⁹² Authors presented gold nanorods (about 10 x 35 nm) protected by thiolated Azo monolayer, dispersed in organic solvents, including dichloromethane. However, significant distortions of both plasmonic bands of AuNRs could have been observed on the UV-Vis extinction spectra (**Figure 67a**). Moreover, the contribution of the photochromic component was relatively weak and essentially no photoswitching was observed, which means that crucial property of one of the components was severely limited in the process. In another work, Wang *et al.* presented relatively big (27.8 x 114.5 nm) AuNRs with anionic Azo derivative adsorbed on the surface.³⁹³ Authors postulated dynamic exchange between CTAB and chosen ligand at different Azo concentrations and upon UV and Vis irradiation. CTAB was constantly present to some degree and seemed to be crucial in maintaining structures' stability. Nevertheless, in this case as well, severe distortion of plasmonic band occurred upon hybrids preparation and further upon their irradiation, indicating aggregation of the structures. Due to the limited presentation of UV-Vis extinction spectra (**Figure 67b**), the assessment of hybrids' functionality is difficult. Only damping of I-LSPR band was presented, and no conclusions can be drawn on the photochromic

properties of the samples. This work confirms how difficult it is to obtain hybrid materials exhibiting both photochromism and stable plasmonic properties.

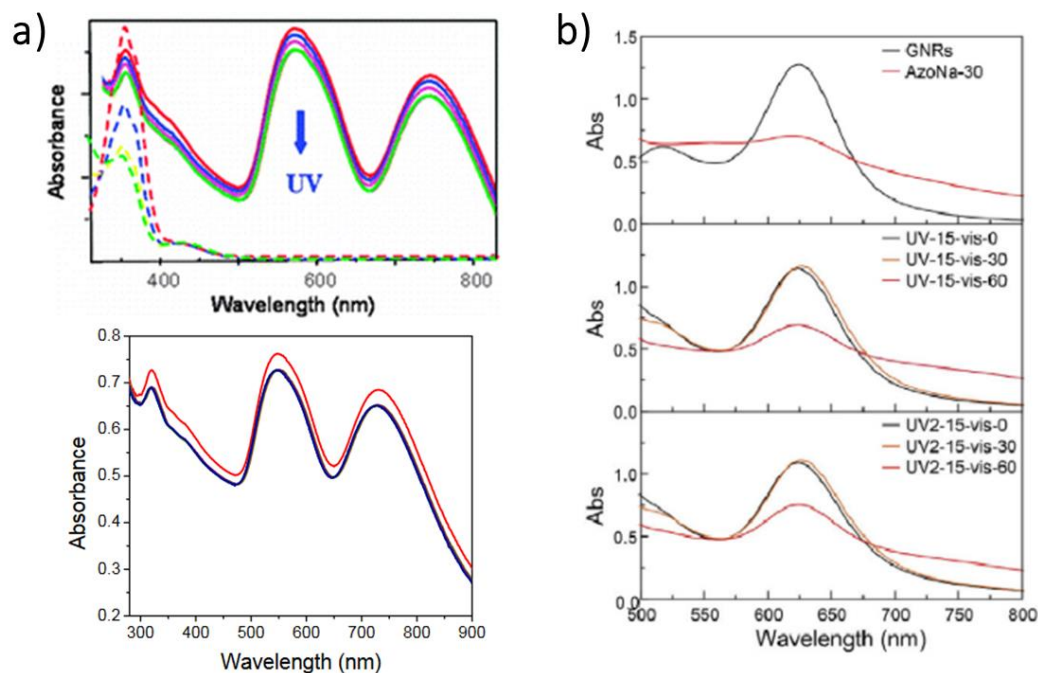


Figure 67. Azo-AuNPs hybrids based on rod-like plasmonic cores. **a)** The top panel presents optical properties of thiol monolayer-protected AuNRs upon UV irradiation and compares it with photoswitching of free Azo molecules. The bottom panel presents stability of nanostructures over time (red – initial profile, dark blue – sample in the dark after 20 min). Reprinted from ³⁹². **b)** L-LSPR band changes of AuNRs (GNRs, top panel, black line) 30 min after AzoNa ligand addition (top panel, red line) and after sequences of UV (365 nm, 5 W) and Vis (>440 nm 500 W) irradiations (middle and bottom panels). Reprinted from ³⁹³.

Typically, Azo-AuNPs hybrids are prepared via covalent linkage of the components. However, as presented in the work of Wang *et al.* discussed above,³⁹³ photochromic molecules exhibiting electrostatic charge may also interact with nanostructures. Such systems display dynamic behaviour. Lysyakova *et al.* presented a cationic Azo surfactant-like molecule that decorated AuNSs.³⁴³ Surface coverage of the structures led to different 3D organizations of AuNPs. However, contrary to the examples presented above, these hybrids exhibited typical Azo photoswitching both upon irradiation and in the dark. Nevertheless, the aggregation of nanoparticles after exposure to UV was not avoided.

Finally, most of the Azo-AuNPs hybrids are functional in organic solvents, which limits their application and excludes such systems, e.g. from bio-related research. The above-mentioned works of Wang *et al.*³⁹³ and Lysyakova *et al.*³⁴³ presented water-functional hybrids, however, with limited stability of plasmonic properties. On the other hand, Chu *et al.* used typical thiolated Azo ligands and polar background ligands to induce dispersion of photochrome-

decorated 2.5 nm spherical AuNPs in water and mixtures of water with other solvents.³³⁹ Hybrids retained their photoswitching without affecting the stability of AuNSs. These results, however, were again limited to small, spherical nanoparticles.

Although all of the crucial aspects of plasmonic-photochromic formulations seem to be addressed in different research articles, they are usually not addressed simultaneously. And although it may seem that every necessary step has been undertaken, somehow, the approaches cannot be combined, and there is virtually no example of a system fulfilling all of the requirements at the same time. This is why some of the novel plasmonic-photochromic materials utilize also a third, inert component serving as a scaffold or matrix for the two functional constituents. Although such a class of hybrid materials has not been officially recognized yet, the formulations constituted an important inspiration for undertaking research presented within this chapter (**Figure 68**).

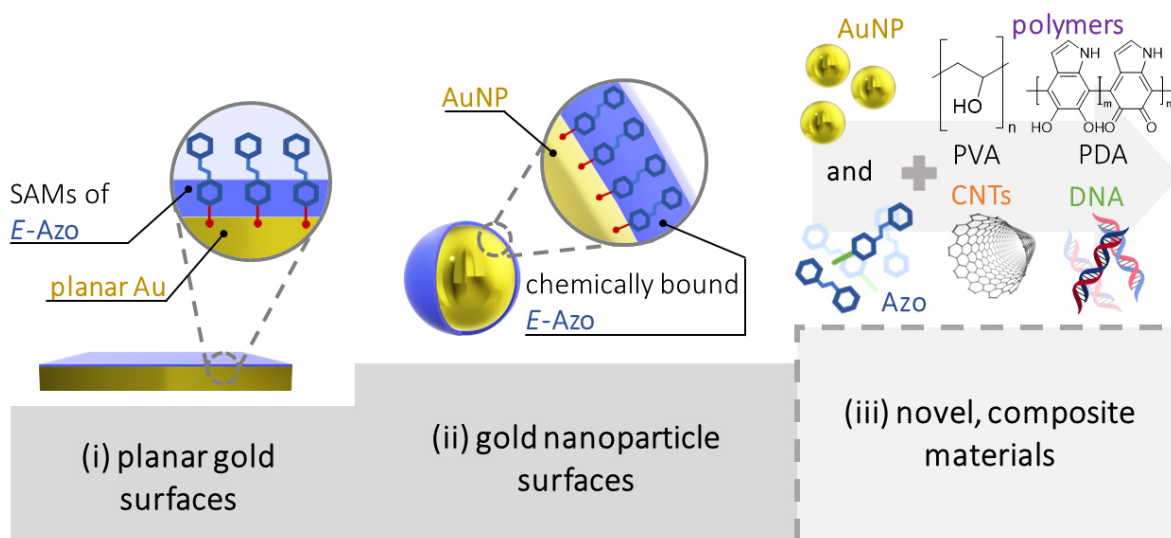


Figure 68. The evolution of Azo-Au hybrid structures and surfaces. The recognition of a new category of plasmonic-photochromic materials relying on use of a third, inert component as a scaffold or matrix is proposed within this dissertation.

Use of scaffold or matrix enables control over macroscopic properties of the material, further enlarges its surface area, and prevents uncontrolled Brownian motion of the functional structures. In the literature different types of a third component have been proposed, including poly(vinyl alcohol),³⁹⁴ polydopamine,^{395,396} DNA,³⁹⁷ or carbon nanotubes.³⁹⁸

Kunfi *et al.* reduced gold on the surface of polydopamine deposited on a glass substrate, hence creating AuNPs, and further decorated the surface with photochromic ligands (thioalkyl- or aminoalkyl-azobenzenes).³⁹⁵ Authors observed both photochromic and plasmonic properties of the material. System exhibited single plasmon band around 550 nm and characteristic $\pi \rightarrow \pi^*$ band of Azo components. Azo ligands maintained their photoswitching ability, that could have been induced upon UV-Vis irradiation for many cycles. Moreover, the isomerization of

photochromic component did not distort optical properties of nanoparticles (**Figure 69a**). As-prepared hybrid surfaces were susceptible to ligand exchange processes and hence, different photochromic components could have been introduced.

Dong *et al.* used poly(vinyl alcohol) films doped with AuNPs (15 nm, spherical) and tri-azobenzene to store thermal energy.³⁹⁴ Authors presented, that stored energy can be released upon addressing with proper light source and targeting simultaneously AuNPs and Azo (due to the overlapping of Azo $n \rightarrow \pi^*$ band and AuNPs LSPR band) to accelerate the release at room temperature. For such systems temperature increase of about 9°C was observed. On the other hand, Wang *et al.* presented optically controlled inclusion-exclusion interactions between Azo-decorated carbon nanotubes and cyclodextrin-capped AuNPs (**Figure 69b**).³⁹⁸ Authors demonstrated that plasmonic component could have been reversibly attached and detached and postulated that such mechanism enables adjustment of electronic properties of the carbon nanostructures.

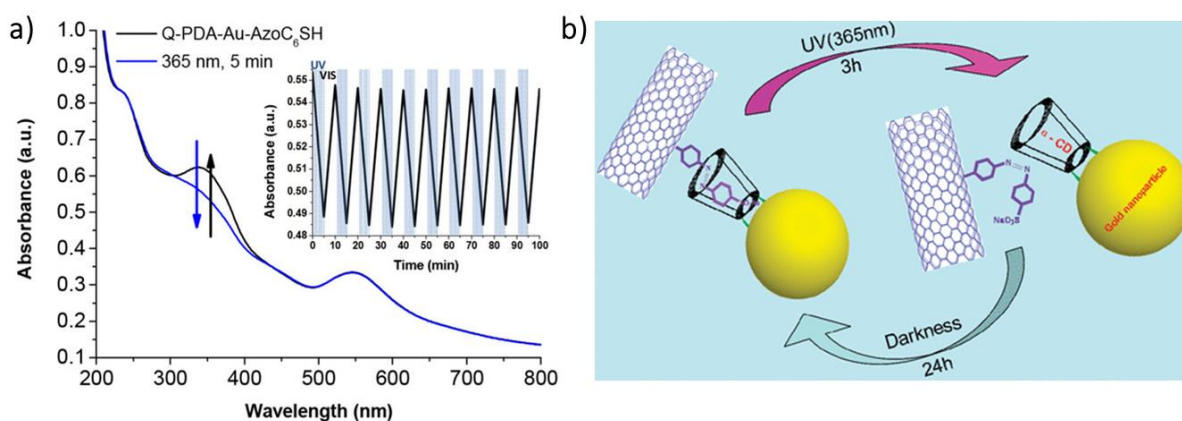


Figure 69. a) Changes in the UV-Vis spectra (solid state) of plasmonic-photochromic glass-polydopamine surfaces upon irradiation. Inset presents stability of the photochromic properties over many irradiation cycles. Reprinted from ³⁹⁵. b) Reversible attachment and detachment of cyclodextrin-decorated AuNPs able to interact with Azo-covered carbon nanotubes. Reprinted from ³⁹⁸.

The main objective of this chapter is to address challenges described above and prepare multifunctional plasmonic-photochromic material by using CNFs as a third, inert component (**objective 2**). Based on the possible interactions between nanocellulose and AuNPs (subsection 2.3.2. of the dissertation) as well as nanocellulose and dyes (subsection 2.3.3. of the dissertation), it can be hypothesised that CNFs may serve as a scaffold for both types of functional units (**hypothesis 3**). Due to stabilization of both components, it can be perceived that their optical properties and functionalities will be maintained (**hypothesis 4**).

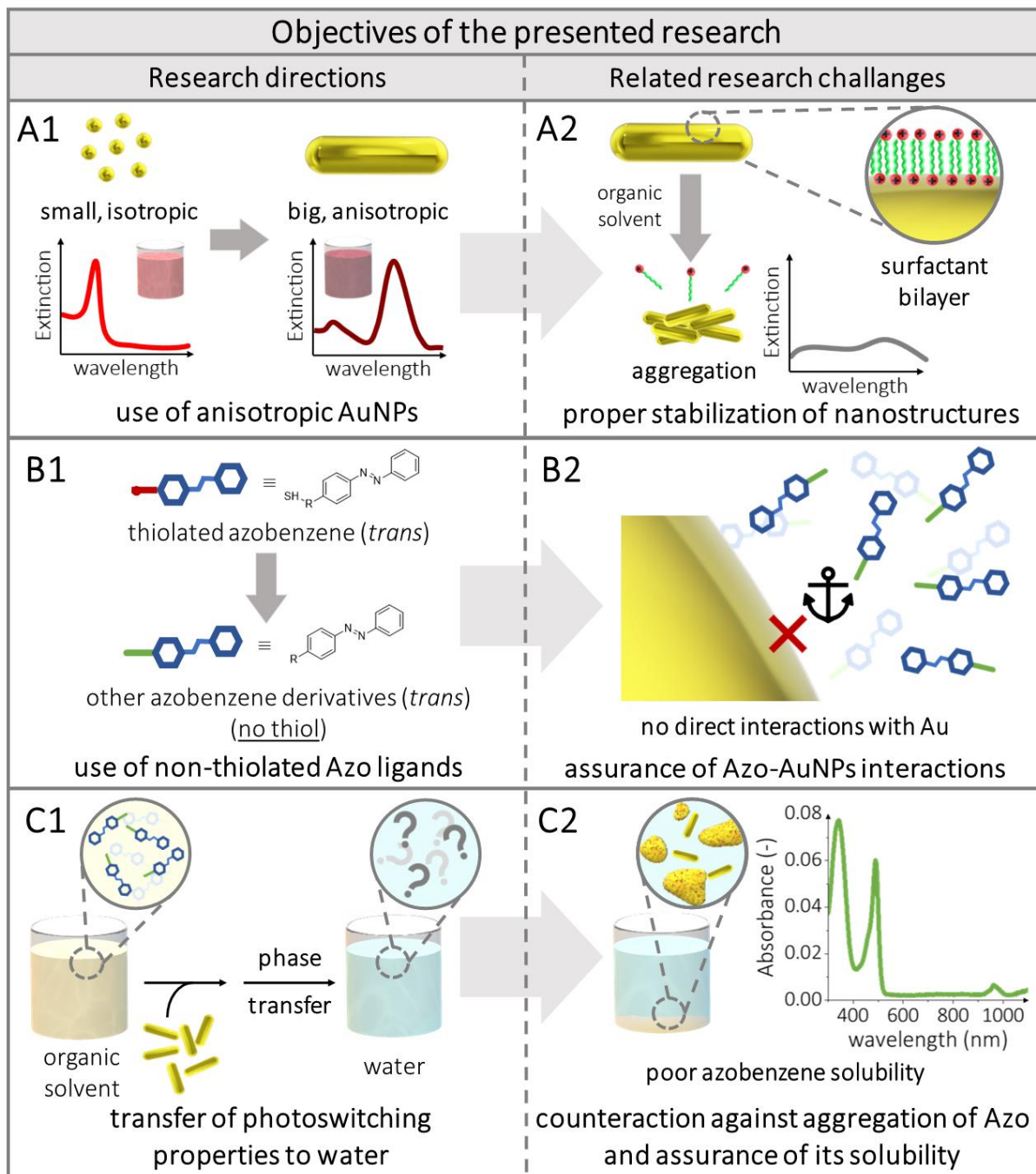


Figure 70. Schematic depiction of the challenges in the design of novel plasmonic-photochromic hybrid systems addressed in this chapter.

4.2. Materials and methods

4.2.1. Materials and techniques

Materials

Chemicals used for the experiments were commercially available and did not require purification. In all experiments deionized water with the resistivity of 18.2 M Ω ·cm (Millipore Milli-Q grade) was used. If not indicated otherwise, chemicals were purchased from Sigma-Aldrich. For the synthesis of AuNSs and AuNRs the following reagents were used:

- metallic precursor: gold(III) chloride trihydrate (HAuCl₄·3H₂O),
- surface stabilizing agent: for AuNRs – cetyltrimethylammonium bromide (CTAB), and for AuNSs – cetyltrimethylammonium chloride (CTAC),
- reducing agents: for seed preparation – sodium borohydride (NaBH₄), for growth solution – L-ascorbic acid (AA),
- other additives: silver nitrate (AgNO₃), and hydrochloric acid (HCl, 37%, Scharlab).

Support for nanoparticles: TEMPO-oxidized cellulose nanofibres (CNFs) supplied by CelluForce (Canada).

Reagents for the synthesis of Azo molecules are not listed, because the ready-to-use compounds were supplied by other researchers.

Techniques

UV–Vis–NIR extinction spectra measurements were performed using JASCO V-730 spectrophotometer equipped with Peltier UV-Vis cuvette holder. Transmission electron microscopy (TEM) images were acquired using Hitachi H-800 microscope. The ATR FT–IR spectra were collected using a Bruker Vertex 70v Fourier transform infrared spectrometer equipped with an air-cooled DTGS detector and diamond attenuated total reflection infrared cell in the middle-infrared (4000 – 400 cm⁻¹) region at room temperature. Instrument control and initial data processing were performed using OPUS Software (v. 7.0, Bruker Optics, Ettlingen Germany). For the irradiation experiments the Hamamatsu L9588 LightningCure LC8 spot light source was used. The exact wavelengths were selected using bandpass filters. Irradiation intensities were measured with Thorlabs S425C Thermal Power Sensor and Thorlabs PM100D Compact Power and Energy Meter Controller.

4.2.2. Nanoparticles synthesis

AuNSs synthesis

AuNSs were synthesised according to the literature protocol.³⁹⁹ First, gold seeds were prepared by reducing HAuCl₄ (5 mL, 0.25 mM) in aqueous CTAB solution (100 mM) with freshly prepared, ice-cold NaBH₄ (0.3 mL, 10 mM) under vigorous stirring. Seeds were aged for 30 min at 27°C before further use. Optical characteristics and visual appearance of the seeds were matching the data presented in **Figure 48** (subsection 3.2.2. of Chapter 3) and hence are not repeated here.

To the growth solution containing CTAC (100 ml, 100 mM), HAuCl₄ (0.36 ml, 50 mM), and AA (0.36 mL, 100 mM) an aliquot of seed solution (0.6 mL) was added under vigorous stirring. Subsequently, the resulting mixture was left undisturbed for 12 h at room temperature. The as-obtained **AuNSs** were further centrifuged (7000g, 2h) to remove the remaining reagents and were subsequently redispersed in water. The final concentration of gold was around 0.14 mM. The diameter of as-prepared **AuNSs** was 17.9 ± 2.1 nm with a plasmon band positioned at 523 nm (**Figure 71**).

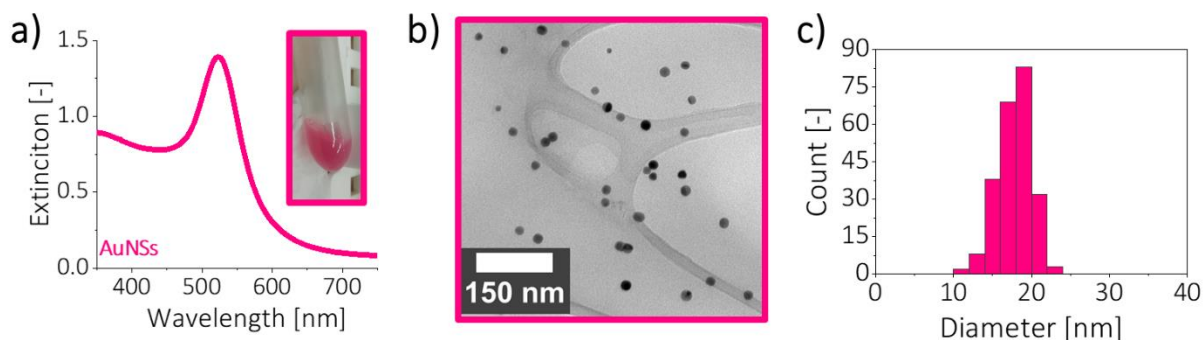


Figure 71. a) UV-Vis extinction spectra of AuNSs water dispersion. Inset presents visual appearance of the sample. b) TEM image of the as-synthesised AuNSs. c) Size histogram of the nanoparticles, average diameter: 17.9 ± 2.1 nm, number of nanoparticles measured $N = 235$.

AuNRs synthesis

AuNRs were prepared according to silver-assisted seeded growth approach, based on the protocol of Chang *et al.*⁴⁰⁰

In the first step seeds were prepared by reducing gold precursor, HAuCl₄ (0.25 mL, 0.010 M) in aqueous solution of CTAB (9.75 mL, 0.10 M) with ice-cold NaBH₄ (0.6 mL, 0.010 M) added under vigorous stirring. The mixture was left for 10 min under mild stirring and subsequently for 2 h at 27°C (unstirred) to assure seed formation and reducing agent decomposition. Optical characteristics and visual appearance of the seeds were matching the data presented in **Figure 48** (subsection 3.2.2. of Chapter 3) and hence are not repeated here.

In the second step, Ag-assisted seeds overgrowth was performed in the solution containing HAuCl_4 (0.5 mL, 0.010 M), CTAB (8 mL, 0.1 M), HCl (0.2 mL, 1.0 M), AgNO_3 (0.030 mL, 0.010 M), and AA (0.08 mL, 0.1 M) upon the addition of Au seed solution (2.0 mL). AuNRs growth solution was left undisturbed for at least 16–20 h at 27°C. As-prepared nanostructures were purified on the next day via centrifugation at 16 000g for 35 min. The supernatant was subjected to the second centrifugation step. Pellets from both steps were combined and redispersed in water. Final concentration of metallic gold was 0.0007 M.

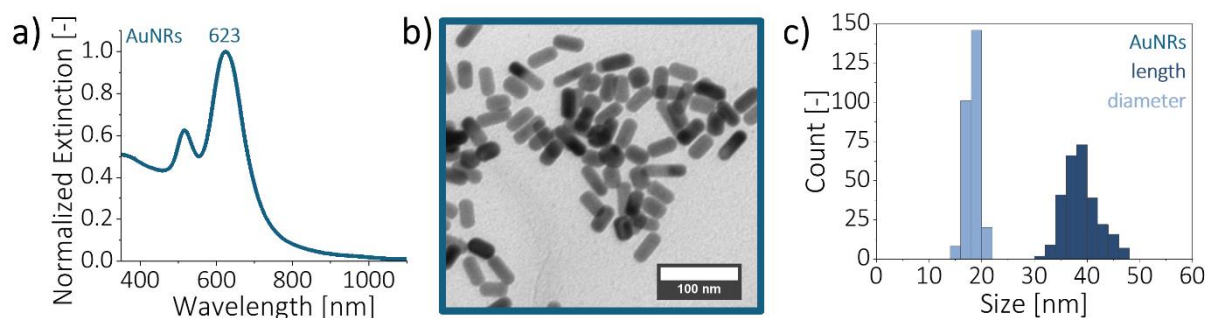


Figure 72. a) UV-Vis extinction spectra of AuNRs water dispersion. b) Representative TEM image of the as-synthesised AuNRs. c) Size histograms of the nanoparticles, average length: 38.9 ± 3.3 nm, average diameter: 18.3 ± 1.3 , AR = 2.13, number of nanoparticles measured $N = 275$. Panels reprinted from own source preprint³⁸⁸.

4.2.3. Azo derivative synthesis

AzoSH and AzoSS ligands presented in Figure 73 below, were provided by Dr Marek Grzelczak (Centro de Física de Materiales, CSIC-UPV/EHU) and Dr Marta Dudek (Faculty of Chemistry, Wrocław University of Science and Technology), respectively. Because these are well-known ligands commonly used in the preparation of Azo-Au hybrids systems (as described for AzoSH in^{336,340,350} and AzoSS in^{329,330}), their synthesis will not be discussed here.

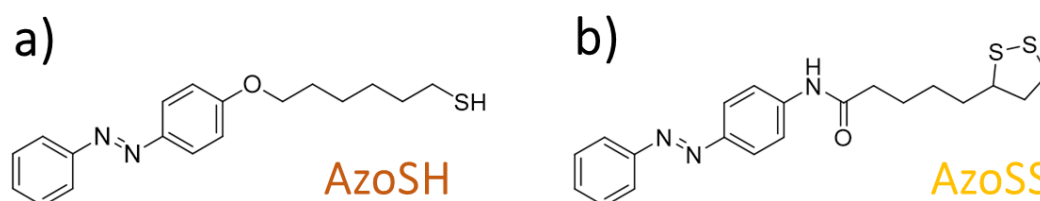


Figure 73. Chemical structures of the photochromic Azo ligands able to create covalent bonds with Au and used in this chapter, namely a) AzoSH and b) AzoSS. Figure reprinted from own source preprint³⁸⁸.

On the other hand, **AzoGly** ligand, a central photochromic component used in this dissertation, was synthesised and characterised by **Dr Marta Dudek** (Faculty of Chemistry, Wrocław University of Science and Technology). Its synthesis and characterisation are presented below.

Synthetic and general analytical methods

Solvents and reagents were purchased from commercial suppliers and were used without further purification. Column chromatography was performed using silica gel (Acros 60, 40–60 mesh). ^1H - and ^{13}C NMR-spectra were recorded on a JEOL 400 MHz spectrometer or a Bruker Avance 600 MHz NMR spectrometer at 25°C (residual protonated solvent signals were used as internal standards). High resolution mass spectra (HRMS) were obtained with a WATERS LCT Premier XE mass spectrometer (ESI).

Synthesis

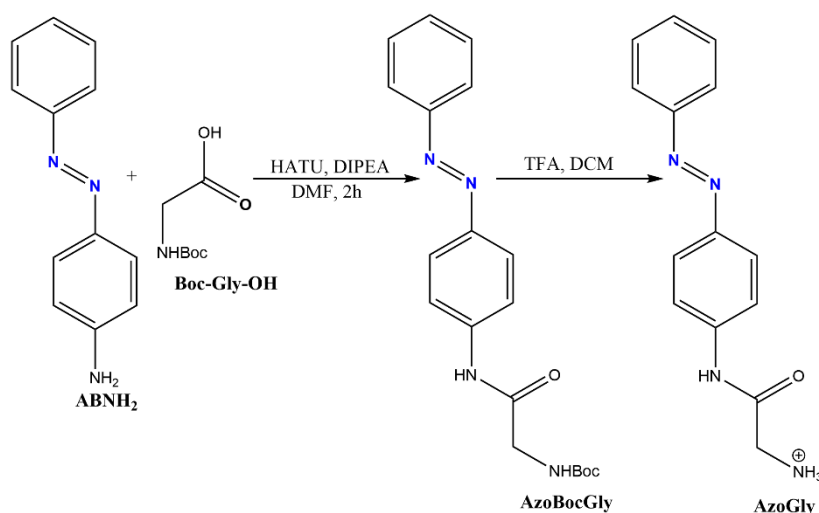


Figure 74. Schematic depiction of the AzoGly synthetic route. Figure reprinted from own source preprint³⁸⁸.

AzoBocGly

To a solution of Boc-Gly-OH (0.32 g, 1.83 mmol, 1.2 equiv.) in DMF (10 mL), 4-aminoazobenzene (0.30 g, 1.52 mmol, 1 eq.) was added followed by addition of DIPEA (0.17 g, 1.3 mmol, 2.4 equiv.) and HATU (0.69 g, 1.83 mmol, 1.2 equiv.). The mixture was stirred for 2 hours at room temperature. Subsequently, water was added to the solution and the as-formed precipitate was separated by filtration, washed with water, and dried. The resulting crude residue was purified by column chromatography on SiO₂ gradient from DCM to 1% MeOH in DCM to yield AzoBocGly in a form of an orange powder (0.4 g, 74%).

^1H NMR (601 MHz, Methanol-*d*₄) δ : 7.93 – 7.86 (m, 4H), 7.80 – 7.75 (m, 2H), 7.55 – 7.45 (m, 3H), 3.90 (s, 2H), 1.48 (s, 9H).

HRMS m/z (ESI): C₁₉H₂₂N₄O₃ [M+H]⁺, calculated: 355.1770, found: 355.1541.

AzoGly

To a solution of AzoBocGly (0.1 g, 0.18 mmol, 1 eq.) in DCM (10 mL) trifluoroacetic acid (0.41 g, 3.6 mmol, 20 eq.) was added. The mixture was stirred overnight. Afterwards the solvent was removed under reduced pressure to give AzoGly as TFA salt in a form of an orange solid (quantitative).

¹H NMR (601 MHz, Methanol-*d*₄) δ: 7.93 – 7.87 (m, 4H), 7.81 – 7.79 (m, 2H), 7.55 – 7.47 (m, 3H), 3.47 (s, 2H).

¹³C NMR (101 MHz, Methanol-*d*₄) δ: 164.4, 152.7, 149.0, 140.7, 130.8, 128.9, 123.5, 122.4, 119.6, 40.5.

HRMS m/z (ESI): C₁₄H₁₄N₄O [M+H]⁺, calculated: 255.1346, found: 255.1345.

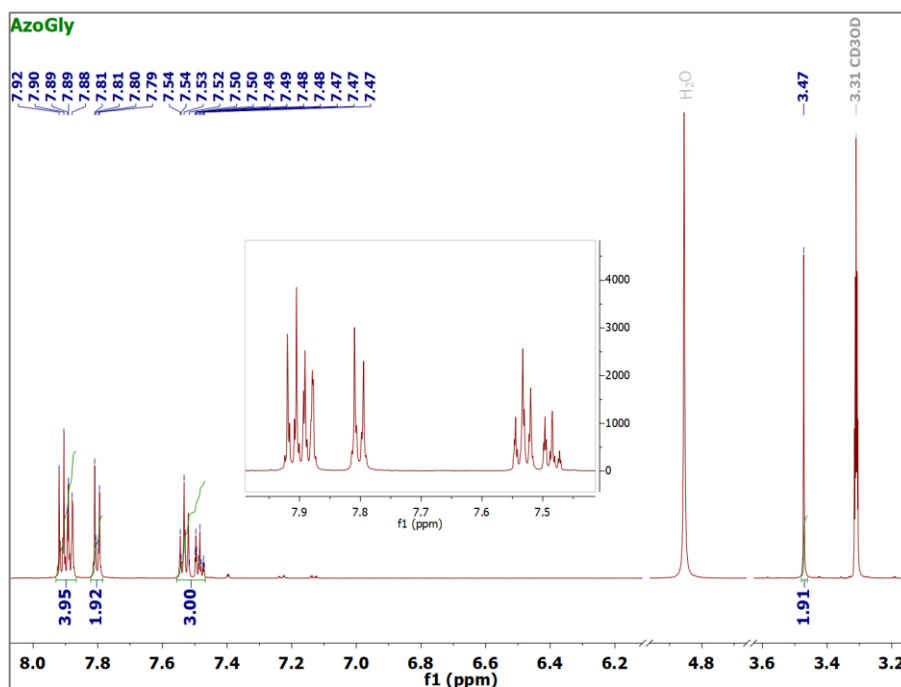


Figure 75. AzoGly in CD₃OD - ¹H-NMR spectra. Reprinted from own source preprint ³⁸⁸.

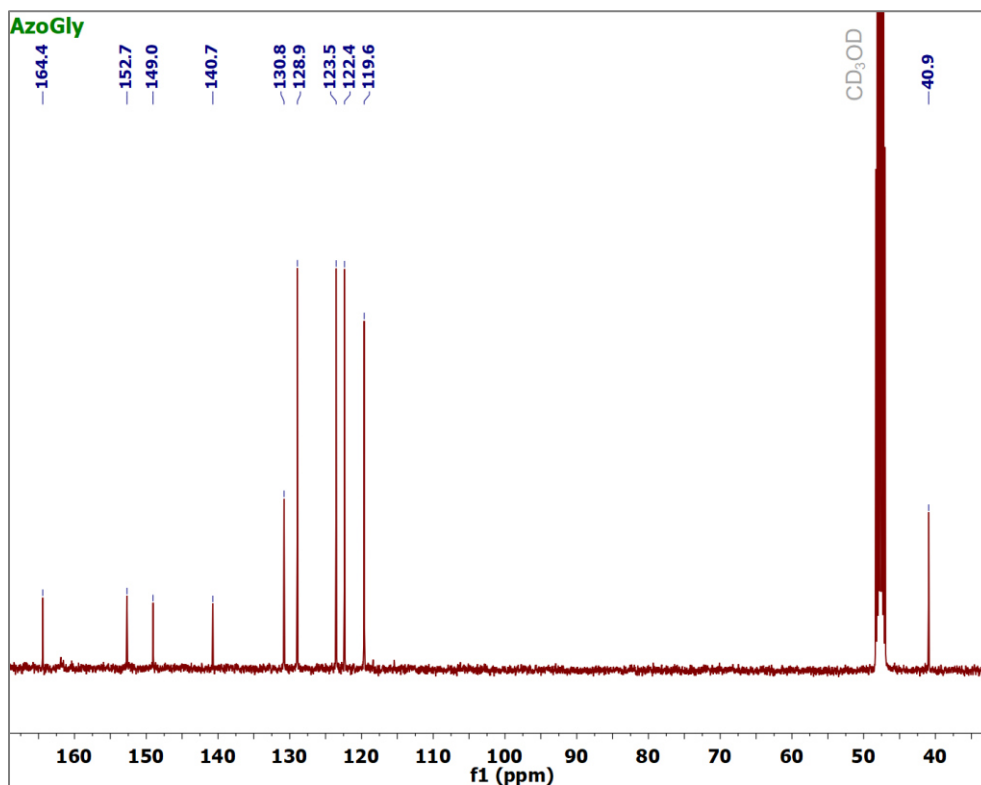


Figure 76. AzoGly in CD_3OD - ^{13}C -NMR spectra. Reprinted from own source preprint ³⁸⁸.

Photostationary states (PSSs) composition

The photoinduced isomerization reactions of AzoGly molecule were performed using Hamamatsu L9588 LightningCure LC8 spot light source equipped with 365 nm and 436 nm filters. The compositions of photostationary states (PSS_E and PSS_Z) were determined by ^1H NMR spectroscopy. Prior to recording the NMR spectra sample (8.8 mM in CD_3OD solution at 25°C) was irradiated for 10 minutes either at 365 nm or 436 nm. Compositions of the respective PSSs (PSS_E for 436 nm irradiation and PSS_Z for 365 nm irradiation) were calculated from the intensity ratios of the integrals of the corresponding peaks on the NMR spectra, as presented in **Figure 77c**.

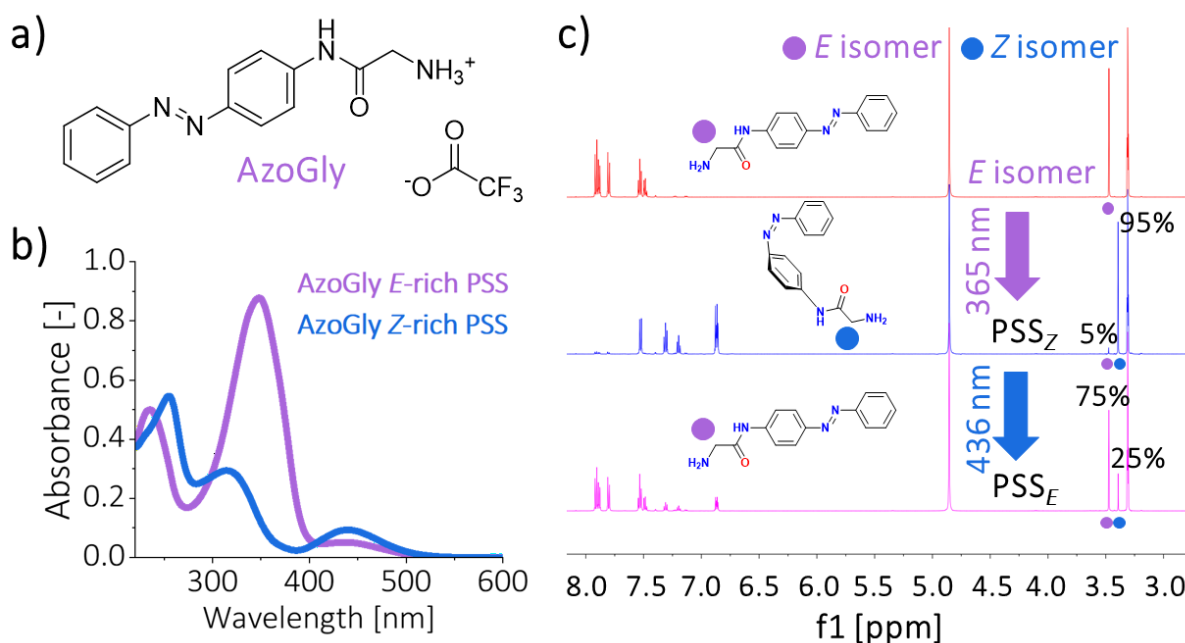


Figure 77. a) Chemical structure of AzoGly photochromic component. It is important to emphasise that in all experiments AzoGly was used in a form of its salt with trifluoroacetic acid. b) Representative UV-Vis absorption spectra of the E-rich and Z-rich photostationary states of AzoGly in ethanol. c) Quantification of the AzoGly PSS_E and PSS_Z composition by ¹H NMR. Reprinted from own source preprint³⁸⁸.

4.2.4. Hybrid materials

AuNPs-CNFs pre-composites

AuNPs-decorated CNFs were prepared according to the protocol established in Chapter 3. Such materials are considered to be ‘pre-composites’, an intermediate in the preparation of the final hybrid plasmonic-photochromic formulation. Such naming convention will be used further in the text.

Dispersions of as-prepared AuNPs (AuNSs or AuNRs) were washed twice via centrifugation and redispersed in 1 mM CTAB. Subsequently, solutions of plasmonic nanostructures were titrated with the aqueous 0.5 wt% CNFs solution at room temperature and under vigorous stirring. The AuNPs/CNFs volume ratio equalled 2:1. The as-prepared samples were left until the next day to promote material sedimentation. On the next day pellets were collected, and washed two times with water via centrifugation (540g, 5 min). Hence, the excess of surfactant was removed. The resulting Au-CNFs pre-composites were subjected to visual inspection and UV-Vis-NIR characterization.

AzoGly-AuNPs-CNFs composites

This chapter is devoted to development of novel protocols enabling preparation of functional Azo-AuNPs-CNFs composites. Hence, all the undertaken steps resulting in the final procedure will be described and analysed within the following sections of the chapter.

Photoswitching Tests of AzoGly-AuNPs-CNFs Composites

In the photoswitching experiments the Hamamatsu L9588 LightningCure LC8 spot light source was used. Isomerization of the photochromic component in the hybrid formulation was induced with UV irradiation (365 nm, irradiation intensity 1.93 ± 0.06 mW/cm²) and visible light (405 nm, light intensity: 4.7 ± 0.1 mW/cm²; and 500-800 nm, light intensity: around 200-300 mW/cm²). Irradiation intensities were measured with Thorlabs S425C Thermal Power Sensor and Thorlabs PM100D Compact Power and Energy Meter Controller. The course of isomerization reactions was monitored using UV-Vis absorption measurements.

4.3. Results and discussion

The design of plasmonic-photochromic system described within this chapter relies on using CNFs-stabilized AuNPs. As presented in chapter 3, the presence of CNFs does not alter optical properties of Au nanocrystals, moreover nanofibres stabilize the nanostructures in harsh conditions that would normally lead to the aggregation of AuNPs. Presence of CNFs enables also removal of the excess surfactant, which usually prevents the preparation of Azo-AuNPs hybrids out of big, anisotropic nanostructures. Hence, the first attempts described in the 4.3.1. subsection below rely on use of spherical nanoparticles, although bigger than the ones typically used in the literature reports. Simultaneously, in these attempts typical thiolated Azo ligands are used to mimic the well-known literature protocols. Based on the conclusions of subsection 4.3.1. proper adjustments in the protocol are introduced and discussed in the following subsections, ultimately leading to the desired Azo-AuNPs-CNFs formulation.

In this chapter only the most relevant and successful experimental attempts are described, although more procedures were tested in the course of the project. The initial conditions chosen for materials preparation were based on typical literature protocols,^{339,340,401} e.g. amounts of photochromic ligands were adjusted to correspond with the number of Azo molecules per nm² of total gold surface as described in the literature. Subsequently, if possible, Azo ligands concentrations were increased to advance photochromic properties of the composites.

Calculations for the established protocols relied on the following information that might be derived from the literature:

- (1) The extinction of AuNPs dispersions at 400 nm, $Ext(400)$, represents total concentration of atomic Au, $[Au^0]$ (mM).^{380,402} The extinction coefficient at 400 nm is nearly constant for AuNPs of different sizes⁴⁰³ and shapes, which was confirmed for spherical³⁸⁰ and rod-like gold nanostructures.^{86,381} A formula enabling calculation of $[Au^0]$ is presented below:³⁸¹

$$\text{Equation 19. } [Au^0] \text{ (mM)} = Ext(400) \times 0.44$$

As presented in chapter 3, immobilization of AuNPs on CNFs is quantitative, hence for each pre-composite $[Au^0]$ value can be recalculated into the total number of Au atoms in the sample, N_{Au} .

- (2) Based on TEM pictures the spherical shape of AuNSs and rod-like shape of AuNRs can be assumed. This enables calculation of volume of a single nanostructure based on the geometrical parameters determined from TEM images. Moreover, the bulk crystal structure of gold, FCC, with a unit cell dimension $a = 0.408$ nm and volume $V = 0.0679$ nm³, as well as the number of gold atoms per unit cell equal to 4 were assumed.^{404–406} Combining this information with volume of a single nanostructure and N_{Au} value, enables the calculation of the total number of AuNPs in the sample, N_{AuNPs} .
- (3) Based on the sizes estimated from TEM images surface of a single nanoparticle, S_{AuNP} can be calculated. By multiplying S_{AuNP} by the total number of nanostructures in the sample, N_{AuNPs} , the total surface of Au can be calculated, S_{Au} . This value allows for adjusting Azo ligand concentration to obtain the desired number of Azo molecules per total Au surface. Moreover, to better compare approaches presented here to the literature protocols the amounts of Azo can be also given as excess with respect to the number of binding sites of Azo on Au (single thiolated Azo-moiety occupies the area of 0.214 nm² on the surface of gold).

4.3.1. Composites prepared with AuNSs and thiolated Azo ligand

The total Au content in the AuNSs-CNFs pre-composite used for the preparation of hybrid plasmonic-photochromic materials was about 1.1 wt% with respect to the mass of CNFs. Hence, the plasmon band of immobilized AuNSs was not as pronounced as for the colloidal solution (Figure 78a). Most importantly, however, plasmon peak position remained unchanged, only a slight blueshift of 4 nm was observed. The pre-composite exhibited typical

macroscopic form (**Figure 78b**), which indicates that as long as the AuNPs are stabilized with the cationic surfactant their immobilization on anionic CNFs is not shape-dependent.

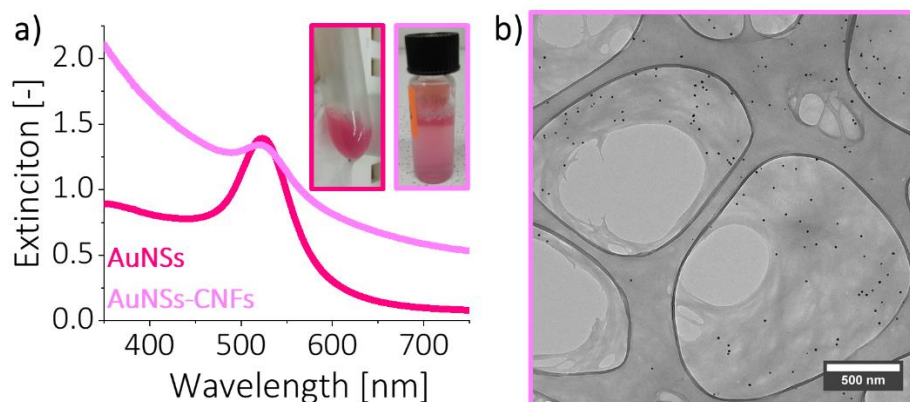


Figure 78. a) Comparison of the optical properties (UV-Vis spectra) of AuNSs and AuNSs-CNFs. Inset shows physical appearance of the samples (colour of the frames indicates type of the sample accordingly to the colours presented on the spectra). b) TEM image of the AuNSs-CNFs pre-composite.

Importance of pre-composite pretreatment

First, to follow previous literature protocols describing preparation of Azo-AuNPs hybrids, thiolated **AzoSH** ligand was used (**Figure 73a**). Due to its chemical structure, AzoSH can be covalently bound to the surface of Au. Molecule was soluble in tetrahydrofuran (THF), which is miscible with water.

Protocol no 1. To the THF solution of AzoSH a matching volume of aqueous dispersion of **AuNSs-CNFs** was added (1:1, v/v; Au/cellulose ratio ~1.1 wt %) under vigorous stirring. Total amount of Azo corresponded to 20-fold excess with respect to the number of binding sites on Au. After 5 min of stirring the vial with mixture was carefully sealed with parafilm and left for at least 17.5 hours at room temperature. On the next day the sample was examined and centrifuged in order to redisperse hybrid material in water.

Sample examined on the next day did not separate even after centrifugation, hence its optical properties were determined for the whole mixture. As presented in the **Figure 79a**, only the $\pi \rightarrow \pi^*$ and $n \rightarrow \pi^*$ bands of AzoSH can be distinguished, since separation from the excess photochrome was not possible. Plasmonic properties of AuNSs are not distinguishable at all. In fact, metallic aggregates on the inside walls of the vial were observed, indicating loss of one of the key features of the sample. After reviewing the available literature on surfactant-CNFs interactions and their solvent stability the idea of proper **AuNSs-CNFs** pretreatment was created.

The nature of AuNPs and CNFs interactions within the proposed pre-composite rely on the electrostatic attraction between components, mediated by CTAB. Pre-composite is prepared in 1 mM CTAB solution to prevent the aggregation of nanoparticles and ensure their efficient immobilization. CMC of CTAB equals 0.9 mM in water,⁴⁰⁷ which means that not only positively charged AuNPs, but also CTAB micelles are present in the solution upon pre-composite preparation. Hence, phase separation of the AuNPs-CNFs material occurs not only due to the immobilization of AuNPs, but also due to the interactions between the CTAB micelles and cellulose nanofibres. This, as a result, leads to material flocculation and phase separation. For the water+THF mixtures the CMC value of CTAB is not necessarily the same as for pure water. Misra *et al.* indicate that with the increasing THF addition the CMC_{CTAB} increases, e.g. for 25 vol% addition of THF CMC_{CTAB} can reach 24 mM at room temperature.⁴⁰⁸ On the other hand, Rahmanzadeh *et al.* reported that the increasing THF content increases CMC_{CTAB} , however not drastically, e.g. for 40 wt% addition of THF CMC_{CTAB} equals about 0.987 mM at room temperature.⁴⁰⁹ Such slight changes were also reported by other authors.⁴¹⁰ This suggests, that mixing AuNSs-CNFs dispersed in water with AzoSH dispersed in THF at 1:1 volume ratio, does not result in the drastic increase of the CMC_{CTAB} and the surface of nanoparticles might not be entirely unblocked and made accessible for the Azo ligands. Hence, there are no characteristic Azo bands on the UV-Vis spectra of the resulting sample. Notably, THF is known to form hydrogen bonds with $-OH$ groups of cellulose,⁴¹¹ which should prevent hybrid material from aggregation and stabilize it. However, if the micelles of CTAB are still covering the surface of cellulose nanofibres it is very likely that the stabilizing effect of THF cannot be entirely manifested and – as a result – the whole system is inherently not compatible. This leads to the conclusion that the remaining CTAB needs to be removed to promote efficient interactions between Azo component and the pre-composite. In order to do so, AuNSs-CNFs should be first pre-treated in such a way that CTAB will be removed not only from the surface of Au, but also from the vicinity of cellulose nanofibres. The approach should be effective and easy to not overcomplicate the whole protocol. Hence, utilization of ethanol (EtOH) was proposed. EtOH is known for its destructive influence over the stability of CTAB molecular arrangements. CMC of CTAB in EtOH is equal to 240 mM at room temperature.⁴⁰⁷ This value is drastically higher than CMC_{CTAB} in water or in water+THF mixtures (regardless of the source for their values). This means that both any remaining CTAB micelles as well as the CTAB bilayer covering the surface of AuNSs will be disassembled upon pre-composite transfer to EtOH.

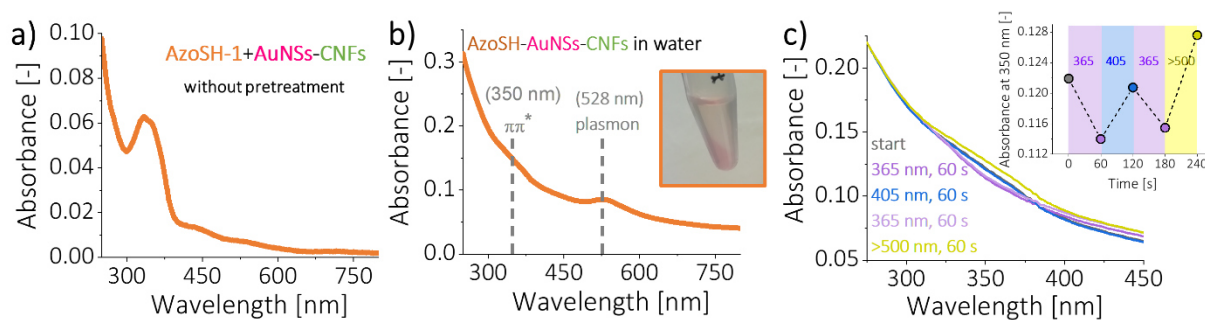


Figure 79. **a)** UV-Vis absorption spectra of the AzoSH and AuNSs-CNFs mixture (1 mm cuvette) after attempted unsuccessful purification via centrifugation. Sample prepared without pre-composite pretreatment. **b)** UV-Vis spectra of the AzoSH-AuNSs-CNFs hybrid material redispersed in water (1 mm cuvette) prepared after pre-composite pretreatment with EtOH. Inset shows appearance of the sample. **c)** Photoswitching of the AzoSH-AuNSs-CNFs hybrid material redispersed in water. Inset shows evolution of the $\pi \rightarrow \pi^*$ band of AzoSH in the composite.

Protocol no 2. Pre-composite (Au/cellulose ratio ~1.1 wt %) was centrifuged (800g, 5 min) and the supernatant was collected, while the remaining pellet was redispersed in EtOH. Pre-composite redispersed well in the new solvent and no aggregation of AuNSs was observed. Subsequently, to the THF solution of AzoSH a matching volume of EtOH-dispersed **AuNSs-CNFs** was added (1:1, v/v) under vigorous stirring. Total amount of Azo corresponded to 20-fold excess with respect to the number of binding sites on Au. After 5 min of stirring the vial with mixture was carefully sealed with parafilm and left for at least 17.5 hours at room temperature. On the next day sample was examined, centrifuged twice and redispersed in water.

Important role of CNFs as a stabilizer for AuNPs was confirmed upon pre-composite pretreatment with EtOH. Usually, redispersion of nanostructures stabilized by surfactant in alcohols (methanol, ethanol) leads to their aggregation, due to the decomposition of stabilizing surfactant bilayer. Here, although decomposition of the CTAB arrangements remaining in the pre-composite was promoted, stabilization of AuNPs was maintained due the presence of CNFs and no aggregation or change of the macroscopic appearance of the **AuNSs-CNFs** upon redispersion in EtOH was observed. Notably, the final **AzoSH-AuNSs-CNFs** material maintained the phase-separated characteristics of pre-composite and was easily separated from solution via centrifugation. Hence, it can be stated that AuNSs are firmly immobilized on the cellulose nanofibres, and EtOH is not compromising the system's integrity in any way. There are two possible explanations for that **(1)** CNFs replace CTAB as stabilizer and interact with the surface of Au nanocrystals or **(2)** CTAB mediating AuNPs-CNFs interactions constitutes a different fraction from the excess surfactant, serves as a molecular glue, and is not removed

from the material after EtOH treatment. This aspect is further explored and discussed in the subsection 4.3.3. of this chapter.

Moreover, as presented in **Figure 79b**, the resulting **AzoSH-AuNSs-CNFs** composite exhibited weak $\pi \rightarrow \pi^*$ band of the photochromic component and clear, although weak, plasmon band. No aggregation of nanoparticles was noticed this time. Resulting material exhibited photoswitching typically observed for Azo derivatives (**Figure 79c**), although the overall evolution of the $\pi \rightarrow \pi^*$ band was very weak. UV irradiation (365 nm, 60 s, irradiation intensity: 1.93 ± 0.06 mW/cm² for this and all further described irradiations) caused the drop of the $\pi \rightarrow \pi^*$ band, while blue light irradiation (405 nm, 60 s, irradiation intensity: 4.7 ± 0.1 mW/cm² for this and all further described irradiations) led to its recovery, thus indicating the occurrence of *trans*→*cis* and *cis*→*trans* isomerization reactions, respectively. As presented in the inset of **Figure 79c** irradiation in a 500-800 nm range for 60 s (irradiation intensity around 200-300 mW/cm² for this and all further described irradiations) also led to the recovery of the *trans* isomer. Such irradiation range addresses the position of AuNSs plasmon band, however is also very close to the position of $n \rightarrow \pi^*$ absorption band of the photochromic component. Hence, such irradiation conditions naturally lead to the recovery of the *trans* form. This is why for material formulations containing Au nanospheres, potential plasmon-assisted processes are difficult to evaluate, because the contributions of plasmon-related effects and direct triggering of Azo isomerization occur in the same spectral range and cannot be separated.

Importance of Azo derivative concentration

Because the optical properties of the first hybrid **AzoSH-AuNSs-CNFs** material were not very pronounced, the question arose how the number of Azo molecules remaining in the composite can be increased. As presented in the literature before, for Azo-AuNPs hybrids, factors such as presence of supporting ligands and ratio between them and Azo ligand need to be taken into account. Yet, in the following attempt it was decided to simply utilize a higher excess of AzoSH. Such attempt also helped to estimate roughly how the ligand concentration may affect the preparation protocol.

Protocol 2 was hence repeated, with the increased total amount of Azo, which corresponded to 200-fold excess with respect to the number of binding sites on Au (10 times increase in comparison to original Protocol 2). As-obtained hybrid material was redispersed in water.

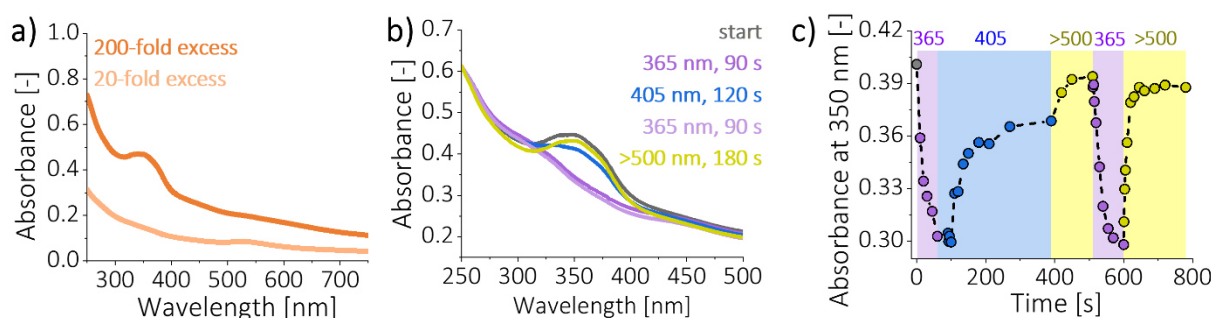


Figure 80. *AzoSH-AuNSs-CNFs* hybrid materials. **a)** Comparison of UV-Vis spectra of the materials prepared with 20-fold and 200-fold excess of AzoSH. **b)** Photoswitching of the hybrid material (200-fold AzoSH excess) redispersed in water. **c)** Changes in the intensity of the $\pi \rightarrow \pi^*$ band of AzoSH in the hybrid formulation (200-fold AzoSH excess) as a function of irradiation wavelength and time.

Comparison of the optical properties presented in **Figure 80a** confirmed that Azo content can be increased within material structure by increasing Azo concentration during preparation step. The $\pi \rightarrow \pi^*$ band of AzoSH component was more pronounced, however, plasmon band of AuNSs was clearly more dumped and almost not visible compared to the 20-fold excess sample, which compromised the overall plasmonic properties of the material. Nevertheless, sample exhibited characteristic Azo photoswitching, more pronounced than for the 20-fold excess sample (**Figure 80b**). As indicated in the **Figure 80c**, UV irradiation (365 nm, 90 s) caused the drop of the $\pi \rightarrow \pi^*$ band (Abs_{350}), while blue light irradiation (405 nm, 300 s) led to its recovery, thus indicating the occurrence of *trans* \rightarrow *cis* and *cis* \rightarrow *trans* isomerization reactions. Similarly to the observations made for the 20-fold excess sample, above 500 nm irradiation for 120 s or 180 s also led to the recovery of *trans* isomer. The resulting photostationary state (PSS_E) was even richer in *trans* form of Azo comparing to the PSS_E reached after 405 nm irradiation (higher Abs_{350} values). Richer PSS_E could have been also obtained for above 500 nm irradiation if the sample was initially irradiated with a blue light. This proves contribution of plasmon-related effects either in a form of charge carrier transfer or a thermoplasmonic effect, since relaxation of Azo derivatives induced thermally typically leads to PSS_E richer in *trans*-Azo comparing to photoinduced isomerization. Nevertheless, the close proximity of the initial absorption bands of Azo and AuNSs does not enable determination of the exact contributions.

4.3.2. AzoGly and CNFs interactions leading to formation of hybrid materials

Since plasmonic-photochromic **AzoSH-AuNSs-CNFs** hybrids did not exhibit satisfactory optical properties, the decision was made to work out another approach relying on

Azo-CNFs interactions instead (**hypothesis 3**). For this purpose another type of Azo molecule needed to be employed and a positively charged Azo derivative, **AzoGly**, was selected as a model molecule, thus representing a class of positively charged Azo photochromes. General structure and photochromic properties of this compound are presented in **Figure 77**. AzoGly lacks $-SH$ group in its structure and is $-NH_3^+$ terminated instead. In all experiments this molecule is used in a form of its salt with trifluoroacetic acid (TFA). Moreover, AzoGly is soluble in ethanol, which aligns well with the pre-composite pretreatment step.

To verify if AzoGly is able to interact with CNFs efficiently enough to form photochromic nanofibres, the experimental procedure established in the previous section has been repeated with appropriate adjustments.

Protocol no 3. Solution of 1 mM CTAB was titrated with the aqueous 0.5 wt% solution of CNFs under vigorous stirring at room temperature. Volume ratio of CTAB/cellulose was 2:1. The as-obtained sample was left overnight to promote material sedimentation. The obtained pellet was washed two times with water by centrifugation (540g, 5 min) in order to remove the excess of surfactant.

Subsequently, pre-composite pretreatment with EtOH was performed. **CTAB-CNFs** pre-composite was centrifuged (780g, 5 min), the supernatant was discarded and pellet (pre-composite) was redispersed in EtOH.

Afterwards, pre-composite in EtOH was added dropwise to the ethanol solution of AzoGly (1:1, v/v) under vigorous stirring. The amount of Azo was varied from 0.00 mM to 2.62 mM. After 5 min of stirring vials with mixtures were carefully sealed with parafilm and left for at least 17.5 hours at room temperature in order to promote CNFs impregnation with the photochrome. After this time samples were examined, purified by centrifugation, redispersed in water, and subjected to UV-Vis absorption spectra measurements.

In this initial experiment, CNFs were not covered with AuNPs, to investigate direct AzoGly-CNFs interactions. For the comparison, for **AuNSs-CNFs** pre-composites used in the protocols described above, 200-fold excess of AzoSH corresponded to 0.69 mM concentration. Hence, the starting point for this experimental section also equaled 0.69 mM. The upper limit of the concentration range was set closer to the solubility limit of AzoGly in ethanol (about 3 mM). The as-determined concentration range was arbitrarily separated into 7 distinct experimental points. Reference point with pure ethanol (no Azo – 0.00 mM) was also prepared as a control sample.

During purification step it became apparent, that the higher the concentration of the photochrome, the better the phase separation of the CNFs, which became more prone to

centrifugation and could have been easily separated. At the same time, for the two lowest concentrations – control 0.00 mM and 0.69 mM – separation and purification was rather problematic. This emphasises crucial role of AuNPs, that weight down and presumably stiffen the structure of fibres and make the purification procedure of the resulting composite much more facile, even for concentrations in the lower range (as for the **AzoSH-AuNSs-CNFs** hybrid material discussed in the previous section).

Results presented in **Figure 81a** depict a straightforward dependency between AzoGly concentration used during impregnation and the population of the photochrome adsorbed on CNFs. Namely, the higher the concentration, the higher the population of AzoGly in the final material (represented by the intensity of the $\pi \rightarrow \pi^*$ band, see **Figure 81b**, **direct values**). This also explains why at higher AzoGly concentrations material separation was more efficient. Higher population of AzoGly results in the higher overall hydrophobicity of the fibres, which promotes phase separation in water. Cellulose nanofibres do not contribute to the extinction of the composite, only to its scattering, which is also reflected in the sloped nature of all spectra and the tilted profile of AzoGly bands. Nevertheless, the position of AzoGly absorption bands was not drastically changed compared to the pristine AzoGly solution ($\pi \rightarrow \pi^*$ band position: 343 nm in composite vs 348 nm in pristine AzoGly, see **Figure 77**). Most importantly, the intensity of the bands was much more pronounced compared to the **AzoSH-AuNSs-CNFs** sample.

To better visualize the observed tendencies and account for the differences in the retrieval rate of the materials, spectral profiles of the **AzoGly-CNFs** hybrids were adjusted at 600 nm. As determined in chapter 3, only below 600 nm the contribution of CNFs scattering to the optical properties of the composites becomes significant. Moreover, at 600 nm absorption of the photochrome is at the 0.0 level and hence, there is no contribution from photochromic component at this wavelength. Such adjustment is possible if the homogenous impregnation of CNFs with AzoGly is assumed. Only then the amount of AzoGly remaining in the hybrid material via interactions with CNFs is representative to the whole impregnation process and does not depend on the composite retrieval rate. Each sample was corrected separately in such a way that the spectral profile of bare CNFs was first adjusted at 600 nm to match profile of the sample and was subsequently subtracted from the sample spectra (as depicted in **Figure 81a**). The as-obtained corrected intensity values of the $\pi \rightarrow \pi^*$ AzoGly band were plotted against concentration of AzoGly used during impregnation (**Figure 81b**, **corrected values**). The increasing trend observed for the **direct values** was maintained, however the deviation from the trend in the middle of concentration range was mitigated. In general, the intensity of the $\pi \rightarrow \pi^*$ band increases about 26 times for about 3.8 times increase in the photochrome

concentration used during impregnation step. This clearly emphasizes profits stemming from impregnations performed at higher concentrations of the photochrome.

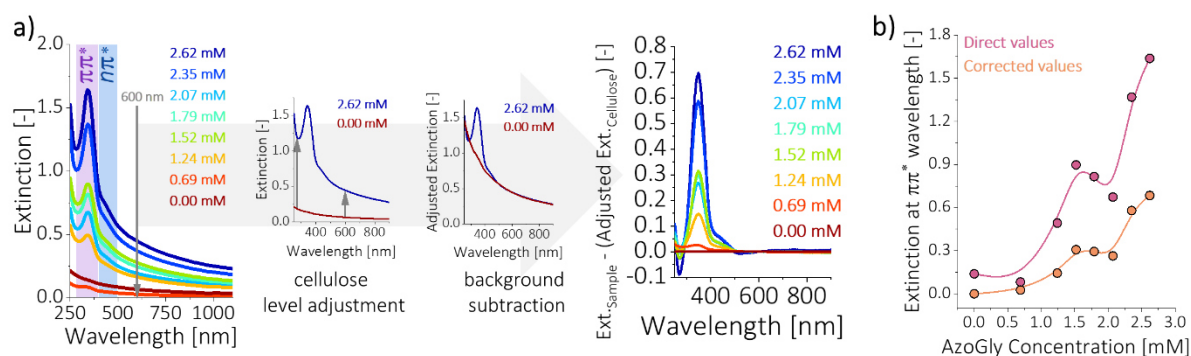


Figure 81. Optical properties of the photochromic CNFs redispersed in water (AzoGly-CNFs without Au). **a)** The applied correction approach and the resulting spectra for samples prepared with different Azo concentrations. **b)** Extinction values at the peak of $\pi \rightarrow \pi^*$ band of AzoGly as a function of photochrome concentration during impregnation procedure. Comparison of direct values and values derived from correction procedure. Reprinted from own source preprint³⁸⁸.

It is important to note, that AzoGly, even in a form of salt with TFA, is not soluble in water. Nevertheless, to investigate whether the photochromic contributions in the hybrid materials are a result of AzoGly-CNFs interactions or rather free AzoGly molecules remaining in water, two solutions of AzoGly in water and in ethanol were prepared at concentrations of ~ 0.7 mM, which was the lowest concentration of the photochrome used during impregnation procedure. It was observed, that AzoGly did not dissolve in water and crude compound was left at the bottom of the vial. Nevertheless, both samples were diluted to obtain $30 \mu\text{M}$ solutions, which would grant viable spectroscopic measurements with absorbance below 1.0. The results presented below clearly show that AzoGly is not soluble in water and hence its EtOH solutions need to be used for the impregnation. Most importantly, however, these results emphasise role of CNFs as a platform for the photochrome transfer to the environment it is not compatible with. Comparing spectra in **Figure 82** with spectra of the hybrid materials dispersed in water presented in **Figure 81** it can be stated that the intense bands of AzoGly in the hybrid samples are not a serendipity, but a result of Azo-CNFs interactions.

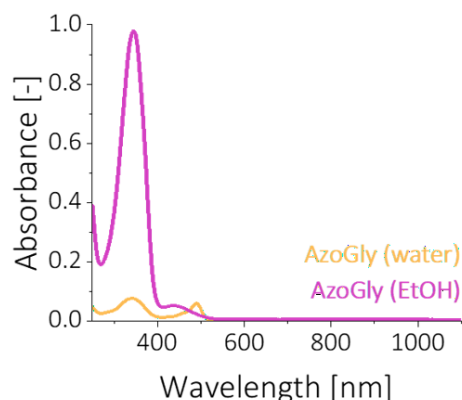


Figure 82. UV-Vis absorption spectra of AzoGly dissolved in ethanol and water. $30\mu\text{M}$ AzoGly solution in EtOH was easy to prepare and its spectrum exhibits typical features of Azo type photochrome. The aqueous solution of Azo was not possible to prepare without compound aggregation. Distorted profile of the spectrum at low photochrome concentration confirms AzoGly insolubility in water.

AzoGly-CNFs interactions were further investigated via IR spectroscopy, as described in the following subsection (4.3.3.), devoted to the preparation protocol of the final Azo-AuNRs-CNFs formulation. This subsection is concluded with the verification of protocol no. 3 for **AuNSs-CNFs** pre-composite. To compare this approach with previously presented **AzoSH-AuNSs-CNFs** hybrids, the concentration of AzoGly was matched to the one used in protocol 3 and the notation of Azo concentration as an excess with respect to the number of binding sites of Au was maintained.

Protocol no 4. **AuNSs-CNFs** pre-composite (~ 1.1 wt% Au/cellulose ratio) was first centrifuged (780g, 5 min) and the resulting pellet was redispersed in EtOH. Subsequently, to the EtOH solution of AzoGly the **AuNSs-CNFs** dispersion in EtOH was added dropwise (1:1, v/v) under vigorous stirring. Total amount of AzoGly corresponded to either 20-fold or 200-fold excess with respect to the number of binding sites on Au. After 5 min of stirring the vial with mixture was carefully sealed with parafilm and left for at least 17.5 hours at room temperature. On the next day both samples were examined, centrifuged, washed two times, and redispersed in water.

As presented in **Figure 83a** **AzoGly-AuNSs-CNFs** samples exhibited promising optical characteristics, significantly better than both **AzoSH-AuNSs-CNFs** samples prepared according to protocol 2 for the same concentration of ligand. The $\pi \rightarrow \pi^*$ band of AzoGly was very pronounced and its intensity was increasing with the increasing excess of Azo used during impregnation procedure. Additionally, both samples exhibited a clear plasmon band and no damping was observed in contrary to samples prepared with AzoSH, despite the fact that Au

content was the same for all of the hybrid materials. This proves higher efficiency of the process when non-thiolated ligand able to interact with the scaffold is used (**hypothesis 3**). Redispersion of AzoGly-containing hybrids in water was not problematic. Both materials maintained the form of phase-separated system and precipitated after some time. Nevertheless, hybrid samples can be easily dispersed again simply by shaking the sediment.

Importantly, composites exhibited very pronounced photoswitching. As presented in **Figure 83b,c** for hybrids prepared with 20-fold AzoGly excess, UV irradiation (365 nm, 90 s) caused the drop of the $\pi \rightarrow \pi^*$ band, similarly to blue light irradiation (405 nm, 90 s). Positions of the $\pi \rightarrow \pi^*$ and $n \rightarrow \pi^*$ bands of AzoGly are different than for AzoSH, and hence, irradiation of AzoGly with blue light at relatively short wavelength (405 nm) also leads to the *trans*→*cis* isomerization. Finally, irradiation above 500 nm for 90 s led to the recovery of *trans* isomer in hybrid material. Similarly to AzoSH, irradiation above 500 nm is very close to the $n \rightarrow \pi^*$ band of the AzoGly photochrome, and hence also leads to the recovery of *trans* isomer. Similar results are presented in the **Figure 83d-f** for hybrids prepared with 200-fold excess of AzoGly. However, due to the higher concentration of Azo molecules in the final formulation, the hybrid material exhibited much better and more consistent photoswitching and better resolution of the changes occurring at 343 nm. The evolution of absorbance at $\pi \rightarrow \pi^*$ band enabled determination of the rate constants and half-lives of the observed isomerization reactions in the **AzoGly-AuNSs-CNFs** hybrids, which was not possible for the samples prepared with AzoSH ligand. Importantly, for all irradiation conditions at room temperature, sample exhibited first order kinetics, just as pristine and free Azo molecules do in the solution, which was confirmed by very high R^2 values of the first-order kinetic equation fits (as presented in **Figure 83f**). However, this chapter focuses solely on the overall qualitative photoswitching properties of the hybrid materials, and the relative differences between the rate constant values are not discussed. AuNPs influence on Azo isomerization is investigated in chapter 5 and 6. Nevertheless, it needs to be emphasised, that PSS_Z achieved after UV exposure (365 nm) was significantly richer in the *cis* isomer compared to isomerization triggered by short wavelength blue light irradiation (405 nm). Moreover, the back-isomerization triggered by irradiation above 500 nm was also observed.

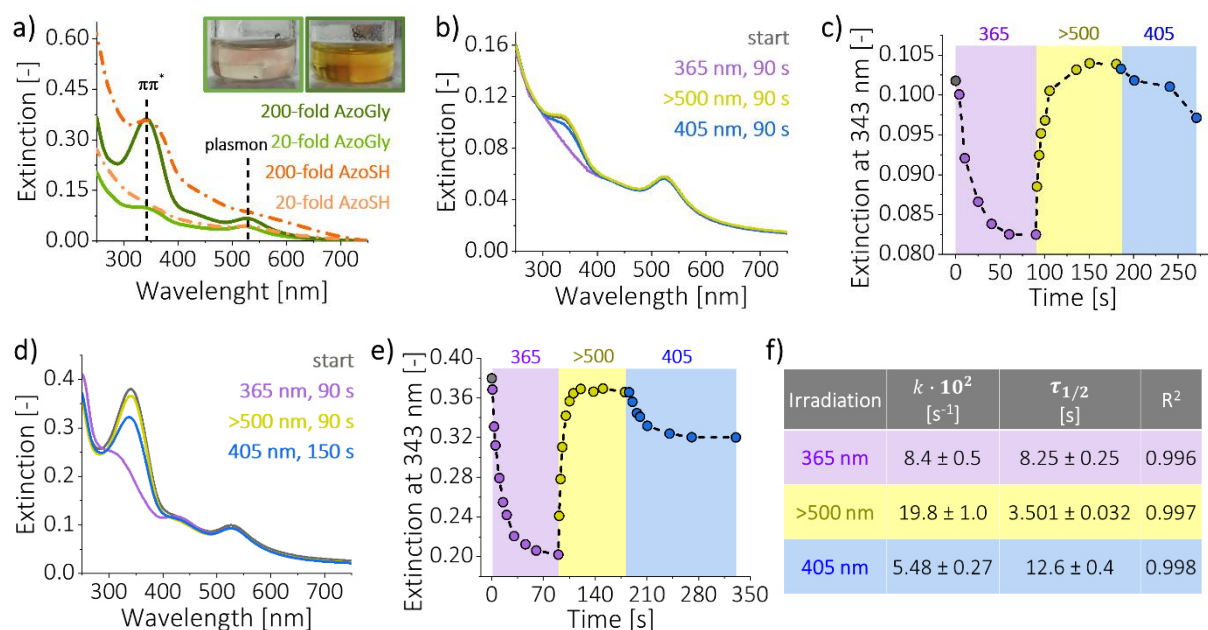


Figure 83. *AzoGly-AuNSs-CNFs hybrid materials. a) UV-Vis spectra of samples prepared with 20-fold and 200-fold excess of AzoGly compared with AzoSH-AuNSs-CNFs hybrids. Inset presents physical appearance of the samples during impregnation. b) AzoGly-AuNSs-CNFs material (20-fold excess) redispersed in water – photoswitching and c) changes in the intensity of the $\pi \rightarrow \pi^*$ band of AzoGly as a function of irradiation wavelength and time. d) AzoGly-AuNSs-CNFs material (200-fold excess) redispersed in water – photoswitching and e) changes in the intensity of the $\pi \rightarrow \pi^*$ band of AzoGly as a function of irradiation wavelength and time. f) Juxtaposition of the rate constants for the isomerization reactions depicted in panel e). Table includes coefficient of determination (R^2) for the first order kinetics fits.*

To conclude, results of the experiments presented in this subsection prove that CNFs can serve as a functional scaffold for the immobilization of both AuNPs and charged Azo ligands. The resulting materials exhibit promising optical characteristics and maintained properties of functional components, such as photoswitching of Azo and stable plasmonic properties of AuNPs. The following subsection verifies whether the established protocol (protocol number 4) can be used to prepare hybrid materials containing both AzoGly and AuNRs.

4.3.3. Composites prepared with AuNRs and new Azo ligand – the final formulation

Protocol no 4 was repeated for the **AuNRs-CNFs** composite with increased Au content. Amount of Au in the pre-composite was increased, in order to improve plasmon contribution to the spectra of the final hybrid material, since for low Au content, ~1.1 wt% for AuNSs, the

plasmon band of AuNPs was visible, although not very pronounced. This subsection explores first the optimization of protocol no 4 for AuNRs, followed by presentation of final preparation protocol, and investigation of the interactions between components in the final **AzoGly-AuNRs-CNFs** hybrids.

Protocol optimization

Influence of EtOH. As already postulated in the previous subsection, pre-composite pretreatment with EtOH is essential for efficient CNFs impregnation with AzoGly. Although proven successful for AuNSs, it was investigated whether such pretreatment approach is also viable for AuNRs. It was determined, that EtOH pretreatment does not compromise stability of the **AuNRs-CNFs** pre-composite, as presented in **Figure 84a**. The less scattering nature of the pre-composite after pretreatment (lower extinction values below 600 nm, where CNFs scattering of a two-phase system is manifested) confirms good dispersion of the Au-decorated nanofibres in the new solvent, which makes them more accessible for the sorption of dye molecules. Moreover, stable positions of both t-LSPR and l-LSPR bands without any distortions confirm sturdy immobilization of AuNRs. It can be also stated that the stability of pre-composite is not affected upon impregnation procedure. **Figure 84b** presents impregnation mixture before separation and purification of the hybrid fibres. Stable dispersion of components (reflected also in the colour of the mixture which combines colour of both initial solutions), without any aggregation can be observed.

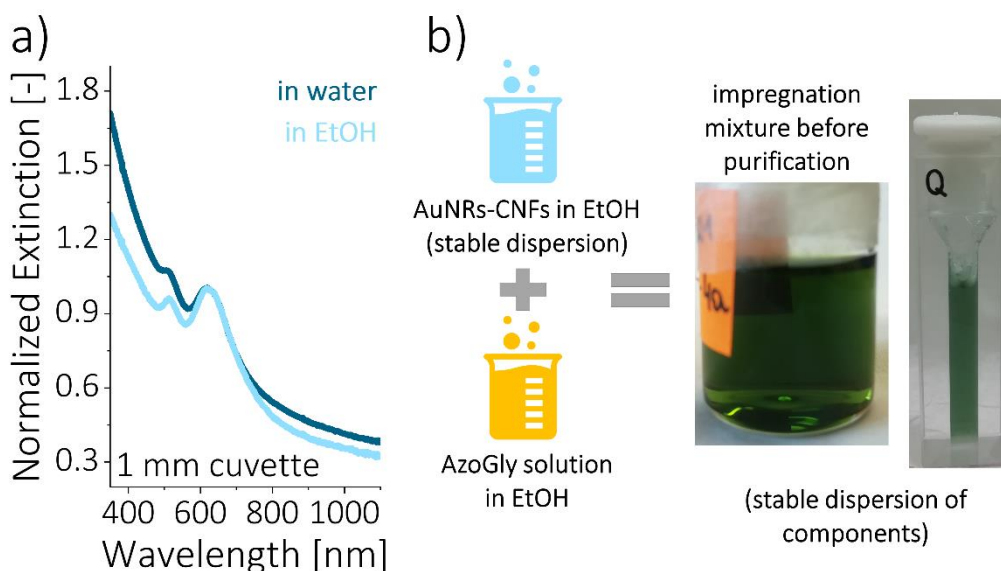


Figure 84. Influence of EtOH pretreatment on stability of AuNRs-CNFs. **a)** UV-Vis-NIR extinction spectra of the pre-composite in water (before EtOH pretreatment) and in EtOH (after pretreatment). **b)** Schematic depiction of the impregnation procedure and visual appearance of the mixture before purification and hybrid material separation. No aggregates are visible and

the colour of the impregnation mixture (green) reflects homogenous conditions of impregnation (combination of blue colour of the pre-composite and yellow colour of the AzoGly solution).

Purification protocol. For all the already discussed preparation protocols, two-step centrifugation was proposed, hence constituting two-step purification procedure. First centrifugation enables hybrid material separation and transfer to water. Second centrifugation aims for composite purification from any unbound excess Azo ligand. Hence, it was investigated if such purification procedure is justified and whether it can be improved.

There are three key goals of the proposed purification procedure that need to be balanced in order to efficiently prepare functional hybrid materials:

- (1) **Removal of the excess photochrome and residual ethanol.** For the sake of impregnation step efficiency, Azo molecules are introduced to the process in an excess amount. This means, that after impregnation, the excess Azo needs to be removed. Since AzoGly is not soluble in water but is well soluble in ethanol, Azo removal aligns with the need to remove residual ethanol during material transfer to water.
- (2) **Efficient material transfer to the solvent of choice** (here: from ethanol to water). The resulting hybrid material was designed to be functional in water. Moreover, stability of the hybrid fibres in water and in ethanol differs, and hence, the purification procedure needs to be arranged in such a way that the majority of hybrid fibres is retrieved from ethanol and efficiently transferred to water.
- (3) **Preservation of both photochromic and plasmonic properties of the material.** Due to the non-covalent nature of interactions between all components purification procedure cannot compromise neither the stability nor the properties of hybrid fibres.

The chosen purification protocol relies on the centrifugation, due to the nature of the proposed material, which is a dispersion of a micrometre scale cellulose nanofibres covered with AuNRs and impregnated with Azo dye. In EtOH material forms clear and stable dispersion, hence, to separate the resulting plasmonic-photochromic CNFs from EtOH higher speeds and longer times (e.g. 7000g, 10-20 min) are required. Depending on the chosen separation parameters, the resulting supernatants may contain more or less material, and hence can also be subjected to prolonged centrifugation to increase material's retrieval rate. On the other hand, components of the separated hybrid materials are bound via electrostatic interactions, hence purification step (second centrifugation) requires lower speeds. Also, to not compromise the integrity of the materials and avoid their aggregation, the centrifugation times need to be adjusted. These aspects open a potentially endless cycle of consecutive centrifugations, separation and washing steps, and hence, the fundamental questions arise: when to stop and what factors limit this

cycle? Hence, parameters of purification protocol were thoroughly investigated for hybrids prepared using pre-composite containing ~4.8 wt% of Au and solution with 250-fold excess of AzoGly. Optical properties of each precipitate after its redispersion and any remaining supernatants were monitored using UV-Vis absorption spectroscopy. To ensure proper resolution in the spectral region of interest (around plasmon bands and 960 nm) 1 cm cuvette was used for all measurements.

After first, initial centrifugation, which serves as a necessary separation step (~540-1400g, 10-20 min), some percentage of the prepared hybrid material remains in the supernatant (**Figure 85a**, green line). To increase the efficiency of material's retrieval and not destabilize functional components, the follow-up centrifugation steps can be applied to supernatant and not the initial mixture. Such reattempted separations (~7000g, 10-20 min) can be performed up to three times to recover about 60% of the material that remained in the supernatant after initial separation (**Figure 85b**, assessed based on the intensity of the l-LSPR band of AuNRs). Hence, if necessary, material's retrieval rate can be conveniently increased. If AuNRs-CNFs or AzoGly-CNFs interactions are weakened in any way at this stage, the as-formed free species will be removed from the dispersion in the following washing steps.

Once all of the collected precipitates are combined and redispersed in water, at least one washing of the sample is necessary to remove any residues of AzoGly or ethanol or any species unbound from CNFs during separation step. As clearly visible in **Figure 85a**, if the baseline for the UV-Vis measurement is water and the measured solution is ethanol-based, the spectra include drop in the absorbance around 960 nm. Hence, it is possible to assess if there is any residual ethanol simply by observing spectra of the sample after every washing step in the region of this drop. Its presence confirms that there is not only EtOH remaining in the sample, but presumably also some unbound AzoGly, due to molecule's solubility. **Figure 85c** presents spectral region of interest for samples after separation and two washing steps. After separation (green line) drop at 960 nm is present, indicating that residual ethanol remains in the sample and hybrid fibres require at least one washing. After first washing (turquoise line, ~4850g, 10-20 min) the drop at 960 nm is no longer present. The same is true for the sample after second washing (navy line, ~4850g, 10-20 min). This proves, that if purification procedure is done with appropriate care, one washing step is enough to remove any remaining ethanol and free AzoGly. However, if necessary, the washing procedure can be repeated.

Thus, two steps of purification are recommended. The first one – separation of hybrid material from the impregnation mixture – can be repeated on the supernatant up to 3 times after initial centrifugation. The second one – washing of the combined precipitates if properly executed can be done only once. This means, that some portions of the material can be centrifuged up to even

5 times (separation, three follow-up centrifugations, and one washing) and hence, one more question requires addressing. Does any subsequent washing after the first one compromises the plasmonic-photochromic properties of the hybrid fibres? In order to assess that, the optical properties of the material after two, consecutive washing steps were compared. Spectra presented in **Figure 85d** were measured in the 1 cm cuvette, to provide appropriate measurement resolution. The observations are purely qualitative and despite the fact that the bands arising from the presence of AzoGly are either exceeding Y axis or ragged, measurement's conditions were maintained, since these characteristics (perceived often as spectral profile defects) are also very informative for this analysis. Profile of the sample after separation is dominated by free AzoGly remaining in the excess, due to the residual ethanol that is not removed yet. Concentration of the remaining photochrome is too high to be measured accurately, yet this proves that purification protocol cannot rely only on one separation step. Sample spectrum after first washing (turquoise line) is much better presented, yet the profile is ragged at the maximum of the $\pi \rightarrow \pi^*$ band. Nevertheless, the qualitative comparison of this spectrum (turquoise line) with spectrum of the sample after second washing (navy line) makes evident, that after second washing the $\pi \rightarrow \pi^*$ band of AzoGly is significantly damped. Hence, the elongation of the purification protocol by even one more washing step might be severely damaging for the photochromic properties of the material.

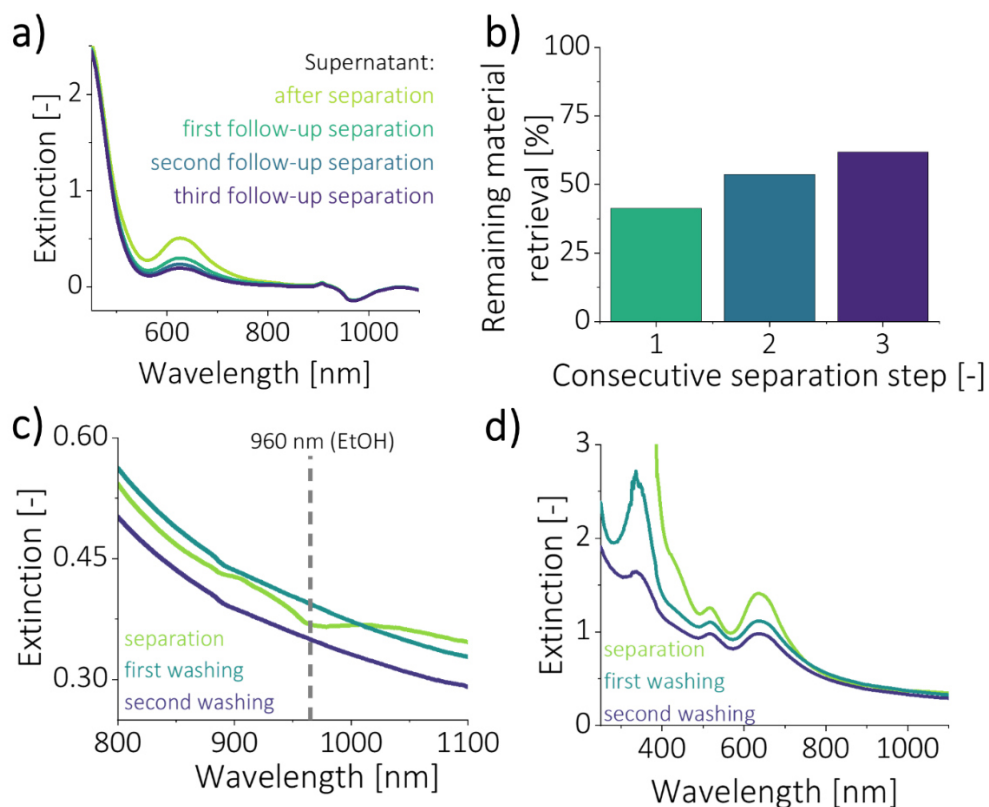


Figure 85. Spectroscopic evaluation of the hybrid material purification protocol. Applicable to all spectra: optical pathlength – 1 cm, baseline – water. **a)** UV-Vis spectra of supernatants

(ethanol) after the initial and follow-up separations via centrifugation. **b)** Retrieval of the hybrid material remaining in the first supernatant as a function of the number of follow-up centrifugation steps. **c)** Observation of spectral changes around 960 nm were the assessment method of choice to exclude presence of ethanol residues. **d)** Differences in the spectra of AzoGly-AuNRs-CNFs hybrid material after three consecutive washing steps.

Final procedure, summarizing necessary purification steps is presented in the **Figure 86**. To sum up, two purification steps are required: separation (enhanced if performed up to three times on the remaining supernatant) and washing of the combined precipitates. If performed with appropriate care, those steps yield a purified material, exhibiting well-established plasmonic and photochromic properties.

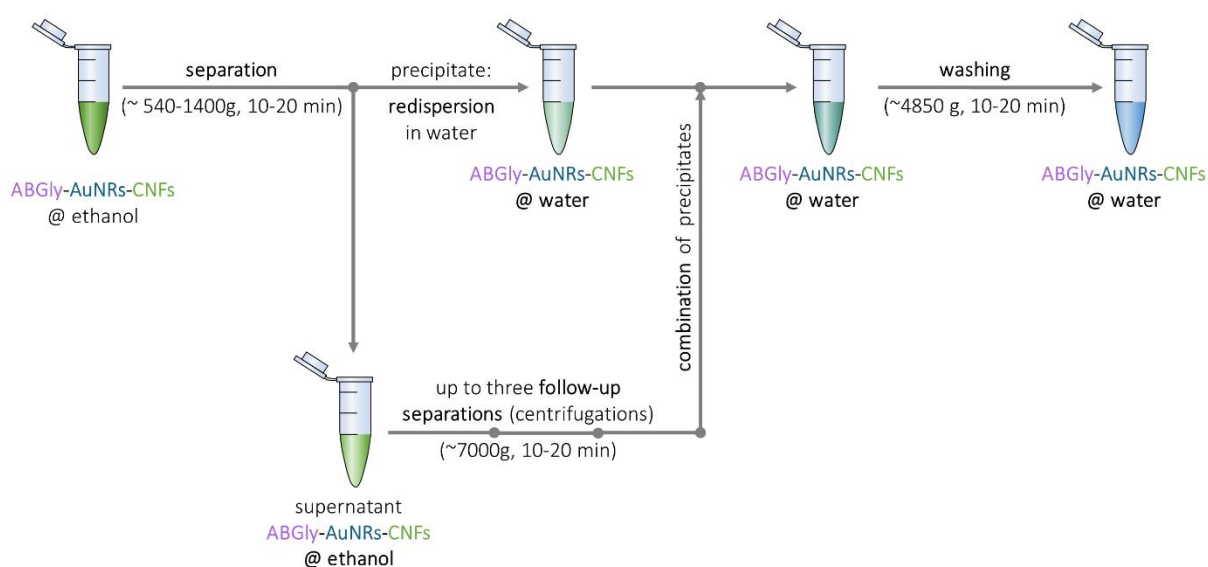


Figure 86. Schematic depiction summarizing optimized protocol of the AzoGly-AuNRs-CNFs hybrid materials purification.

Comment on additional aspects. In the course of the development of the presented plasmonic-photochromic material preparation protocol, also some other aspects were investigated. It was decided to sum them up in a short paragraph:

- (1) **Order of components mixing.** It was observed, that only the pre-composite addition to Azo solution efficiently yields functional materials.
- (2) **Strengthening of photochromic properties.** It is not possible to increase the content of AzoGly component in the final material after the already performed impregnation. The repeated attempt at impregnation does not strengthen the photochromic properties of the material and, at best, the functionality of hybrids remains the same. It might be motivated by the possible weakening of the interactions during the repeated purification protocol required after second impregnation attempt.

- (3) **Impregnation conditions.** It was found out that impregnation should be performed without mixture stirring. Otherwise, the spectral contribution of photochromic component is weakened.
- (4) **Influence of AuNRs loading.** For higher Au loadings (around 18 wt% of Au with respect to the mass of CNFs), the intensity of the $\pi \rightarrow \pi^*$ band of AzoGly is clearly lower. It can be attributed to the increased material's tendency to sedimentation and hence, more scattering nature, which results in the higher scaffold contribution to the optical properties below 600 nm (in the region of Azo photochromism).

Final hybrid plasmonic-photochromic material preparation protocol

Protocol no 5. AuNRs-CNFs pre-composite (~5.4 wt% Au with respect to the mass of CNFs) was centrifuged (780g, 5 min) and redispersed in ethanol. The resulting clear dispersion was subsequently added dropwise to the solution of AzoGly in ethanol under vigorous stirring. Concentration of the photochromic component was adjusted to ~3.1 mM (which corresponded to ~250-fold excess with respect to number of binding sites on Au). Mixture was stirred for 5 min and then left undisturbed for at least 17.5 hours at room temperature. On the next day, as-obtained hybrid photochromic-plasmonic composite was separated from ethanol via centrifugation (540-1400g, 10-15 min). The supernatants were subjected to three follow-up material separations (7000g, 10-20 min). The combined pellets were transferred to water and were subsequently washed once (4850g, 20 min) to remove any remaining ethanol and the unbound AzoGly excess. The as-prepared composite was subjected to visual inspection, UV-Vis-NIR characterization, and further in-depth investigation.

Similarly, to the results of preliminary experiments with AuNSs, AuNRs-decorated CNFs were accessible for AzoGly sorption during an overnight incubation step due to the EtOH pretreatment of the pre-composite. Trifluoroacetate counterion (TFA^-) of AzoGly salt does not remain in the hybrid material, due to the negative surface functionalization of CNFs. It can be rationally assumed that TFA^- is entirely removed from the system after hybrid material purification from any unbound species. AzoGly, however, remains in the material, due to interactions with CNFs, as concluded in the discussion presented in the previous subsections, and further fortified by the interpretation of the IR spectra of four different samples presented below. Liquid dispersions of pristine constituents were investigated, namely bare CNFs in water, AzoGly in EtOH, and **AuNRs-CNFs** pre-composite in water (**Figure 87**).

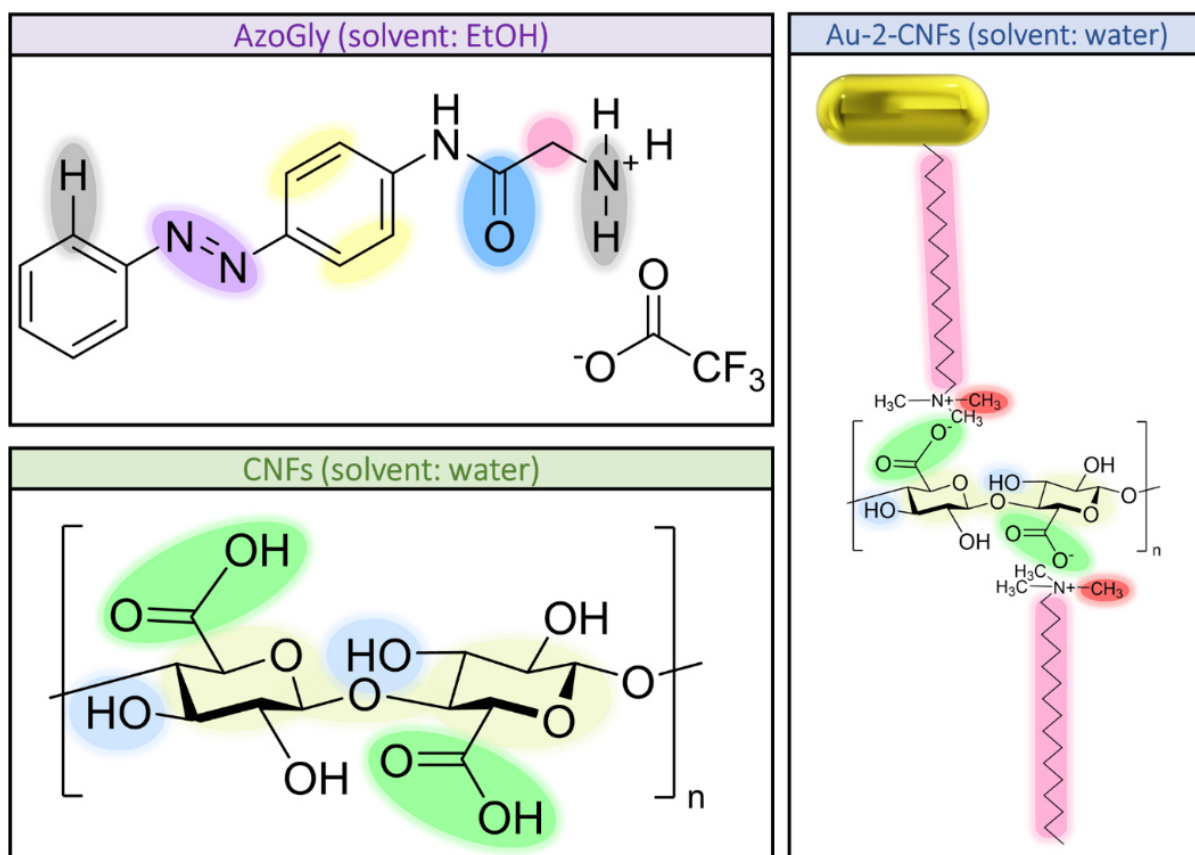


Figure 87. Chemical structures of the individual, pristine hybrid material components: AzoGly in a form of salt with TFA, CNFs, and the proposed structure of the AuNRs-CNFs pre-composite, for which two presumed forms of CTAB are indicated, namely bilayer on the surface of AuNRs, mediating Au-CNFs interactions, and free CTAB molecules interacting with CNFs (AuNRs are presented schematically, not to scale). Reprinted from own source preprint³⁸⁸.

IR spectrum of the water dispersion of hybrid **AzoGly-AuNRs-CNFs** material was juxtaposed with the spectra of pristine components to identify all crucial signals in **Figure 88**. Their summary is presented in **Table 2** below. Colour codes between **Figure 87** and **Figure 88** are matching.

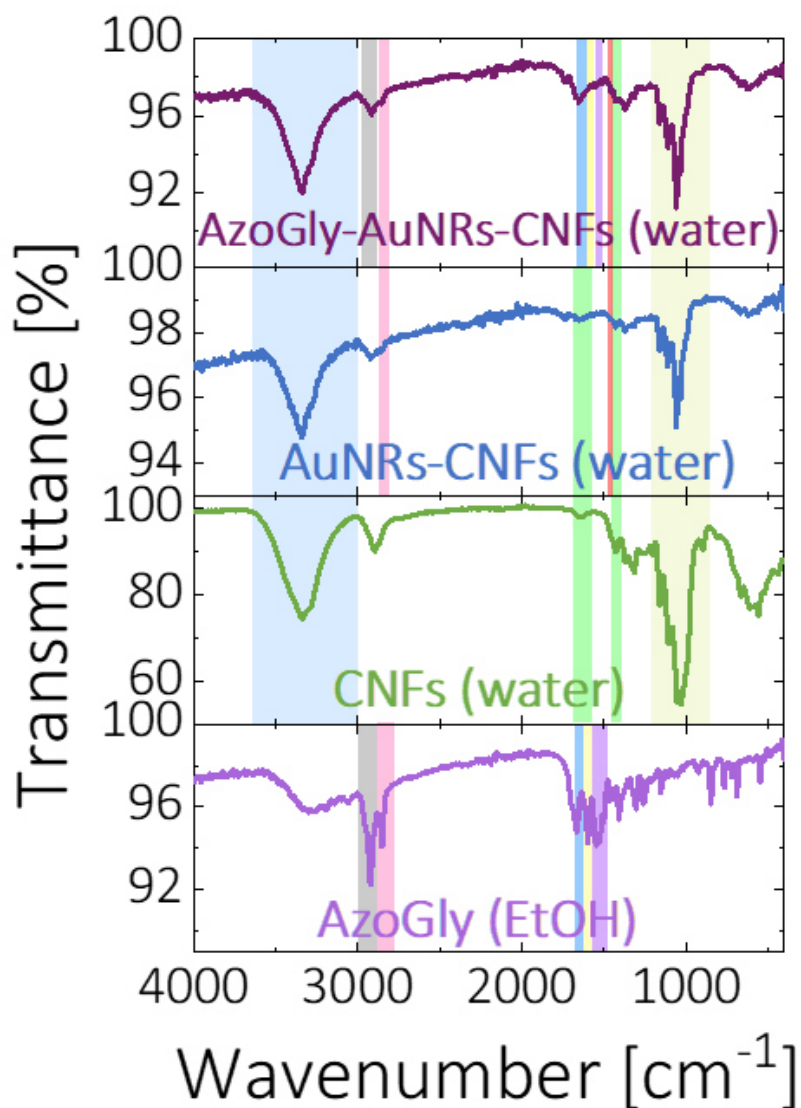


Figure 88. IR spectra of pristine hybrid material components, namely AzoGly, CNFs, and pre-composite, compared with the IR spectrum of the final hybrid-material, AzoGly-AuNRs-CNFs. Comparison reveals importance of the underlying interactions for material's structural integrity. Reprinted from own source preprint ³⁸⁸.

Table 2. Summary of the relevant IR signals identified in the Figure 88. The following abbreviations are used: ν – stretching vibration, ν_{as} – asymmetrical and ν_s – symmetrical vibration, γ – out of plane and δ – in-plane deformation vibration. Table reprinted from own source preprint³⁸⁸.

Signal	Band position [cm ⁻¹]			
	AzoGly (@EtOH)	CNFs (@water)	AuNRs-CNFs (@water)	AzoGly-AuNRs-CNFs (@water)
CNFs identification				
$O - H$ (ν)	3000-3500 (center: 3300, weak, round)	3000-3500 (center: 3338)	3000-3500 (center: 3344)	3000-3500 (center: 3342)
$-COO^-$ (ν_{as})	1699 (trifluoroacetate)	1641	1653 (weak)	part of 1653 (broad)
$-COO^-$ (ν_s)	1409 (trifluoroacetate)	1427	1429	1419
$C - C$ ring (ν)	-	1159	1161	1161
$C - O - C$ pyranose ring (ν_s)	-	850-1200 (center: 1032)	850-1200 (center: 1059)	850-1200 (center: 1059)
$C - O - C$ β -glycosidic linkages	-	899	910 (weak)	905 (weak)
$O - H$ (γ)	-	663	667 (weak)	667 (weak)
$O - H$ bending of the absorbed water	-	1641	1653 (weak)	part of 1653 (broad)
CTAB identification				
$C - H$ (ν_s)	2852	-	2858 (weak)	2854 (weak)
$C - H$ (ν_{as})	-	2897	2922	2918
$-CH_3$ (ν) of ammonium salt	-	-	1456 (weak, part of 1429)	1456 (weak, part of 1419)
$C - N$ (ν , weak, shoulder)	-	-	906 (very weak)	906 (very weak)
AzoGly identification				
$N = N$ (ν)	1545	-	-	1541 (part of 1653)
$C = C$ (ν) in plane	1599	-	-	1558 (part of 1653)
$C = O$ (ν)	1666	-	-	1653
$-N - H$ (ν) amine salt (strong) and $=C - H$ (ν , medium)	2924	-	2922	2918
$=C - H$ (γ)	768	-	-	758

Identification of several peaks in the **AzoGly-AuNRs-CNFs** hybrid material confirmed its structural integrity and presence of all components. Presence of CNFs was confirmed by signals marked with pale yellow appearing at 1161 cm^{-1} , 1059 cm^{-1} , and 905 cm^{-1} for $C - C$ cellulose ring stretching, $C - O - C$ cellulose pyranose ring stretching, and $C - O - C$ cellulose β -glycosidic linkages, respectively. Presence of the photochromic component (AzoGly) in the hybrid formulation was confirmed by bands occurring as a part of the broad 1653 cm^{-1} peak. The $N = N$ moiety (pale purple), $-C = O$ amide signal (vivid green), and $C = C$ in-plane deformation signal (bright yellow) were identified.

Moreover, comparative IR spectra analysis was used to verify two main hypotheses regarding final material formulation. The first one assumes importance of intermolecular AzoGly-CNFs interactions, mainly electrostatic attraction of the components. The coherent $6\text{-}10\text{ cm}^{-1}$ spectral shifts at the IR spectra observed for the chemical groups involved in the interactions corroborate this hypothesis. At 2924 cm^{-1} the $-N - H$ stretching signal of $-NH_3^+$ AzoGly end group appears for free photochromic molecules (grey highlight). This signal is shifted to 2918 cm^{-1} in the hybrid material. Similar spectral shift is observed for the $-COO^-$ symmetrical vibration band of CNFs (vivid green highlight) and the original peak shifts from 1429 cm^{-1} (as identified for the pre-composite) to 1419 cm^{-1} in the hybrid formulation. Moreover, the initial position of the $O - H$ stretching band of CNFs in the pre-composite (highlighted with a pale blue colour), centered at 3344 cm^{-1} is slightly shifted towards lower wavenumbers in the **AzoGly-AuNRs-CNFs** material, where this peak appears at 3342 cm^{-1} . Based on the literature data, this suggests the formation of hydrogen bonds between the available hydroxyl groups of CNFs scaffold and chosen photochromic molecule, AzoGly.^{412,413}

The second hypothesis concerns potential presence and role of CTAB in the final formulation. As already discussed, CTAB assures immobilization of AuNPs on CNFs upon pre-composite preparation. Hence, CTAB presence was determined based on the identification of $C - H$ symmetric stretching band of $-CH_2 -$ group (blush highlight) when bare CNFs and pre-composite IR spectra were compared. For bare CNFs no CTAB was present and hence, no peak was observed, while for the **AuNRs-CNFs** CTAB presence was confirmed by a peak at 2858 cm^{-1} . Upon material pretreatment with EtOH, it can be assumed that CTAB molecular assemblies such as bilayer on the AuNRs surface or micelles interacting with CNFs are disassembled. However, the unexpected stability of the AuNRs upon such solvent transfer (see **Figure 84**) can be explained simultaneously by two effects. One of them is passivation of AuNRs surface with CNFs. The other is the possibility that CTAB mediating AuNRs-CNFs interactions remains in-between AuNRs and CNFs even in EtOH, when other assemblies are

destroyed. Here, the strength of CTAB-CNFs interactions described in the literature,^{414,415} as well as the stabilizing van der Waals forces between hydrophobic CTAB tails within surfactant bilayer⁴¹⁶ are taken into account. The IR spectra analysis of the **AzoGly-AuNRs-CNFs** sample enabled verification of this hypothesis. However, the signal of $-CH_2-$ group could not be used to probe surfactant presence, because AzoGly also contributes to this very signal and another spectral band needed to be selected. Hence, the evolution of two bands was analysed, namely 1456 cm^{-1} (vivid red highlight) of the $-CH_3$ group of ammonium salt (**Figure 89**) and 906 cm^{-1} (very weak shoulder of the β -glycosidic band) of $-C-N^+$ stretching. Both bands were present in the IR spectra of the hybrid material, hence confirming presence of residual CTAB in the final formulation. It needs to be emphasised, that due to several steps of washing and centrifugation during the composite purification procedure, the surfactant cannot simply be present in the solution in a form of free molecules. Hence, it is reasonable to assume surfactant intercalation in hybrids either **(1)** as a residual bilayer exhibiting lower integrity, but nevertheless mediating interactions between AuNRs and CNFs, or **(2)** solely on the surface of CNFs. Thus, role of CTAB as molecular glue in the plasmonic-photochromic formulation was confirmed.

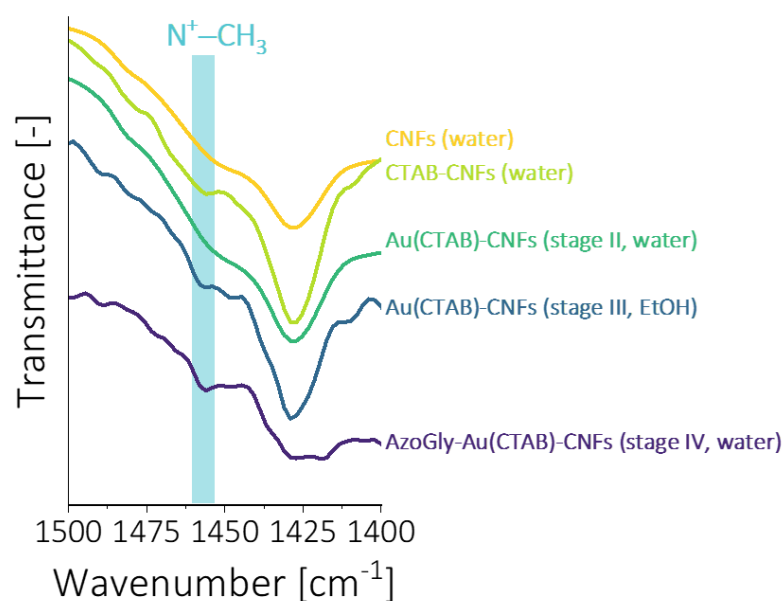


Figure 89. Evolution of the presence of $N^+ - CH_3$ stretching band on IR spectra probed throughout the whole preparation protocol, namely for AuNRs pre-composite before and after solvent transfer (stage II and III, respectively) and for the final hybrid formulation (stage IV). Spectra of bare CNFs and CNFs with the adsorbed CTAB are presented for comparison. Reprinted from own source preprint³⁸⁸.

All of the fundamental interactions crucial for **AzoGly-AuNRs-CNFs** material formation and its stability in water, derived from results presented above, are presented in **Figure 90a**.

Homogenous material structure without aggregation of the AzoGly component is presented in **Figure 90b**. Typically, water-insoluble photochromes transferred on nanocellulose platform, aggregate in the aqueous environment.⁴¹⁷ Yet, the formulation presented here does not contain any AzoGly aggregates. The proposed protocol enables uniform impregnation of CNFs, thus assuring homogeneity of the composite.

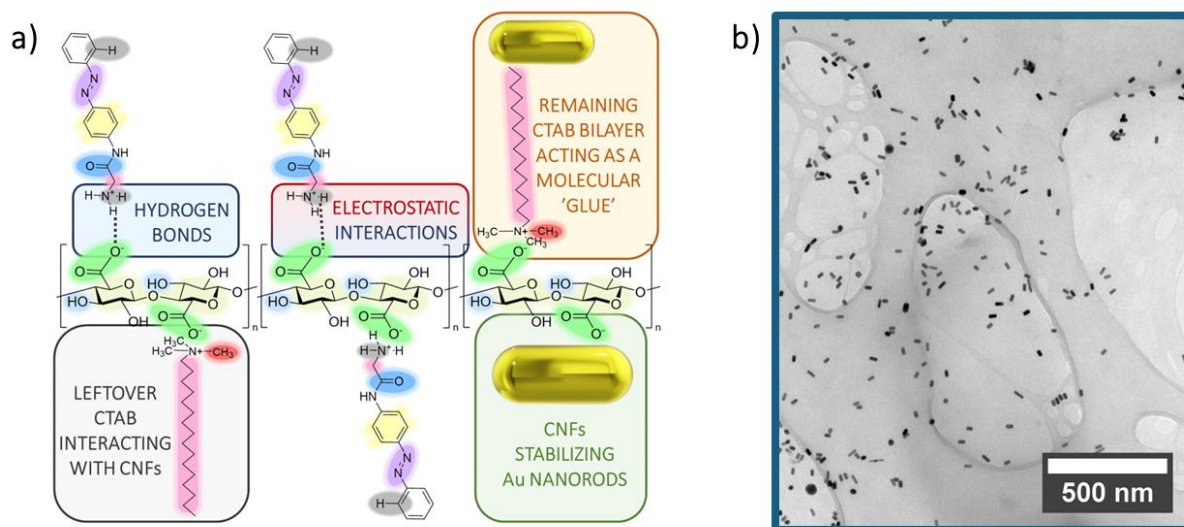


Figure 90. AzoGly-AuNRs-CNFs, a plasmonic-photochromic hybrid material. **a)** The proposed chemical structure emphasising the underlying interactions. **b)** TEM image of the hybrid sample. Reprinted from own source preprint³⁸⁸.

CNFs scaffold ensured system's stability, and thus, the hybrid material maintained its dual plasmonic-photochromic functionality, as depicted in the UV-Vis-NIR absorption spectra of the sample (**Figure 91a**, **hypothesis 3**). Contributions of both functional components were distinctly visible. The intensities of both photochromic bands in aqueous environment undoubtedly confirmed the success of the proposed material design. The small shifts in the bands positions compared to pristine AzoGly could be attributed to the interactions with the scaffold⁴¹⁷ and solvent change.^{300,418} t-LSPR and l-LSPR bands of AuNRs were also very distinct and well separated from the optical contributions of the photochrome. Moreover, plasmon bands were not distorted and only slight spectral shifts were observed (**Figure 91b**), presumably due to the change in the effective refractive index after removal of most of the CTAB from the surface of AuNRs.

Hybrid material exhibited stable photoswitching upon exposure to UV (365 nm) and Vis (436 nm) irradiation (**Figure 91c**, **hypothesis 4**). Photoswitching is stable over many cycles and can be repeatedly induced. Importantly, the intensity of the $\pi \rightarrow \pi^*$ band in the respective photostationary states, was very stable upon the interval irradiation. Hence, it can be concluded, that there is no degradation of photochromic component or material as a whole. Most

importantly, however, the optical characteristics of **AzoGly-AuNRs-CNFs** hybrid formulation have crucial implications in the context of challenges in the field of plasmonic-photochromic materials, particularly for plasmon-assisted Azo isomerization. As depicted in **Figure 91a**, three different spectral regions of the sample can be distinguished. First region (1) covers both of the absorption bands of the photochromic component. This spectral range can be utilized to directly address photoswitching of the photochrome. This aspect will be investigated in Chapter 5. Second spectral region (2) corresponds with the t-LSPR band of AuNRs. However, due to the partial overlap with the $n \rightarrow \pi^*$ band of the photochrome, this region cannot be used in the plasmon-assisted experiments. Such spectral overlapping complicates the assessment of the phenomenon responsible for the photocontrol of the monitored reaction. The third spectral region (3), which covers the l-LSPR band of AuNRs is far enough from region 2 to be the most suitable to investigate plasmon-assisted photochromism. Irradiation in this spectral window enables triggering of plasmon-related phenomena, which potentially grants an indirect control over Azo isomerization, as described in Chapter 6. Hence, the benefit of the proposed formulation containing both AuNRs and Azo molecules is entirely manifested.

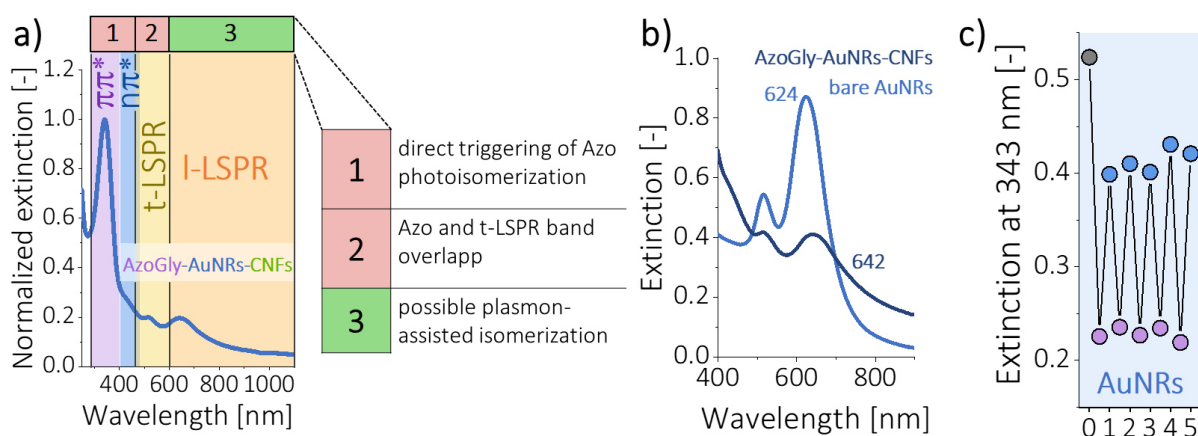


Figure 91. Functional AzoGly-AuNRs-CNFs formulation. **a)** UV-Vis-NIR spectrum of the sample, depicting three important spectral regions of the sample. **b)** Depiction of the spectral changes in the position of l-LSPR band in the final sample vs. bare AuNRs (18 nm redshift). **c)** Distinct and stable photoswitching of the photochromic component in the hybrid formulation upon interval UV (3 min) and Vis (3 min) irradiation. Purple and blue points indicate $\pi \rightarrow \pi^*$ band intensity at PSS_Z and PSS_E , respectively. Reprinted from own source preprint³⁸⁸.

Finally, the chapter is concluded with an important control experiment in which for the same pre-composite material the established preparation protocol no 5 was performed to test impregnation with traditional sulphur-containing ligands, namely **AzoSH** (dissolved in THF) and **AzoSS** (dissolved in EtOH). Since it can be assumed, that CTAB is removed from most of the AuNRs surface after EtOH pre-treatment, gold becomes accessible for Au-S interactions.

Nevertheless, the theoretical synergy between AuNRs and the sulphur-containing ligands did not grant satisfactory results and material properties were compromised (**Figure 92**). Composites were heavily aggregated and did not exhibit neither photochromic nor plasmonic properties. Moreover, materials did not disperse well in water in contrary to hybrids prepared with AzoGly. Hence, the proposed protocol, relying on use of charged Azo derivative constitutes an important contribution to the field.

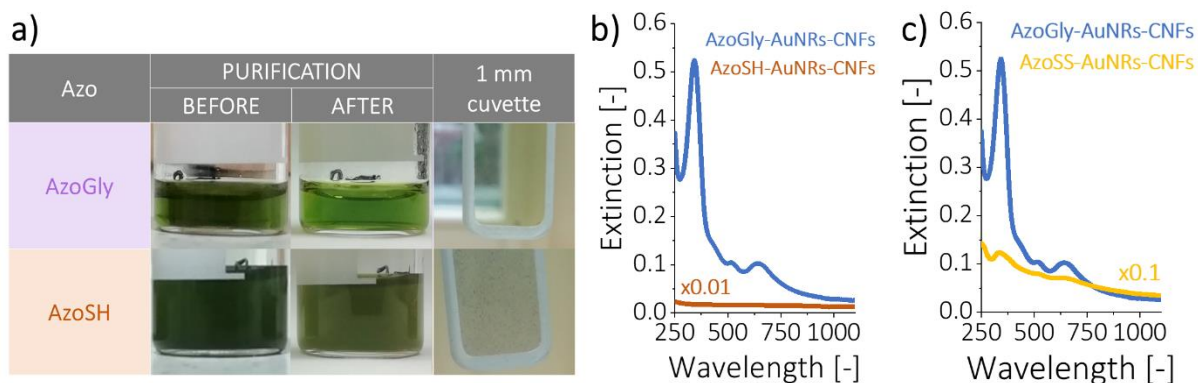


Figure 92. a) Visual comparison of the hybrid samples prepared using different Azo ligands. Aggregates of the composite prepared with AzoSH are clearly visible in the “1 mm cuvette” column. Internal width of the cuvette is 10 mm. Spectral differences between samples impregnated with AzoGly vs. b) AzoSH and c) AzoSS are also depicted. Due to the highly scattering nature of the samples prepared with sulphur-containing ligands, the extinction profiles were multiplied by 0.01 and 0.1, respectively. Reprinted from own source preprint³⁸⁸.

4.4. Conclusions

This chapter establishes general protocol for the preparation of multifunctional, hybrid plasmonic-photochromic material based on cellulose-stabilized AuNRs and model azobenzene-type photochrome (**objective 2**). Results presented here address current challenges in the field of plasmonic-photochromic hybrids, and hence, the established protocol enables preparation of water-functional composite, operating without aggregation, and prepared with use of non-thiolated Azo ligand able to interact with CNFs scaffold.

Based on the results and analysis presented above, a schematic depiction of the proposed preparation protocol is demonstrated in **Figure 93**. This depiction summarizes all of the crucial protocol steps and underlying components interactions at the foundation of the efficient impregnation of scaffold with the chosen photochromic dye, mainly electrostatic attraction and hydrogen bonds formation between AzoGly and CNFs. Moreover, the presence of CTAB as a molecular glue grants material with great structural integrity, without aggregation of the

components (**hypothesis 3**). Material exhibits well-defined optical characteristics and preserved plasmonic and photochromic features. Plasmon band of the immobilized AuNRs remains unchanged and the photochromic AzoGly component exhibits stable and distinct photoswitching upon UV-Vis irradiation over many cycles (**hypothesis 4**). Beneficial spectral separation of the optical properties of Azo and AuNRs can be used to potentially perform plasmon-assisted isomerization of the photochrome, which will be investigated in the following chapters.

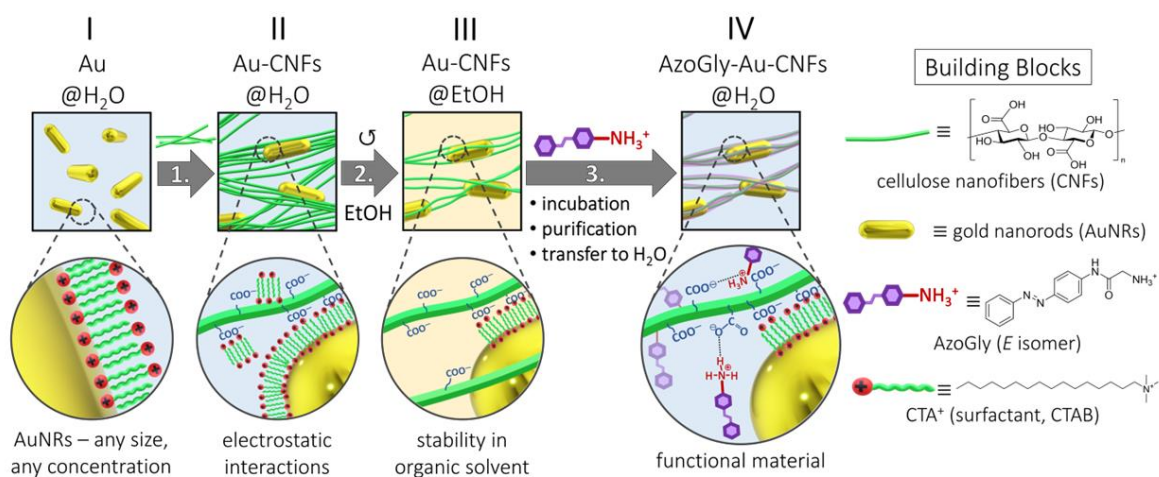


Figure 93. Preparation of AzoGly-AuNRs-CNFs hybrid material and the depiction of the fundamental interactions between components. Reprinted from own source preprint³⁸⁸.

Chapter 5. *Catalytic Influence of Gold Nanorods on Azobenzene Isomerization*

This chapter describes *E-Z* and *Z-E* isomerization reactions of the photochromic component (chosen model AzoGly molecule) in the hybrid Azo-AuNRs-CNFs plasmonic-photochromic formulation. First, photoisomerization reactions triggered directly by UV (365 nm) and Vis (436 nm) irradiation are investigated. Subsequently, chapter focuses on thermal relaxations (*Z-E* isomerization) of the photochromic component in the dark. A set of thermodynamic and kinetic parameters of the reaction is determined for hybrid materials and compared with pristine free AzoGly. Catalytic influence of AuNRs is investigated by comparing the ongoing isomerization reactions for composites with and without Au. Moreover, influence of AuNRs aspect ratio on the reactions is explored. Hence, the results presented here challenge Objective 3 and verify hypotheses 5 and 6 of the dissertation.

Objective 3: To investigate the mutual interactions of plasmonic and photochromic components and the kinetics of azobenzene photoswitching in the dark and upon UV-Vis irradiation in the presence of AuNRs.

Hypothesis 5: AuNRs catalyse Azo photoswitching via the electron transfer mechanism, both in the dark and under illumination.

Hypothesis 6: The catalytic effect of AuNRs is size-dependent.

Part of the results presented within this chapter is available as a preprint:
³⁸⁸ N. Tarnowicz-Staniak, M. Staniak, M. Dudek, M. Grzelczak, K. Matczyszyn, *Gold Nanorods Grant an ON-OFF Control over the Kinetics of the Z-E Isomerization of Azobenzene-Based Photoswitch via Thermoplasmonic Effect*, preprint ChemRxiv **2024**, <https://doi.org/10.26434/chemrxiv-2024-vnj32>.

5.1. Motivation

Isomerization of the photochromes remains extensively investigated and for azobenzene derivatives research attention focused on their photoswitching has not stopped since 1937.²⁹⁰ It is mostly motivated by a broad range of applications of Azo molecules, including photoactuators,⁴¹⁹ molecular electronics,⁴²⁰ chemical biology,^{421,422} and catalysis,⁴²³ to name a few.²⁸² Also multicomponent systems employing Azo compounds to harness their collective photoactivity became broadly investigated,^{277,424,425} because presence of the adjacent chemical species can influence the photoswitching of Azo photochromes.^{339,426,427}

Although catalytic properties of AuNPs are well known, as described in Chapter 2, and the Azo-AuNPs hybrids have been extensively explored, as presented in Table 1 (Chapter 2), the catalytic influence of Au nanostructures on the photoinduced Azo isomerization remains virtually unexplored. In fact, for some of the presented formulations, the photoswitching of photochromic component might be even hindered.³⁵⁰ This is why structures of Azo ligands used for the preparation of hybrids typically include linkers, enabling more efficient photoswitching of the photochromic component.³⁴⁰ Nevertheless, since azobenzene is a T-type photochrome, AuNPs have been acknowledged as modulators of Azo thermal relaxations or – in other words – Azo *Z-E* isomerization in the dark.^{428,429}

The mechanism of Azo *Z-E* thermal relaxation in the presence of AuNPs via electron transfer (eT) was first proposed by Hallett-Tapley *et al.*³⁵² Authors presented AuNPs-mediated modulation of the Azo *Z-E* isomerization kinetics without prior anchoring of the photochromic molecules to the surface of AuNPs. Spherical (~12 nm in diameter), pseudo-naked nanostructures were prepared via laser ablation and authors postulated two separate electron transfers occurring during Azo *Z-E* isomerization in the dark. The first eT occurs from the Azo molecule in its *cis* form to the Au nanostructure and, as a result, Azo radical cation intermediate is formed. Subsequently, the intermediate undergoes rotation about the $N - N^+$ bond, followed by the second eT from the surface of AuNP back to the Azo molecule. Hence, the rotational mechanism of Azo isomerization is also supported. This sequence is mirrored in the increasing first order rate constant of the Azo *Z-E* isomerization in the presence of Au nanostructures (**Figure 94**). Authors investigated isomerization of four different 4- and 4,4'-substituted Azo molecules and found that their molecular dipole moment was more determining for the catalytic increase of the rate constant than the electron nature of substituents. Experiments were carried out in the organic solvents native for Azo molecules and the main identified hindrance was the drastically varying catalytic activity of the AuNPs batches, which is typical for AuNPs prepared via laser ablation. Catalytic activity of such

nanostructures is typically dictated by their surface chemistry, age, and homogeneity of the applied laser beam.^{430,431}

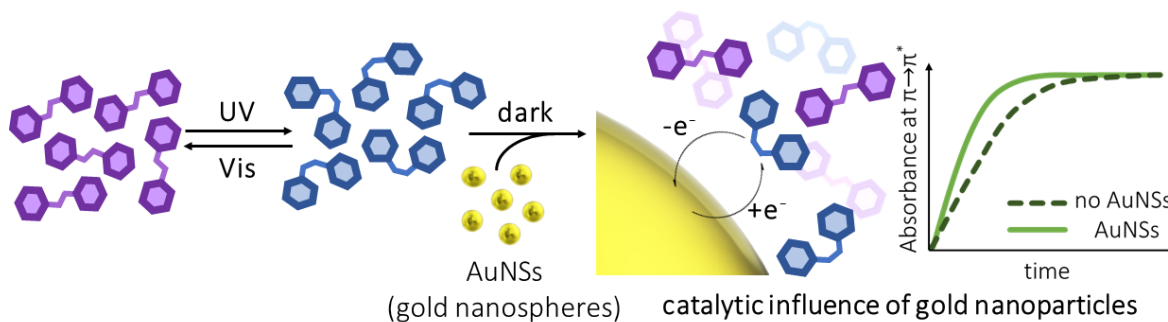


Figure 94. Schematic depiction of the typical research scenario for the investigation of catalytic influence of AuNPs on Azo thermal Z-E isomerization. Purple structures represent E-Azo and blue structures represent Z-Azo.

The electron transfer mechanism was confirmed in experimental and theoretical studies carried out by Titov *et al.*⁴³² Authors investigated influence of bare AuNPs prepared via laser ablation (~10 nm in diameter) on different Azo derivatives, including also molecules with positively charged substituents, thus exhibiting structural similarity to surfactants used in the synthesis of AuNPs, such as CTAB. Authors suggested fitting of the experimental data with multiexponential fit and proposed determination of two Z-Azo lifetimes, related to different populations of molecules. One (shorter) isomerization lifetime was related to molecules experiencing catalytic effect of AuNPs, and the other (longer) to those unaffected by the presence of gold, due to the distance between both species. However, each population still exhibited first order kinetics. Similar experimental results and conclusions were also presented by authors in another publication.³⁴³ Such fittings were possible for all of the investigated Azo molecules, despite their different affinities towards Au surface. Although such an approach is mathematically possible, it might be questioned from the theoretical point of view. Nonetheless, authors also provided theoretical calculations confirming that both electron acceptance by and withdrawal from Azo molecule lead to the reduction of isomerization activation energy compared to isomerization of neutral Azo species (**Figure 95**). Ultimately, it was found that the Azo cation formation energy on Au surface is smaller than anion formation energy, and hence conclusions of Hallett-Tapley *et al.* were supported.

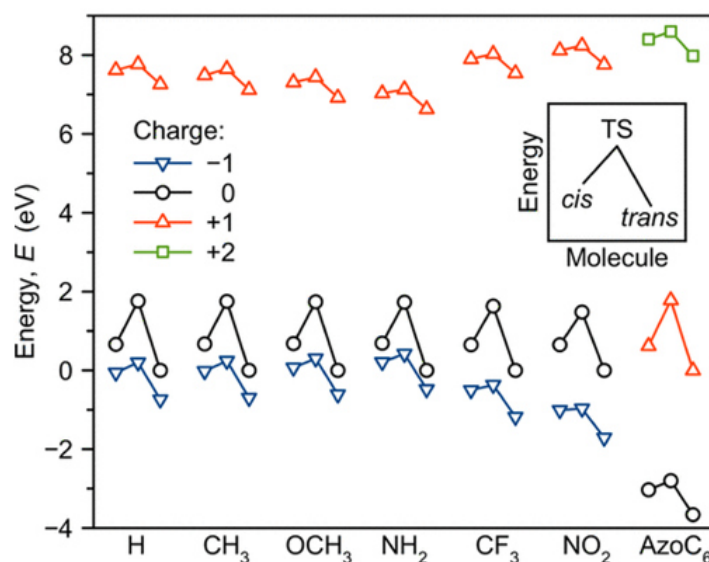


Figure 95. Energies of the transition states (TS), Z-, and E-Azo isomers of 4-R-Azo molecules (different substituents, R, are labelled on the X axis), recalculated relatively to the energy value for E-Azo in the reference state. Reprinted from ⁴³².

Moreover, as found out by Simoncelli *et al.* Z-E isomerization of Azo in the presence of AuNPs exhibits a predominantly surface catalytic character.⁴³³ Authors investigated influence of 15 nm AuNSs coated with poly(vinyl pyrrolidone) (PVP) on thermal Z-E isomerization of nine 4- and 4,4'-substituted Azo derivatives in acetonitrile:water mixtures (5:1, v/v) and compared the results with those obtained for citrate-capped AuNSs of the same size. Citrate binds strongly to {111} crystallographic facets, while PVP to {100} facets and the latter were found to be more reactive. Moreover, by using SiO₂-coated AuNSs (with varying silica shell thickness), authors determined that process is diffusion controlled. Importantly, all of the relaxations exhibited first order kinetics and for some of the investigated photochromes the catalytic acceleration in the presence of AuNPs was even by 2 up to 4 orders of magnitude using citrate-stabilized AuNSs.

A common denominator for these examples is utilization of small, spherical AuNPs. Moreover, in all experiments the conditions did not reflect real material conditions for typically prepared Azo-AuNPs hybrids. Shape-limitation of plasmonic cores is understandable due to the certain aggregation of bigger and anisotropic nanostructures in the presence of Azo, especially in organic solvents. Nonetheless, by using small, isotropic nanoparticles exhibiting limited light-harvesting properties, studies became restricted to the exclusive investigation of Azo dark (thermal) Z-E isomerization. This chapter addresses investigation of mutual AuNPs-Azo interactions and the kinetics of Azo photoswitching in the presence of AuNRs both upon UV-Vis irradiation and in the dark for real, macroscopic hybrid materials (**objective 3**). In the formulation central for the dissertation AuNRs are used instead of AuNSs, nevertheless it can

be hypothesised, that this geometry of nanoparticles can also catalyse the Azo photoswitching by the same mechanism of eT (**hypothesis 5**). Moreover, this chapter verifies the postulate of aspect-ratio-dependent catalytic influence of AuNRs on AzoGly isomerization (**hypothesis 6**).

5.2. Materials and methods

5.2.1. Materials and techniques

Materials

Chemicals used for the experiments were commercially available and did not require purification. In all experiments deionized water with the resistivity of 18.2 M Ω ·cm (Millipore Milli-Q grade) was used. If not indicated otherwise, chemicals were purchased from Sigma-Aldrich. For the synthesis of AuNRs the following reagents were used:

- metallic precursor: gold(III) chloride trihydrate (HAuCl₄·3H₂O),
- surface stabilizing agent: cetyltrimethylammonium bromide (CTAB),
- reducing agents: sodium borohydride (NaBH₄), L-ascorbic acid (AA), hydroquinone (HQ),
- other additives: silver nitrate (AgNO₃), and hydrochloric acid (HCl, 37%, Scharlab).

Support for nanoparticles: TEMPO-oxidized cellulose nanofibres (CNFs) supplied by CelluForce (Canada).

Photochromic component: AzoGly molecule provided by Dr Marta Dudek (Faculty of Chemistry, Wrocław University of Science and Technology) – see **Figure 77**.

Techniques

UV–Vis–NIR extinction spectra measurements were performed using JASCO V-730 spectrophotometer equipped with Peltier UV-Vis cuvette holder. Transmission electron microscopy (TEM) images were acquired using Hitachi H-800 microscope. For the irradiation experiments the Hamamatsu L9588 LightningCure LC8 spot light source was used. The exact wavelengths were selected using bandpass filters. Irradiation intensities were measured with Thorlabs S425C Thermal Power Sensor and Thorlabs PM100D Compact Power and Energy Meter Controller.

5.2.2. Hybrid materials preparation

AuNRs synthesis

Three separate batches of AuNRs were prepared, **AuNRs-1**, **AuNRs-2**, and **AuNRs-3** (also labelled further in the text as **Au-1**, **Au-2**, and **Au-3**) according to the following protocol.⁴⁰⁰

In the first step seeds were prepared by reducing gold precursor, HAuCl₄ (0.25 mL, 0.010 M) in aqueous solution of CTAB (9.75 mL, 0.10 M) with ice-cold NaBH₄ (0.6 mL, 0.010 M) added under vigorous stirring. The mixture was left for 10 min under mild stirring and subsequently for 2 h at 27°C (unstirred) to assure seed formation and reducing agent decomposition. Optical characteristics and visual appearance of the seeds were matching the data presented in **Figure 48** (subsection 3.2.2. of Chapter 3) and hence are not repeated here.

In the second step, for **Au-1** and **Au-2** samples, Ag-assisted seeds overgrowth was performed in the solution containing HAuCl₄ (0.5 mL, 0.010 M), CTAB (8 mL, 0.1 M), HCl (0.2 mL, 1.0 M), AgNO₃ (0.030 mL and 0.075 mL, 0.010 M for batches **Au-1** and **Au-2**, respectively), and AA (0.08 mL, 0.1 M) upon the addition of Au seed solution (2.0 mL). For **Au-3** to the solution containing HAuCl₄ (0.5 mL, 0.010 M), CTAB (9 mL, 0.1 M), AgNO₃ (0.045 mL, 0.033 M), and HQ (0.5 mL, 0.1 M), a seed solution (1.0 mL) was added. All growth solutions were left undisturbed for at least 16–20 h at 27°C. As-prepared nanostructures were purified on the next day via centrifugation at 16 000g for 35 min. The supernatant was subjected to the second centrifugation step. Pellets from both steps were combined and redispersed in water. Final concentration of metallic gold was 0.0007 M.

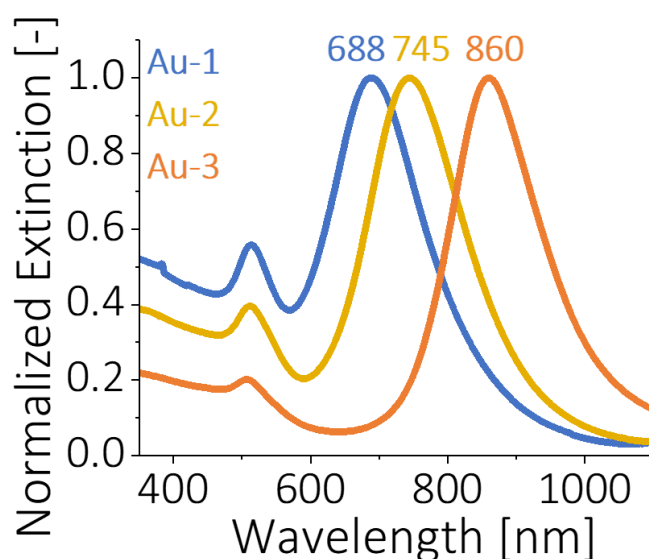


Figure 96. UV-Vis extinction spectra of the as-prepared AuNRs samples. Colour codes are matching with Figure 97.

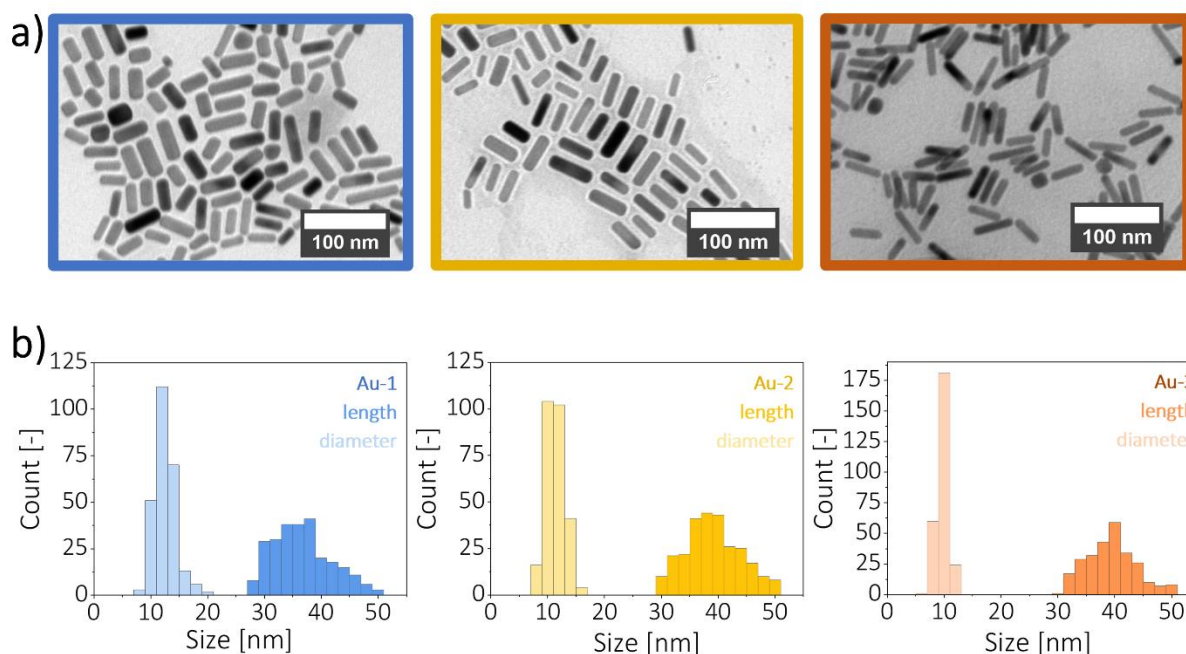


Figure 97. a) Representative TEM images and b) histograms of the AuNRs samples. The average sizes of the AuNRs were as follows: **Au-1** average length: 36.6 ± 5.1 nm, average diameter: 12.4 ± 2.0 nm, number of nanoparticles measured $N = 257$, aspect ratio $AR = 2.95$; **Au-2** average length: 39.1 ± 4.9 nm, average diameter: 11.4 ± 1.7 nm, number of nanoparticles measured $N = 267$, aspect ratio $AR = 3.43$; and **Au-3** average length: 39.3 ± 4.3 nm, average diameter: 9.75 ± 1.1 nm, number of nanoparticles measured $N = 268$, aspect ratio $AR = 4.03$.

AzoGly-AuNRs-CNFs composites preparation

Pre-composites preparation. Dispersions of AuNRs were washed twice with water (16 000 g, 30 min for **Au-1** to **Au-3**) and redispersed in 1 mM CTAB. Subsequently, AuNRs were titrated with aqueous CNFs solution (0.5 wt%) at room temperature and under vigorous stirring (AuNRs/CNFs = 2:1, v/v). The resulting materials contained ~3.9 wt% of Au with respect to the mass of CNFs. Pre-composites were left until the next day to promote materials sedimentation. On the next day the collected pellets were centrifuged twice (540 g, 5 min) and redispersed in water.

Pre-composites impregnation with AzoGly. Pre-composites were centrifuged (780 g, 5 min) and redispersed in ethanol. The as-obtained clear dispersions were subsequently added dropwise to the solution of AzoGly in ethanol under vigorous stirring. The concentration of the photochromic component was adjusted to ~3.1 mM for all samples, hence granting about 200-fold Azo excess per binding site on Au for each AuNRs batch. Mixtures were stirred for 5 min and then left undisturbed for at least 17.5 hours at room temperature. On the next day impregnated composites were centrifuged in a few step procedure. First, separation from ethanol via centrifugation was performed (540-1400g, 10-15 min). Subsequently, supernatants

were subjected to three follow-up separations (7000g, 10-20 min each). All of the combined pellets (for each sample) were transferred to water and washed once (4850g, 20 min). The resulting composites were subjected to visual inspection, UV–Vis–NIR characterization (**Figure 98a**), and further in-depth investigation.

Control AzoGly-CNFs composites without Au. To prepare composites without AuNRs, 1 mM CTAB solution was titrated with the aqueous CNFs solution (0.5 wt%) under vigorous stirring and at room temperature (CTAB/CNFs = 2:1, v/v). The as-prepared pre-composite sample was left until the next day to promote sedimentation of the fibres. Pre-composite was centrifuged twice (540 g, 5 min) and redispersed in water to remove the excess CTAB. Subsequently, pre-composite pretreatment with EtOH was performed (centrifugation, 780 g, 5 min followed by material redispersion in EtOH). Next, the pretreated material was added dropwise to the solution of AzoGly in ethanol (~3.1 mM) under vigorous stirring. Mixture was stirred for 5 min and then left at room temperature, undisturbed for at least 17.5 hours. On the next day mixture was purified via centrifugation in a few step procedure. First, separation from ethanol via centrifugation was performed (540-1400g, 10-15 min). Subsequently, supernatant was subjected to three follow-up separations (7000g, 10-20 min each). All of the combined pellets were transferred to water and washed once (4850g, 20 min). The resulting control composite (**Figure 98b**) was redispersed in water and used in all control experiments.

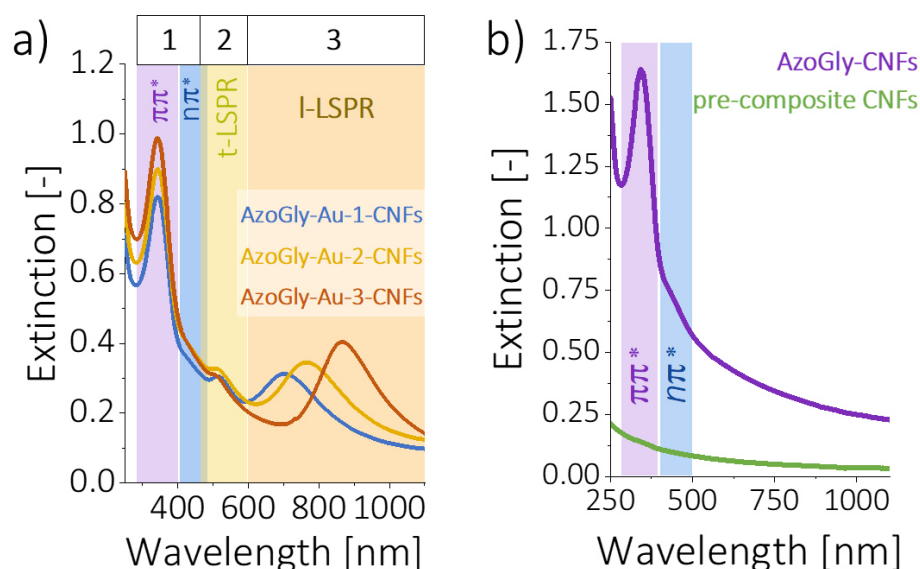


Figure 98. a) UV-Vis-NIR extinction spectra of the AzoGly-AuNRs-CNFs hybrid materials containing plasmonic cores exhibiting different AR. Optical features of plasmonic and photochromic components are clearly visible and three spectral regions identified in Chapter 4 are labelled on top of the spectra. b) UV-Vis-NIR extinction spectra of the AzoGly-CNFs

control hybrid material without Au. Spectrum of bare CNFs before impregnation with Azo dye is presented for comparison. Panel b) reprinted from own source preprint³⁸⁸.

5.2.3. Isomerization of photochromic component in hybrid materials

Photostability and Photoswitching Tests

In the photoswitching experiments the Hamamatsu L9588 LightningCure LC8 spot light source was used. The exact irradiation wavelengths were selected with bandpass filters (**Figure 99**). Irradiation intensities were measured with Thorlabs S425C Thermal Power Sensor and Thorlabs PM100D Compact Power and Energy Meter Controller. *E-Z* and *Z-E* isomerizations in the composite materials with and without Au were induced with UV irradiation (365 nm, irradiation intensity: 1.93 ± 0.06 mW/cm²) and visible light (435 nm, light intensity: 5.1 ± 0.1 mW/cm²), respectively. Reactions were monitored by measuring UV-Vis absorption spectra of the samples until reaching respective PSSs.

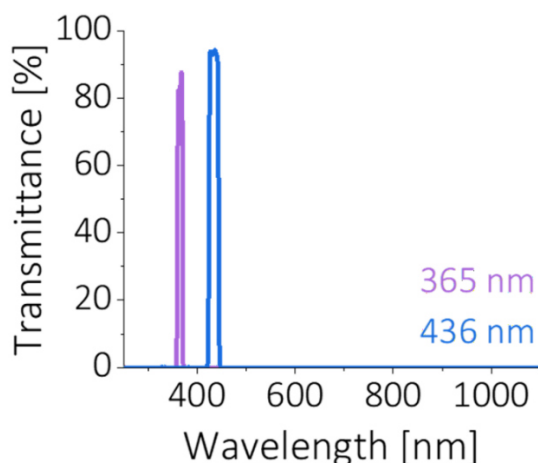


Figure 99. Transmission spectra of the filters used in the photoswitching and photostability experiments. Reprinted from own source preprint³⁸⁸.

Thermal Relaxations

Z-E isomerization of AzoGly in the dark was investigated for hybrid materials with and without Au (water-based dispersions), as well as for free Azo molecules (38 μ M EtOH-based solutions). First, AzoGly *E-Z* isomerization was induced by UV irradiation of samples (365 nm for 3-5 min, until PSS_Z was achieved). Subsequently, the extinction changes at wavelength corresponding to the position of the $\pi \rightarrow \pi^*$ band were measured at different temperatures as a function of time. Extinction values were probed every 10 seconds until samples reached PSS_E. Thermal relaxations were measured for each sample at four consecutive temperatures from the set: 20, 25, 30, 35, and 40°C.

5.3. Results and discussion

5.3.1. UV-Vis-induced direct Azo photoswitching in hybrid materials

The proposed **AzoGly-AuNRs-CNFs** formulation exhibited both distinct plasmonic and photochromic optical properties for all used plasmonic cores (**Figure 98a**). The l-LSPR bands, which are sensitive towards any changes in the surroundings of nanostructures, remained distinct, although for all samples l-LSPR redshift was observed compared to initial band position for respective free AuNRs dispersions (**Figure 100**). The redshift originates mostly from CTAB removal upon pre-composite EtOH pretreatment and possible interactions with CNFs.

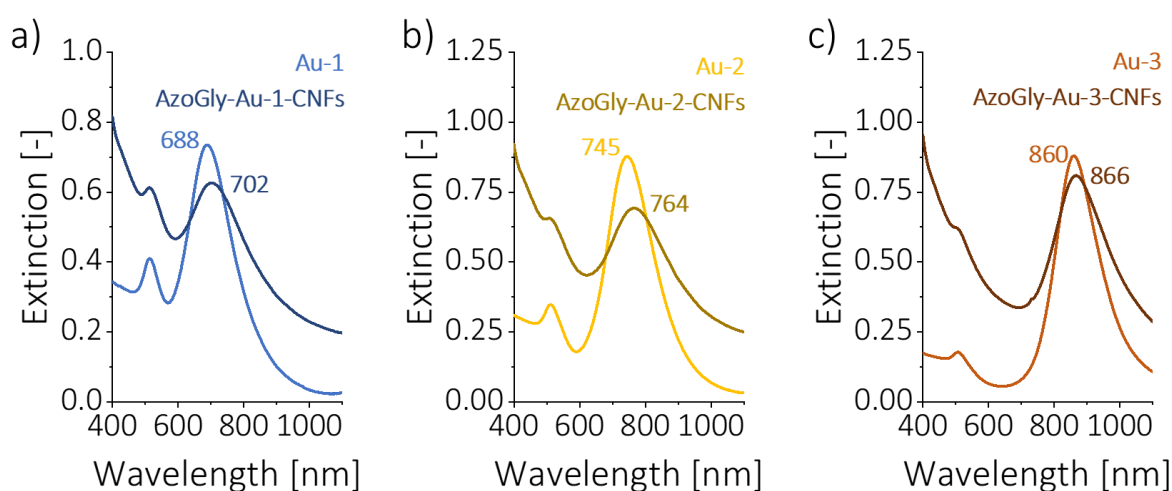


Figure 100. Positions of the l-LSPR bands of the hybrid samples differing in size of the plasmonic core compared with the positions of the l-LSPR bands of the initial dispersions of AuNRs. **a) Au-1** (14 nm redshift), **b) Au-2** (19 nm redshift), and **c) Au-3** (6 nm redshift).

In case of photochromic properties of the composites, it is essential to test and describe the kinetics and robustness of photoswitching. Hence, composites were subjected to UV-Vis irradiation (365 nm and 436 nm respectively) in the first spectral range defined for hybrid samples (see **Figure 98**). This range enables direct triggering of the *E-Z* and *Z-E* isomerization of the photochromic component. As depicted in **Figure 101** for hybrid sample containing AuNRs-1, the photochromic component maintained its functionality in the hybrid material and the changing intensity of the $\pi \rightarrow \pi^*$ band indicated the efficient triggering of the *E-Z* and *Z-E* isomerizations upon UV and Vis irradiation, respectively. Photoswitching of Azo component was also accompanied by a reversible change in the position of l-LSPR band. Upon UV irradiation and *E-Z* Azo isomerization a 2 nm blueshift was observed, while after Vis light exposition and *Z-E* Azo isomerization, a redshift to the initial position of the band occurred. No

other changes such as band broadening or damping were observed, hence indicating stability of plasmonic properties exhibited by the hybrid materials.

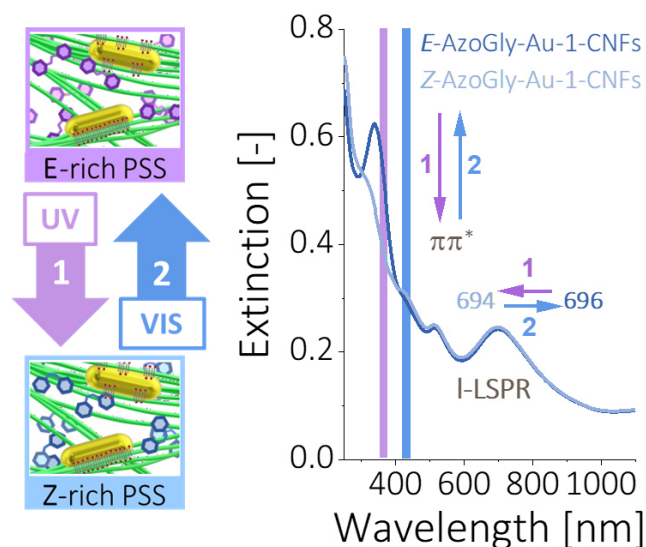


Figure 101. Photochromism of AzoGly-AuNRs-CNFs hybrid sample containing AuNRs-1 plasmonic cores. The left-hand side presents schematic depiction of the process and the right-hand side presents differences in the optical properties of hybrids in the E-rich and Z-rich PSSs. Irradiation order is described by appropriate numbers, namely 1 – UV, 2 – Vis. Numbering and the colour codes for specific irradiations are matching between figures. Figure based on own source preprint³⁸⁸.

IMPORTANT

It is typical, that the position of I-LSPR band of AuNRs blueshifts over time, due to the shortening of structures in the solution. Atomic gold oxidizes particularly on the tips of AuNRs, which leads to their shortening and, as a result, the position of I-LSPR band changes. Experiments described within this chapter were carried out at different times, so the initial positions of I-LSPR bands may differ between different figures. Nevertheless, experiments were always designed in such a way that bands positions are compared within a specific experimental context.

All hybrid systems (including control sample without gold) exhibited efficient AzoGly photoswitching between the respective PSSs, as presented in **Figure 102**. The observed reversible shifts of the I-LSPR band positions were also coherent for samples containing Au-2 and Au-3 plasmonic cores. The nature of the observed shifts of the plasmon bands is discussed further in the text.

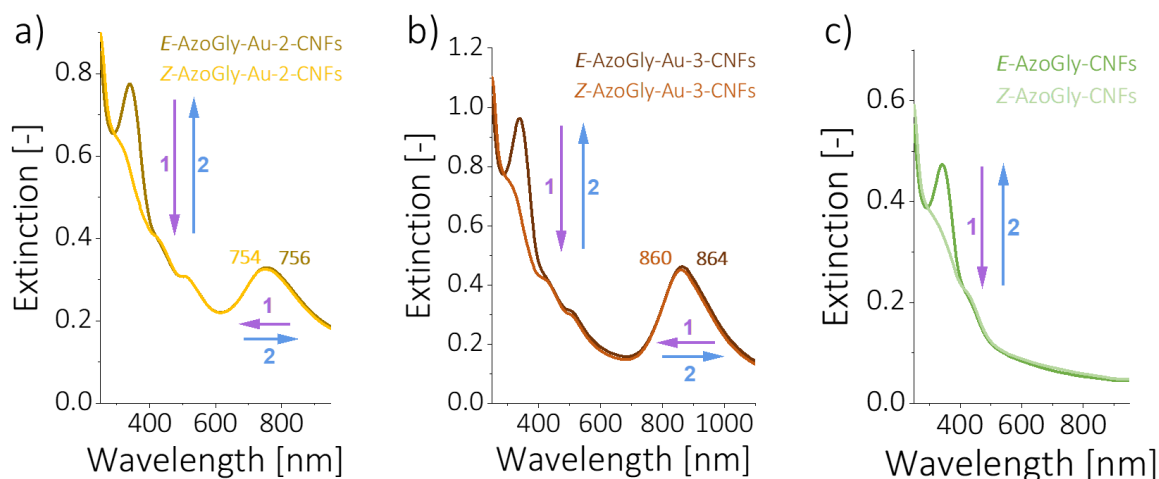


Figure 102. Photoswitchability test – general tendencies in the spectral changes for samples containing **a) Au-2** core, **b) Au-3** core and for **c) control** sample without gold (**no Au**).

First, the photochromism of hybrid samples was investigated and changes in the intensity of the $\pi \rightarrow \pi^*$ band of AzoGly upon irradiation were monitored over time until PSS_Z or PSS_E were achieved. The photoswitching of hybrid materials with and without gold exhibited first order kinetics, as depicted in **Figure 103**, where monoexponential fits of the data are presented.

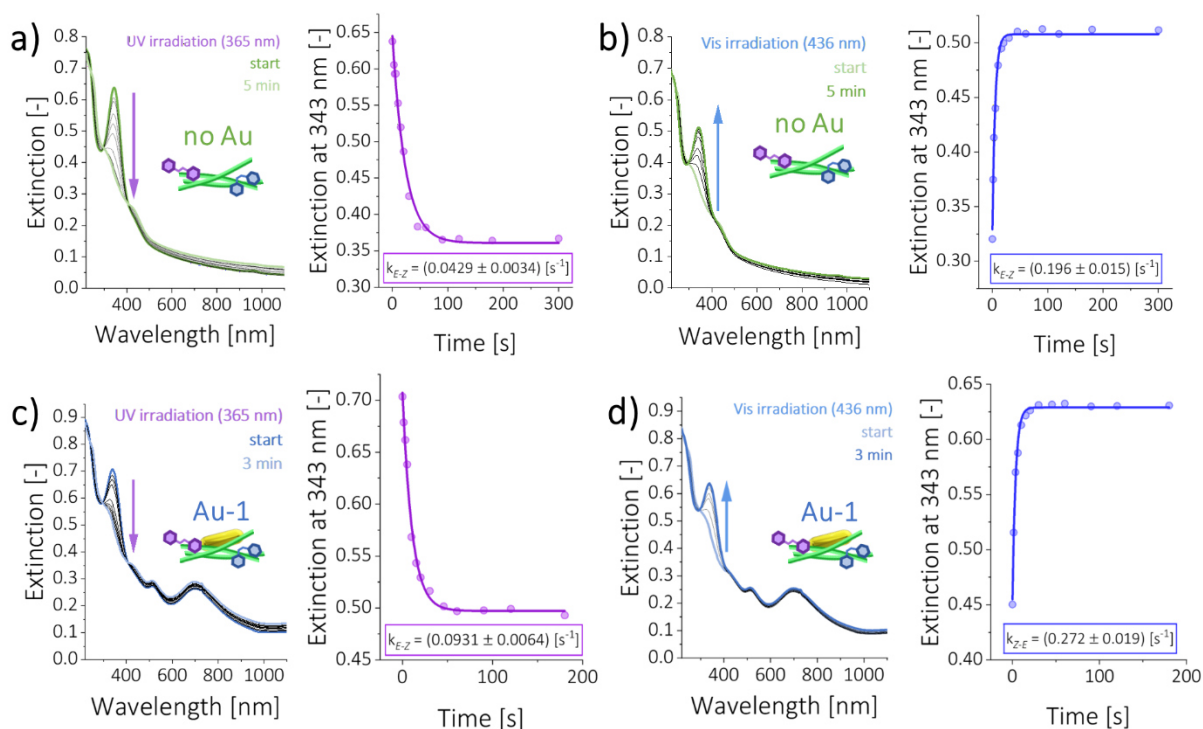


Figure 103a-d. Photochromism of hybrid samples with and without Au in water. Evolution of spectral profiles and extinction changes as a function of time. **a) E-Z** and **b) Z-E** isomerization of control sample (**no Au**). **c) E-Z** and **d) Z-E** isomerization of sample containing **Au-1** plasmonic core. Panels a-b) reprinted from and panels c-d) inspired by own source preprint³⁸⁸.

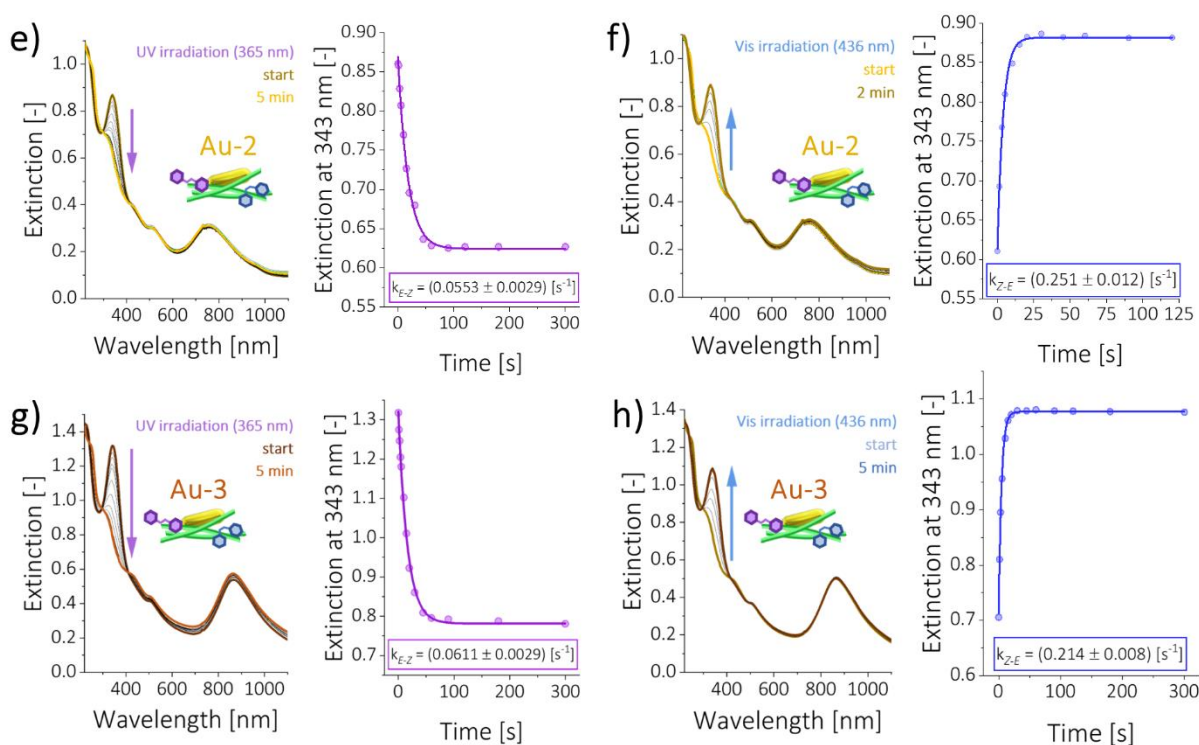


Figure 103e-h. Photochromism of hybrid samples with and without Au in water. Evolution of spectral profiles and extinction changes as a function of time. **e)** E-Z and **f)** Z-E isomerization of sample containing **Au-2** plasmonic core. **g)** E-Z and **h)** Z-E isomerization of sample containing **Au-3** plasmonic core. Panels e-h) inspired by own source preprint³⁸⁸.

In general, all Au-containing samples exhibited kinetic boost of both Azo isomerization reactions, hence manifesting catalytic influence of AuNRs in the hybrid formulation and confirming partially **hypothesis 5**. Comparison of the rate constant values (**Figure 104**) indicated that presence of AuNRs in the hybrid formulation may lead even to 117.0% increase in the rate constant of the E-Z isomerization and 38.8% increase in the rate constant of the Z-E isomerization when control material without Au is compared with material containing the smallest Au plasmonic cores (Au-1). For Z-E isomerization the rate constant values were decreasing with the increasing AR of nanostructures. For the E-Z isomerization, despite slight disruption for Au-2 plasmonic core, tendency remains relatively the same. These observations tentatively corroborate **hypothesis 6** and the exact nature of catalytic enhancement is discussed further in the text. It is important to note, that no comparison with isomerization of free AzoGly is presented, since isomerizations of hybrid materials were investigated in aqueous environment and the chosen photochrome is not soluble in water.

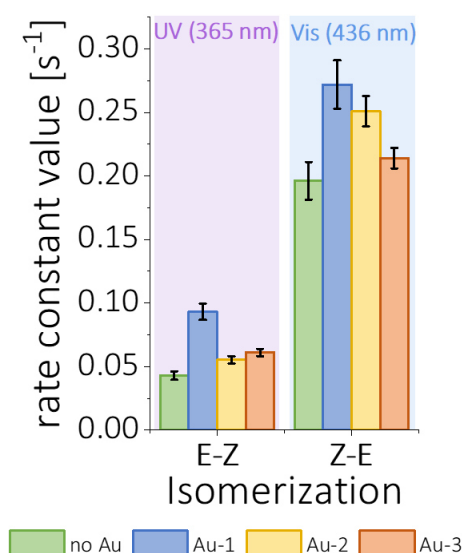


Figure 104. Comparison of the rate constant values of E-Z and Z-E AzoGly isomerization reactions investigated for hybrid samples with and without Au.

Importantly, the photoswitching properties of hybrid materials remained stable over many cycles and both isomerization reactions could have been induced repeatedly. Hence, it can be concluded, that no degradation of the photochromic component occurs in the presence of AuNRs.

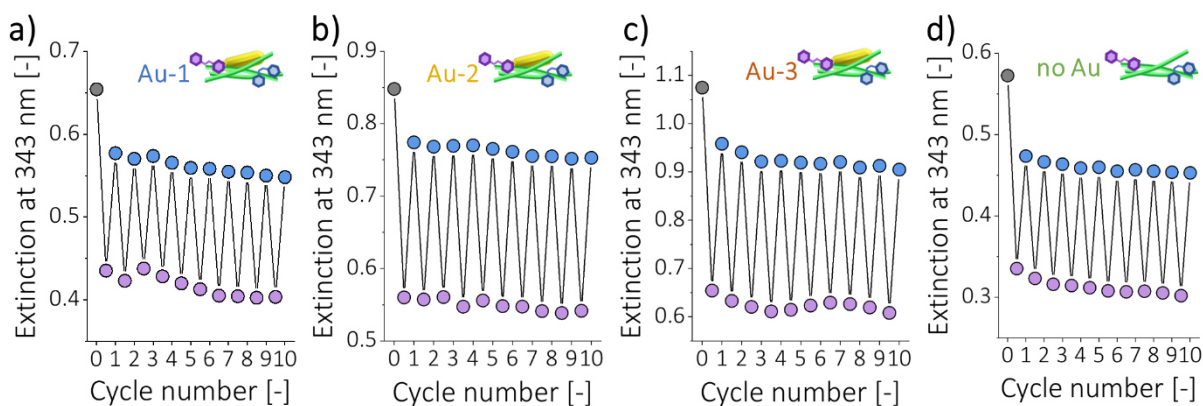


Figure 105. Interval UV-Vis irradiation of hybrid samples – photostability test. Intensity of the $\pi \rightarrow \pi^*$ band is depicted at respective PSS_Z (after UV irradiation for 3 min, purple circles) and PSS_E (after Vis irradiation for 3 min, blue circles). Plots are presented for samples containing AuNRs exhibiting different AR, namely **a)** Au-1, **b)** Au-2, **c)** Au-3, and for **d)** control sample without gold (no Au).

Hybrid materials exhibited also great stability of plasmonic properties throughout many cycles of UV-Vis irradiation. No damping or broadening of l-LSPR bands were observed. Only a slight successive blueshift occurred as a result of the photostability test, as depicted in **Figure 106**. These results manifest fundamental difference between the formulation proposed in this dissertation and literature examples of Azo-AuNPs hybrids. For literature

plasmonic-photochromic systems optical properties of plasmonic components are typically lost in one of the PSS, as a result of UV-Vis irradiation. Here, only a coherent changes in the l-LSPR band position occur without drastic change to the overall plasmonic properties.

Nevertheless, the reversible changes in l-LSPR position depicted in Figure 101 and Figure 102 were also coherently occurring during interval UV-Vis irradiation (**Figure 106**). By analysing the hybrid material design, it can be proposed, that although collective, the molecular motion of the photochromic component induced upon irradiation is not causative enough to result in global changes in the material three dimensional structure, due to the macroscopic size of CNFs. Moreover, the whole system dispersed in water is dynamic in nature, hence, it is not likely, that these changes originate from e.g. changeable distance between nanostructures, due to the motion of CNFs triggered by AzoGly isomerization. Taking into account the catalytic effect of AuNRs exhibited through the increased AzoGly isomerization rate constants, it can be proposed that the observed changes are a manifestation of this catalytic influence.

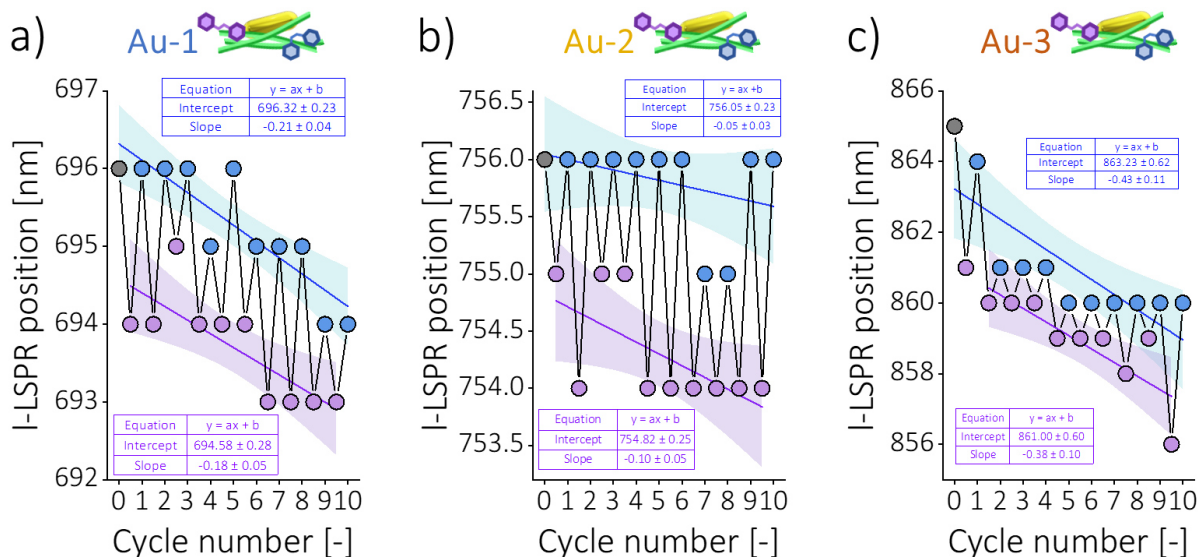


Figure 106. l-LSPR band position changes monitored during photostability tests for samples containing a) Au-1, b) Au-2, and c) Au-3 nanorods. Blue circles represent band position at PSS_E while purple circles represent the position at PSS_Z. Generally, during course of the experiments, a slight progressive blueshift of the l-LSPR bands occurs. This tendency is depicted by the linear fitting of the datasets at respective PSS, represented by fitting line and 95% confidence bands.

Importantly, such l-LSPR changes do not occur for bare AuNRs irradiated with UV-Vis (**Figure 107**). And since electron donating character of CNFs was excluded in Chapter 3, it can be rationally assumed that the observed effect does not stem from presence of cellulose.

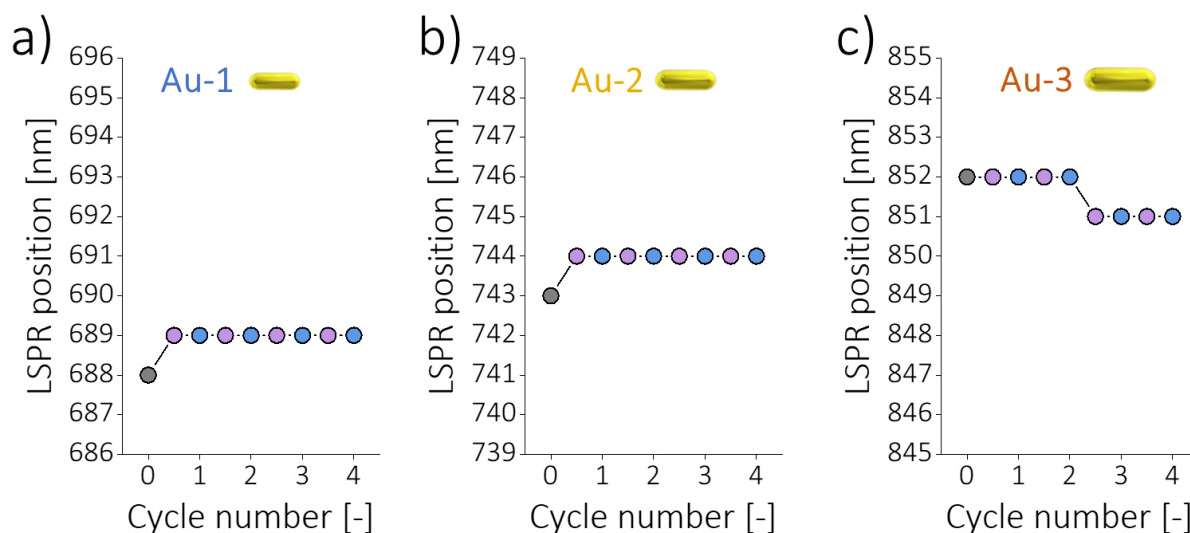


Figure 107. Changes in the position of the l-LSPR band of free AuNRs (no CNFs, no AzoGly, dispersion in water) upon UV-Vis irradiation. **a)** Au-1 core, **b)** Au-2 core, and **c)** Au-3 core. Positions of l-LSPR bands remain stable upon and only singular disruptions occur, usually at the beginning of experiment.

Notably, the evolution of l-LSPR band position in hybrid materials agrees with the overall trend of the evolution of the $\pi \rightarrow \pi^*$ band of AzoGly (**Figure 108**). Thus, it might be concluded, that the observed changes for both constituents are related and are a result of mutual interactions between plasmonic and photochromic component. Since in the presence of AuNRs the values of the *E-Z* and *Z-E* isomerization rate constants are higher compared to control sample without gold, it is proposed that the observed changes are the manifestation of the catalytic influence of AuNRs.

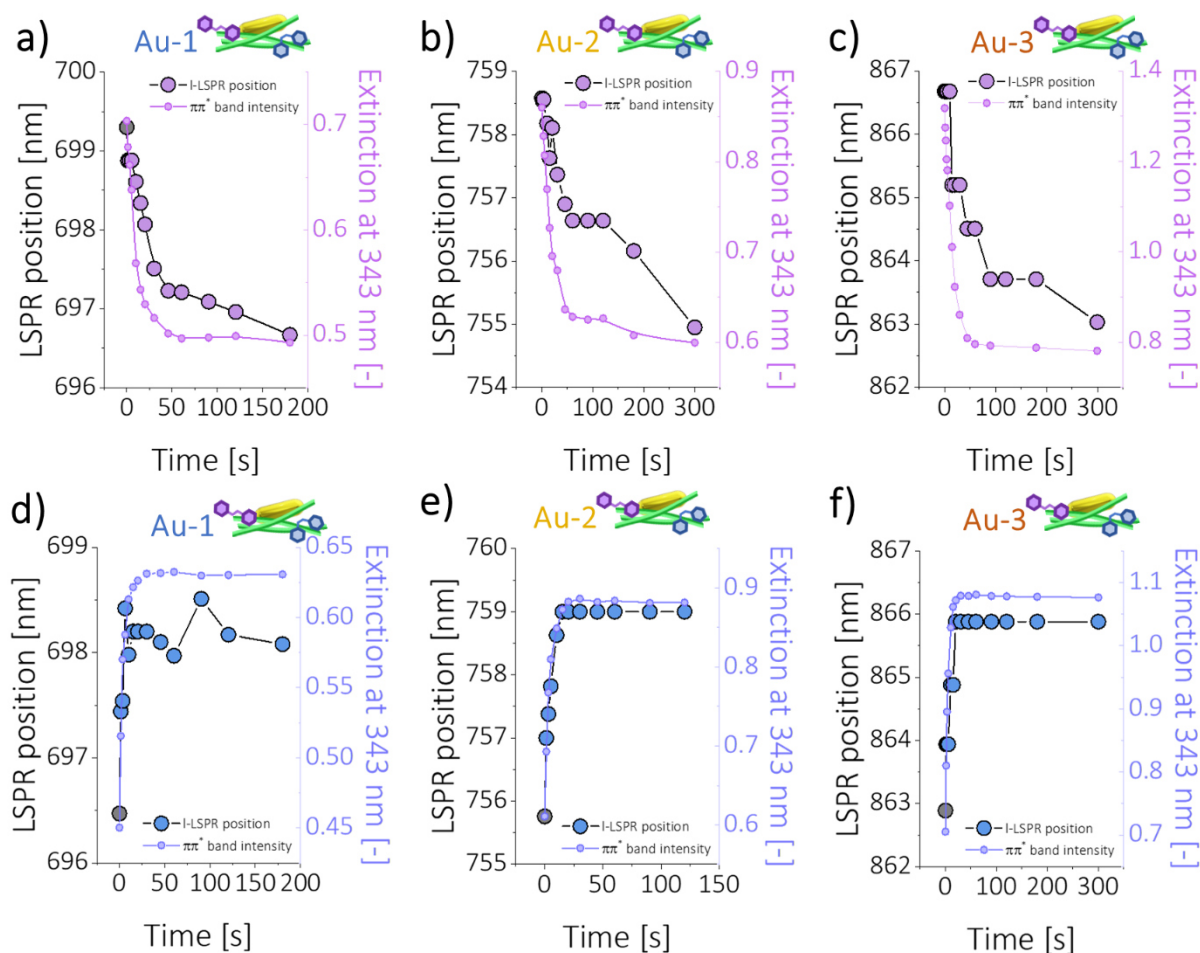


Figure 108. Changes in the position of the l-LSPR band of AuNRs in the hybrid AzoGly-AuNRs-CNFs materials (dispersions in water) upon UV-Vis irradiation compared with the simultaneous changes in the intensity of the $\pi \rightarrow \pi^*$ band of AzoGly. **a-c)** changes upon UV irradiation for samples containing **a) Au-1**, **b) Au-2**, and **c) Au-3** core. **d-f)** changes upon Vis irradiation for samples containing **a) Au-1**, **b) Au-2**, and **c) Au-3** core.

To confirm these observations, real-time monitoring of l-LSPR band position was performed for AzoGly-AuNRs-CNFs hybrid samples containing Au-2 and Au-3 plasmonic cores under UV-Vis irradiation. In these experiments the UV-Vis-NIR absorption spectra measurements were performed using Maya2000 Pro High-Sensitivity Spectrometer (Ocean Insight) coupled via fibre optics to DH-mini UV-Vis-NIR Deuterium-Halogen Light Source. Spectra were collected every 1 second. For the irradiation G2V Pico Small Area LED Solar Simulator was used (UV irradiation at 361-372 nm, irradiation intensity: 1.2 mW/cm², Vis irradiation at 425-456 nm, irradiation intensity: 1.5 mW/cm²) and the room temperature of the samples during experiment was maintained using Linkam MC60 heating stage. Both hybrid materials exhibited advancing blueshift upon UV irradiation and redshift to the initial band position upon Vis irradiation.

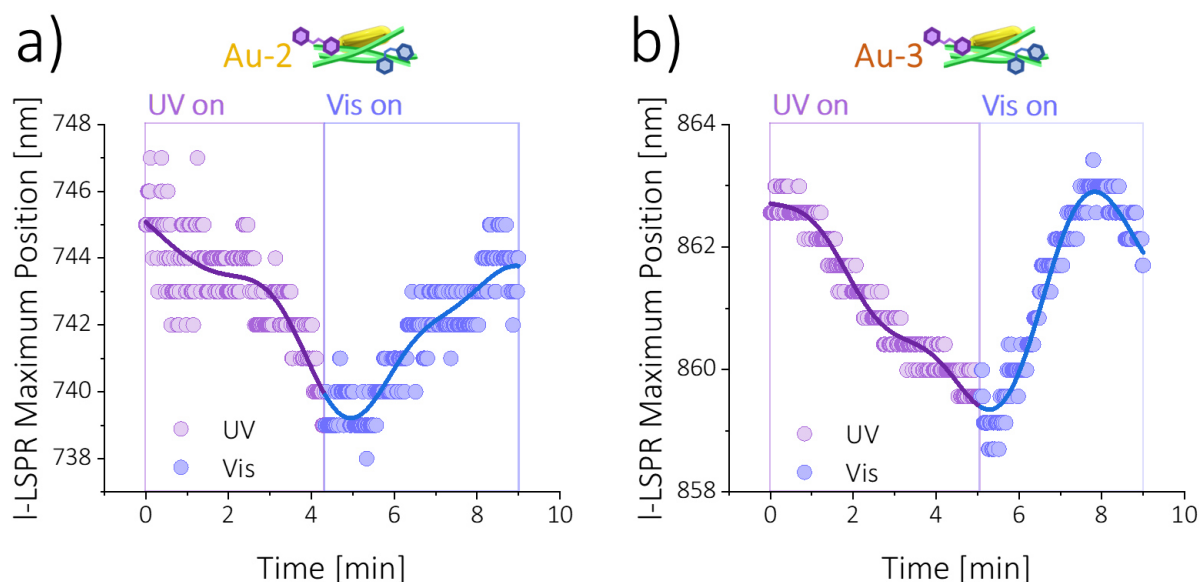


Figure 109. Changes in the position of the l-LSPR band of AuNRs for hybrid samples (water dispersions) containing **a) Au-2** cores and **b) Au-3** cores, during UV-induced Azo E-Z isomerization and Vis light-induced Z-E isomerization of the photochromic component.

The observed l-LSPR position shifts can be attributed to the catalytic influence of AuNRs on the UV-Vis induced Azo isomerization via electron transfer. Electron catalysis is considered a valuable chemical tool⁴³⁴ also in the context of azobenzene photoswitching.⁴²⁸ Here, upon UV irradiation, when AzoGly E-Z isomerization is directly triggered, interband transitions of AuNRs are also addressed. Under these conditions, AuNPs generate hot carriers, greater in number but lower in energy compared to hot carriers generated upon LSPR irradiation. As presented by Toste *et al.*¹⁸⁰ as well as Link and co-workers,⁴³⁵ transfer of those carriers to other chemical species (such as Azo molecules in case of the presented hybrid material) might be accompanied by the etching of the tips of AuNRs, which is reflected in the blueshift of their l-LSPR band. Such blueshift was indeed observed for all Au-containing samples after UV irradiation. But most importantly, a progressive l-LSPR blueshift was observed for all hybrid materials during the course of the photostability tests when UV-Vis irradiation was applied in the consecutive cycles. Hence, the overall changes depicted in **Figure 106** arise from the etching of AuNRs tips during catalytic eT that boosts up AzoGly E-Z isomerization. On the other hand, the redshift observed during Azo Z-E isomerization (after each Vis light exposition) can be interpreted through the lens of information provided by Mulvaney and co-workers,^{436,437} who showed LSPR redshift of the elongated AuNPs upon discharge of the excess electrons after catalytic reaction. Authors emphasised that those electrons can be also involved in the reduction of the ionic gold in the vicinity of nanostructures and, hence, contributed the observed redshift to the elongation of the AuNRs. Results presented in this chapter correspond well with this literature example. As described in the section 5.1.,

Azo *Z-E* isomerisation in the dark and in the presence of AuNPs occurs via electron transfer from photochrome to Au nanostructure. Coherent redshifts of the I-LSPR bands of AuNRs during photoinduced (436 nm) Azo *Z-E* isomerization in the hybrid material may indicate towards the same mechanism.

Since no shifts of the I-LSPR bands are observed for bare AuNRs upon UV-Vis irradiation in the interband transitions spectral region (Figure 107), yet spectral changes are evident when both Azo and AuNRs are present in the hybrid material (Figure 106, Figure 108, Figure 109), it can be concluded that the charge transfer might be the underlying mechanism (**hypothesis 5**) of the catalysis and in the presence of Au nanostructures AzoGly isomerizes via charged intermediate state.

5.3.2. Thermal relaxation of hybrid materials in the dark

Azobenzenes are T-type photochromes,⁴³⁸ which means that isomerization between their *cis* and *trans* state (namely from less to more thermodynamically stable form) can progress in the absence of light via thermal energy. Hence, it was essential to investigate course of this reaction in the proposed **AzoGly-AuNRs-CNFs** hybrid materials.

As described in the motivation of this chapter, so far the catalytic influence of AuNPs on Azo isomerization was investigated in the dark. The results were, however, limited to the experiments performed at room temperature.^{343,352,432,433} Thus, to thoroughly examine kinetic and thermodynamic differences of the process in hybrid materials with and without gold, thermal relaxation of the photochromic component was measured at several temperatures. In order to induce *Z-E* isomerization of Azo, hybrid samples needed to be first UV irradiated to reach PSS_Z. In contrary to some of the previous literature reports,^{352,432,433} for real material compositions, such as the formulation proposed in this dissertation or hybrids proposed by Lysyakova *et al.*³⁴³ or Chu *et al.*,³³⁹ addition of AuNPs cannot be temporally separated from UV irradiation, because plasmonic nanostructures are already present in the material together with the photochromic component.

The experiments carried out for **AzoGly-AuNRs-CNFs** and **AzoGly-CNFs** hybrid materials indicated that thermal back-isomerization of the photochromic component exhibits first-order kinetics both with and without Au (**Figure 110, Figure 111**). All samples exhibited faster thermal relaxation at higher temperature, which is typical for Azo-type photochromes. These observations further confirm that AzoGly component maintained its full photochromic functionality in the final formulation.

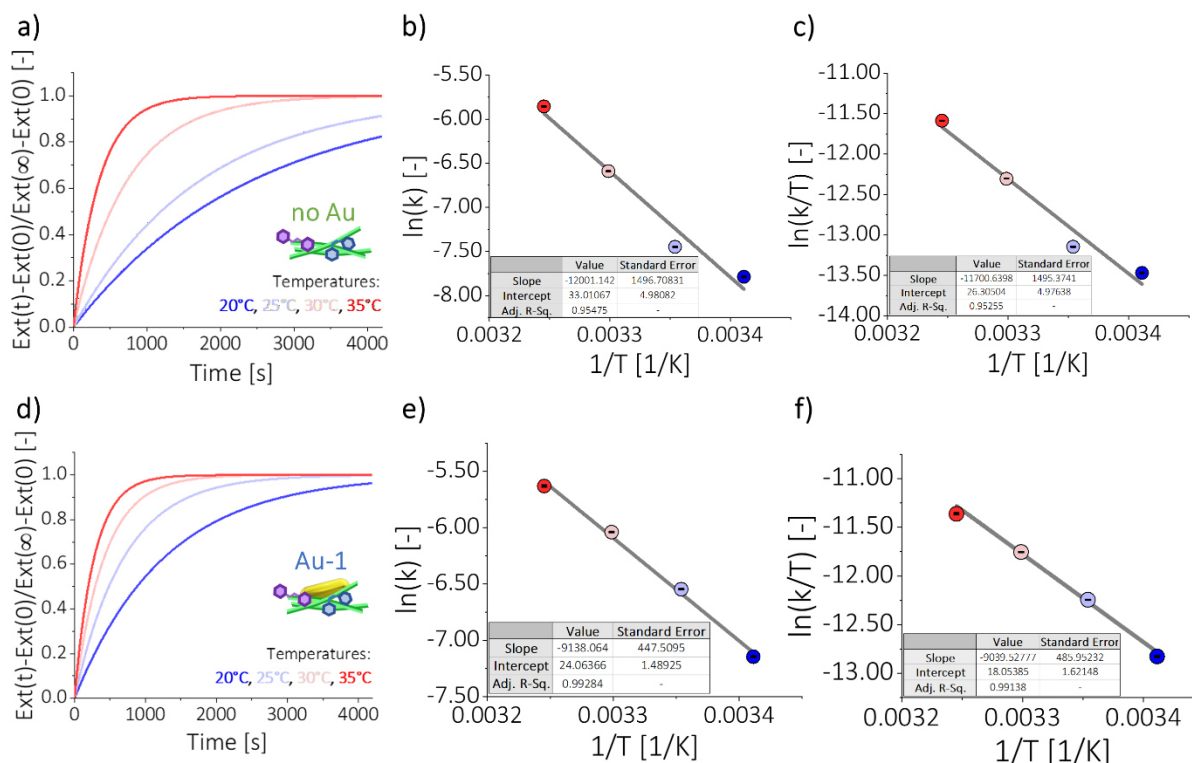


Figure 110. a, d) Thermal relaxation curves (Z-E isomerization) of the photochromic component in hybrid materials without AuNRs (*no Au* – top panels) and with *Au-1* plasmonic cores (bottom panels), accompanied by b, e) Arrhenius and c, f) Eyring plots. Panels a-c) reprinted from own source preprint³⁸⁸.

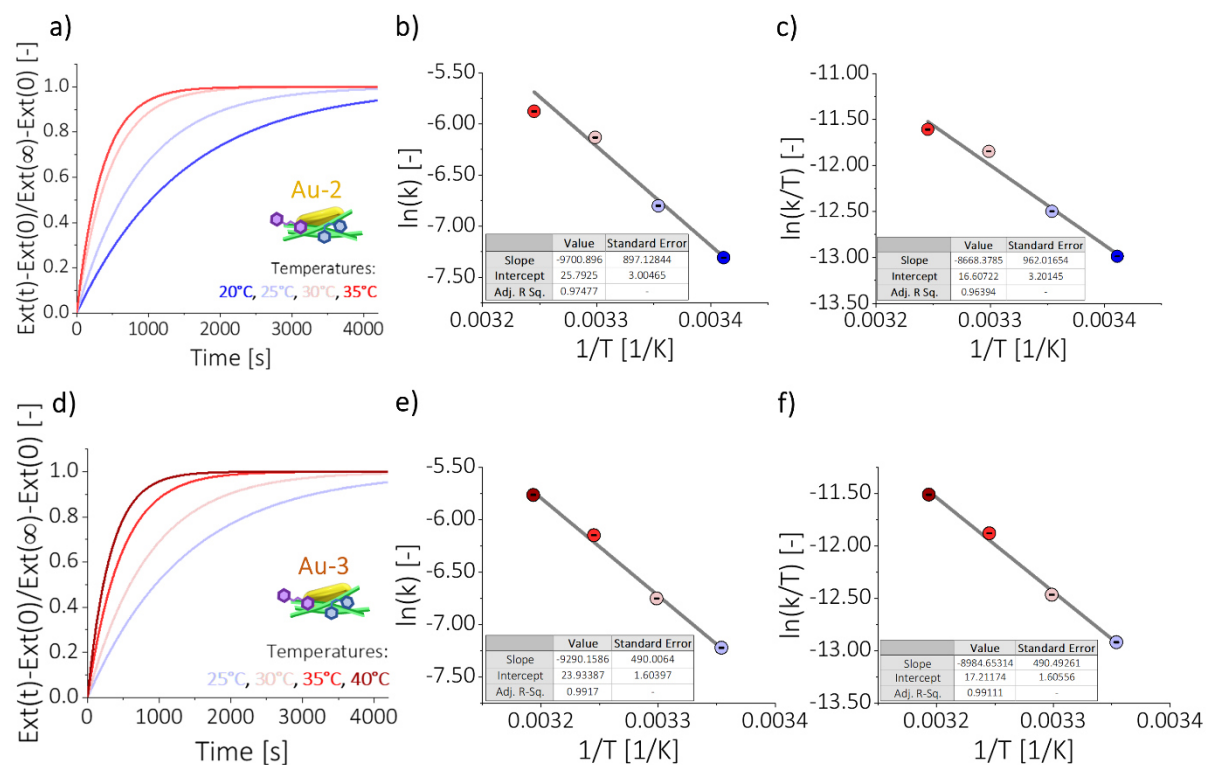


Figure 111. a, d) Thermal relaxation curves (Z-E isomerization) of the photochromic component in hybrid materials with *Au-2* (top panels) and *Au-3* (bottom panels) plasmonic cores, accompanied by b, e) Arrhenius and c, f) Eyring plots.

Notably, comparison of the results obtained at room temperature (25°) indicated that AzoGly isomerizes faster in the presence of AuNPs and that, moreover, the reaction rate increases with the decreasing AR of AuNRs. Hence, influence of aspect ratio of AuNRs on the catalytic enhancement of Azo isomerization (**hypothesis 6**) was manifested.

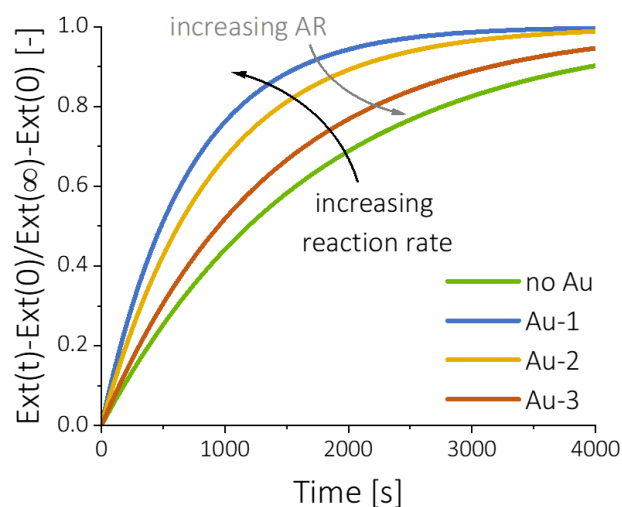


Figure 112. Comparison of the AzoGly thermal relaxation curves measured at room temperature (25°) for samples containing different Au plasmonic cores and control sample without Au.

By measuring AzoGly thermal relaxations in hybrid materials at different temperatures and by employing Arrhenius (**Equation 20**) and Eyring (**Equation 21**) equations it was possible to estimate kinetic and thermodynamic parameters of the ongoing reaction.

$$\text{Equation 20. } k_{Z-E} = A e^{-\frac{E_a}{RT}}$$

$$\text{Equation 21. } k_{Z-E} = \frac{k_B T}{h} e^{-\frac{\Delta G^\ddagger}{RT}} = \frac{k_B T}{h} e^{\frac{\Delta S^\ddagger}{R}} e^{-\frac{\Delta H^\ddagger}{RT}}$$

k_{Z-E} [s^{-1}] is rate constant of thermal Z-E isomerization at 298 K and for reactions exhibiting first order kinetics this parameter can be recalculated into thermal half-life, $\tau_{1/2}$ [s] as follows: $\tau_{1/2} = \frac{\ln 2}{k}$. A [s^{-1}] is Arrhenius prefactor, R [J/(mol·K)] is universal gas constant, T [K] is temperature, k_B [J/K] is Boltzmann constant, h [J·s] is Planck's constant. Moreover, a set of thermodynamic parameters was determined, namely activation energy E_a [kJ/mol], activation free energy ΔG^\ddagger [kJ/mol], activation entropy ΔS^\ddagger [J/(molK)], and activation enthalpy ΔH^\ddagger [kJ/mol]. During preparation of this dissertation no literature examples of such dataset of kinetic and thermodynamic parameters were found for Azo-AuNPs hybrids or plasmonic-photochromic materials.

Direct comparison of the determined parameters can be used to quantitatively visualize and discuss catalytic influence of AuNRs on the thermal back-isomerization of AzoGly. The calculated values of the parameters are presented in **Table 3**.

Table 3. Kinetic and thermodynamic parameters of AzoGly thermal relaxation in hybrid materials with different plasmonic cores and without Au.

Parameter	Sample			
	no Au	Au-1	Au-2	Au-3
$\ln(k_{Z-E}) [-]^a$	-7.24 ± 7.10	-6.59 ± 2.13	-6.74 ± 4.33	-7.23 ± 2.39
$k_{Z-E} [s^{-1}]$	$7.16 \cdot 10^{-4}$	$1.38 \cdot 10^{-3}$	$1.18 \cdot 10^{-3}$	$7.28 \cdot 10^{-4}$
$\tau_{1/2} [\text{min}]$	16.13	8.37	9.81	15.87
$A [s^{-1}] \cdot 10^{-11}$	2200 ± 2200	0.28 ± 0.22	1.6 ± 1.6	0.25 ± 0.20
$E_a [\text{kJ/mol}]$	99.8 ± 12.5	76.0 ± 3.8	80.7 ± 7.5	77.2 ± 4.2
$\Delta G^\ddagger [\text{kJ/mol}]$	91.0 ± 18.1	89.3 ± 6.2	89.8 ± 12.7	90.9 ± 6.2
$\Delta S^\ddagger [\text{J}/(\text{molK})]$	21 ± 42	-47 ± 15	-59 ± 30	-54 ± 15
$\Delta H^\ddagger [\text{kJ/mol}]$	97.3 ± 12.5	75.2 ± 4.2	72.1 ± 8.4	74.7 ± 4.2

^a Estimated from Arrhenius equation at 298 K.

All of the fittings presented in Figure 110 and Figure 111 were very good (adjusted $R^2 > 0.95$), particularly for samples exhibiting such complicated structure and composition. Due to the error propagation and exponential dependencies between parameters, the calculated uncertainties for some of the values are high, although not atypical. This fact, however, does not compromise the validity of the presented values. Moreover, parameters determined for hybrid sample without Au constitute reference points for samples with AuNRs, because kinetic and thermodynamic parameters need to be compared for hybrid, water-dispersed materials in which AzoGly is bound to CNFs. Neither of the parameters can be compared with the respective values for free AzoGly, due to difference in the environment.

Comparison of parameters describing AzoGly relaxation in different hybrid materials undoubtedly manifested the catalytic influence of AuNRs. For all AuNRs-containing samples $\tau_{1/2}$ and E_a were lower than for control sample without gold ([hypothesis 5](#), see **Table 3**, **Figure 113**). Notably, the biggest catalytic boost was observed for hybrid material containing AuNRs-1. The calculated Z-isomer half-life at 298 K was ~1.93-times lower for Au-1 sample as indicated by the drop from 16.13 min for control sample to 8.37 min.

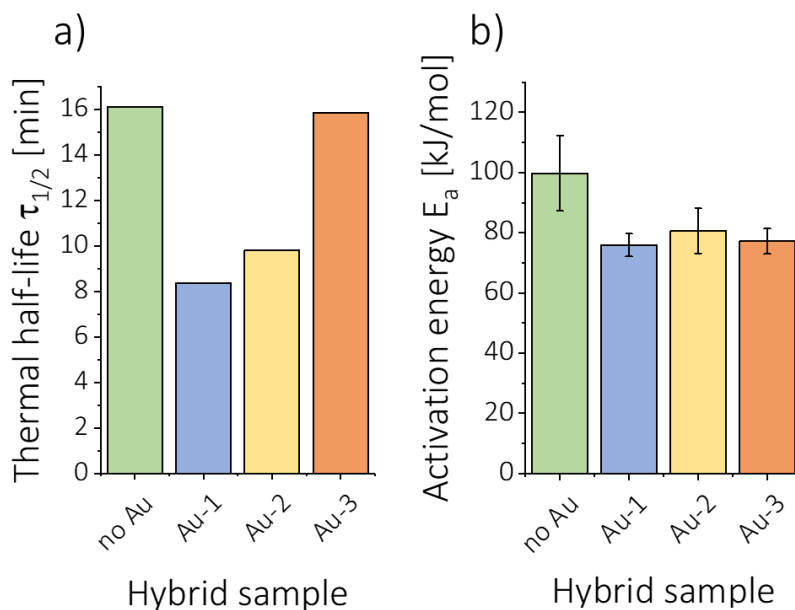


Figure 113. Hybrid plasmonic-photochromic samples and control sample without Au – comparison of the **a)** thermal half-lives and **b)** activation energies.

Activation energies of AuNRs-containing samples were about 20 kJ/mol lower than for the control sample without gold. Moreover, values for samples with AuNRs were comparable and oscillated around (78.0 ± 5.6) kJ/mol, compared to (99.8 ± 12.5) kJ/mol for **no Au** sample, which confirms common mechanism of catalysis for all sizes of Au nanostructures.

As already proposed by Hallett-Tapley *et al.*, AuNPs catalyse thermal back-isomerization of Azo via electron transfer.³⁵² To verify if the same is true for AuNRs in the hybrid materials, similarly to the approach presented in the subsection 5.3.1., positions of I-LSPR band were investigated in real time during AzoGly isomerization for hybrids with Au-2 and Au-3 plasmonic cores (**Figure 114a,b**). In the experiment the UV-Vis-NIR absorption spectra measurements were performed using Maya2000 Pro High-Sensitivity Spectrometer (Ocean Insight) coupled via fibre optics to DH-mini UV-Vis-NIR Deuterium-Halogen Light Source. Spectra were collected every 1 second. For the irradiation G2V Pico Small Area LED Solar Simulator was used (UV irradiation at 361-372 nm, irradiation intensity: 1.2 mW/cm^2) and the room temperature of the samples during experiment was maintained using Linkam MC60 heating stage. For both hybrid materials coherent shifts were observed upon UV-triggered *E-Z* isomerization (about 4 nm blueshift for Au-2 and 2 nm blueshift for Au-3) as well as for *Z-E* thermal relaxation in the dark (redshift to the initial position for both types of plasmonic cores). Such I-LSPR position changes indicate participation of AuNRs in the electron transfer,^{436,437} which can be, hence, identified as the underlying mechanism of the observed catalytic effect. Notably, intensity of the plasmon bands was maintained throughout the whole process, thus indicating stability of hybrid material's plasmonic properties (**Figure 114c,d**).

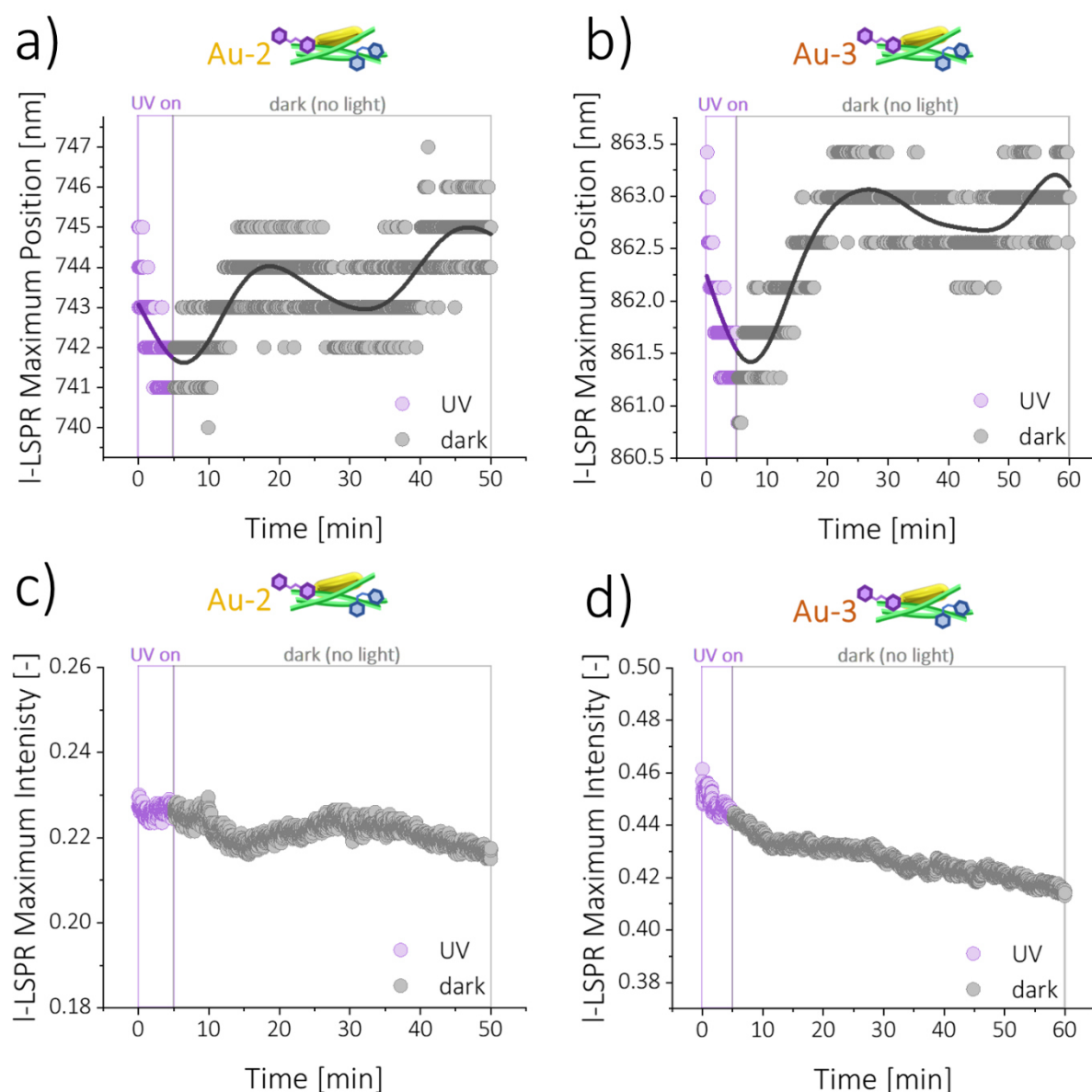


Figure 114. Changes in the position of the l-LSPR band of AuNRs for hybrid samples (water dispersions) containing **a) Au-2** and **b) Au-3** cores, during UV-induced Azo E-Z isomerization and thermal Z-E isomerization in the dark. Intensity of the l-LSPR band during the ongoing reactions for materials containing **c) Au-2** and **d) Au-3** plasmonic cores.

To further investigate catalytic effect of AuNRs and the effect of the aspect ratio, the k_{Z-E} at 298 K values were analysed. Both lower $\tau_{1/2}$ and higher k_{Z-E} confirmed catalytic effect of Au. However, as depicted in Figure 113, for the increasing AR of AuNRs, the values of rate constant were decreasing. Hence, it can be hypothesised that despite the same catalysis mechanism (comparable E_a values), the overall catalytic boost derived from presence of Au nanostructures is size-dependent. Such conclusions are in a good agreement with the general intuition since, AuNRs with higher AR exhibited lower surface of single nanoparticle (see also **Table 4** below), which may translate to less effective eT. However, the increasing AR translated also to a higher surface-volume ratio of AuNRs. To effectively compare different descriptors

related to AuNRs and their structure, such as total surface area, atomic gold concentration, total number of nanoparticles, k_{Z-E} values were normalized by division (**Table 4**, rows with yellow background), as proposed by Piella *et al.* for degradation of organic dyes on AuNSs of different sizes.⁴³⁹ In general, the results of normalization presented a very coherent picture, and the decreasing tendencies for all normalized k_{Z-E} values were observed with the increasing AR (size/volume ratio) of a single AuNR.

However, also another normalization approach can be proposed to account for presence of the photochromic component (**Table 4**, row with blue background), namely the k_{Z-E} normalization per AzoGly population and total surface area of Au combined. This normalization includes two important factors: the total surface area of gold and the population of Azo molecules per nm^2 of nanostructures. The extinction at the position of $\pi \rightarrow \pi^*$ band can represent total AzoGly content and to extract this value, spectra of **AuNRs-CNFs** pre-composites were subtracted from the spectra of hybrid samples. The resulting intensities at the position of $\pi \rightarrow \pi^*$ band were subsequently divided by the initial extinction of the sample at this wavelength. This approach accounted for varying material retrieval rates during the preparation protocol. To clarify, AzoGly content could not have been recalculated in other way due to the lack of data on photochrome's molar extinction coefficient in water (AzoGly is not soluble in water). Rate constants normalized via this approach were again decreasing with the increasing AR.

Table 4. Comparison of AuNRs structural properties and the values of normalized first-order rate constants. In the brackets modules of the relative difference between parameters (calculated with regard to the relevant parameter of Au-1-containing sample) are given.

Sample	Au-1	Au-2	Au-3
Size [nm x nm] ^a (length x diameter)	36.6 x 12.4	39.1 x 11.4	39.3 x 9.75
AR	2.95	3.43	4.03
Surface of 1 AuNR $S_{1\text{AuNR}}$ [nm^2] ^a	1426	1400 [1.82%]	1204 [15.57%]
Volume of 1 AuNR $V_{1\text{AuNR}}$ [nm^3] ^a	3921	3603 [8.11%]	2692 [31.34%]
$S_{1\text{AuNR}} / V_{1\text{AuNR}}$ [nm^{-1}]	0.364	0.389 [6.87%]	0.447 [22.80%]
[Au ⁰] [mM] ^b	0.5032	0.4537 [9.84%]	0.5180 [2.94%]
Number of AuNRs in the sample N_{AuNRs} [NP] ^b	$1.312 \cdot 10^{12}$	$1.287 \cdot 10^{12}$ [1.91%]	$1.967 \cdot 10^{12}$ [49.92%]
Total Au surface in the sample S_{tot} [nm^2] ^b	$1.871 \cdot 10^{15}$	$1.803 \cdot 10^{15}$ [3.63%]	$2.368 \cdot 10^{15}$ [26.56%]

Approximated intensity of the AzoGly $\pi \rightarrow \pi^*$ band corrected for Au-CNFs scattering Ext_{corr} [-] ^c	0.4239	0.4373 [3.16%]	0.4167 [1.70%]
k_{Z-E} [s⁻¹]	$1.38 \cdot 10^{-3}$	$1.18 \cdot 10^{-3}$ [14.49%]	$7.28 \cdot 10^{-4}$ [47.25%]
k_{Z-E} / [Au⁰]_d [s⁻¹·mM⁻¹]	$2.74 \cdot 10^{-3}$	$2.60 \cdot 10^{-3}$ [5.11%]	$1.41 \cdot 10^{-3}$ [48.54%]
k_{Z-E} / N_{AuNRs}_d [s⁻¹·NP⁻¹]	$1.05 \cdot 10^{-15}$	$9.17 \cdot 10^{-16}$ [12.67%]	$3.70 \cdot 10^{-16}$ [64.76%]
k_{Z-E} / S_{tot} [s⁻¹·nm⁻²]^d	$7.38 \cdot 10^{-19}$	$6.55 \cdot 10^{-19}$ [11.25%]	$3.07 \cdot 10^{-19}$ [58.40%]
k_{Z-E} / (Ext_{corr} / S_{tot}) [s⁻¹·nm²]	$6.09 \cdot 10^{12}$	$4.86 \cdot 10^{12}$ [20.20%]	$4.14 \cdot 10^{12}$ [32.02%]

^a Shape of a single AuNR was assumed to resemble cylinder capped with half-spheres on both ends (based on TEM images).

^b As described in the beginning of subchapter 4.3

^c This value was calculated upon subtraction of the pre-composite spectra of appropriate sample from the hybrid sample spectrum. Such corrected extinction at $\pi \rightarrow \pi^*$ was divided by the initial extinction before subtraction to account for varying retrieval rates during material preparation.

^d Normalized rate constant values, as proposed by Piella *et al.*⁴³⁹

Coherence of the presented analysis is not coincidental. To fortify the conclusions, samples containing **Au-2** and **Au-3** plasmonic cores were compared with **Au-1** sample exhibiting the biggest catalytic enhancement. For **Au-2** and **Au-3** samples the modules of relative differences in sample descriptors and the k_{Z-E} values between them and **Au-1** sample were calculated (values in italics and brackets in Table 4). The resulting data was visualised as box charts (**Figure 115**). Based on this comparison it can be stated that sample properties varied on average only by 5% between **Au-1** and **Au-2**, yet the average relative difference between all presented variants of k_{Z-E} were about 13%. Similarly, the **Au-3** sample was structurally different on average by 22% compared to **Au-1**, but relative difference of rate constants was even more striking and reached 50%. This corroborates that observed tendency of inverse proportion between AR of AuNRs and k_{Z-E} is not circumstantial and is an effect of more than one sample property (**hypothesis 6**). **Au-3** sample exhibits the highest surface-volume ratio, the highest total surface of Au, and the highest number of AuNRs in the sample, yet its k_{Z-E} value is the lowest, regardless of the normalization approach. The reason for this may lie in the potential passivation of AuNRs' surface with CNFs for bigger AuNPs, which influences the catalytic activity of nanocrystals and introduces additional interplay between key descriptors. It is also

very probable, that properties of individual nanoparticles are more decisive than the total surface or content of Au.

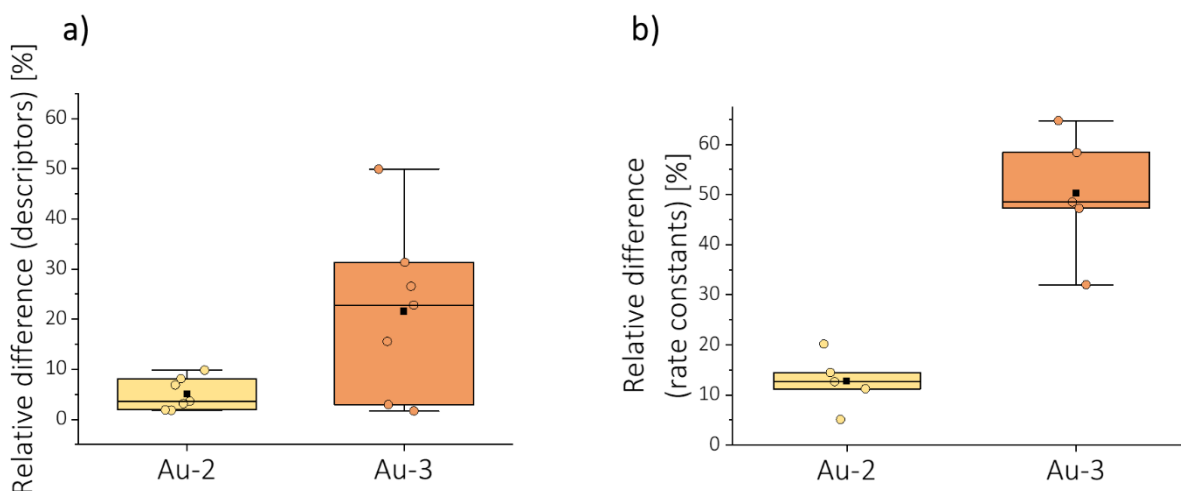


Figure 115. Box charts visualizing relation between modules of relative differences (with respect to **Au-1** sample) of **a)** sample descriptors and **b)** rate constants. **Au-2** sample is on average more similar to **Au-1** sample, yet for both **Au-2** and **Au-3** differences in rate constants are bigger than differences for descriptors. Hence, the results confirm a not coincidental relationship between AR of AuNRs and k_{Z-E} .

Finally, the overall stability of the photochromic component with respect to the material formulation was investigated. It needs to be emphasised, that by addressing the challenge of transferring AzoGly functionality to water by impregnation of CNFs, a scenario and environment were created in which AzoGly thermal *Z-E* isomerization was significantly accelerated. For free AzoGly dissolved in ethanol (**Figure 116**), *Z*-isomer half-life at 298 K equalled 24.6 hours. Yet, for Azo-impregnated CNFs without Au the *Z*-isomer half-life was drastically decreased to 16.13 min. Although such a significant destabilization of the *Z*-isomer upon change of the solvent is not unusual, it can be postulated that it may also originate from CNFs-AzoGly interactions.

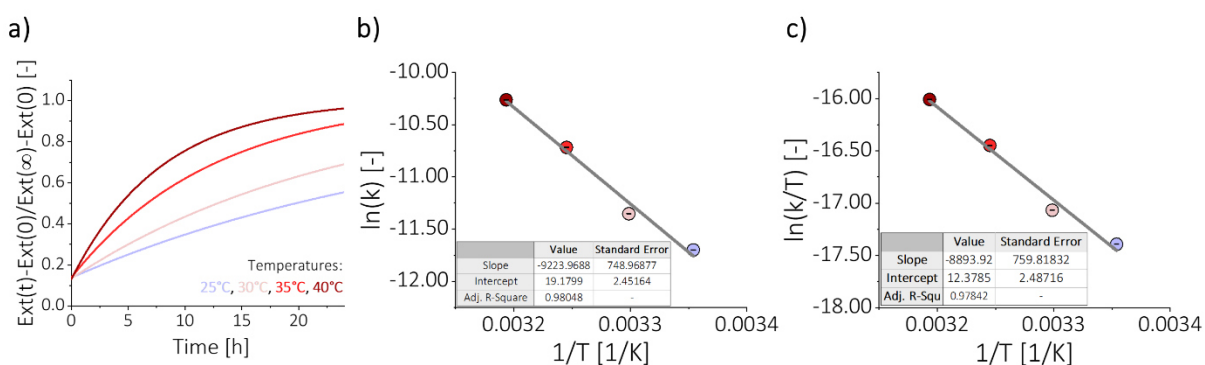


Figure 116. **a)** Thermal relaxation (*Z-E* isomerization) of free AzoGly in EtOH, accompanied by **b)** Arrhenius and **c)** Eyring plots. Figure reprinted from own source preprint ³⁸⁸.

Hence, thermal relaxations of hybrid materials without AuNRs were measured for samples containing different amounts of bare cellulose nanofibres. Different CNFs contents were subjected to impregnation with AzoGly in the same conditions and, thus, three samples were obtained: **20%[CNFs]** (5-fold decrease in CNFs content), **100%[CNFs]** (presented above as the ‘**no Au**’ control sample), and **300%[CNFs]** (3-fold increase in CNFs content). It was observed that isomerization rate constant at 25°C increases with the increasing CNFs amount (**Figure 117**). Treating the k_{Z-E} of **100%[CNFs]** as a reference value ($k_{Z-E} = (5.826 \pm 0.027) \cdot 10^{-4} \text{ [s}^{-1}\text{]}$) relative enhancement of two other samples was calculated. Sample with lower CNFs content (**20%[CNFs]**) exhibited a kinetic slowdown of about -28.5%, while sample with higher CNFs amount (**300%[CNFs]**) exhibited a kinetic boost of +107.7%. As it was determined in the sections above, AzoGly exhibited first-order kinetics of thermal isomerization in hybrid materials. Hence, k_{Z-E} of the reaction in the dark is not dependent on photochrome’s concentration and different amounts of AzoGly impregnating the scaffold for the discussed samples cannot be explained by the observed changes.

The proposed explanation relies on the consideration of environmental constraints imposed on the photochrome. Azobenzenes tend to exhibit decreased switchability at low degree of conformational freedom.⁴⁴⁰ In the proposed material design, AzoGly is anchored to the scaffold via a short, glycine-like side group and simultaneously, the scaffold forms an entangled, interpenetrated network. Both aspects contribute to the limited movement and lower steric freedom experienced by the photochrome. For the increasing CNFs content, the network created by fibres becomes denser and, thus, bigger environmental constraints are imposed on Azo molecules. Nevertheless, nature of the confinement is not too rigid, since a distinct and stable photoswitchability of AzoGly was maintained in the hybrid materials. Moreover, as presented by Chu *et al.*, Azo intermolecular interactions with the environment, including background ligands, can accelerate the isomerization upon confinement even by two orders of magnitude.³³⁹ Although the proposed formulation does not include any background ligands, it is possible that hydroxyl groups of CNFs interact with nitrogen atoms of N=N bond and participate in such a mechanism, causing the observed dramatic decrease of $\tau_{1/2}$.

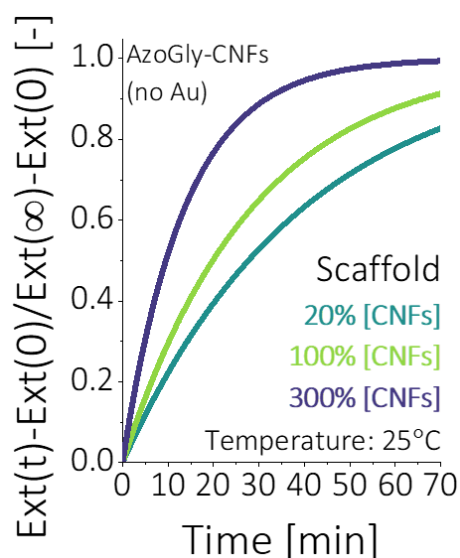


Figure 117. Influence of bare CNFs on the AzoGly thermal back-isomerization in hybrid materials at 25°C. Figure reprinted from own source preprint ³⁸⁸.

Role of CNFs scaffold is also further explored in Chapter 6, where additional proofs for inert character of the nanofibres are provided.

5.4. Conclusions

This chapter analyses mutual interactions between plasmonic and photochromic components in the hybrid **AzoGly-AuNRs-CNFs** materials, particularly the influence of AuNRs on the isomerization of AzoGly (**objective 3**).

In the hybrid formulations AzoGly exhibits distinct and stable photochromic properties without degradation, both under repeated UV-Vis irradiation and in the dark. *E-Z* and *Z-E* photoinduced isomerizations as well as *Z-E* thermal relaxation in the dark occur faster in materials containing AuNRs. Coherent changes in the position of 1-LSPR band of AuNPs (order of a few nanometers), namely blueshifts during *E-Z* and redshifts during *Z-E* isomerizations (under Vis irradiation and in the dark), indicate catalytic enhancement via electron transfer mechanism, as hypothesised based on literature reports for AuNSs (**hypothesis 5**).

For all hybrid samples a complete set of thermodynamic parameters describing thermal back-isomerization of Azo was determined. For all Au-containing materials, thermal relaxations in the dark are characterized by lower activation energy (by 20 kJ/mol) compared with hybrid **AzoGly-CNFs** material without gold, which further confirms catalytic influence of AuNRs. Nevertheless, the kinetic parameters of AzoGly isomerization differ for materials containing plasmonic cores of different aspect ratios. As confirmed by the analysis of thermal relaxation rate constants with regard to structural descriptors of hybrid materials, the catalytic

enhancement increases with the decreasing AR of AuNRs, which confirms **hypothesis 6**. The analysis indicates the observed size effect is most probably a convolution of more than one structural parameter of the materials, including number of Azo molecules per surface of Au and passivation of AuNRs surface with CNFs. Moreover, the results indicate that AzoGly Z-isomer half-life is drastically shortened in hybrid materials due to solvent transfer and steric constraints imposed by CNFs scaffold, including possible intermolecular interactions between hydroxyl groups of cellulose and N=N moiety.

Chapter 6. *Plasmon-Assisted Isomerization of Azobenzene and Its Control via Plasmon-Related Effects*

This chapter describes how plasmon-related effects can be utilized to indirectly control *Z-E* isomerization of Azo photochromes. In all experiments red-NIR irradiation is used (650-1100 nm) and hence, only the 1-LSPR band of the AuNRs is addressed, which enables triggering of the thermoplasmonic effect. First, AuNRs-CNFs pre-composite is used to investigate catalytic influence of AuNRs on *Z-E* isomerization of free Azo molecules in ethanol upon red-NIR irradiation. As the experiments are carried out in the native solvent of AzoGly, a proper resolution of measurements is assured. This subsection also proposes a new role for Azo photochromes as molecular thermometers enabling e.g. assessment of the extent of the thermoplasmonic effect. Subsequently, plasmon-assisted isomerization of AzoGly is investigated in the hybrid Azo-AuNRs-CNFs formulation. Statistical modelling of the results reveals that under proper irradiation conditions, indirect control over Azo *Z-E* isomerization in an ON-OFF manner is possible. Thus, a new application for the Autoregressive Integrated Moving Average (ARIMA) statistical model is proposed. The results presented here challenge Objective 4 and verify hypothesis 7 of the dissertation.

Objective 4: To investigate the possibility of plasmon-assisted Azo isomerization and reaction control via plasmon-related effects.

Hypothesis 7: Kinetics of the Azo isomerization can be controlled via red-NIR irradiation (at wavelengths not absorbed by a photochrome) due to the thermoplasmonic effect of AuNRs.

Results presented within this chapter are available as a part of the preprint:
³⁸⁸ N. Tarnowicz-Staniak, M. Staniak, M. Dudek, M. Grzelczak, K. Matczyszyn, *Gold Nanorods Grant an ON-OFF Control over the Kinetics of the Z-E Isomerization of Azobenzene-Based Photoswitch via Thermoplasmonic Effect*, preprint ChemRxiv **2024**, <https://doi.org/10.26434/chemrxiv-2024-vnj32>.

6.1. Motivation

The most common requirements for new azobenzene photoswitches include modulation of their isomerization beyond what is already known for this class of the photochromes. Two particularly popular demands are the shifts of $\pi \rightarrow \pi^*$ and $n \rightarrow \pi^*$ bands into the red or near-infrared (NIR) range^{426,427,441} and modulation of the *Z*-Azo lifetimes.^{442,443} Both aspects are especially valuable e.g. for photopharmacology⁴⁴⁴ and neuronal activity control.⁴⁴⁵ For many years, the most popular approach to the modulation of Azo photoswitching has been synthetic modification of the already-known structures.^{303,307,446–449} Typical synthetic modifications rely on tetra-*ortho*-fluorination,^{307,446} tetra-*ortho*-chlorination,^{447,450} or the overall tetra-*ortho*-substitution³⁰⁶ and result in both change in the *Z*-isomer thermal stability and shift of Azo excitation wavelengths entirely to the Vis range.³⁰³ Even though the synthetic procedures are still being developed and become more and more feasible,^{303,448,449,451} many approaches remain laborious or result in low or moderate yields.

Fortunately, the synthetic path is not the only possible way of influencing the photoswitching properties of Azo photochromes. There are also alternative strategies relying on the indirect excitation of azobenzene molecules via intra- or intermolecular energy transfer^{300,304,417,418,452–461} or on the electron transfer.^{426,428,429,462,463} The energy transfer scenario can be executed using diverse sensitizing techniques, such as multiphoton phenomena,^{300,417,452,453} triplet photosensitization,^{304,418,458–461} or upconversion process.^{454–456} Multiphoton sensitisation is a broad topic addressed by review articles.³⁰⁰ Typical examples of chemical species used in this approach include plasmonic nanoparticles⁴⁵⁷ and multiphoton absorbing antennae (grafted on the same surface as Azo⁴⁵² or incorporated in its chemical structure^{417,453}). The second approach, namely triplet photosensitisation, can be accomplished, for instance, by using porphyrins,⁴⁶⁰ iodine,³⁰⁴ or dual-dye upconversion systems employing triplet-triplet annihilation.⁴⁶¹ Finally, upconversion-based energy transfer is commonly executed using lanthanide-doped upconverting nanoparticles.^{454–456} The other class of indirect excitation strategies relies on the electron transfer from or to the azobenzene photoswitch. Conjugation of Azo *Z-E* isomerisation with redox reactions of photoelectron transfer agents, such as ferrocene⁴⁶² or iridium complexes,⁴²⁸ enables omitting high-energy irradiation, greatly amplifies the process and improves its sensitivity and efficiency.^{429,463} The alternative modification pathways are particularly appealing for multi-component, Azo-containing systems. First, they broaden and modify properties of the already existing molecules. Second, the photoswitching modifications are a result of the presence of other material components.

Hence, the intrinsic limitations of the compounds can be exceeded and all profitable features of such photoswitches, e.g. robustness, are maintained.

Plasmonic nanostructures are mostly recognized as potential multiphoton sensitizers for indirect modification of photochromes switching, however there are also works presenting plasmonic nanoparticles as external species enabling modulation of isomerization reaction via light-triggered plasmon-related phenomena. However, in most of the reports small, isotropic AuNPs exhibiting limited light-harvesting properties are used and hence, the knowledge about potential plasmon-assisted isomerization of photochromes remains limited.

Most of literature examples presenting indirect modification of the photoswitching of photochromes via use of plasmonic nanoparticles focuses on diarylethenes (DE). For instance, Nishi *et al.* investigated DE-coated AuNSs and observed an enhancement of molecules' photocycloreversion reaction upon CW (halogen lamp) irradiation with selected wavelengths from 450-700 nm range, corresponding to the position of LSPR band of nanostructures.⁴⁶⁴ The main enhancement mechanism postulated by authors was local field enhancement, since for larger nanoparticles faster photocycloreversion was observed. Moreover, upon the increasing distance between components the enhancement was determined to decay, which further corroborated the postulated mechanism. The structure of the chromophore was determined to have negligible effect on the process, which disfavoured charge transfer mechanism. Authors confirmed these conclusions also for DE-decorated 19 nm Ag nanospheres in another research paper, using Xe lamp as irradiation source (**Figure 118a**).⁴⁶⁵ Catalytic boost via local field enhancement mechanism was also proposed for DE photochromism in the polymer film deposited on AuNPs-integrated glass substrate by Tsuboi *et al.* in a plasmon-assisted two-photon process triggered upon CW laser irradiation at 808 nm (**Figure 118b**).⁴⁶⁶

In case of DE however, e.g. the influence of thermoplasmonic effect cannot be determined, because these compounds are P-type photochromes. Nevertheless, there are examples of indirect photoswitching modulation via plasmonic nanoparticles investigated for another classes of photochromes. For instance, Padilla *et al.* investigated plasmon-based photocatalysis in the system with supramolecular hosts (**Figure 118c**).⁴⁶⁷ Authors used 14 nm spherical nanoparticles, decorated with β -cyclodextrin to prepare complexes driven by hydrophobic effects, able to interact with many potential reactants. Stilbene *Z-E* isomerization was selected to evaluate the proposed system. Stilbenes, similarly to azobenzenes are T-type photochromes and undergo photoinduced *E-Z* and *Z-E* isomerizations about the C=C bond, as well as *Z-E* thermal relaxation. To trigger plasmon-related phenomena 532 nm pulsed laser was used (6 ns, 10 Hz) and hence, potential multiphoton sensitization was ruled out. The observed catalytic enhancement was postulated to originate from two plasmon-related effects, namely

photothermal effect and charge carriers transfer. Conclusion on the first mechanism was based on qualitative similarity between *Z-E* isomerization in the dark and plasmon-assisted process. However, because the catalytic enhancement was dependent on the photochrome's structure, participation of other mechanism was proposed. Based on the theoretical calculations of energy barriers for the respective radical cations and correlation between results of cyclic voltammetry measurements and the observed tendencies of the catalytic enhancement, charge transfer mechanism was proposed to accompany the photothermal effect of AuNSs. Anisotropic, rod-like Ag nanoparticles were used by Ho *et al.* to investigate plasmon-assisted isomerization of the modified chromene.⁴⁶⁸ Photochrome and nanoparticles were placed in a soft sol-gel matrix to decrease isomerization barrier and increase reaction efficiency. Presence of Ag nanostructures enabled recovery process of the photochrome, which was otherwise negligible. Finally, plasmon-induced isomerization of AzoSH-decorated 10 nm AuNSs was presented by Stiévenard *et al.* for nanoparticle self-assembled networks.⁴⁶⁹ Authors presented more efficient process in a 3D network, compared to 2D systems under 365, 470, and 590 nm CW illumination, due to an antenna effect. For the experiments with irradiation corresponding to the position of AuNSs LSPR band, authors ruled out direct triggering of Azo isomerization, photothermal effects (experiments were performed at low irradiation intensities), and two-photon absorption. The postulated mechanism was plasmon-induced resonance energy transfer, possible to occur under conditions of spectral overlapping between photochromic and plasmonic components.

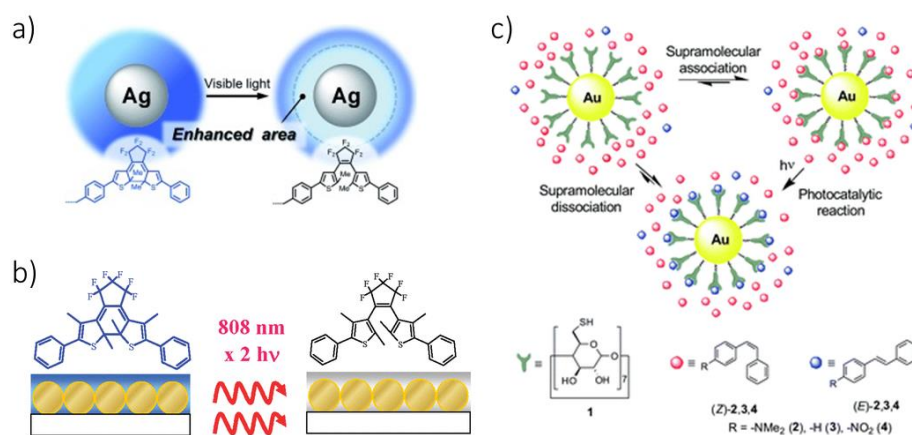


Figure 118. Literature examples of plasmonic-photochromic systems designed to investigate plasmon-assisted isomerization. **a)** DE-decorated Ag nanospheres showcasing plasmon-assisted isomerization via local field enhancement mechanism. Reprinted from ⁴⁶⁵. **b)** DE-doped polymer films deposited on AuNSs-integrated glass showcasing plasmon-assisted two-photon sensitization. Reprinted from ⁴⁶⁶. **c)** Cyclodextrin-decorated AuNSs interacting with stilbene molecules showcasing plasmon-assisted isomerization via photothermal effect and charge carrier transfer. Reprinted from ⁴⁶⁷.

Material formulation proposed in this dissertation assures stability of plasmonic properties even during isomerization of the Azo component. Hence, it is essential to investigate the plasmon-assisted isomerization in the hybrid material. Additionally, proposed formulation contains big, anisotropic nanostructures, exhibiting better light-harvesting properties compared to typical literature examples of systems containing small, 10-15 nm AuNSs. This lays foundation for the potential control over the Azo isomerization via plasmon-related effects (**objective 4**). Because the L-SPR band of AuNRs is spectrally separated from the absorption bands of the photochrome, this chapter investigates the mechanism of Azo isomerization upon irradiation in the red-NIR spectral range and verifies the hypothesis regarding main influence of the thermoplasmonic effect on Azo isomerization under such conditions (**hypothesis 7**).

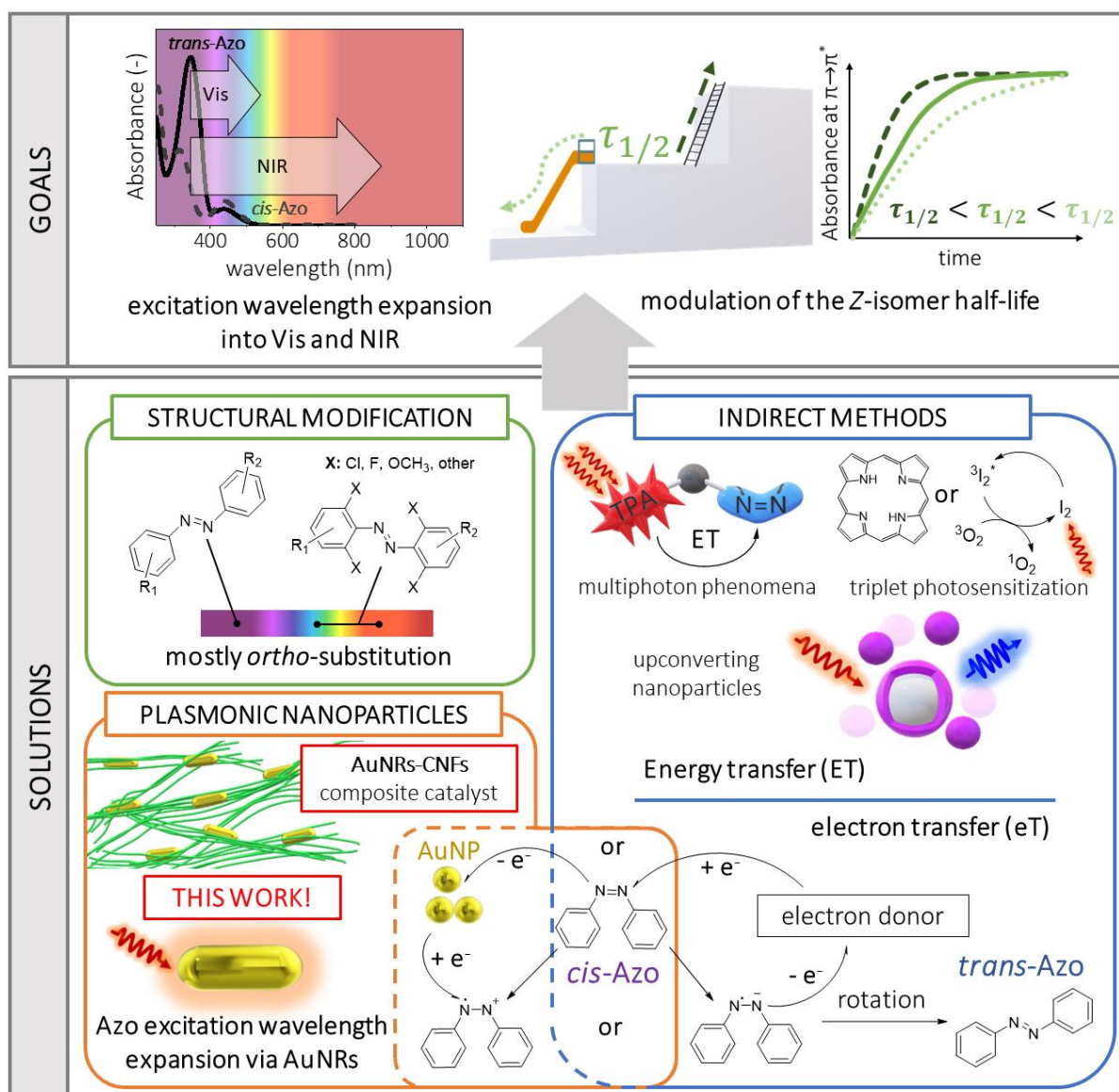


Figure 119. Schematic depiction of the indirect Azo photoswitching modification pathways placing the results of the dissertation in the broad literature context.

6.2. Materials and methods

6.2.1. Materials and techniques

Materials

Chemicals used for the experiments were commercially available and did not require purification. In all experiments deionized water with the resistivity of 18.2 M Ω ·cm (Millipore Milli-Q grade) was used. If not indicated otherwise, chemicals were purchased from Sigma-Aldrich. For the synthesis of AuNRs the following reagents were used:

- metallic precursor: gold(III) chloride trihydrate (HAuCl₄·3H₂O),
- surface stabilizing agent: cetyltrimethylammonium bromide (CTAB),
- reducing agents: sodium borohydride (NaBH₄), L-ascorbic acid (AA),
- other additives: silver nitrate (AgNO₃).

Support for nanoparticles: TEMPO-oxidized cellulose nanofibres (CNFs) supplied by CelluForce (Canada).

Photochromic component: AzoGly molecule provided by Dr Marta Dudek (Faculty of Chemistry, Wrocław University of Science and Technology) – see **Figure 77**.

Techniques

Basic UV–Vis–NIR extinction spectra measurements were performed using Cary UV-Vis-NIR 3500 spectrophotometer equipped with Multicell Peltier UV-Vis cuvette holder. Transmission electron microscopy (TEM) images were acquired using JEOL JEM-F200 microscope. For the irradiation experiments the G2V Pico Small Area LED Solar Simulator with custom irradiation programmes was used. Real-time monitoring of plasmon-assisted reactions was carried out using Maya2000 Pro High-Sensitivity Spectrometer (Ocean Insight) coupled via fibre optics to DH-mini UV-Vis-NIR Deuterium-Halogen Light Source with shutter and UV-Vis cuvette holder.

6.2.2. Hybrid materials preparation

AuNRs synthesis

AuNRs were synthesised using a Ag-assisted seeded growth method according to the following protocol.^{79,83}

In the first step seeds were prepared by reducing gold precursor, HAuCl₄ (0.025 mL, 0.05 M) in aqueous solution of CTAB (4.7 mL, 0.1 M) with ice-cold NaBH₄ (0.3 mL, 0.01 M) added under vigorous stirring. The mixture was left for 30 min under mild stirring. Optical

characteristics and visual appearance of the seeds were matching the data presented in **Figure 48** (subsection 3.2.2. of Chapter 3) and hence are not repeated here.

In the second step Ag-assisted seeds overgrowth was performed in the solution containing HAuCl₄ (1.75 mL, 0.05 M), CTAB (175 mL, 0.1 M), AgNO₃ (1.75 mL, 0.005 M), and AA (1.31 mL, 0.1 M) upon the addition of Au seed solution (1.75 mL). The growth solution was left undisturbed for at least 2 h at 25°C. Final concentration of metallic gold was 0.0005 M.

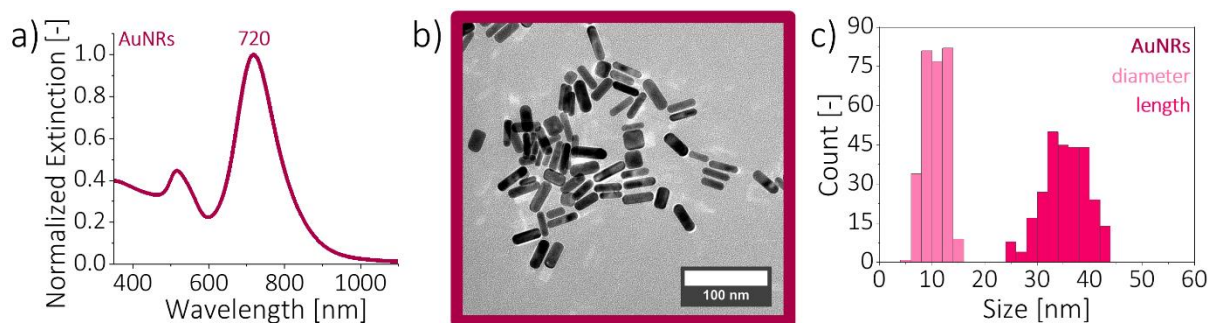


Figure 120. a) Normalized UV-Vis extinction spectra of the as-prepared AuNRs. b) Representative TEM image and c) histograms of the nanostructures. The average dimensions of the AuNRs were as follows: average length: 35.3 ± 4.2 nm, average diameter: 10.7 ± 2.1 nm, number of nanoparticles measured $N = 277$, aspect ratio $AR = 3.30$. Reprinted from own source preprint³⁸⁸.

AzoGly-AuNRs-CNFs composite preparation

Pre-composite preparation. Dispersion of AuNRs was first concentrated to obtain ~19.6 wt% of Au with respect to the dry mass of CNFs in the pre-composite. Dispersion was washed twice with water (7000g, 15 min) and redispersed in 1 mM CTAB. Subsequently, AuNRs were titrated with aqueous CNFs solution (0.5 wt%) at room temperature and under vigorous stirring (AuNRs/CNFs = 2:1, v/v). Pre-composite was left until the next day to promote material sedimentation. On the next day the collected pellet was centrifuged twice (540 g, 5 min) and redispersed in water.

Pre-composite impregnation with AzoGly. Pre-composite was centrifuged (780 g, 5 min) and redispersed in ethanol. The as-obtained clear dispersion was subsequently added dropwise to the solution of AzoGly in ethanol under vigorous stirring. The concentration of the photochromic component was adjusted to ~3.1 mM. Mixture was stirred for 5 min and then left undisturbed for at least 17.5 hours at room temperature. On the next day impregnated composite was centrifuged in a few step procedure. First, separation from ethanol via centrifugation was performed (540-1400g, 10-15 min). Subsequently, supernatant was subjected to three follow-up separations (7000g, 10-20 min each). All of the combined pellets were transferred to water

and washed once (4850g, 20 min). The resulting composite was subjected to visual inspection, UV–Vis–NIR characterization, and further in-depth investigation.

Control AzoGly-CNFs composite without Au. To prepare composite without AuNRs, 1 mM CTAB solution was titrated with the aqueous CNFs solution (0.5 wt%) under vigorous stirring and at room temperature (CTAB/CNFs = 2:1, v/v). The as-prepared pre-composite sample was left until the next day to promote sedimentation of the fibres. Pre-composite was centrifuged twice (540 g, 5 min) and redispersed in water to remove the excess CTAB. Subsequently, pre-composite pretreatment with EtOH was performed (centrifugation, 780 g, 5 min followed by material redispersion in EtOH). Next, the pretreated material was added dropwise to the solution of AzoGly in ethanol (~3.1 mM) under vigorous stirring. Mixture was stirred for 5 min and then left at room temperature, undisturbed for at least 17.5 hours. On the next day mixture was purified via centrifugation in a few step procedure. First, separation from ethanol via centrifugation was performed (540-1400g, 10-15 min). Subsequently, supernatant was subjected to three follow-up separations (7000g, 10-20 min each). All of the combined pellets were transferred to water and washed once (4850g, 20 min).

6.2.3. Plasmon assisted isomerization of AzoGly

Plasmon-assisted isomerization of AzoGly in the presence of AuNRs and under proper irradiation conditions was investigated by monitoring the UV-Vis-NIR extinction spectra in real time using Maya2000 Pro High-Sensitivity Spectrometer (Ocean Insight) coupled via fibre optics to DH-mini UV-Vis-NIR Deuterium-Halogen Light Source with shutter and UV-Vis cuvette holder. To assure irradiation of the samples without additional heating by the light beam, LED light source was utilized, namely G2V Pico Small Area LED Solar Simulator with custom irradiation programmes. Both spectral range and irradiation intensities applied during particular experiments are specified in the sections below. Moreover, to assure constant, room temperature (25°C) of the samples, heating stage controlled by Linkam MC60 controller was used.

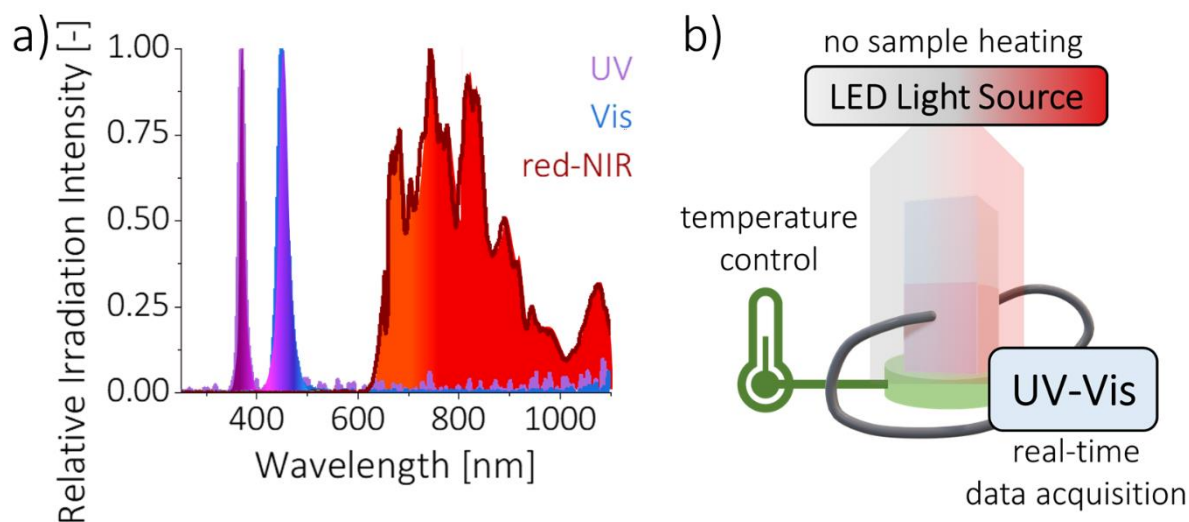


Figure 121. a) Irradiation conditions applied during investigation of plasmon-assisted isomerization of AzoGly. b) Schematic depiction of the custom setup used for the real-time data acquisition during experiments. Reprinted from own source preprint³⁸⁸.

Experimental scenarios

Continuous irradiation: free AzoGly isomerization in EtOH in the presence of AuNRs-CNFs pre-composite. First, AzoGly (0.1 mM in EtOH) was irradiated to ensure total conversion of *E*-AzoGly to *Z*-AzoGly (UV, 370 nm, 2.2 mW/cm² for about 5 min). Second, to the AzoGly PSS_Z EtOH-dispersion the AuNRs-CNFs pre-composite was added, keeping 2:1 volume ratio. Finally, *Z*-*E* isomerization of the photochrome was monitored either in the dark or upon red-NIR irradiation (650-1100 nm, 64.9 mW/cm²) for 1 hour, in real time, collecting UV-Vis-NIR extinction spectra every 1 second. Control experiments were performed in which instead of pre-composite bare CNFs or pure EtOH were added.

OFF-ON interval experiments: AzoGly isomerization in hybrid materials. First, water-based dispersions of AzoGly-AuNRs-CNFs hybrid materials were irradiated to ensure total conversion of *E*-AzoGly to *Z*-AzoGly (UV, 370 nm, 2.2 mW/cm² for about 5 min). Second, *Z*-*E* isomerization of the photochromic component was monitored under interval dark and red-NIR (650-1100 nm, various irradiation intensities) conditions for 1 hour, in real time, collecting UV-Vis-NIR extinction spectra every 1 second. For each sample at least fourteen consecutive intervals (namely seven pairs of the OFF-ON intervals) were collected. Such interval experiment is further referred to as an OFF-ON experiment. Control measurements for the hybrid sample without gold AzoGly-CNFs was also performed.

Statistical Analysis of the OFF-ON Interval Experiments

Statistical modelling was performed in collaboration with **Mateusz Staniak** from Mathematical Institute, University of Wrocław.

The OFF-ON experiments can be perceived as interrupted time series experimental design. Hence, the collected extinction spectra were appropriately transformed. First, intensities of the AzoGly $\pi \rightarrow \pi^*$ band were extracted as a function of time, leading to the formation of datasets represented as a sequence (t, Ext_t) for each sample, where t – time [s], Ext_t – extinction value at that time [-]. Second, for each dataset the Ext_t values were linearized according to the formula: $Y_t = \ln \left(\frac{Ext_{\infty} - Ext_t}{Ext_{\infty} - Ext_0} \right)$, where Ext_{∞} and Ext_0 represent extinction before and after UV irradiation, respectively. Finally, an Autoregressive Integrated Moving Average (ARIMA)-based approach⁴⁷⁰ was applied.

Because the interrupted time series design is applied to the experiments where observations are collected before and after an intervention, each transformed dataset was split into appropriate sub-series. In case of the proposed OFF-ON experiments, there were two types of intervention, namely switching irradiation source on and turning it off. Additionally, for each sample the irradiation source was switched on and off multiple times, so the intervention occurred multiple times as well. Hence, each pair of the consecutive sub-sets, namely dark and light or light and dark segments, was considered separately for each sample.

ARIMA model parameters were estimated using the `auto.arima` function of forecast package⁴⁷¹ available in the R statistical environment.⁴⁷² Parameter describing the Ramp effect was selected as crucial, since it corresponds to change in slope of the data as a result of the intervention. Hence, for each sample (with and without Au and measured under different irradiation conditions), the ARIMA model was fitted for each pair of the consecutive time segments, namely dark and light or light and dark intervals. Subsequently, the significance of Ramp effect was tested for each model. This enabled detection of the statistically significant change in slope of the linearized data occurring as a result of the intervention. Moreover, the Benjamini-Hochberg correction⁴⁷³ was applied in order to account for multiple comparisons.

6.3. Results and discussion

In order to present plasmon-assisted *Z-E* isomerization of AzoGly a proof of concept experiments were designed to investigate the process for two forms of the photochrome, namely (1) free molecules in their native solvent and (2) Azo in the hybrid **AzoGly-AuNRs-CNFs**

material. In case of the first scenario, **AuNRs-CNFs** pre-composite was added to the EtOH solution of the photochrome, taking advantage of the great stability of CNFs-immobilized nanostructures in this solvent. In case of the second experimental scenario, the beneficial spectral separation of Azo and AuNRs in hybrid materials was utilized, to avoid direct triggering of the isomerization of the photochrome. Moreover, both pre-composite and hybrid composite contained AuNRs characterized by high anisotropy ($AR = 3.30$) and, thus, exhibiting also better light-harvesting properties compared to AuNSs, which are typically used in such investigations as described in the section 6.1. of this chapter. All these aspects guaranteed that any changes observed either in the kinetics or in the course of the Azo *Z-E* isomerization stem directly from plasmon-related effects triggered upon proper irradiation.

To properly adjust spectral range of irradiation both position of 1-LSPR band of AuNRs and effect of different wavelengths of irradiation on the AzoGly *Z-E* isomerization were taken into account. Hence, pristine AzoGly solution in EtOH in the PSS_Z was monitored under different modes of irradiation selected using colour glass filters from the Hamamatsu L9588 Lightningcure LC8 halogen lamp used as a light source. The influence of the following modes, exhibiting irradiation intensities in a 200-300 mW/cm² range, was investigated, namely 500-800 nm (>500 nm), 550-800 nm (>550 nm), and 600-800 nm (>600 nm). The results were compared with *Z-E* thermal relaxation of Azo monitored in the dark. Only in case of the irradiation in the 600-800 nm spectral range, the relaxation profile of AzoGly resembled purely thermal *Z-E* isomerization of the photochrome (**Figure 122**). The observed small increasing tendency (as depicted in Figure 122) originated from sample temperature change, as measured inside of the cuvette using PT1000 temperature sensor. Measurement indicated a 5°C temperature rise, which was attributed to the heating caused by the irradiation beam. Hence, in further experiments, to verify the assumptions of the possible plasmon-assisted process, a custom setup was used for real-time UV-Vis-NIR spectra acquisition, sample irradiation, and temperature control of the process. To assure that the changes in Azo isomerization are not a result of the sample heating by irradiation beam a LED light source and a heating stage were used. Moreover, in all plasmon-assisted experiments irradiation starting above 600 nm was applied.

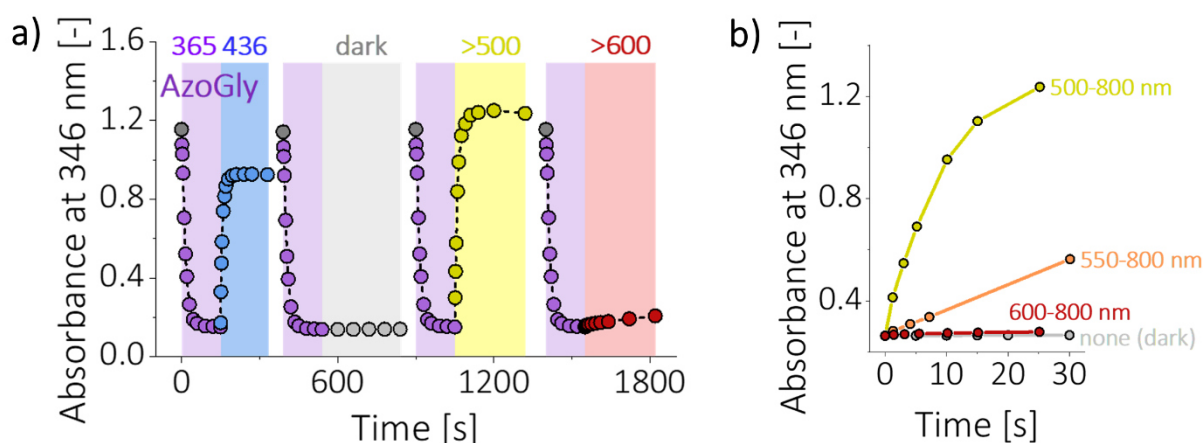


Figure 122. a) Evolution of the $\pi \rightarrow \pi^*$ band intensity of free AzoGly in EtOH upon Z-E thermal relaxation accompanied by different modes of irradiation. b) Even for irradiation starting from 550 nm a significant deviation from thermal relaxation in the dark occurs within 30 seconds. Upon proper temperature control of the sample only the spectral range above 600 nm does not affect the monitored reaction. Reprinted from own source preprint ³⁸⁸.

Another factor introduced to increase the efficiency of the plasmon-assisted process was the increased loading of AuNRs on CNFs (~19.6 wt%) compared to hybrid materials described in the previous chapters of the dissertation. Such increased loading translates into more pronounced plasmon-derived phenomena, particularly the thermoplasmonic effect, since collective effects might be manifested.

6.3.1. Plasmon-assisted Z-E isomerization of free AzoGly in ethanol solution

First, the discussion is focused on the plasmon-assisted Z-E isomerization of free AzoGly molecules. This aspect can be treated as an introduction to proper understanding of the process in the hybrid formulation. This subsection concerns experimental scenario in which to the EtOH solution of the photochrome the AuNRs-CNFs pre-composite is added.

By investigating reaction in the native solvent of the photochrome (EtOH), temporal resolution of the process was increased compared to AzoGly-AuNRs-CNFs hybrid material, because as presented in Chapter 5, thermal half-life of AzoGly at room temperature equals 24.6 hours. Moreover, in this experimental scenario AuNRs were added to the PSS_Z of AzoGly, and, hence, nanostructures were separated from the stage of UV exposure. This approach excludes participation of intraband excitations in the investigated process. Figure 123 depicts chosen irradiation conditions (650-1100 nm, 64.9 mW/cm²) and how well they corresponded with the position of the l-LSPR band of AuNRs in the pre-composite material.

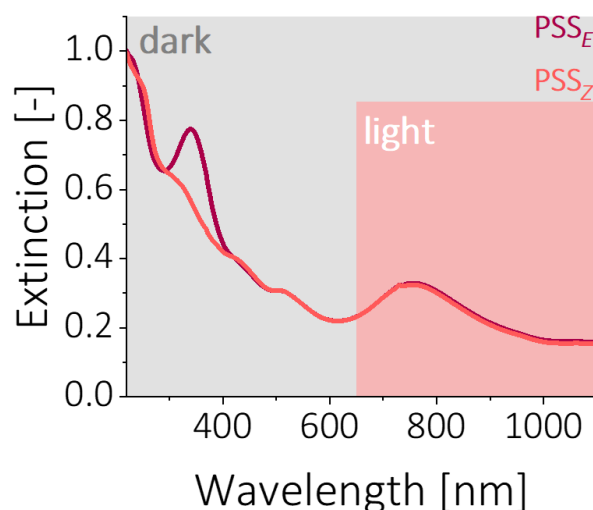


Figure 123. Schematic depiction of the chosen irradiation conditions (650-1100 nm). Spectral range was chosen to match the position of *l*-LSPR band of AuNRs and to not trigger AzoGly isomerization. Reprinted from own source preprint ³⁸⁸.

The *Z-E* isomerization of AzoGly was not affected by irradiation conditions and the relaxation profiles were almost identical to AzoGly relaxation in the dark (**Figure 124a**). Moreover, upon the addition of bare cellulose nanofibres under dark and light conditions, only negligible change to the relaxation profiles was observed (**Figure 124b**). To determine quantitatively whether irradiation or addition of CNFs affected *Z-E* isomerization of AzoGly, relative differences between each pair of experiments were calculated, as follows:

- addition of bare CNFs (dark vs. light conditions): 8.56%,
- pristine AzoGly solution (dark vs. light conditions): 3.68%,
- light conditions (pristine AzoGly solution vs. bare CNFs): 2.61%,
- dark conditions (pristine AzoGly solution vs. bare CNFs): 2.27%.

The calculated values were in a good agreement with typically observed errors for the repetitions of Azo photochromes kinetic measurements, as reported by Gille *et al.*,⁴⁷⁴ thus indicating that in fact all of these relaxations are comparable. Hence, the influence of bare CNFs scaffold on AzoGly *Z-E* isomerization was determined to be negligible, both in the dark and under illumination and the inert nature of the scaffold was proved one more time.

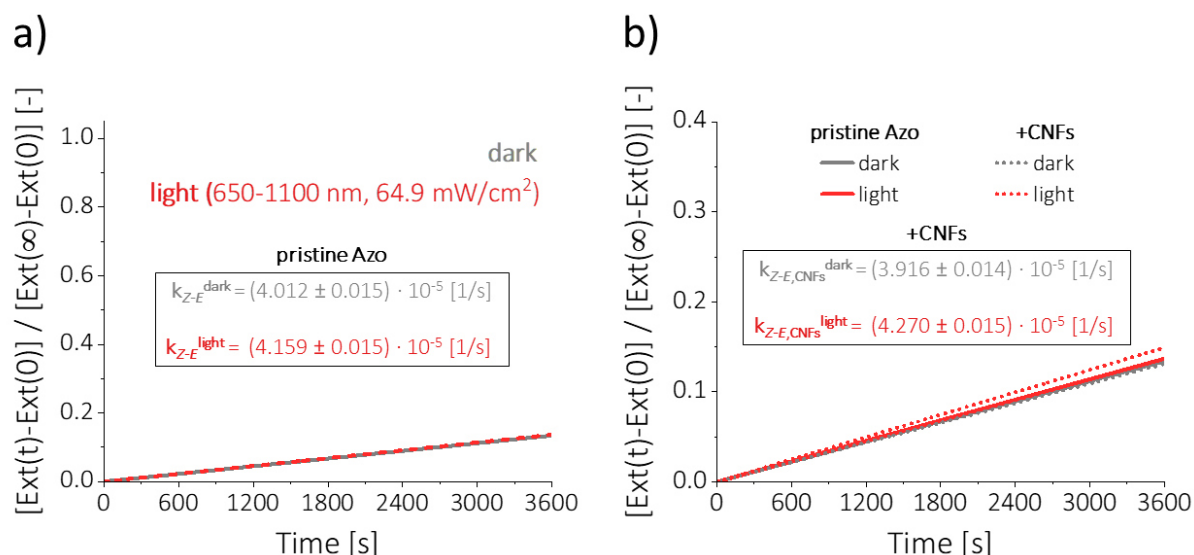


Figure 124. Comparison of the AzoGly thermal relaxation profiles measured at room temperature (25°C) to determine influence of **a)** the chosen irradiation conditions (no effect) and **b)** CNFs scaffold (negligible effect). Reprinted from own source preprint³⁸⁸.

The addition of **AuNRs-CNFs** pre-composite to the pristine solution of AzoGly at 25°C resulted in the drastic change of the relaxation profile both in the dark and under illumination (**Figure 125a**). The rate constant value of the Z-E isomerization in the dark was determined to be one order of magnitude higher, compared to pristine AzoGly ($k_{Z-E,\text{Au}}^{\text{dark}} = (7.09 \pm 0.04) \cdot 10^{-4} \text{ s}^{-1}$). Upon the applied red-NIR irradiation, the observed catalytic boost in the presence of AuNRs was even more pronounced and the increase of two orders of magnitude compared to pristine AzoGly was observed ($k_{Z-E,\text{Au}}^{\text{light}} = (3.15 \pm 0.03) \cdot 10^{-3} \text{ s}^{-1}$). To provide a visual measure of the catalytic influence of AuNRs, thermal half-lives can be compared. Upon addition of AuNRs in the dark $\tau_{1/2}$ of AzoGly was reduced from 24.6 hours to 16.3 minutes. Upon the irradiation in the presence of AuNRs further shortening of $\tau_{1/2}$ to 3.7 min was observed.

The observation of catalytic effect of AuNRs in such plasmon-assisted process may constitute a sole purpose of the research. However, this dissertation proposes utilization of the obtained data to get more insight into the investigated system. The obtained rate constants of the process in the presence of AuNRs ($k_{Z-E,\text{Au}}^{\text{dark}}$ and $k_{Z-E,\text{Au}}^{\text{light}}$) can be translated, based on the Arrhenius equation, to temperatures in which equivalent Azo Z-E isomerization would occur at the same rate, assuming dark conditions and no Au present.

For this recalculation the parameters of Arrhenius equation, $\ln k = a \cdot \frac{1}{T} + b$, determined for pristine AzoGly were used, namely $a = -9224.0 [\text{K}]$, and $b = 19.2 [-]$, based on Figure 116a. This approach recalculates $k_{Z-E,\text{Au}}^{\text{dark}}$ and $k_{Z-E,\text{Au}}^{\text{light}}$ into ‘virtual temperatures’ of the process, 76°C for $k_{Z-E,\text{Au}}^{\text{dark}}$ and 97°C for $k_{Z-E,\text{Au}}^{\text{light}}$ (**Figure 125b**). It does not mean that these reactions

progress at such temperatures, especially if the boiling point of EtOH is considered (about 78°C and no boiling of the samples was observed). Instead, these values represent temperatures at which pristine Azo thermal relaxation in the dark would need to occur in order to be described by the same rate constant values. Hence, catalytic effect of AuNRs, both in the dark and in the plasmon-assisted process, can be quantitatively measured as the proposed ‘virtual temperatures’.

In the dark, as already discussed in Chapter 5, AuNRs catalyse Azo *Z-E* isomerization via electron transfer. As it will be discussed further in the text, under the proposed irradiation conditions the most dominant plasmon-derived phenomenon is thermoplasmonic effect, especially for materials with such high AuNRs loading (~19.6 wt%). Hence, the catalytic boost in the plasmon-assisted process can be recalculated into the quantitative measure of the collective heating of AuNRs.¹⁵⁸ After accounting for contribution of the eT mechanism in the absence of irradiation (97°C - 76°C), it can be assumed that the thermoplasmonic effect causes temperature rise of 21°C.

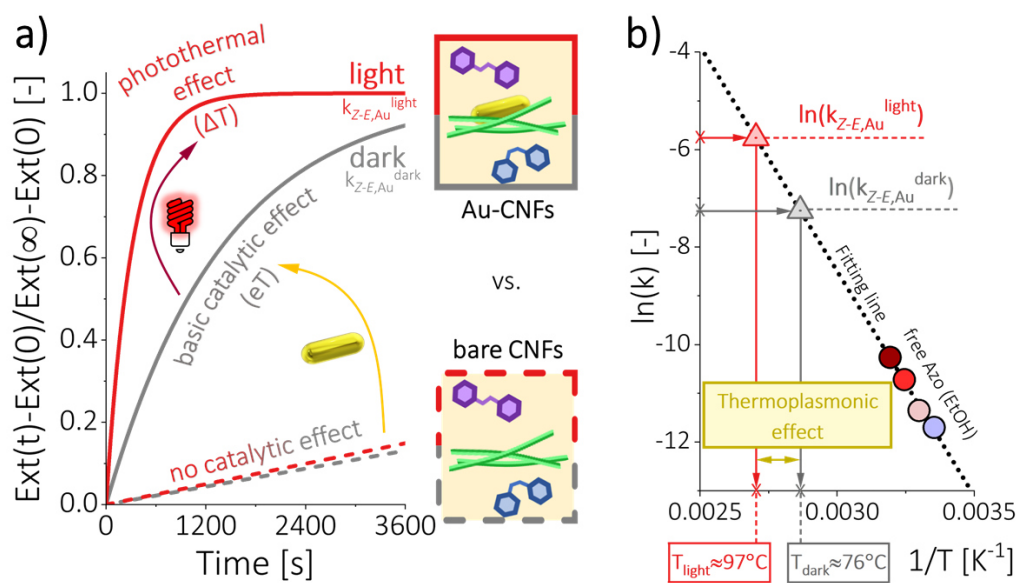


Figure 125. **a)** Comparison of the free AzoGly thermal relaxation profiles in EtOH upon the addition of bare CNFs (dashed lines, no effect) and AuNRs-CNFs (solid lines, clear catalytic enhancement). AuNRs catalyse Azo isomerization in the dark via electron transfer and upon irradiation the catalytic boost stems mainly from thermoplasmonic effect. **b)** The extent of the thermoplasmonic effect can be estimated due to the proposed recalculation of the rate constant values of Azo isomerization in the presence of AuNRs into ‘virtual temperatures’ of the process. Reprinted from own source preprint³⁸⁸.

One of the arguments presented within this chapter for more dominant contribution of the thermoplasmonic effect under red-NIR irradiation, compared to other plasmon-related

phenomena, is the dependency between the observed *Z-E* isomerization rate constants (measured for hybrid **AzoGly-AuNRs-CNFs** materials) and power density of the incident irradiation (650-1100 nm). As presented in **Figure 126**, the exponential fit of the data can be proposed, which is in a good agreement with the Arrhenius law. Such experimental verification clearly implies towards more significant contribution of the thermoplasmonic effect during the plasmon-assisted process.¹⁶⁰

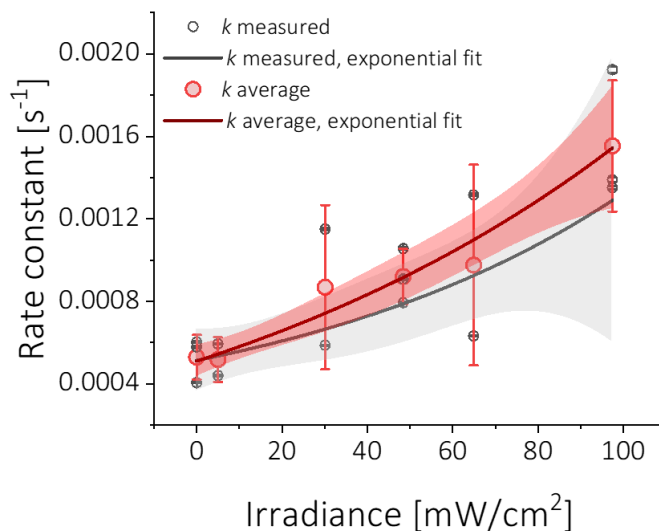


Figure 126. Exponential fitting of the rate constants of Azo *Z-E* isomerization (determined for hybrid **AzoGly-AuNRs-CNFs** materials) vs. red-NIR (650-1100 nm) light irradiance according to Arrhenius law implies predominant contribution of the thermoplasmonic effect in the plasmon-assisted process. Reprinted from own source preprint³⁸⁸.

6.3.2. Plasmon-assisted *Z-E* isomerization of AzoGly in the hybrid material

This subsection concerns plasmon-assisted isomerization of the photochromic component in the hybrid **AzoGly-AuNRs-CNFs** formulation dispersed in water. Heavy loading of CNFs with AuNRs (~19.6 wt%) resulted in a lower resolution of the observed $\pi \rightarrow \pi^*$ band changes (**Figure 127**), due to the highly scattering nature of the scaffold. Moreover, the increased loading contributed to faster composite sedimentation and randomized the macroscopic behaviour of the hybrid material. Additionally, the aqueous environment decreased temporal resolution of isomerization as described in previous chapters. These aspects made consecutive spectroscopic experiments less comparable and required new experimental design.

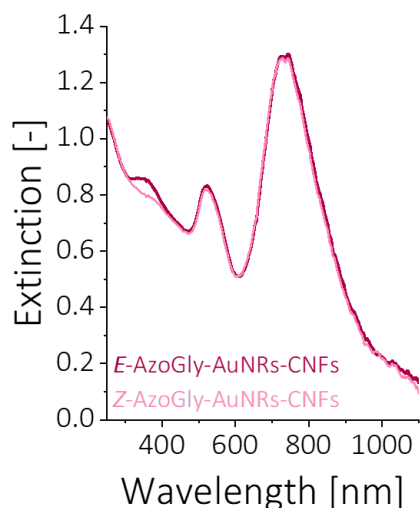


Figure 127. Hybrid *AzoGly-AuNRs-CNFs* material in PSS_E and PSS_Z . The intensity of the $\pi \rightarrow \pi^*$ band is decreased due to the highly scattering nature of the AuNRs-CNFs at high Au loading. Reprinted from own source preprint ³⁸⁸.

To assure that AzoGly Z-E isomerization monitored in the dark and under illumination can be compared, an OFF-ON experiment had been designed in which hybrid material was subjected to alternating irradiation conditions. Hence, during the whole relaxation process, monitored in a single experiment, hybrid material was subjected to the consecutive intervals of dark and light (red-NIR, 650-1100 nm, 145.8 mW/cm²) conditions. Thus, several aspects were assured. First, possibility of the occurrence of systematic and random errors was minimized, because random deviations resulting from e.g. material sedimentation were affecting dark and light segments in the same way. Second, such experimental design enabled visualisation of hybrid system's susceptibility to light. Apart from the alternating irradiation, the same conditions of the experiment were kept throughout the whole relaxation process. Duration of dark and light segments was adjusted, so both intervals lasted either 5.0 or 2.5 minutes each. Behaviour of hybrid materials with and without Au was investigated, as presented in **Table 5**. Numbering proposed in the table will be used further in the text to refer to appropriate sample.

Table 5. Samples and irradiation conditions for the OFF-ON experiments. Hybrid materials with and without Au were investigated and two variants of intervals duration were applied (2.5 or 5.0 min). Reprinted from own source preprint ³⁸⁸.

Sample Number	Au present?	Spectral range [nm]	Power density [mW/cm ²]	Interval duration [min]
1	YES	650-1100	145.8	5.0
2	YES			2.5
3	NO			5.0
4	NO			2.5

During the OFF-ON experiment the whole spectrum of hybrid sample was measured every 1 second. Subsequently, the recorded data were processed according to the methodology presented in the subsection 6.2.3. of this chapter. Essentially, data describing evolution of the $\pi \rightarrow \pi^*$ band intensity in time were linearized to conform with the assumptions of the subsequently applied statistical model.⁴⁷⁵

In the OFF-ON experiments hybrid samples were subjected to two types of intervention, namely switching irradiation on and off. In the analysis, the evolution of the data before and after each intervening event was compared. It can be hypothesised, that for AuNRs-containing materials upon irradiation the plasmon-assisted Azo *Z-E* isomerization takes place. Based on the conclusions of the previous subsection on the predominant contribution of the thermoplasmonic effect upon irradiation, it can be assumed that the collective heating of AuNRs triggered by red-NIR illumination leads to the temperature increase in the vicinity of nanoparticles. Hence, the *Z-E* isomerization of AzoGly should occur faster, which should be manifested for the linearized data as the slope increase. Upon proper adjustment of experimental conditions and material formulation such slope changes should be easy to assess via naked eye observation.

To account for a complex composition of the proposed formulation and to provide quantitative measures of the observed effects, appropriate statistical tools were applied. Because of autocorrelation typical in time-varying data (since every subsequent extinction value was a direct evolution of the previous extinction values), the assumptions of classical linear models were violated and the datasets needed to be analysed with a different model. Hence, in the analysis the Autoregressive Integrated Moving Average (ARIMA) model⁴⁷⁰ was used.

There are four components to this approach, namely autoregressive model (AR), moving average model (MA), seasonal model, and differencing (integration). Because the seasonal part did not apply to the analysed data, a non-seasonal ARIMA model was used, which is described by a set of parameters (p, d, q) denoting degree of seasonality and defined, respectively, as the order of the autoregressive part of the model (p), the degree of non-seasonal differencing (d), and the order of the moving average part of the model (q).

Single variable Y_t is represented in the model as a function of the variable's previous value (e.g. Y_{t-1}), the occurring random error (ϵ_t), as well as the random error's previous values (e.g. ϵ_{t-1}). Moreover, optional covariates, differencing, and seasonal effect can also be included. The optional covariates enable modelling of the data with additional independent variables to describe the effect of the intervention on the dataset. In case of the analysed datasets only one of the covariates was expected to appear, as only the change in the slope of the data was expected to be observed. Such slope change is described by a so-called Ramp effect. ARIMA approach enables estimation of this effect while taking into account the autocorrelation.

Thus, the linearized datasets were modelled as a function of previous values (AR model), error term's previous values (MA model), differencing, and the Ramp variable (**Figure 128**).

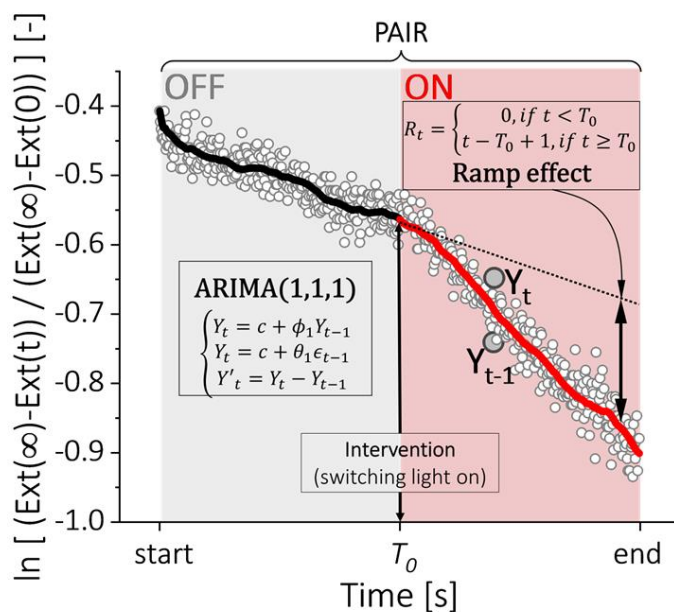


Figure 128. Schematic depiction of the applied statistical modelling approach (ARIMA) for the analysis of the AzoGly Z-E isomerization in the water-dispersed hybrid AzoGly-AuNRs-CNFs material. Depiction includes representation of ARIMA (1,1,1). Influence of irradiation on the sample is manifested as the slope change of the dataset in the ON region, triggered upon intervention (at a time T_0). Hence, the Ramp effect estimation was chosen to evaluate influence of the intervention. Although ARIMA is a linear model, the predicted values (represented by solid lines) will not lie on the same line, because they are forecast based on the varying set of previous values (datapoints are represented by circles). Reprinted from own source preprint³⁸⁸.

In case of each OFF-ON experiment the intervention occurred several times, hence, in modelling the appropriate intervals were paired up in a particular order, depending on the type of intervention. For 'switching irradiation on' as an intervention, dark and the subsequent light intervals were paired and each pair was modelled separately for the respective sample. For 'switching irradiation off' as an intervention, light and the subsequent dark intervals were paired and analysed. For each experiment at least four consecutive dark-light or light-dark pairs were modelled, particularly for the times corresponding to the biggest change in the extinction of the $\pi \rightarrow \pi^*$ band. In all cases statistical modelling resulted in quantitative measures of Ramp effect for each modelled pair. Moreover, additional testing was performed to determine which pairs were characterized by statistically significant differences in slope (statistically significant Ramp effect), which was assessed based on the calculated p-values. Significant test results indicated that difference between the consecutive intervals cannot be ascribed to random data variation,

but is a direct result of a slope change (and hence also change of the isomerization rate) due to the intervention.

First, the results of modelling for the intervention defined as ‘switching irradiation on’ are presented and discussed. Selected parameters of ARIMA modelling and the estimated Ramp effect values for all samples are summarized in the appendix (section 6.5.) in **Table 8** and **Table 9**, respectively. Negative values of Ramp effect estimates presented in **Table 9** indicated that slope increased after the intervention, which means that rate of the AzoGly *Z-E* isomerization is faster during irradiation, compared to dark conditions. For the experiments with 5.0 min intervals duration, the comparison of samples **1** (Au) and **3** (no Au) indicated that intervention induced slope change solely for sample **1**. Changes in the data trend can be assessed even with a naked eye by looking at the **Figure 129a**, where the linear trend of the dataset is disrupted exactly at times of the intervention. Visual assessment of the data also revealed slope increase in the light intervals. In contrary, for sample **3** (control sample without Au), dataset presented smooth linear trend without any slope disruptions upon sample irradiation (**Figure 129a**). Similar conclusions can be drawn from comparison of samples **2** (Au) and **4** (no Au) for the experiments with 2.5 min intervals duration (**Figure 130a,b**).

However, the qualitative visual assessment and sole values of Ramp effect estimates cannot be used to formulate conclusive statistical statements. Hence, p-values for tests of significance of the Ramp effect were calculated, as presented in **Table 6**. The calculated effects with p-values < 0.05 can be treated at 5% significance level as different from 0 and are marked with green colour. Based on the testing results it can be stated, that statistically significant Ramp effects were observed upon irradiation only for samples containing AuNRs (values indicated with green colour in **Table 6**), as presented in both **Figure 129b** and **Figure 130c**. For the fourth modelled pair for sample **1** (marked with yellow colour), the calculated p-value was higher than 0.05, nevertheless it was still significantly lower compared to sample **3**. For the control samples without AuNRs, Ramp estimates were not statistically significant (values indicated with red colour in **Table 6**).

Since the observed changes are triggered by direct irradiation of AuNRs and not AzoGly, it can be concluded, that plasmonic component of the hybrid material enables indirect control over the kinetics of the AzoGly *Z-E* isomerization under red-NIR irradiation. Moreover, the induced kinetic changes, observed for the hybrid materials under interval irradiation, can be triggered in an ON-OFF manner.

Table 6. Adjusted p -values for Ramp effect tests of significance for each modelled OFF-ON pair. Intervention defined as ‘switching irradiation on’. Values relatively close to the $p=0.05$ level are indicated with yellow colour. Reprinted from own source preprint³⁸⁸.

Sample	Content	Pair 1	Pair 2	Pair 3	Pair 4	Pair 5
1	Au	0.00028	0.00000	0.00000	0.12451	0.01207
2	Au	0.00000	0.00073* (0.00073)	0.00073* (0.00052)	0.00073* (0.00067)	-
3	no Au	0.82276* (0.63962)	0.82276* (0.76667)	0.82276* (0.58053)	0.82276* (0.55923)	0.23613
4	no Au	0.38182	0.38182	0.07253	0.99606	0.06671

* Values are not equal before Benjamini-Hochberg correction, as indicated in the brackets.

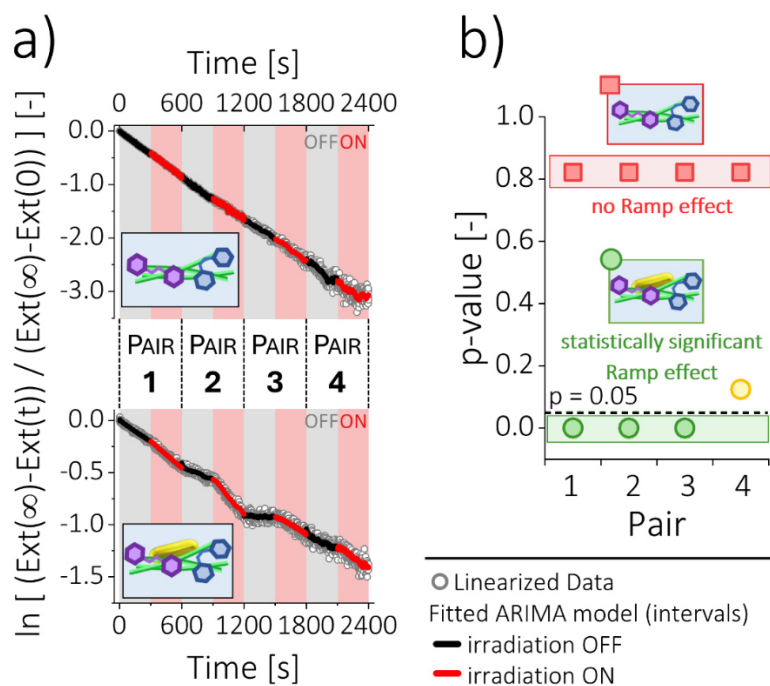


Figure 129. a) Statistical modelling results for samples (top) without AuNRs (3) and (bottom) with AuNRs (1). The considered intervention – ‘switching irradiation on’ (5.0 min intervals, OFF-ON pairs modelled). b) Adjusted p -values for Ramp effect tests of significance indicate indirect control over Azo isomerization only in the presence of AuNRs. The overall structure of the figure indicates how intervals were paired and visually correlates the results between panels a) and b). Reprinted from own source preprint³⁸⁸.

For the third modelled pair for sample 4 (no Au), a slight disruption of the dataset occurred (Figure 130b), which could be ascribed to the sedimentation of the hybrid material, even despite the fact that data were initially corrected at the isosbestic point of the hybrid samples.

These observations emphasise the significance of the proposed OFF-ON experimental design for the impartial comparison of the investigated processes based not on the determined rate constant values, but statistical parameters of properly chosen models.

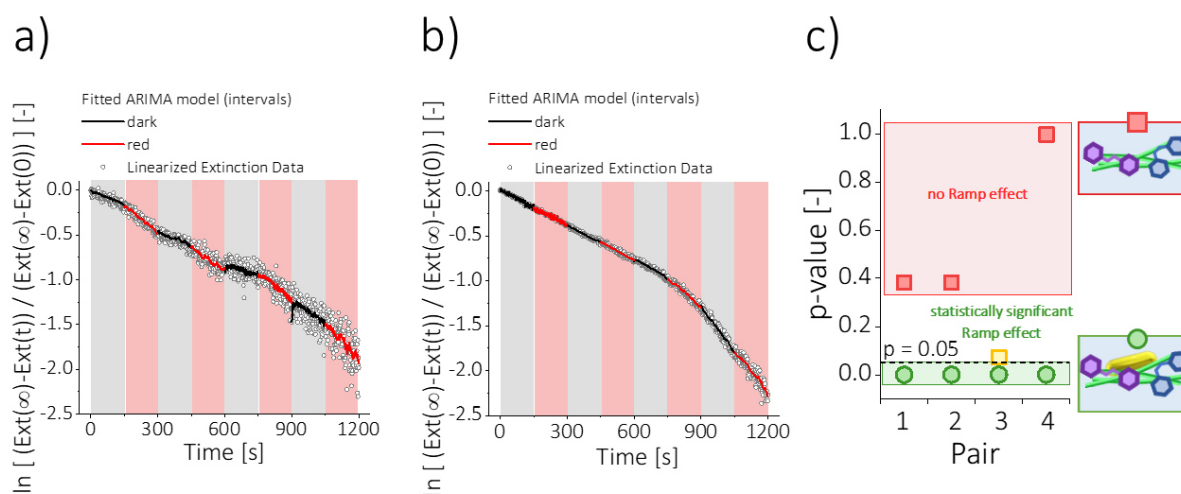


Figure 130. Statistical modelling results for samples **a)** with AuNRs (2) and **b)** without AuNRs (4). The considered intervention – ‘switching irradiation on’ (2.5 min intervals, OFF-ON pairs modelled). **c)** Adjusted p-values for Ramp effect tests of significance indicate indirect control over Azo isomerization only in the presence of AuNRs. Reprinted from own source preprint³⁸⁸.

Upon considering second type of intervention, namely ‘switching irradiation off’, statistical modelling of the datasets revealed more arguments for the predominant role of the thermoplasmonic effect in the plasmon-assisted Azo *Z-E* isomerization. Selected parameters of ARIMA model, for the light-dark pairing, and the estimated Ramp effect values for all samples are summarized in the appendix (section 6.5.) in **Table 10** and **Table 11**, respectively. Here, the positive values of Ramp effect estimates presented in **Table 11** indicated slope decrease after the intervention, which means that rate of the AzoGly *Z-E* isomerization is slower in the dark, compared to light conditions. Results presented in **Table 7** and in **Figure 131** and **Figure 132** clearly show slope changes only for hybrid samples containing AuNRs, similar to the results for the first type of the intervention. Comparison of **Figure 131c** and **Figure 132c**, however, revealed quantitative differences between experiments performed for AuNRs-containing samples, however differing in the intervals duration. As indicated in **Figure 132c**, the calculated p-values were slightly larger than the assumed $p=0.05$ level. Hence, it can be concluded, that the influence of intervention defined as switching irradiation off is more subtle, when the irradiation intervals are shortened.

It is important to note that, by definition, the estimation of Ramp effect enables detection of the immediate changes induced by the analysed intervention. Hence, it can be assumed that the slightly higher values of the p-level for sample 2 ($p=0.06823$ for pairs 1-3), do not dismiss the

occurrence of the slope change as a result of switching irradiation off, but rather emphasise that the observed changes are not as instantaneous as for other type of intervention. This information can be used to conclude on the mechanism of the plasmon-assisted process triggered in the hybrid material upon irradiation. In case of the pure contribution from hot charge carriers generated upon irradiation, due to their short lifetime (few tens of fs), the observed changes in the evolution of the $\pi \rightarrow \pi^*$ band should be instantaneous both for switching irradiation on and off. Moreover, there should be no dependency on the intervals length. However, in case of the contribution from thermoplasmonic effect, heat dissipation needs to be considered, particularly for the water-dispersed hybrid material exhibiting such complexity as the proposed formulation. Hence, in the real life system influence of the thermoplasmonic effect exhibits much longer timeframe. Accordingly, for the shortened intervals the observed slope change becomes less pronounced. These conclusions correlate well with the exponential dependency between $Z-E$ isomerization rate constants determined in the hybrid material plotted vs. intensity of the irradiation, as presented in **Figure 126** and constitute basis for the conclusion on the dominant contribution of the thermoplasmonic effect in the performed plasmon-assisted Azo isomerization.

Table 7. Adjusted p -values for Ramp effect tests of significance for each modelled ON-OFF pair. Intervention defined as ‘switching irradiation off’. Values relatively close to the $p=0.05$ level are indicated with yellow colour. Reprinted from own source preprint³⁸⁸.

Sample	Content	Pair 1	Pair 2	Pair 3	Pair 4	Pair 5
1	Au	0.00000	0.00000	0.13287	0.03655	0.00005
2	Au	0.06823* (0.04048)	0.06823* (0.05117)	0.06823* (0.0209)	0.09004	-
3	no Au	0.98750* (0.98750)	0.98750* (0.75944)	0.98750* (0.93775)	0.98750* (0.95901)	0.98750* (0.97923)
4	no Au	0.86521	0.80271	0.00000	0.34725	0.80271

* Values are not equal before Benjamini-Hochberg correction, as indicated in the brackets.

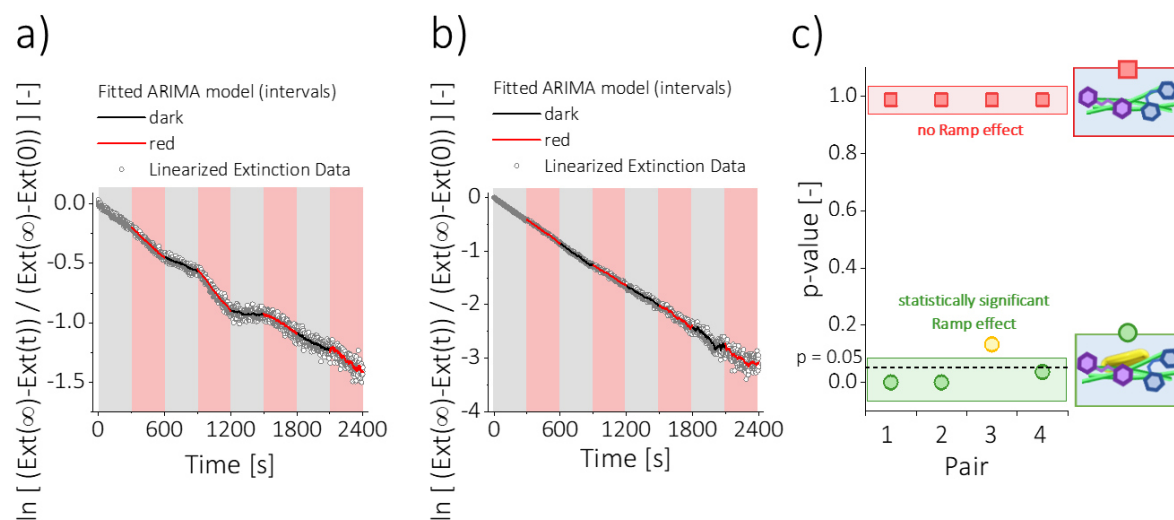


Figure 131. Statistical modelling results for samples **a)** with AuNRs (1) and **b)** without AuNRs (3). The considered intervention – ‘switching irradiation off’ (5.0 min intervals, ON-OFF pairs modelled). **c)** Adjusted *p*-values for Ramp effect tests of significance indicate kinetic changes in the Azo isomerization as a result of turning irradiation off only in the presence of AuNRs. Reprinted from own source preprint³⁸⁸.

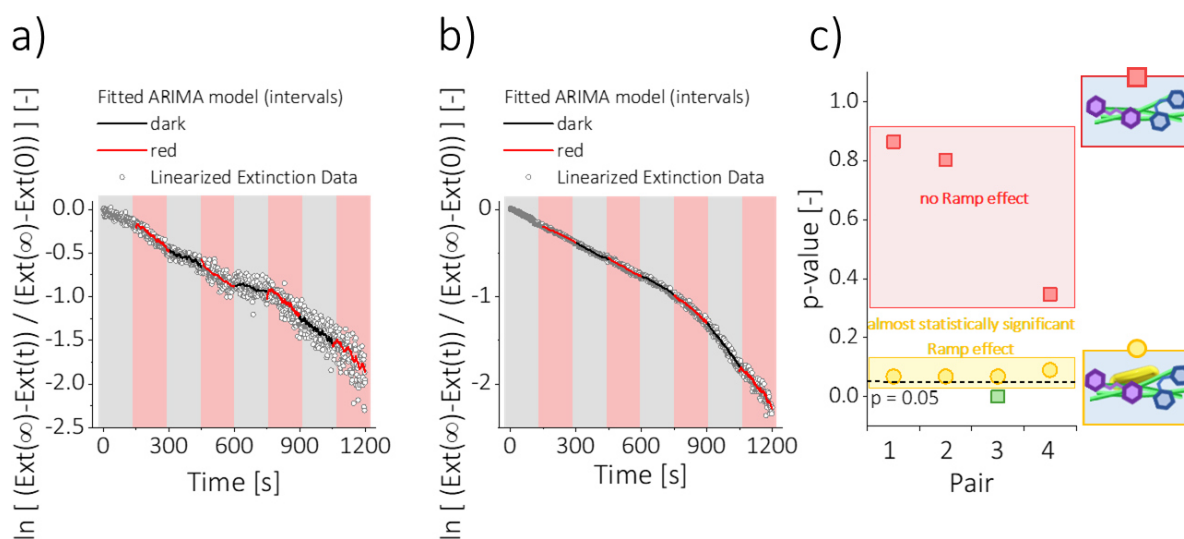


Figure 132. Statistical modelling results for samples **a)** with AuNRs (2) and **b)** without AuNRs (4). The considered intervention – ‘switching irradiation off’ (2.5 min intervals, ON-OFF pairs modelled). **c)** Adjusted *p*-values for Ramp effect tests of significance indicate kinetic changes in the Azo isomerization (although less pronounced than for longer intervals) as a result of turning irradiation off only in the presence of AuNRs. Reprinted from own source preprint³⁸⁸.

6.4. Conclusions

This chapter summarizes the investigation of plasmon-assisted *Z-E* isomerization of AzoGly in two forms, namely free photochrome molecules in solution and CNFs-bound components of the hybrid **AzoGly-AuNRs-CNFs** formulation. Moreover, the possibility of indirect reaction control via plasmon-related effects is presented and thus, the **objective 4** of the dissertation was challenged. *Z-E* isomerization of free AzoGly molecules in EtOH and in the presence of **AuNRs-CNFs** pre-composite exhibited dramatic kinetic increase by one order of magnitude in the dark and by two orders of magnitude as a result of triggering of the plasmon-assisted process upon red-NIR irradiation (650-1100 nm, spectral range not absorbed by the photochrome). This corroborates part of the **hypothesis 7** of the dissertation. The kinetic changes were used to assess the temperature of the sample at the nanoscale in order to quantify the extent of the thermoplasmonic effect. Hence, the dissertation proposes use of Azo type photochromes as molecular thermometers. Further investigation of the plasmon-assisted process in the water-dispersed hybrid **AzoGly-AuNRs-CNFs** material was performed by carrying out an OFF-ON experiment with varying, interval irradiation conditions. Results revealed that the presence of AuNRs enables indirect photocontrol over the *Z-E* isomerization of Azo in the ON-OFF manner. The applied statistical modelling (ARIMA-based approach) quantitatively visualized that both types of interventions, namely switching irradiation off and on, lead to statistically significant kinetic changes only for samples containing Au. Statistical modelling also contributed to the final conclusion of the predominant contribution of the thermoplasmonic effect in the plasmon assisted process, which confirmed **hypothesis 7**.

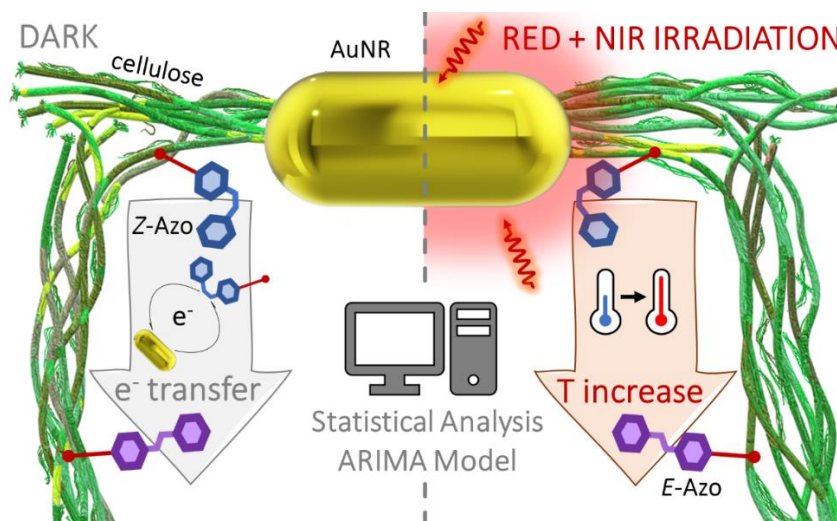


Figure 133. Under red-NIR irradiation plasmon-assisted AzoGly *Z-E* isomerization occurs. The conversion of the energy absorbed by AuNRs into heat ensues via thermoplasmonic effect. Hence, the instantaneous ON-OFF indirect control over the kinetics of Azo isomerization is

enabled, as revealed by statistical modelling using ARIMA-based approach. Reprinted from own source preprint ³⁸⁸.

6.5. Appendix

Table 8. ARIMA (p, d, q) parameters for the analysed intervention – ‘switching irradiation on’. Reprinted from own source preprint ³⁸⁸.

Sample	OFF-ON pair	p (AR order)	d (degree of differencing)	q (MA order)
1	1	1	1	1
	2	1	1	2
	3	2	0	1
	4	3	1	2
	5	0	1	2
	6	1	1	4
2	1	2	1	2
	2	1	1	1
	3	2	1	2
	4	1	1	1
	5	1	0	1
3	1	1	2	0
	2	4	2	0
	3	0	1	1
	4	0	1	1
	5	0	1	2
	6	5	1	0
4	1	1	2	0
	2	0	1	1
	3	1	1	1
	4	0	1	1
	5	1	1	1

Table 9. Ramp effect estimates for each OFF-ON pair for the considered intervention – ‘switching irradiation on’. Reprinted from own source preprint ³⁸⁸.

Sample	Content	Pair 1	Pair 2	Pair 3	Pair 4	Pair 5
1	Au	-0.00019	-0.00074	-0.00056	-0.00025	0.00119
2	Au	-0.00207	-0.00160	-0.00146	-0.00275	-
3	no Au	-0.00502	-0.00301	-0.00015	0.00045	-0.00178
4	no Au	0.01356	-0.00015	-0.00066	0.00000	-0.00403

Table 10. ARIMA (p, d, q) parameters for the analysed intervention – ‘switching irradiation off’. Reprinted from own source preprint ³⁸⁸.

Sample	ON-OFF pair	p (AR order)	d (degree of differencing)	q (MA order)
1	1	0	1	2
	2	0	1	1
	3	0	1	2
	4	2	1	2
	5	0	1	2
	6	0	1	2
2	1	0	1	1
	2	0	1	1
	3	1	1	1
	4	0	1	1
3	1	2	2	2
	2	0	1	1
	3	0	1	1
	4	1	1	1
	5	2	1	4
	6	4	1	0
4	1	0	1	1
	2	0	1	1
	3	1	1	2
	4	2	1	1
	5	1	1	0

Table 11. Ramp effect estimates for each ON-OFF pair for the considered intervention – ‘switching irradiation off’. Reprinted from own source preprint ³⁸⁸.

Sample	Content	Pair 1	Pair 2	Pair 3	Pair 4	Pair 5
1	Au	0.00045	0.00108	0.00014	-0.00080	-0.00117
2	Au	-0.00125	0.00090	-0.00183	-0.00215	-
3	no Au	0.00001	0.00005	0.00005	-0.00003	0.00007
4	no Au	-0.00002	-0.00008	-0.00117	-0.00115	-0.26463

III SUMMARY

Chapter 7. *Conclusions and Perspectives*

The main outcomes of this dissertation are, first, the development of novel, advanced, functional materials based on cellulose nanofibres and plasmonic nanoparticles, in particular on gold nanorods, and, second, presentation of their application in the photocontrol of the chemical processes. The proposed formulations in which CNFs serve as an inert and robust scaffold, enabled stabilization of the optical properties of AuNRs under various conditions, including intense irradiations, environment of organic solvents, and extreme pH conditions. Such stabilization was further utilized to optically address AuNRs and gain control over reactions, such as cofactor regeneration or isomerization of photochromic molecules. The proposed material design also enabled preparation of a new type of plasmonic-photochromic materials in which both components maintained their functionality. The established protocols are facile and easy to replicate, because all material formulations rely mainly on electrostatic interactions between components.

Chapter 3 establishes general protocol for the preparation of AuNRs-CNFs materials. Influence of components concentration is presented in a form of quasi-phase diagram of the system. Immobilization of AuNRs on macroscopic cellulose nanofibers grants great stability of nanocrystals' plasmonic properties under intense illumination, elevated temperatures, and at wide pH range, hence, confirming **hypothesis 1** of the dissertation. Moreover, crucial role of CTAB (a stabilizing agent inherently present after synthesis of AuNRs on their surface) in the creation of the hybrid formulation was confirmed.

This chapter presents also functionality of the proposed formulation as a photocatalyst and introduces a conceptually new plasmon-assisted photochemical process of simultaneously coupled dehydrogenation of sodium formate and regeneration of NADH cofactor molecules in the presence of AuPdNRs-CNFs hybrid material and visible light irradiation. Immobilization of plasmonic nanostructures on the CNFs scaffold enabled efficient excess CTAB removal, which excluded hindering effect of the surfactant. Thus, **hypothesis 2** of the dissertation was confirmed. The plasmon resonance-driven character of the process, performed at the determined optimal conditions, lead to up to 40% of NADH regeneration within 2 hours without use of reaction mediators. Results also confirmed surface-dependent nature of the reaction, important role of Pd as a co-catalyst, and limitations derived from NADH back-oxidation at low pH.

Outcomes of this chapter can be further implemented to develop macroscopic, processable materials, e.g. by employing 3D printing. Moreover, the new material formulations can be prepared starting from different AuNRs-CNFs phase forms, including gels or viscous solutions.

Results presented in Chapter 3 became a starting point for the investigation presented in Chapter 4, which addresses current challenges in the field of plasmonic-photochromic hybrid systems. This chapter establishes general protocol for the preparation of multifunctional, hybrid plasmonic-photochromic materials based on AuNRs-CNFs and a model azobenzene-type photochrome. Protocol relies on CNFs scaffold impregnation with the chosen non-thiolated Azo ligand, mainly via electrostatic attraction and hydrogen bonds formation. Contribution of the $\pi \rightarrow \pi^*$ band to the overall optical properties of the hybrid material increased with the increasing photochrome concentration during impregnation step, namely about 26 times band intensity increase was a result of 3.8 times increase in the photochrome concentration. The resulting formulation was entirely water-functional and operated without aggregation, in contrary to the most popular Azo-AuNPs hybrids. Thus, results presented in chapter 4 corroborate **hypothesis 3** of the dissertation.

The proposed protocol includes a pretreatment step in which AuNRs-CNFs pre-composite is transferred to EtOH without any negative impact on the optical properties of the nanocrystals. The comparative analysis of the IR spectra confirmed role of CTAB in maintaining material's structural integrity. Both, plasmonic and photochromic features of the system were maintained and the photochromic component exhibited stable and distinct photoswitching upon UV-Vis irradiation over many cycles in contrary to control materials prepared with traditional thiolated Azo ligands, which confirms **hypothesis 4**. Incorporation of big, anisotropic nanostructures in the hybrid formulation constitutes an important step forward, since the beneficial spectral separation of the optical properties of Azo and AuNRs is introduced.

Future endeavours may be focused on protocol adaptation to other photochromic ligands, including structures with two functional groups, that are able to anchor to the surface of more than one fibre. Moreover, systems containing multiple photochromic components might be explored to further broaden multifunctionality of the proposed formulation.

The knowledge gained from chapter 4 was implemented in chapter 5 to examine mutual interactions between plasmonic and photochromic components in the hybrid AzoGly-AuNRs-CNFs formulation. The influence of nanostructures exhibiting different aspect ratios on the thermally- and UV-Vis-induced AzoGly isomerization was investigated. Kinetic enhancement of the reactions was observed in materials containing AuNRs, namely 117.0% increase in the rate constant of the *E-Z* photoisomerization and 38.8% for the

Z-E photoisomerization for samples containing nanostructures with the smallest AR. This chapter postulates catalytic enhancement of the ongoing reactions via electron transfer mechanism, based on the coherent and reversible changes in the position of 1-LSPR band of AuNPs (about 2-4 nm). Upon the *E-Z* isomerization a blueshift of the band was observed, while for the *Z-E* isomerization a redshift occurred, as hypothesised based on literature reports for AuNSs (**hypothesis 5**).

Moreover, the chapter presents a complete sets of thermodynamic parameters describing thermal back-isomerization of Azo component in the hybrid materials. For all Au-containing samples, thermal relaxations in the dark were characterized by activation energy lower by 20 kJ/mol compared to hybrid sample without Au. A distinct change of the *Z*-isomer half-life occurred solely due to the photochrome's transfer to the aqueous environment, since $\tau_{1/2}$ was reduced from 24.6 hours for free photochrome in EtOH to 16.13 min for control sample without Au in water. Nevertheless, for hybrid AuNRs-containing materials the kinetic boost was manifested by further $\tau_{1/2}$ decrease to 8.37 min. The analysis of thermal relaxation rate constants, considering structural descriptors of the samples, indicated that catalytic enhancement increases with the decreasing AR of AuNRs, hence, confirming **hypothesis 6** of the dissertation. It is proposed, that the postulated size effect is a convolution of more than one structural descriptor.

Outcomes of this chapter can be further broadened by investigating hybrid formulations containing photochromic component characterized by higher thermal stability of the *Z*-isomer, to increase the temporal resolution of the measurements. Moreover, the stability and the photoswitching of hybrid materials can be investigated in other solvents.

The outcomes of chapters 3-5 found their fulfilment in chapter 6, focused on the plasmon-assisted *Z-E* isomerization of the photochrome. This chapter summarizes investigation of plasmon-assisted process for free molecules in EtOH solution and CNFs-bound components of the hybrid formulation in water. It was determined that free AzoGly molecules in EtOH experience dramatic increase of their *Z-E* isomerization kinetics in the presence of AuNRs and under appropriately selected red-NIR irradiation (650-1100 nm). Based on the correlation between isomerization rate constants in hybrid materials and irradiation intensity, the predominant influence of thermoplasmonic effect was proposed. Moreover, the dissertation introduces application of Azo type photochromes as molecular thermometers and presents how such strategy can be executed. In case of the investigated system, the extent of the thermoplasmonic effect was estimated to equal 21°C based on the changes in the AzoGly isomerization kinetics.

Chapter 6 proposes also specific experimental design in which hybrid AzoGly-AuNRs-CNFs material is subjected to the interval dark and light irradiation conditions. Novel, at least from chemical point of view, statistical analysis tools are also proposed to unravel relevant information from the obtained data. The ARIMA-based approach enabled calculation of the Ramp effect estimates, describing the slope change occurring in the linearized datasets upon irradiation. ARIMA modelling enabled conclusion on the statistical significance of the observed effects, which indicated that in the presence of AuNRs indirect photocontrol over the *Z-E* isomerization of Azo in the ON-OFF manner is possible. Statistical modelling also enabled final conclusion on the predominant contribution of the thermoplasmonic effect triggered upon irradiation and, hence, **hypothesis 7** of the dissertation was confirmed.

Results presented here can be applied particularly in the investigation of the temperature changes occurring at the nanoscale. First, the already existing Azo structures can be tested as molecular thermometers in different environments and scenarios and compared with the already existing nanothermometers, such as upconverting nanoparticles. Moreover, further implementation of the statistical modelling, including ARIMA-based approach, can be investigated in the analysis of the chemical phenomena.

The dissertation accomplishes all of the objectives set in Chapter 1. Not only reliable protocols enabling preparation of advanced hybrid materials are presented, but also the functionality of these hybrid formulations in the photocontrol over the course of two chemical processes is showcased. The first chemical process is simultaneous sodium formate dehydrogenation and cofactor regeneration, as discussed in chapter 3. The other chemical process is isomerization of Azo photochrome investigated in different modes, namely UV-induced *E-Z* isomerization, Vis-induced *Z-E* isomerization, thermal *Z-E* relaxation (all three discussed in chapter 5), and plasmon-assisted *Z-E* isomerization (chapter 6).

In summary, this dissertation provides important insight into the preparation and operation of hybrid plasmonic and plasmonic-photochromic CNFs-based materials. AuNRs incorporated in the proposed systems enable control over the course of the chemical process via light-induced plasmon-related effects. Presented work is at the intersection of chemical sciences and material science and contributes to both fields.

Scientific Curriculum

Publications related to the dissertation

1. N. Tarnowicz-Staniak^{*}, M. Staniak, M. Dudek, M. Grzelczak^{*}, K. Matczyszyn^{*}, *Gold Nanorods Grant an ON-OFF Control over the Kinetics of the Z-E Isomerization of Azobenzene-Based Photoswitch via Thermoplasmonic Effect*, ChemRxiv, preprint, **2024**, doi.org/10.26434/chemrxiv-2024-vnj32
Publication is currently (June 2024) under second revision in *Small*.
2. N. Tarnowicz-Staniak, S. Vázquez-Díaz, V. Pavlov, K. Matczyszyn^{*}, M. Grzelczak^{*}, *Cellulose as an Inert Scaffold in Plasmon-Assisted Photoregeneration of Cofactor Molecules*, ACS Applied Materials & Interfaces, **2020**, 12, 17, 19377–19383, doi.org/10.1021/acsami.9b21556

Other publications

1. M. Dudek^{*}, N. Tarnowicz-Staniak, M. Deiana, Z. Pokładek, M. Samoć, K. Matczyszyn^{*}, *Two-photon absorption and two-photon-induced isomerization of azobenzene compounds*, RSC Advances, **2020**, 10, 40489-40507, doi.org/10.1039/D0RA07693G
2. K. Nadolski, E. Benichou, N. Tarnowicz-Staniak, C. Jonin, A. Źak, K. Matczyszyn^{*}, P. Brevet^{*}, *Adverse Role of Shape and Size in Second Harmonic Scattering from Gold Nanoprisms*, Journal of Physical Chemistry C, **2020**, 124, 27, 14797–14803, doi.org/10.1021/acs.jpcc.0c03489
3. M. Deiana, Z. Pokładek, M. Ziemianek, N. Tarnowicz, P. Młynarz, M. Samoć, K. Matczyszyn^{*}, *Probing the binding mechanism of photoresponsive azobenzene polyamine derivatives with human serum albumin*, RSC Advances, **2017**, 7, 5912-5919, doi.org/10.1039/C6RA26033K

Chapter in the reviewed conference proceedings

1. N. Tarnowicz, L.K. Jagadamma, I.D.W. Samuel^{*}, K. Matczyszyn, *Gold nanotriangles for applications in organic photovoltaics*, chapter in *Optoelectronics and Microsystems Packaging: proceedings of 2018 International Students and Young Scientists Workshop: 22-24 November 2018, Dresden, Germany* / [eds. S. Patela, W. Kijaszek, D. Przybylski], ISBN: 978-83-951333-3-6. Wrocław: Wydawnictwo GMORK, **2019**, s. 92-98, <https://www.dbc.wroc.pl/dlibra/publication/113041/edition/62778>

Publications in preparation

1. N. Tarnowicz-Staniak, M. Grzelczak, K. Matczyszyn, *Catalytic Influence of Gold Nanoparticles on the Azobenzene Isomerization Revisited*, research paper
2. N. Tarnowicz-Staniak, D. Kosik, K. Matczyszyn, *Fluorescein-Decorated Gold Nanorods – Synthesis and Characterisation*, research paper

Grants

1. NCN PRELUDIUM 20 (2021/41/N/ST5/04470) – *Two-Photon Absorption of Bimetallic Plasmonic Nanorods - Systematic Studies*, project leader, 1 June 2022 – 31 May 2025, total funding: 210 000.00 PLN
2. NCN OPUS 18 (2019/35/B/ST4/03280) – *Non-linear optical properties of organometallic assemblies for biophotonic applications*, scholarship (PhD student), 1 July 2022 – 31 May 2024, project leader: Prof. Katarzyna Matczyszyn
3. MEiN Social Responsibility of Science/Excellent Science, application module: "Popularisation of Science and Promotion of Sport" (SONP/SP/468162/2020) – "*All that glitters is not gold - series of scientific photography exhibitions on the streets of the city of Wrocław*", author of grant proposal and manager of the project, 1 January 2020 – 31 December 2021, total funding: 42 223.00 PLN

Internships

7.09.2021-6.12.2021 – Centro de Física de Materiales, Donostia-San Sebastián, Spain, topic: *Synthesis and surface modification of plasmonic nanoparticles and their applications in photocatalysis*, supervisor: Dr Marek Grzelczak

28.01.2020-8.02.2020 – Claude Bernard University Lyon 1, Lyon, France, topic: *Investigation of Hyper-Rayleigh Scattering from Plasmonic Nanoparticles*, supervisor: Prof. Pierre-François Brevet

7.07.2019-7.09.2019 – Donostia International Physics Center, Donostia-San Sebastian, Spain, topic: *Plasmonic nanoparticles of various shapes and compositions for photocatalysis*, supervisor: Dr Marek Grzelczak

Awards and recognitions

May 2023 - 1st award for the best oral presentation during PhD student symposium (X Łódzkie Sympozjum Doktorantów Chemii) granted by Scientific Committee and PTChem Łódź

November 2022 - first honorary recognition in the scholarship programme of Wrocław Academic Hub (WCA) and the president of Wrocław in physical and chemical sciences

August 2022 - 3rd award for the best scientific photography in the *Microscopic Art Non-limited International Annual Contest - MANIAC 2022*, Wrocław University of Science and Technology, Wrocław, Poland

May 2022 - conference grant awarded by Dean of Faculty of Chemistry, Wrocław University of Science and Technology

November 2021 - first honorary recognition in the scholarship programme of Wrocław Academic Hub (WCA) and the president of Wrocław in physical and chemical sciences

September 2021 - 1st award for the best oral presentation during *III Pomeranian Students' Symposium in Chemistry*, Gdańsk, Poland

July 2021 - Wrocław University of Science and Technology *Primus* award for the authors of high-impact scientific publications

May 2021 - 1st award for the best scientific photography in the *Microscopic Art Non-limited International Annual Contest - MANIAC 2021*, Wrocław University of Science and Technology, Wrocław, Poland (total submissions: 34)

March 2021 - 1st award for the best oral presentation during *II Pomeranian Students' Symposium in Chemistry*, Gdańsk, Poland

November 2020 - 3rd award (tie four ways) for the best scientific photography in the *NanoArtography* competition, A. J. Drexel Nanomaterials Institute and Purdue School of Engineering & Technology at IUPUI, Philadelphia, USA (total submissions: 143)

October 2020 - award of the Dean of Faculty of Chemistry, Wrocław University of Science and Technology for the best PhD students

September 2020 - 2nd award for the best scientific photography in the *Microscopic Art Non-limited International Annual Contest - MANIAC 2020*, Wrocław University of Science and Technology, Wrocław, Poland (total submissions: 21)

August 2020 - special recognition of a scientific photography as *Image of the Month* in the *NanoArtography* competition, A. J. Drexel Nanomaterials Institute and Purdue School of Engineering & Technology at IUPUI, Philadelphia, USA

May 2019 - recognition for the best diploma thesis defended in the 2017/2018 academic year in Poland, funded by ABB Group (award for Master's thesis alongside two awards for PhD theses), Kraków, Poland

November 2018 - award for the best graduate student of Faculty of Chemistry WUST (Master's degree), Wrocław, Poland.

July 2018 - 1st award for the best poster presentation at the International Conference on Nanophotonics ICNP 2018, Wrocław, Poland

June 2018 - award of the Dean of Faculty of Chemistry Wrocław University of Science and Technology for the academic year 2017/2018

December 2017 - 2nd place in the *Golden Chemistry Medal Poland 2017* competition for the best Engineer's thesis in Chemistry organized by the Polish Academy of Science, Warsaw, Poland

December 2017 - People's Choice - the best presentation during the *Golden Chemistry Medal Poland 2017* competition, Warsaw, Poland.

Scholarships

September 2021 - funding for internship stay awarded in a competition within BioTechNan programme at Wrocław University of Science and Technology

April 2021 - special scholarship for the best PhD students granted by Wrocław University of Science and Technology Foundation

2017/2018 academic year - Polish Ministry of Science and Higher Education scholarship for remarkable students

International Conferences

7-10 November 2023 - N. Tarnowicz-Staniak, M. Dudek, M. Grzelczak, K. Matczyszyn, *Gold Nanorods-Assisted Isomerization of Azobenzene Derivatives*, poster presentation, 10th International Symposium on Photochromism 2023, Nara, Japan

14 October 2023 - N. Tarnowicz-Staniak, K. Matczyszyn, *AuPd Nanorods: Possibilities Stemming from Linear and Nonlinear Optical Properties*, oral and poster presentation, SKCM2 Symposium for Young Scientists in Europe, Wrocław, Poland

15-19 May 2023 – N. Tarnowicz-Staniak, K. Matczyszyn, *Plasmonic Nanoparticles for Organic Photovoltaics – Synthesis and Postprocessing*, poster presentation, PANIC Summer School 2023, Wrocław, Poland

17-20 July 2022 - N. Tarnowicz-Staniak, M. Grzelczak, K. Matczyszyn, *Z-E Isomerization of Azobenzenes in Organic Solvents: Enhancement and Expansion into Red and Near-Infrared Range Caused by Gold Nanorods*, video presentation available online, Gold 2022 International Conference, Quebec City, Canada

30 May - 3 June 2022 - N. Tarnowicz-Staniak, M. Grzelczak, K. Matczyszyn, *Indirect Excitation of Azobenzene Molecules – Plasmon-Assisted Approach*, oral presentation, PhoBiA Annual Nanophotonics International Conference – PANIC Summer School 2022, Wrocław, Poland

24 - 25 June 2021 - N. Tarnowicz-Staniak, K. Matczyszyn, M. Grzelczak, *Bioinspired, Cellulose-supported, and AuPd-nanorod-assisted Photocatalysis*, oral presentation, Chemistry & Biotechnology International Conference ChemBiotIC, online conference, Wrocław, Poland

26 May 2021 - N. Tarnowicz-Staniak, M. Grzelczak, K. Matczyszyn, *Catalytic Effect of Gold Nanoparticles on the Z-E isomerization of azobenzene*, oral presentation, Phobia Annual Nanophotonics International Conference PANIC 2021, Wrocław, Poland

12 - 14 October 2020 - N. Tarnowicz-Staniak, K. Matczyszyn, *Anisotropic gold nanoparticles decorated with azobenzene ligands*, oral presentation, Phobia Annual Nanophotonics International Conference PANIC 2020, Wrocław, Poland

30 - 31 January 2020 - N. Tarnowicz-Staniak, K. Matczyszyn, M. Grzelczak, *AuPd-nanorod-assisted and Cellulose-supported Photocatalysis*, oral presentation, Magnetism and Optics in Nanoalloys. Properties and Applications. Thematic Workshop 2020, Lyon, France

23 - 27 September 2019 - N. Tarnowicz-Staniak, A. Kordiak, M. Dudek, K. Matczyszyn, *Preparation and photochemistry of gold nanoparticles decorated with azobenzene derivative with lipoic acid*, oral presentation, 9th International Symposium on Photochromism, Paris, France

30 June - 5 July 2019 - N. Tarnowicz, K. Matczyszyn, M. Grzelczak, *Cellulose doped with plasmonic nanoparticles: liquid crystalline properties and photocatalytic performance*, poster presentation, 15th European Conference on Liquid Crystals, Wrocław, Poland

15 - 17 May 2019 - N. Tarnowicz-Staniak, K. Matczyszyn, M. Grzelczak, *Hybrid plasmonic photocatalyst for cofactor regeneration under Vis-IR light*, oral presentation, Phobia Annual Nanophotonics International Conference PANIC 2019, Wrocław, Poland

14 - 15 March 2019 - N. Tarnowicz, K. Matczyszyn, M. Grzelczak, *Gold nanorods immobilized on nanocellulose fibers and their photocatalytic properties in the proces of cofactor regeneration*, oral presentation, Conference Annuelle du Groupement de Recherche Or-Nano, Rennes, France

22 - 24 November 2018 - N. Tarnowicz, L.K. Jagadamma, I.D.W. Samuel, K. Matczyszyn, *Gold nanotriangles for applications in organic photovoltaics*, oral presentation, 2018 International Young Scientists and Students Workshop Optoelectronics and Microsystems Packaging, Dresden, Germany

2 - 6 July 2018 - N. Tarnowicz, L.K. Jagadamma, I.D.W. Samuel, K. Matczyszyn, *Gold nanotriangles synthesised by chemical seedless approach for organic solar cells*, oral and poster presentation, International Conference on Nanophotonics ICNP 2018 and Phobia Annual Nanophotonics International Conference PANIC 2018, Wrocław, Poland

Local conferences

18-19 May 2023 – N. Tarnowicz-Staniak, K. Matczyszyn, *How Thermoplasmonic Effect Affects Isomerization of Azobenzene Derivatives*, oral presentation, X Łódzkie Sympozjum Doktorantów Chemii, Łódź, Poland

12 - 15 June 2022 - N. Tarnowicz-Staniak, K. Matczyszyn, M. Grzelczak, *Cellulose as a Versatile Support for Plasmon-Induced and Bioinspired Photoregeneration of NADH*, oral presentation, XVIII Ogólnopolskie Seminarium „Na pograniczu chemii i biologii”, Smardzewice, Poland

21 - 22 May 2022 - N. Tarnowicz-Staniak, M. Grzelczak, K. Matczyszyn, *Influencing the Z-E Isomerization of Azobenzenes with Gold Nanorods*, oral presentation, XIX Wrocławskie Studenckie Sympozjum Chemiczne, Wrocław, Poland

19 - 20 May 2022 - N. Tarnowicz-Staniak, M. Grzelczak, K. Matczyszyn, *Gold Nanorods-Based Composite as a Catalyst of the Z-E Isomerization of Azobenzene*, oral presentation, IX Łódzkie Sympozjum Doktorantów Chemii, Łódź, Poland

23 - 24 April 2022 - N. Tarnowicz-Staniak, D. Kosik, L.K. Jagadamma, I.D.W. Samuel, K. Matczyszyn, *Plasmonic Nanoparticles – Synthesis and Postprocessing for Applications in*

Organic Photovoltaics, poster presentation, IV Pomorskie Studenckie Sympozjum Chemiczne, online conference, Gdańsk, Poland

18 - 19 September 2021 - N. Tarnowicz-Staniak, M. Grzelczak, K. Matczyszyn, *Catalysis of the Z-E isomerization of azobenzene by gold nanorods*, oral presentation, III Pomorskie Studenckie Sympozjum Chemiczne, online conference, Gdańsk, Poland

20 - 21 March 2020 - N. Tarnowicz-Staniak, K. Matczyszyn, M. Grzelczak, *Formation of Hybrid AuPd Nanorods-Cellulose Composite and its Applications in Photocatalysis*, II Pomorskie Studenckie Sympozjum Chemiczne, oral presentation, online conference, Gdańsk, Poland

30 November - 1 December 2019 - N. Tarnowicz-Staniak, K. Matczyszyn, *Przygotowanie i kinetyka fotoprzełączania nanocząstek złota funkcjonalizowanych pochodną azobenzenu*, XV Wrocławskie Studenckie Sympozjum Chemiczne, oral presentation, Wrocław, Poland

18 - 19 May 2019 - N. Tarnowicz-Staniak, M. Grzelczak, K. Matczyszyn, *Materiały hybrydowe bazujące na celulozie i nanocząstkach złota*, XIV Wrocławskie Studenckie Sympozjum Chemiczne, oral presentation, Wrocław, Poland

17 - 18 November 2018 - N. Tarnowicz, L.K. Jagadamma, I.D.W. Samuel, K. Matczyszyn, *Wykorzystanie nanocząstek złota w fotowoltaice*, XIII Wrocławskie Studenckie Sympozjum Chemiczne, oral presentation, Wrocław, Poland

Bibliography

- (1) European Commission. *Strategic Plan 2020-2024. DG Research and Innovation*; 2020. https://research-and-innovation.ec.europa.eu/document/download/03c65795-5c04-4feb-a701-30bc7ea9dc4b_en (accessed 2024-05-04).
- (2) *Key enabling technologies - European Commission*. https://research-and-innovation.ec.europa.eu/research-area/industrial-research-and-innovation/key-enabling-technologies_en (accessed 2024-05-04).
- (3) European Commission, D.-G. for R. and I. *Communication on Advanced Materials for Industrial Leadership*; Publications Office of the European Union, 2024. <https://doi.org/10.2777/401624>.
- (4) Advanced Materials 2030 Initiative. *Strategic Materials Agenda*; 2023. <https://www.ami2030.eu/wp-content/uploads/2023/04/Ami2030-Dossier-2.pdf> (accessed 2024-05-04).
- (5) Yang, B.; Chen, Y.; Shi, J. Exosome Biochemistry and Advanced Nanotechnology for Next-Generation Theranostic Platforms. *Advanced Materials* **2019**, *31* (2), 1802896. <https://doi.org/10.1002/ADMA.201802896>.
- (6) Lu, C.; Wu, M.; Lin, L.; Liu, J. M. Single-Phase Multiferroics: New Materials, Phenomena, and Physics. *Natl Sci Rev* **2019**, *6* (4), 653–668. <https://doi.org/10.1093/NSR/NWZ091>.
- (7) Grzelczak, M.; Liz-Marzán, L. M.; Klajn, R. Stimuli-Responsive Self-Assembly of Nanoparticles. *Chem Soc Rev* **2019**, *48*, 1342–1361. <https://doi.org/10.1039/c8cs00787j>.
- (8) Merindol, R.; Walther, A. Materials Learning from Life: Concepts for Active, Adaptive and Autonomous Molecular Systems. *Chem Soc Rev* **2017**, *46* (18), 5588–5619. <https://doi.org/10.1039/C6CS00738D>.
- (9) Devasia, D.; Das, A.; Mohan, V.; Jain, P. K. Control of Chemical Reaction Pathways by Light–Matter Coupling. *Annu Rev Phys Chem* **2021**, *72* (1), 423–443. <https://doi.org/10.1146/annurev-physchem-090519-045502>.
- (10) Scientific Committee on Emerging and Newly Identified Health Risks (SCENIHR); European Commission. *The Appropriateness of Existing Methodologies to Assess the Potential Risks Associated with Engineered and Adventitious Products of Nanotechnologies*; 2006. http://ec.europa.eu/health/ph_risk/documents/synth_report.pdf (accessed 2023-08-04).
- (11) Jan Kozubowski. *Nanotechnologia*. Encyklopedia PWN [online]. <https://encyklopedia.pwn.pl/haslo/nanotechnologia;3945658.html> (accessed 2023-08-04).
- (12) International Organization for Standardization. ISO 80004-1:2023(En), Nanotechnologies – Vocabulary — Part 1: Core Vocabulary. 2022. <https://www.iso.org/obp/ui/en/#iso:std:iso:80004:-1:ed-1:v1:en> (accessed 2023-08-04).
- (13) Hochella, M. F.; Mogk, D. W.; Ranville, J.; Allen, I. C.; Luther, G. W.; Marr, L. C.; McGrail, B. P.; Murayama, M.; Qafoku, N. P.; Rosso, K. M.; Sahai, N.; Schroeder, P. A.; Vikesland, P.; Westerhoff, P.; Yang, Y. Natural, Incidental, and Engineered Nanomaterials and Their Impacts on the Earth System. *Science (1979)* **2019**, *363* (6434). <https://doi.org/10.1126/science.aau8299>.
- (14) Lespes, G.; Faucher, S.; Slaveykova, V. I. Natural Nanoparticles, Anthropogenic Nanoparticles, Where Is the Frontier? *Front Environ Sci* **2020**, *8*, 545805. <https://doi.org/10.3389/fenvs.2020.00071>.
- (15) Sharma, V. K.; Filip, J.; Zboril, R.; Varma, R. S. Natural Inorganic Nanoparticles – Formation, Fate, and Toxicity in the Environment. *Chem Soc Rev* **2015**, *44* (23), 8410–8423. <https://doi.org/10.1039/C5CS00236B>.

- (16) Karthick, B.; Maheshwari, R. Lotus-Inspired Nanotechnology Applications. *Resonance* **2008**, *13* (12), 1141–1145. <https://doi.org/10.1007/s12045-008-0113-y>.
- (17) Jonas, R.; Farah, L. F. Production and Application of Microbial Cellulose. *Polym Degrad Stab* **1998**, *59* (1–3), 101–106. [https://doi.org/10.1016/S0141-3910\(97\)00197-3](https://doi.org/10.1016/S0141-3910(97)00197-3).
- (18) Walter, P.; Welcomme, E.; Hallégot, P.; Zaluzec, N. J.; Deeb, C.; Castaing, J.; Veysseyre, P.; Bréniaux, R.; Lévêque, J.-L.; Tsoucaris, G. Early Use of PbS Nanotechnology for an Ancient Hair Dyeing Formula. *Nano Lett* **2006**, *6* (10), 2215–2219. <https://doi.org/10.1021/nl061493u>.
- (19) Colomban, P.; Tournié, A.; Ricciardi, P. Raman Spectroscopy of Copper Nanoparticle-Containing Glass Matrices: Ancient Red Stained-Glass Windows. *Journal of Raman Spectroscopy* **2009**, *40* (12), 1949–1955. <https://doi.org/10.1002/JRS.2345>.
- (20) Shi, J.; Kantoff, P. W.; Wooster, R.; Farokhzad, O. C. Cancer Nanomedicine: Progress, Challenges and Opportunities. *Nat Rev Cancer* **2016**, *17* (1), 20–37. <https://doi.org/10.1038/nrc.2016.108>.
- (21) Sanna, V.; Sechi, M. Therapeutic Potential of Targeted Nanoparticles and Perspective on Nanotherapies. *ACS Med Chem Lett* **2020**, *11* (6), 1069–1073. <https://doi.org/https://doi.org/10.1021/acsmchemlett.0c00075>.
- (22) Vega-Vásquez, P.; Mosier, N. S.; Irudayaraj, J. Nanoscale Drug Delivery Systems: From Medicine to Agriculture. *Front Bioeng Biotechnol* **2020**, *8*, 507143. <https://doi.org/10.3389/fbioe.2020.00079>.
- (23) Ramachandran, K.; Boopalan, V.; Bear, J. C.; Subramani, R. Multi-Walled Carbon Nanotubes (MWCNTs)-Reinforced Ceramic Nanocomposites for Aerospace Applications: A Review. *J Mater Sci* **2022**, *57* (6), 3923–3953. <https://doi.org/10.1007/s10853-021-06760-x>.
- (24) Karakuş, E.; Erdemir, E.; Demirbilek, N.; Liv, L. Colorimetric and Electrochemical Detection of SARS-CoV-2 Spike Antigen with a Gold Nanoparticle-Based Biosensor. *Anal Chim Acta* **2021**, *1182*, 338939. <https://doi.org/10.1016/J.ACA.2021.338939>.
- (25) Alfieri, A.; Anantharaman, S. B.; Zhang, H.; Jariwala, D.; Alfieri, A.; Anantharaman, S. B.; Zhang, H.; Jariwala, D. Nanomaterials for Quantum Information Science and Engineering. *Advanced Materials* **2023**, *35* (27), 2109621. <https://doi.org/10.1002/ADMA.202109621>.
- (26) Lin, L.; Jones, T. W.; Wang, J. T.-W.; Cook, A.; Pham, N. D.; Duffy, N. W.; Mihaylov, B.; Grigore, M.; Anderson, K. F.; Duck, B. C.; Wang, H.; Pu, J.; Li, J.; Chi, B.; Wilson, G. J. Perovskite Solar Cells: Strategically Constructed Bilayer Tin (IV) Oxide as Electron Transport Layer Boosts Performance and Reduces Hysteresis in Perovskite Solar Cells. *Small* **2020**, *16* (12), 2070061. <https://doi.org/10.1002/SMLL.202070061>.
- (27) *Sepiolite: Mineral information, data and localities*. <https://www.mindat.org/min-3621.html> (accessed 2024-05-06).
- (28) X. The Bakerian Lecture. —Experimental Relations of Gold (and Other Metals) to Light. *Philos Trans R Soc Lond* **1857**, *147*, 145–181. <https://doi.org/10.1098/RSTL.1857.0011>.
- (29) Wu, Y.; Zhu, K.; Zhang, X.; Du, W.; Song, J.; Yang, H. Emerging Plasmonic Nanoparticles and Their Assemblies for Cancer Radiotherapy. *Adv Drug Deliv Rev* **2023**, *194*, 114710. <https://doi.org/10.1016/J.ADDR.2023.114710>.
- (30) Wang, P.; Krasavin, A. V.; Liu, L.; Jiang, Y.; Li, Z.; Guo, X.; Tong, L.; Zayats, A. V. Molecular Plasmonics with Metamaterials. *Chem Rev* **2022**, *122* (19), 15031–15081. <https://doi.org/10.1021/acs.chemrev.2c00333>.

- (31) Yang, H.; Li, H.; Tang, P.; Lan, X. Progress and Perspective on Chiral Plasmonic Nanostructures Enabled by DNA Programming Methodology. *Mater Adv* **2021**, *2* (22), 7336–7349. <https://doi.org/10.1039/D1MA00781E>.
- (32) Moon, S.; Zhang, Q.; Xu, Z.; Huang, D.; Kim, S.; Schiffbauer, J.; Lee, E.; Luo, T. Plasmonic Nanobubbles—A Perspective. *The Journal of Physical Chemistry C* **2021**, *125* (46), 25357–25368. <https://doi.org/10.1021/acs.jpcc.1c07244>.
- (33) Lu, R.; Ni, J.; Yin, S.; Ji, Y. Responsive Plasmonic Nanomaterials for Advanced Cancer Diagnostics. *Front Chem* **2021**, *9*, 652287. <https://doi.org/10.3389/fchem.2021.652287>.
- (34) Hu, X.; Zhang, Y.; Ding, T.; Liu, J.; Zhao, H. Multifunctional Gold Nanoparticles: A Novel Nanomaterial for Various Medical Applications and Biological Activities. *Front Bioeng Biotechnol* **2020**, *8*, 556510. <https://doi.org/10.3389/fbioe.2020.00990>.
- (35) Borghei, Y.-S.; Hosseinkhani, S.; Ganjali, M. R. “Plasmonic Nanomaterials”: An Emerging Avenue in Biomedical and Biomedical Engineering Opportunities. *J Adv Res* **2022**, *39*, 61–71. <https://doi.org/10.1016/j.jare.2021.11.006>.
- (36) Kim, S.; Kim, J.-M.; Park, J.-E.; Nam, J.-M. Nonnoble-Metal-Based Plasmonic Nanomaterials: Recent Advances and Future Perspectives. *Advanced Materials* **2018**, *30* (42), 1704528. <https://doi.org/10.1002/adma.201704528>.
- (37) *Nanotechnologies: 1. What is nanotechnology?* https://ec.europa.eu/health/scientific_committees/opinions_layman/en/nanotechnologies/1-2/1-introduction.htm (accessed 2024-05-06).
- (38) Schmid, G. Large Clusters and Colloids. Metals in the Embryonic State. *Chem Rev* **1992**, *92* (8), 1709–1727. <https://doi.org/10.1021/cr00016a002>.
- (39) Apai, G.; Hamilton, J. F.; Stohr, J.; Thompson, A. Extended X-Ray—Absorption Fine Structure of Small Cu and Ni Clusters: Binding-Energy and Bond-Length Changes with Cluster Size. *Phys Rev Lett* **1979**, *43* (2), 165–169. <https://doi.org/10.1103/PhysRevLett.43.165>.
- (40) Qi, W. H.; Wang, M. P.; Su, Y. C. Size Effect on the Lattice Parameters of Nanoparticles. *J Mater Sci Lett* **2002**, *21* (11), 877–878. <https://doi.org/10.1023/A:1015778729898>.
- (41) Couchman, P. R.; Jesser, W. A. Thermodynamic Theory of Size Dependence of Melting Temperature in Metals. *Nature* **1977**, *269* (5628), 481–483. <https://doi.org/10.1038/269481a0>.
- (42) Skripov, V. P.; Koverda, V. P.; Skokov, V. N. Size Effect on Melting of Small Particles. *Physica Status Solidi (a)* **1981**, *66* (1), 109–118. <https://doi.org/10.1002/pssa.2210660111>.
- (43) Mori, T.; Hegmann, T. Determining the Composition of Gold Nanoparticles: A Compilation of Shapes, Sizes, and Calculations Using Geometric Considerations. *Journal of Nanoparticle Research* **2016**, *18* (10), 295. <https://doi.org/10.1007/s11051-016-3587-7>.
- (44) Miller, J. T.; Kropf, A. J.; Zha, Y.; Regalbutto, J. R.; Delannoy, L.; Louis, C.; Bus, E.; van Bokhoven, J. A. The Effect of Gold Particle Size on AuAu Bond Length and Reactivity toward Oxygen in Supported Catalysts. *J Catal* **2006**, *240* (2), 222–234. <https://doi.org/10.1016/j.jcat.2006.04.004>.
- (45) Buffat, Ph.; Borel, J.-P. Size Effect on the Melting Temperature of Gold Particles. *Phys Rev A (Coll Park)* **1976**, *13* (6), 2287–2298. <https://doi.org/10.1103/PhysRevA.13.2287>.
- (46) *What gives gold nanoparticles their color? – Sustainable Nano.* <https://sustainable-nano.com/2019/11/12/gold-nanoparticles-color/> (accessed 2024-05-06).
- (47) Dolai, J.; Mandal, K.; Jana, N. R. Nanoparticle Size Effects in Biomedical Applications. *ACS Appl Nano Mater* **2021**, *4* (7), 6471–6496. <https://doi.org/10.1021/acsanm.1c00987>.

- (48) Medintz, I. L.; Uyeda, H. T.; Goldman, E. R.; Mattoussi, H. Quantum Dot Bioconjugates for Imaging, Labelling and Sensing. *Nat Mater* **2005**, *4* (6), 435–446. <https://doi.org/10.1038/nmat1390>.
- (49) Brus, L. E. Electron–Electron and Electron–Hole Interactions in Small Semiconductor Crystallites: The Size Dependence of the Lowest Excited Electronic State. *J Chem Phys* **1984**, *80* (9), 4403–4409. <https://doi.org/10.1063/1.447218>.
- (50) Mattoussi, H.; Radzilowski, L. H.; Dabbousi, B. O.; Thomas, E. L.; Bawendi, M. G.; Rubner, M. F. Electroluminescence from Heterostructures of Poly(Phenylene Vinylene) and Inorganic CdSe Nanocrystals. *J Appl Phys* **1998**, *83* (12), 7965–7974. <https://doi.org/10.1063/1.367978>.
- (51) Kobayashi, M.; Juillerat, F.; Galletto, P.; Bowen, P.; Borkovec, M. Aggregation and Charging of Colloidal Silica Particles: Effect of Particle Size. *Langmuir* **2005**, *21* (13), 5761–5769. <https://doi.org/10.1021/la046829z>.
- (52) Lee, N.; Yoo, D.; Ling, D.; Cho, M. H.; Hyeon, T.; Cheon, J. Iron Oxide Based Nanoparticles for Multimodal Imaging and Magnetoresponse Therapy. *Chem Rev* **2015**, *115* (19), 10637–10689. <https://doi.org/10.1021/acs.chemrev.5b00112>.
- (53) Tong, S.; Quinto, C. A.; Zhang, L.; Mohindra, P.; Bao, G. Size-Dependent Heating of Magnetic Iron Oxide Nanoparticles. *ACS Nano* **2017**, *11* (7), 6808–6816. <https://doi.org/10.1021/acsnano.7b01762>.
- (54) Kreibig, U.; Vollmer, M. *Optical Properties of Metal Clusters*; Springer: Berlin and London, 2011; Vol. 1.
- (55) Bohren, C.; Huffman, D. *Absorption and Scattering of Light by Small Particles*; Wiley-VCH: Weinheim, 2009.
- (56) Baffou, G.; Quidant, R. Thermo-Plasmonics: Using Metallic Nanostructures as Nano-Sources of Heat. *Laser Photon Rev* **2013**, *7* (2), 171–187. <https://doi.org/10.1002/LPOR.201200003>.
- (57) Pérez-Juste, J.; Pastoriza-Santos, I.; Liz-Marzán, L. M.; Mulvaney, P. Gold Nanorods: Synthesis, Characterization and Applications. *Coord Chem Rev* **2005**, *249* (17–18), 1870–1901. <https://doi.org/10.1016/J.CCR.2005.01.030>.
- (58) Gans, R. Über Die Form Ultramikroskopischer Silberteilchen. *Ann Phys* **1915**, *352* (10), 270–284. <https://doi.org/10.1002/ANDP.19153521006>.
- (59) Jain, P. K.; Lee, K. S.; El-Sayed, I. H.; El-Sayed, M. A. Calculated Absorption and Scattering Properties of Gold Nanoparticles of Different Size, Shape, and Composition: Applications in Biological Imaging and Biomedicine. *J Phys Chem B* **2006**, *110* (14), 7238–7248. <https://doi.org/10.1021/jp057170o>.
- (60) Gobin, A. M.; Lee, M. H.; Halas, N. J.; James, W. D.; Drezek, R. A.; West, J. L. Near-Infrared Resonant Nanoshells for Combined Optical Imaging and Photothermal Cancer Therapy. *Nano Lett* **2007**, *7* (7), 1929–1934. <https://doi.org/10.1021/nl070610y>.
- (61) Zhong, Z.; Patskovskyy, S.; Bouvrette, P.; Luong, J. H. T.; Gedanken, A. The Surface Chemistry of Au Colloids and Their Interactions with Functional Amino Acids. *Journal of Physical Chemistry B* **2004**, *108* (13), 4046–4052. <https://doi.org/10.1021/JP037056A>.
- (62) Soenen, S. J.; Manshian, B.; Montenegro, J. M.; Amin, F.; Meermann, B.; Thiron, T.; Cornelissen, M.; Vanhaecke, F.; Doak, S.; Parak, W. J.; De Smedt, S.; Braeckmans, K. Cytotoxic Effects of Gold Nanoparticles: A Multiparametric Study. *ACS Nano* **2012**, *6* (7), 5767–5783. <https://doi.org/10.1021/nn301714n>.
- (63) Feng, Z.; Tang, T.; Wu, T.; Yu, X.; Zhang, Y.; Wang, M.; Zheng, J.; Ying, Y.; Chen, S.; Zhou, J.; Fan, X.; Zhang, D.; Li, S.; Zhang, M.; Qian, J. Perfecting and Extending the Near-Infrared

- Imaging Window. *Light: Science & Applications* **2021**, *10* (1), 1–18. <https://doi.org/10.1038/s41377-021-00628-0>.
- (64) Abid, N.; Khan, A. M.; Shujait, S.; Chaudhary, K.; Ikram, M.; Imran, M.; Haider, J.; Khan, M.; Khan, Q.; Maqbool, M. Synthesis of Nanomaterials Using Various Top-down and Bottom-up Approaches, Influencing Factors, Advantages, and Disadvantages: A Review. *Adv Colloid Interface Sci* **2022**, *300*, 102597. <https://doi.org/10.1016/J.CIS.2021.102597>.
- (65) Grzelczak, M.; Liz-Marzán, L. M. The Relevance of Light in the Formation of Colloidal Metal Nanoparticles. *Chem Soc Rev* **2014**, *43* (7), 2089–2097. <https://doi.org/10.1039/C3CS60256G>.
- (66) Turkevich, J.; Stevenson, P. C.; Hillier, J. A Study of the Nucleation and Growth Processes in the Synthesis of Colloidal Gold. *Discuss Faraday Soc* **1951**, *11* (0), 55–75. <https://doi.org/10.1039/DF9511100055>.
- (67) Frens, G. Controlled Nucleation for the Regulation of the Particle Size in Monodisperse Gold Suspensions. *Nature Physical Science* **1973**, *241* (105), 20–22. <https://doi.org/10.1038/physci241020a0>.
- (68) Bastús, N. G.; Comenge, J.; Puentes, V. Kinetically Controlled Seeded Growth Synthesis of Citrate-Stabilized Gold Nanoparticles of up to 200 Nm: Size Focusing versus Ostwald Ripening. *Langmuir* **2011**, *27* (17), 11098–11105. <https://doi.org/10.1021/la201938u>.
- (69) Foss, C. A.; Hornyak, G. L.; Stockert, J. A.; Martin, C. R. Optical Properties of Composite Membranes Containing Arrays of Nanoscopic Gold Cylinders. *J Phys Chem* **1992**, *96* (19), 7497–7499. <https://doi.org/10.1021/j100198a004>.
- (70) Yu; Chang, S.-S.; Lee, C.-L.; Wang, C. R. C. Gold Nanorods: Electrochemical Synthesis and Optical Properties. *J Phys Chem B* **1997**, *101* (34), 6661–6664. <https://doi.org/10.1021/jp971656q>.
- (71) Dreaden, E. C.; Alkilany, A. M.; Huang, X.; Murphy, C. J.; El-Sayed, M. A. The Golden Age: Gold Nanoparticles for Biomedicine. *Chem Soc Rev* **2012**, *41* (7), 2740–2779. <https://doi.org/10.1039/C1CS15237H>.
- (72) Grzelczak, M.; Pérez-Juste, J.; Mulvaney, P.; Liz-Marzán, L. M. Shape Control in Gold Nanoparticle Synthesis. *Chem Soc Rev* **2008**, *37* (9), 1783–1791. <https://doi.org/10.1039/B711490G>.
- (73) Lohse, S. E.; Murphy, C. J. The Quest for Shape Control: A History of Gold Nanorod Synthesis. *Chemistry of Materials* **2013**, *25* (8), 1250–1261. <https://doi.org/10.1021/cm303708p>.
- (74) Jana, N. R. Gram-Scale Synthesis of Soluble, Near-Monodisperse Gold Nanorods and Other Anisotropic Nanoparticles. *Small* **2005**, *1* (8–9), 875–882. <https://doi.org/10.1002/SMLL.200500014>.
- (75) Jin, R.; Charles Cao, Y.; Hao, E.; Métraux, G. S.; Schatz, G. C.; Mirkin, C. A. Controlling Anisotropic Nanoparticle Growth through Plasmon Excitation. *Nature* **2003**, *425* (6957), 487–490. <https://doi.org/10.1038/nature02020>.
- (76) Johnson, C. J.; Dujardin, E.; Davis, S. A.; Murphy, C. J.; Mann, S. Growth and Form of Gold Nanorods Prepared by Seed-Mediated, Surfactant-Directed Synthesis. *J Mater Chem* **2002**, *12* (6), 1765–1770. <https://doi.org/10.1039/B200953F>.
- (77) Jana, N. R.; Gearheart, L.; Murphy, C. J. Wet Chemical Synthesis of High Aspect Ratio Cylindrical Gold Nanorods. *J Phys Chem B* **2001**, *105* (19), 4065–4067. <https://doi.org/10.1021/jp0107964>.

- (78) Jana, N. R.; Gearheart, L.; Murphy, C. J. Seed-Mediated Growth Approach for Shape-Controlled Synthesis of Spheroidal and Rod-like Gold Nanoparticles Using a Surfactant Template. *Advanced Materials* **2001**, *13* (18), 1389–1393. <https://doi.org/10.1002/1521-4095>.
- (79) Nikoobakht, B.; El-Sayed, M. A. Preparation and Growth Mechanism of Gold Nanorods (NRs) Using Seed-Mediated Growth Method. *Chemistry of Materials* **2003**, *15* (10), 1957–1962. <https://doi.org/10.1021/cm020732l>.
- (80) Scarabelli, L.; Sánchez-Iglesias, A.; Pérez-Juste, J.; Liz-Marzán, L. M. A “Tips and Tricks” Practical Guide to the Synthesis of Gold Nanorods. *J Phys Chem Lett* **2015**, *6* (21), 4270–4279. <https://doi.org/10.1021/acs.jpcclett.5b02123>.
- (81) Imae, T.; Kamiya, R.; Ikeda, S. Formation of Spherical and Rod-like Micelles of Cetyltrimethylammonium Bromide in Aqueous NaBr Solutions. *J Colloid Interface Sci* **1985**, *108* (1), 215–225. [https://doi.org/10.1016/0021-9797\(85\)90253-X](https://doi.org/10.1016/0021-9797(85)90253-X).
- (82) Hubert, F.; Testard, F.; Spalla, O. Cetyltrimethylammonium Bromide Silver Bromide Complex as the Capping Agent of Gold Nanorods. *Langmuir* **2008**, *24* (17), 9219–9222. <https://doi.org/10.1021/la801711q>.
- (83) Liu, M.; Guyot-Sionnest, P. Mechanism of Silver(I)-Assisted Growth of Gold Nanorods and Bipyramids. *J Phys Chem B* **2005**, *109* (47), 22192–22200. <https://doi.org/10.1021/jp054808n>.
- (84) Xia, Y.; Xia, X.; Peng, H.-C. Shape-Controlled Synthesis of Colloidal Metal Nanocrystals: Thermodynamic versus Kinetic Products. *J Am Chem Soc* **2015**, *137* (25), 7947–7966. <https://doi.org/10.1021/jacs.5b04641>.
- (85) Zhang, Q.; Jing, H.; Li, G. G.; Lin, Y.; Blom, D. A.; Wang, H. Intertwining Roles of Silver Ions, Surfactants, and Reducing Agents in Gold Nanorod Overgrowth: Pathway Switch between Silver Underpotential Deposition and Gold–Silver Codeposition. *Chemistry of Materials* **2016**, *28* (8), 2728–2741. <https://doi.org/10.1021/acs.chemmater.6b00389>.
- (86) Scarabelli, L.; Grzelczak, M.; Liz-Marzán, L. M. Tuning Gold Nanorod Synthesis through Prereduction with Salicylic Acid. *Chemistry of Materials* **2013**, *25* (21), 4232–4238. <https://doi.org/10.1021/cm402177b>.
- (87) Sánchez-Iglesias, A.; Winckelmans, N.; Altantzis, T.; Bals, S.; Grzelczak, M.; Liz-Marzán, L. M. High-Yield Seeded Growth of Monodisperse Pentatwinned Gold Nanoparticles through Thermally Induced Seed Twinning. *J Am Chem Soc* **2016**, *139* (1), 107–110. <https://doi.org/10.1021/JACS.6B12143>.
- (88) Rao, A.; Grzelczak, M. Revisiting El-Sayed Synthesis: Bayesian Optimization for Revealing New Insights during the Growth of Gold Nanorods. *Chemistry of Materials* **2024**, *36* (5), 2577–2587. <https://doi.org/10.1021/acs.chemmater.4c00271>.
- (89) DuChene, J. S.; Niu, W.; Abendroth, J. M.; Sun, Q.; Zhao, W.; Huo, F.; Wei, W. D. Halide Anions as Shape-Directing Agents for Obtaining High-Quality Anisotropic Gold Nanostructures. *Chemistry of Materials* **2013**, *25* (8), 1392–1399. <https://doi.org/10.1021/cm3020397>.
- (90) Scarabelli, L.; Coronado-Puchau, M.; Giner-Casares, J. J.; Langer, J.; Liz-Marzán, L. M. Monodisperse Gold Nanotriangles: Size Control, Large-Scale Self-Assembly, and Performance in Surface-Enhanced Raman Scattering. *ACS Nano* **2014**, *8* (6), 5833–5842. <https://doi.org/10.1021/nn500727w>.
- (91) Scarabelli, L.; Liz-Marzán, L. M. An Extended Protocol for the Synthesis of Monodisperse Gold Nanotriangles. *ACS Nano* **2021**, *15* (12), 18600–18607. <https://doi.org/10.1021/acsnano.1c10538>.

- (92) Langille, M. R.; Personick, M. L.; Zhang, J.; Mirkin, C. A. Defining Rules for the Shape Evolution of Gold Nanoparticles. *J Am Chem Soc* **2012**, *134* (35), 14542–14554. <https://doi.org/10.1021/ja305245g>.
- (93) Ye, X.; Zheng, C.; Chen, J.; Gao, Y.; Murray, C. B. Using Binary Surfactant Mixtures To Simultaneously Improve the Dimensional Tunability and Monodispersity in the Seeded Growth of Gold Nanorods. *Nano Lett* **2013**, *13* (2), 765–771. <https://doi.org/10.1021/nl304478h>.
- (94) Ye, X.; Jin, L.; Caglayan, H.; Chen, J.; Xing, G.; Zheng, C.; Doan-Nguyen, V.; Kang, Y.; Engheta, N.; Kagan, C. R.; Murray, C. B. Improved Size-Tunable Synthesis of Monodisperse Gold Nanorods through the Use of Aromatic Additives. *ACS Nano* **2012**, *6* (3), 2804–2817. <https://doi.org/10.1021/nn300315j>.
- (95) Terayama, K.; Sumita, M.; Tamura, R.; Tsuda, K. Black-Box Optimization for Automated Discovery. *Acc Chem Res* **2021**, *54* (6), 1334–1346. <https://doi.org/10.1021/acs.accounts.0c00713>.
- (96) Häse, F.; Aldeghi, M.; Hickman, R. J.; Roch, L. M.; Aspuru-Guzik, A. Gryffin: An Algorithm for Bayesian Optimization of Categorical Variables Informed by Expert Knowledge. *Appl Phys Rev* **2021**, *8* (3), 31406. <https://doi.org/10.1063/5.0048164/998861>.
- (97) Ward, C. J.; Tronndorf, R.; Eustes, A. S.; Auad, M. L.; Davis, E. W. Seed-Mediated Growth of Gold Nanorods: Limits of Length to Diameter Ratio Control. *J Nanomater* **2014**, *2014*. <https://doi.org/10.1155/2014/765618>.
- (98) Gellé, A.; Jin, T.; de la Garza, L.; Price, G. D.; Besteiro, L. V.; Moores, A. Applications of Plasmon-Enhanced Nanocatalysis to Organic Transformations. *Chem Rev* **2020**, *120* (2), 986–1041. <https://doi.org/10.1021/acs.chemrev.9b00187>.
- (99) Hoffmann, M. R.; Martin, S. T.; Choi, W.; Bahnemann, D. W. Environmental Applications of Semiconductor Photocatalysis. *Chem Rev* **1995**, *95* (1), 69–96. <https://doi.org/10.1021/cr00033a004>.
- (100) Han, F.; Kambala, V. S. R.; Srinivasan, M.; Rajarathnam, D.; Naidu, R. Tailored Titanium Dioxide Photocatalysts for the Degradation of Organic Dyes in Wastewater Treatment: A Review. *Appl Catal A Gen* **2009**, *359* (1–2), 25–40. <https://doi.org/10.1016/J.APCATA.2009.02.043>.
- (101) Schultz, D. M.; Yoon, T. P. Solar Synthesis: Prospects in Visible Light Photocatalysis. *Science (1979)* **2014**, *343* (6174). <https://doi.org/10.1126/SCIENCE.1239176>.
- (102) Fox, M. A.; Dulay, M. T. Heterogeneous Photocatalysis. *Chem Rev* **1993**, *93* (1), 341–357. <https://doi.org/10.1021/cr00017a016>.
- (103) Romero, N. A.; Nicewicz, D. A. Organic Photoredox Catalysis. *Chem Rev* **2016**, *116* (17), 10075–10166. <https://doi.org/10.1021/acs.chemrev.6b00057>.
- (104) Gellé, A.; Jin, T.; de la Garza, L.; Price, G. D.; Besteiro, L. V.; Moores, A. Applications of Plasmon-Enhanced Nanocatalysis to Organic Transformations. *Chem Rev* **2020**, *120* (2), 986–1041. <https://doi.org/10.1021/acs.chemrev.9b00187>.
- (105) Brongersma, M. L.; Halas, N. J.; Nordlander, P. Plasmon-Induced Hot Carrier Science and Technology. *Nat Nanotechnol* **2015**, *10* (1), 25–34. <https://doi.org/10.1038/nnano.2014.311>.
- (106) Khurgin, J. B. How to Deal with the Loss in Plasmonics and Metamaterials. *Nat Nanotechnol* **2015**, *10* (1), 2–6. <https://doi.org/10.1038/nnano.2014.310>.
- (107) Link, S.; El-Sayed, M. A. Optical Properties and Ultrafast Dynamics of Metallic Nanocrystals. *Annu Rev Phys Chem* **2003**, *54* (1), 331–366. <https://doi.org/10.1146/annurev.physchem.54.011002.103759>.

- (108) Goldys, E. M.; Sobhan, M. A. Fluorescence of Colloidal Gold Nanoparticles Is Controlled by the Surface Adsorbate. *Adv Funct Mater* **2012**, *22* (9), 1906–1913. <https://doi.org/10.1002/adfm.201102057>.
- (109) Alabastri, A.; Tuccio, S.; Giugni, A.; Toma, A.; Liberale, C.; Das, G.; Angelis, F.; Fabrizio, E.; Zaccaria, R. Molding of Plasmonic Resonances in Metallic Nanostructures: Dependence of the Non-Linear Electric Permittivity on System Size and Temperature. *Materials* **2013**, *6* (11), 4879–4910. <https://doi.org/10.3390/ma6114879>.
- (110) Kats, M. A.; Yu, N.; Genevet, P.; Gaburro, Z.; Capasso, F. Effect of Radiation Damping on the Spectral Response of Plasmonic Components. *Opt Express* **2011**, *19* (22), 21748. <https://doi.org/10.1364/OE.19.021748>.
- (111) Amendola, V.; Pilot, R.; Frascioni, M.; Maragò, O. M.; Iatì, M. A. Surface Plasmon Resonance in Gold Nanoparticles: A Review. *Journal of Physics: Condensed Matter* **2017**, *29* (20), 203002. <https://doi.org/10.1088/1361-648X/AA60F3>.
- (112) Tang, Y.; Ouyang, M. Tailoring Properties and Functionalities of Metal Nanoparticles through Crystallinity Engineering. *Nat Mater* **2007**, *6* (10), 754–759. <https://doi.org/10.1038/nmat1982>.
- (113) Goldys, E. M.; Sobhan, M. A. Fluorescence of Colloidal Gold Nanoparticles Is Controlled by the Surface Adsorbate. *Adv Funct Mater* **2012**, *22* (9), 1906–1913. <https://doi.org/10.1002/adfm.201102057>.
- (114) Zhan, C.; Chen, X. J.; Yi, J.; Li, J. F.; Wu, D. Y.; Tian, Z. Q. From Plasmon-Enhanced Molecular Spectroscopy to Plasmon-Mediated Chemical Reactions. *Nature Reviews Chemistry* **2018**, *2*:9 **2018**, *2* (9), 216–230. <https://doi.org/10.1038/s41570-018-0031-9>.
- (115) Manjavacas, A.; Liu, J. G.; Kulkarni, V.; Nordlander, P. Plasmon-Induced Hot Carriers in Metallic Nanoparticles. *ACS Nano* **2014**, *8* (8), 7630–7638. <https://doi.org/10.1021/nn502445f>.
- (116) Maier, S. A. *Plasmonics: Fundamentals and Applications*; Springer US: New York, NY, 2007. <https://doi.org/10.1007/0-387-37825-1>.
- (117) Linic, S.; Christopher, P.; Ingram, D. B. Plasmonic-Metal Nanostructures for Efficient Conversion of Solar to Chemical Energy. *Nat Mater* **2011**, *10* (12), 911–921. <https://doi.org/10.1038/nmat3151>.
- (118) Kelly, K. L.; Coronado, E.; Zhao, L. L.; Schatz, G. C. The Optical Properties of Metal Nanoparticles: The Influence of Size, Shape, and Dielectric Environment. *J Phys Chem B* **2003**, *107* (3), 668–677. <https://doi.org/10.1021/jp026731y>.
- (119) Anker, J. N.; Hall, W. P.; Lyandres, O.; Shah, N. C.; Zhao, J.; Van Duyne, R. P. Biosensing with Plasmonic Nanosensors. *Nat Mater* **2008**, *7* (6), 442–453. <https://doi.org/10.1038/nmat2162>.
- (120) Sousa-Castillo, A.; Comesaña-Hermo, M.; Rodríguez-González, B.; Pérez-Lorenzo, M.; Wang, Z.; Kong, X.-T.; Govorov, A. O.; Correa-Duarte, M. A. Boosting Hot Electron-Driven Photocatalysis through Anisotropic Plasmonic Nanoparticles with Hot Spots in Au–TiO₂ Nanoarchitectures. *The Journal of Physical Chemistry C* **2016**, *120* (21), 11690–11699. <https://doi.org/10.1021/acs.jpcc.6b02370>.
- (121) Prodan, E.; Radloff, C.; Halas, N. J.; Nordlander, P. A Hybridization Model for the Plasmon Response of Complex Nanostructures. *Science (1979)* **2003**, *302* (5644), 419–422. <https://doi.org/10.1126/science.1089171>.
- (122) Tam, F.; Goodrich, G. P.; Johnson, B. R.; Halas, N. J. Plasmonic Enhancement of Molecular Fluorescence. *Nano Lett* **2007**, *7* (2), 496–501. <https://doi.org/10.1021/nl062901x>.
- (123) Moskovits, M. Surface-enhanced Raman Spectroscopy: A Brief Retrospective. *Journal of Raman Spectroscopy* **2005**, *36* (6–7), 485–496. <https://doi.org/10.1002/jrs.1362>.

- (124) Merlen, A.; Lagugné-Labarthe, F. Imaging the Optical near Field in Plasmonic Nanostructures. *Appl Spectrosc* **2014**, *68* (12), 1307–1326. <https://doi.org/10.1366/14-07699>.
- (125) Aćimović, S. S.; Kreuzer, M. P.; González, M. U.; Quidant, R. Plasmon Near-Field Coupling in Metal Dimers as a Step toward Single-Molecule Sensing. *ACS Nano* **2009**, *3* (5), 1231–1237. <https://doi.org/10.1021/nn900102j>.
- (126) Fayyaz, S.; Tabatabaei, M.; Hou, R.; Lagugné-Labarthe, F. Surface-Enhanced Fluorescence: Mapping Individual Hot Spots in Silica-Protected 2D Gold Nanotriangle Arrays. *The Journal of Physical Chemistry C* **2012**, *116* (21), 11665–11670. <https://doi.org/10.1021/jp302191z>.
- (127) Kazuma, E.; Kim, Y. Mechanistic Studies of Plasmon Chemistry on Metal Catalysts. *Angewandte Chemie International Edition* **2019**, *58* (15), 4800–4808. <https://doi.org/10.1002/anie.201811234>.
- (128) Stampelcoskie, K. G.; Pacioni, N. L.; Larson, D.; Scaiano, J. C. Plasmon-Mediated Photopolymerization Maps Plasmon Fields for Silver Nanoparticles. *J Am Chem Soc* **2011**, *133* (24), 9160–9163. <https://doi.org/10.1021/ja201139z>.
- (129) Li, K.; Hogan, N. J.; Kale, M. J.; Halas, N. J.; Nordlander, P.; Christopher, P. Balancing Near-Field Enhancement, Absorption, and Scattering for Effective Antenna-Reactor Plasmonic Photocatalysis. *Nano Lett* **2017**, *17* (6), 3710–3717. <https://doi.org/10.1021/acs.nanolett.7b00992>.
- (130) Liu, Z.; Hou, W.; Pavaskar, P.; Aykol, M.; Cronin, S. B. Plasmon Resonant Enhancement of Photocatalytic Water Splitting Under Visible Illumination. *Nano Lett* **2011**, *11* (3), 1111–1116. <https://doi.org/10.1021/nl104005n>.
- (131) Awazu, K.; Fujimaki, M.; Rockstuhl, C.; Tominaga, J.; Murakami, H.; Ohki, Y.; Yoshida, N.; Watanabe, T. A Plasmonic Photocatalyst Consisting of Silver Nanoparticles Embedded in Titanium Dioxide. *J Am Chem Soc* **2008**, *130* (5), 1676–1680. <https://doi.org/10.1021/ja076503n>.
- (132) Xie, W.; Schlücker, S. Hot Electron-Induced Reduction of Small Molecules on Photorecycling Metal Surfaces. *Nat Commun* **2015**, *6* (1), 7570. <https://doi.org/10.1038/ncomms8570>.
- (133) Huang, Y.-F.; Zhu, H.-P.; Liu, G.-K.; Wu, D.-Y.; Ren, B.; Tian, Z.-Q. When the Signal Is Not from the Original Molecule To Be Detected: Chemical Transformation of *Para*-Aminothiophenol on Ag during the SERS Measurement. *J Am Chem Soc* **2010**, *132* (27), 9244–9246. <https://doi.org/10.1021/ja101107z>.
- (134) Wang, Q.; Hisatomi, T.; Jia, Q.; Tokudome, H.; Zhong, M.; Wang, C.; Pan, Z.; Takata, T.; Nakabayashi, M.; Shibata, N.; Li, Y.; Sharp, I. D.; Kudo, A.; Yamada, T.; Domen, K. Scalable Water Splitting on Particulate Photocatalyst Sheets with a Solar-to-Hydrogen Energy Conversion Efficiency Exceeding 1%. *Nat Mater* **2016**, *15* (6), 611–615. <https://doi.org/10.1038/nmat4589>.
- (135) Mukherjee, S.; Libisch, F.; Large, N.; Neumann, O.; Brown, L. V.; Cheng, J.; Lassiter, J. B.; Carter, E. A.; Nordlander, P.; Halas, N. J. Hot Electrons Do the Impossible: Plasmon-Induced Dissociation of H₂ on Au. *Nano Lett* **2013**, *13* (1), 240–247. <https://doi.org/10.1021/nl303940z>.
- (136) Christopher, P.; Xin, H.; Linic, S. Visible-Light-Enhanced Catalytic Oxidation Reactions on Plasmonic Silver Nanostructures. *Nat Chem* **2011**, *3* (6), 467–472. <https://doi.org/10.1038/nchem.1032>.
- (137) Kumar, P. V.; Norris, D. J. Tailoring Energy Transfer from Hot Electrons to Adsorbate Vibrations for Plasmon-Enhanced Catalysis. *ACS Catal* **2017**, *7* (12), 8343–8350. <https://doi.org/10.1021/acscatal.7b03174>.

- (138) Bauer, C.; Abid, J. P.; Fermin, D.; Girault, H. H. Ultrafast Chemical Interface Scattering as an Additional Decay Channel for Nascent Nonthermal Electrons in Small Metal Nanoparticles. *J Chem Phys* **2004**, *120* (19), 9302–9315. <https://doi.org/10.1063/1.1710856>.
- (139) Kale, M. J.; Avanesian, T.; Xin, H.; Yan, J.; Christopher, P. Controlling Catalytic Selectivity on Metal Nanoparticles by Direct Photoexcitation of Adsorbate–Metal Bonds. *Nano Lett* **2014**, *14* (9), 5405–5412. <https://doi.org/10.1021/nl502571b>.
- (140) Dong, B.; Fang, Y.; Chen, X.; Xu, H.; Sun, M. Substrate-, Wavelength-, and Time-Dependent Plasmon-Assisted Surface Catalysis Reaction of 4-Nitrobenzenethiol Dimerizing to *p*, *p'*-Dimercaptoazobenzene on Au, Ag, and Cu Films. *Langmuir* **2011**, *27* (17), 10677–10682. <https://doi.org/10.1021/la2018538>.
- (141) Tang, X.; Cai, W.; Yang, L.; Liu, J. Monitoring Plasmon-Driven Surface Catalyzed Reactions in Situ Using Time-Dependent Surface-Enhanced Raman Spectroscopy on Single Particles of Hierarchical Peony-like Silver Microflowers. *Nanoscale* **2014**, *6* (15), 8612–8616. <https://doi.org/10.1039/C4NR01939C>.
- (142) Zhang, L.; Jia, C.; He, S.; Zhu, Y.; Wang, Y.; Zhao, Z.; Gao, X.; Zhang, X.; Sang, Y.; Zhang, D.; Xu, X.; Liu, H.; Zhang, L.; He, S.; Zhu, Y.; Gao, X.; Zhang, X.; Zhang, D.; Xu, X.; Jia, C.; Wang, Y.; Zhao, Z.; Sang, Y.; Liu, H. Hot Hole Enhanced Synergistic Catalytic Oxidation on Pt-Cu Alloy Clusters. *Advanced Science* **2017**, *4* (6), 1600448. <https://doi.org/10.1002/ADVS.201600448>.
- (143) Wu, X.; Thrall, E. S.; Liu, H.; Steigerwald, M.; Brus, L. Plasmon Induced Photovoltage and Charge Separation in Citrate-Stabilized Gold Nanoparticles. *The Journal of Physical Chemistry C* **2010**, *114* (30), 12896–12899. <https://doi.org/10.1021/jp102720r>.
- (144) Christopher, P.; Moskovits, M. Hot Charge Carrier Transmission from Plasmonic Nanostructures. *Annu Rev Phys Chem* **2017**, *68* (1), 379–398. <https://doi.org/10.1146/annurev-physchem-052516-044948>.
- (145) Clavero, C. Plasmon-Induced Hot-Electron Generation at Nanoparticle/Metal-Oxide Interfaces for Photovoltaic and Photocatalytic Devices. *Nature Photonics* **2014**, *8* (2), 95–103. <https://doi.org/10.1038/nphoton.2013.238>.
- (146) DuChene, J. S.; Sweeny, B. C.; Johnston-Peck, A. C.; Su, D.; Stach, E. A.; Wei, W. D. Prolonged Hot Electron Dynamics in Plasmonic-Metal/Semiconductor Heterostructures with Implications for Solar Photocatalysis. *Angewandte Chemie International Edition* **2014**, *53* (30), 7887–7891. <https://doi.org/10.1002/anie.201404259>.
- (147) Li, H.; Qin, F.; Yang, Z.; Cui, X.; Wang, J.; Zhang, L. New Reaction Pathway Induced by Plasmon for Selective Benzyl Alcohol Oxidation on BiOCl Possessing Oxygen Vacancies. *J Am Chem Soc* **2017**, *139* (9), 3513–3521. <https://doi.org/10.1021/jacs.6b12850>.
- (148) Marchuk, K.; Willets, K. A. Localized Surface Plasmons and Hot Electrons. *Chem Phys* **2014**, *445*, 95–104. <https://doi.org/10.1016/j.chemphys.2014.10.016>.
- (149) Wu, K.; Chen, J.; McBride, J. R.; Lian, T. Efficient Hot-Electron Transfer by a Plasmon-Induced Interfacial Charge-Transfer Transition. *Science (1979)* **2015**, *349* (6248), 632–635. <https://doi.org/10.1126/science.aac5443>.
- (150) Foerster, B.; Hartelt, M.; Collins, S. S. E.; Aeschlimann, M.; Link, S.; Sönnichsen, C. Interfacial States Cause Equal Decay of Plasmons and Hot Electrons at Gold–Metal Oxide Interfaces. *Nano Lett* **2020**, *20* (5), 3338–3343. <https://doi.org/10.1021/acs.nanolett.0c00223>.
- (151) Baumberg, J. J. Hot Electron Science in Plasmonics and Catalysis: What We Argue About. *Faraday Discuss* **2019**, *214* (0), 501–511. <https://doi.org/10.1039/C9FD00027E>.

- (152) Richardson, H. H.; Hickman, Z. N.; Govorov, A. O.; Thomas, A. C.; Zhang, W.; Kordesch, M. E. Thermo-optical Properties of Gold Nanoparticles Embedded in Ice: Characterization of Heat Generation and Melting. *Nano Lett* **2006**, *6* (4), 783–788. <https://doi.org/10.1021/nl060105l>.
- (153) Huang, X.; Jain, P. K.; El-Sayed, I. H.; El-Sayed, M. A. Plasmonic Photothermal Therapy (PPTT) Using Gold Nanoparticles. *Lasers Med Sci* **2008**, *23* (3), 217–228. <https://doi.org/10.1007/s10103-007-0470-x>.
- (154) Lal, S.; Clare, S. E.; Halas, N. J. Nanoshell-Enabled Photothermal Cancer Therapy: Impending Clinical Impact. *Acc Chem Res* **2008**, *41* (12), 1842–1851. <https://doi.org/10.1021/ar800150g>.
- (155) Baffou, G.; Quidant, R. Thermo-plasmonics: Using Metallic Nanostructures as Nano-sources of Heat. *Laser Photon Rev* **2013**, *7* (2), 171–187. <https://doi.org/10.1002/lpor.201200003>.
- (156) Kim, K.; Song, B.; Fernández-Hurtado, V.; Lee, W.; Jeong, W.; Cui, L.; Thompson, D.; Feist, J.; Reid, M. T. H.; García-Vidal, F. J.; Cuevas, J. C.; Meyhofer, E.; Reddy, P. Radiative Heat Transfer in the Extreme near Field. *Nature* **2015**, *528* (7582), 387–391. <https://doi.org/10.1038/nature16070>.
- (157) Govorov, A. O.; Richardson, H. H. Generating Heat with Metal Nanoparticles. *Nano Today* **2007**, *2* (1), 30–38. [https://doi.org/10.1016/S1748-0132\(07\)70017-8](https://doi.org/10.1016/S1748-0132(07)70017-8).
- (158) Baffou, G. *Thermoplasmonics*; Cambridge University Press, 2017. <https://doi.org/10.1017/9781108289801>.
- (159) Govorov, A. O.; Zhang, W.; Skeini, T.; Richardson, H.; Lee, J.; Kotov, N. A. Gold Nanoparticle Ensembles as Heaters and Actuators: Melting and Collective Plasmon Resonances. *Nanoscale Res Lett* **2006**, *1* (1), 84. <https://doi.org/10.1007/s11671-006-9015-7>.
- (160) Baffou, G.; Bordacchini, I.; Baldi, A.; Quidant, R. Simple Experimental Procedures to Distinguish Photothermal from Hot-Carrier Processes in Plasmonics. *Light: Science & Applications* **2020**, *9* (1), 1–16. <https://doi.org/10.1038/s41377-020-00345-0>.
- (161) Mukherjee, S.; Zhou, L.; Goodman, A. M.; Large, N.; Ayala-Orozco, C.; Zhang, Y.; Nordlander, P.; Halas, N. J. Hot-Electron-Induced Dissociation of H₂ on Gold Nanoparticles Supported on SiO₂. *J Am Chem Soc* **2014**, *136* (1), 64–67. <https://doi.org/10.1021/ja411017b>.
- (162) Baffou, G.; Rigneault, H. Femtosecond-Pulsed Optical Heating of Gold Nanoparticles. *Phys Rev B* **2011**, *84* (3), 035415. <https://doi.org/10.1103/PhysRevB.84.035415>.
- (163) Bakhtiari, A. B. S.; Hsiao, D.; Jin, G.; Gates, B. D.; Branda, N. R. An Efficient Method Based on the Photothermal Effect for the Release of Molecules from Metal Nanoparticle Surfaces. *Angewandte Chemie International Edition* **2009**, *48* (23), 4166–4169. <https://doi.org/10.1002/anie.200805303>.
- (164) Fasciani, C.; Alejo, C. J. B.; Grenier, M.; Netto-Ferreira, J. C.; Scaiano, J. C. High-Temperature Organic Reactions at Room Temperature Using Plasmon Excitation: Decomposition of Dicumyl Peroxide. *Org Lett* **2011**, *13* (2), 204–207. <https://doi.org/10.1021/ol1026427>.
- (165) Dos Santos, C. G.; Marquez, D. T.; Crites, C.-O. L.; Netto-Ferreira, J. C.; Scaiano, J. C. Plasmon Heating Mediated Friedel-Crafts Alkylation of Anisole Using Supported AuNP@Nb₂O₅ Catalysts. *Tetrahedron Lett* **2017**, *58* (5), 427–431. <https://doi.org/10.1016/j.tetlet.2016.12.048>.
- (166) Long, R.; Rao, Z.; Mao, K.; Li, Y.; Zhang, C.; Liu, Q.; Wang, C.; Li, Z.; Wu, X.; Xiong, Y. Efficient Coupling of Solar Energy to Catalytic Hydrogenation by Using Well-Designed Palladium Nanostructures. *Angewandte Chemie* **2015**, *127* (8), 2455–2460. <https://doi.org/10.1002/ange.201407785>.

- (167) Gangishetty, M. K.; Fontes, A. M.; Malta, M.; Kelly, T. L.; Scott, R. W. J. Improving the Rates of Pd-Catalyzed Reactions by Exciting the Surface Plasmons of AuPd Bimetallic Nanotriangles. *RSC Adv* **2017**, *7* (64), 40218–40226. <https://doi.org/10.1039/C7RA07264C>.
- (168) Petek, H.; Ogawa, S. Femtosecond Time-Resolved Two-Photon Photoemission Studies of Electron Dynamics in Metals. *Prog. in Surf Sci.* **1997**, *56*, 239–310.
- (169) Liu, L.; Li, P.; Adisak, B.; Ouyang, S.; Umezawa, N.; Ye, J.; Kodiyath, R.; Tanabe, T.; Ramesh, G. V.; Ueda, S.; Abe, H. Gold Photosensitized SrTiO₃ for Visible-Light Water Oxidation Induced by Au Interband Transitions. *J Mater Chem A Mater* **2014**, *2* (25), 9875. <https://doi.org/10.1039/c4ta01988a>.
- (170) Zhu, H.; Chen, X.; Zheng, Z.; Ke, X.; Jaatinen, E.; Zhao, J.; Guo, C.; Xie, T.; Wang, D. Mechanism of Supported Gold Nanoparticles as Photocatalysts under Ultraviolet and Visible Light Irradiation. *Chemical Communications* **2009**, No. 48, 7524. <https://doi.org/10.1039/b917052a>.
- (171) Rangel, T.; Kecik, D.; Trevisanutto, P. E.; Rignanese, G.-M.; Van Swygenhoven, H.; Olevano, V. Band Structure of Gold from Many-Body Perturbation Theory. *Phys Rev B* **2012**, *86* (12), 125125. <https://doi.org/10.1103/PhysRevB.86.125125>.
- (172) Lyu, P.; Espinoza, R.; Nguyen, S. C. Photocatalysis of Metallic Nanoparticles: Interband vs Intraband Induced Mechanisms. *The Journal of Physical Chemistry C* **2023**, *127* (32), 15685–15698. <https://doi.org/10.1021/acs.jpcc.3c04436>.
- (173) Pirzadeh, Z.; Pakizeh, T.; Miljkovic, V.; Langhammer, C.; Dmitriev, A. Plasmon–Interband Coupling in Nickel Nanoantennas. *ACS Photonics* **2014**, *1* (3), 158–162. <https://doi.org/10.1021/ph4000339>.
- (174) Link, S.; El-Sayed, M. A. Optical Properties and Ultrafast Dynamics of Metallic Nanocrystals. *Annu Rev Phys Chem* **2003**, *54* (1), 331–366. <https://doi.org/10.1146/annurev.physchem.54.011002.103759>.
- (175) Narang, P.; Sundararaman, R.; Atwater, H. A. Plasmonic Hot Carrier Dynamics in Solid-State and Chemical Systems for Energy Conversion. *Nanophotonics* **2016**, *5* (1), 96–111. <https://doi.org/10.1515/nanoph-2016-0007>.
- (176) Schlather, A. E.; Manjavacas, A.; Lauchner, A.; Marangoni, V. S.; DeSantis, C. J.; Nordlander, P.; Halas, N. J. Hot Hole Photoelectrochemistry on Au@SiO₂@Au Nanoparticles. *J Phys Chem Lett* **2017**, *8* (9), 2060–2067. <https://doi.org/10.1021/acs.jpcclett.7b00563>.
- (177) Bernardi, M.; Mustafa, J.; Neaton, J. B.; Louie, S. G. Theory and Computation of Hot Carriers Generated by Surface Plasmon Polaritons in Noble Metals. *Nat Commun* **2015**, *6* (1), 7044. <https://doi.org/10.1038/ncomms8044>.
- (178) Lyu, P.; Espinoza, R.; Khan, Md. I.; Spaller, W. C.; Ghosh, S.; Nguyen, S. C. Mechanistic Insight into Deep Holes from Interband Transitions in Palladium Nanoparticle Photocatalysts. *iScience* **2022**, *25* (2), 103737. <https://doi.org/10.1016/j.isci.2022.103737>.
- (179) Al-Zubeidi, A.; Hoener, B. S.; Collins, S. S. E.; Wang, W.; Kirchner, S. R.; Hosseini Jebeli, S. A.; Joplin, A.; Chang, W.-S.; Link, S.; Landes, C. F. Hot Holes Assist Plasmonic Nanoelectrode Dissolution. *Nano Lett* **2019**, *19* (2), 1301–1306. <https://doi.org/10.1021/acs.nanolett.8b04894>.
- (180) Zhao, J.; Nguyen, S. C.; Ye, R.; Ye, B.; Weller, H.; Somorjai, G. A.; Alivisatos, A. P.; Toste, F. D. A Comparison of Photocatalytic Activities of Gold Nanoparticles Following Plasmonic and Interband Excitation and a Strategy for Harnessing Interband Hot Carriers for Solution Phase Photocatalysis. *ACS Cent Sci* **2017**, *3* (5), 482–488. <https://doi.org/10.1021/acscentsci.7b00122>.
- (181) French, A. D. Glucose, Not Cellobiose, Is the Repeating Unit of Cellulose and Why That Is Important. *Cellulose* **2017**, *24* (11), 4605–4609. <https://doi.org/10.1007/s10570-017-1450-3>.

- (182) O’Sullivan, A. C. Cellulose: The Structure Slowly Unravels. *Cellulose* **1997**, *4* (3), 173–207. <https://doi.org/10.1023/A:1018431705579>.
- (183) Kamide, K.; Okajima, K.; Kowsaka, K.; Matsui, T. CP/MASS ¹³C NMR Spectra of Cellulose Solids: An Explanation by the Intramolecular Hydrogen Bond Concept. *Polym J* **1985**, *17* (5), 701–706. <https://doi.org/10.1295/polymj.17.701>.
- (184) Wohler, M.; Bensefelt, T.; Wågberg, L.; Furó, I.; Berglund, L. A.; Wohler, J. Cellulose and the Role of Hydrogen Bonds: Not in Charge of Everything. *Cellulose* **2022**, *29* (1), 1–23. <https://doi.org/doi.org/10.1007/s10570-021-04325-4>.
- (185) Reiter, W.-D. Biosynthesis and Properties of the Plant Cell Wall. *Curr Opin Plant Biol* **2002**, *5* (6), 536–542. [https://doi.org/10.1016/S1369-5266\(02\)00306-0](https://doi.org/10.1016/S1369-5266(02)00306-0).
- (186) Kubicki, J. D.; Yang, H.; Sawada, D.; O’Neill, H.; Oehme, D.; Cosgrove, D. The Shape of Native Plant Cellulose Microfibrils. *Sci Rep* **2018**, *8* (1), 13983. <https://doi.org/10.1038/s41598-018-32211-w>.
- (187) Cosgrove, D. J. Plant Cell Growth and Cell Wall Enlargement. In *Encyclopedia of Life Sciences*; Wiley, 2022; Vol. 2, pp 1–14. <https://doi.org/10.1002/9780470015902.a0029421>.
- (188) FAOSTAT. https://www.fao.org/faostat/en/#rankings/countries_by_commodity (accessed 2024-05-28).
- (189) Postek, M. T.; Vladár, A.; Dagata, J.; Farkas, N.; Ming, B.; Wagner, R.; Raman, A.; Moon, R. J.; Sabo, R.; Wegner, T. H.; Beecher, J. Development of the Metrology and Imaging of Cellulose Nanocrystals. *Meas Sci Technol* **2011**, *22* (2), 024005. <https://doi.org/10.1088/0957-0233/22/2/024005>.
- (190) Lombardo, S.; Thielemans, W. Thermodynamics of Adsorption on Nanocellulose Surfaces. *Cellulose* **2019**, *26* (1), 249–279. <https://doi.org/10.1007/s10570-018-02239-2>.
- (191) Moon, R. J.; Martini, A.; Nairn, J.; Simonsen, J.; Youngblood, J. Cellulose Nanomaterials Review: Structure, Properties and Nanocomposites. *Chem Soc Rev* **2011**, *40* (7), 3941. <https://doi.org/10.1039/c0cs00108b>.
- (192) Yamamoto, H.; Horii, F. CPMAS Carbon-13 NMR Analysis of the Crystal Transformation Induced for Valonia Cellulose by Annealing at High Temperatures. *Macromolecules* **1993**, *26* (6), 1313–1317. <https://doi.org/10.1021/ma00058a020>.
- (193) Yamamoto, H.; Horn, F. In Situ Crystallization of Bacterial Cellulose I. Influences of Polymeric Additives, Stirring and Temperature on the Formation Celluloses Ia and Ib as Revealed by Cross Polarization/Magic Angle Spinning (CP/MAS)¹³C NMR Spectroscopy. *Cellulose* **1994**, *1* (1), 57–66. <https://doi.org/10.1007/BF00818798>.
- (194) Belton, P. S.; Tanner, S. F.; Cartier, N.; Chanzy, H. High-Resolution Solid-State Carbon-13 Nuclear Magnetic Resonance Spectroscopy of Tunicin, an Animal Cellulose. *Macromolecules* **1989**, *22* (4), 1615–1617. <https://doi.org/10.1021/ma00194a019>.
- (195) Nishiyama, Y. Structure and Properties of the Cellulose Microfibril. *Journal of Wood Science* **2009**, *55* (4), 241–249. <https://doi.org/10.1007/s10086-009-1029-1>.
- (196) Klemm, D.; Heublein, B.; Fink, H.; Bohn, A. Cellulose: Fascinating Biopolymer and Sustainable Raw Material. *Angewandte Chemie International Edition* **2005**, *44* (22), 3358–3393. <https://doi.org/10.1002/anie.200460587>.
- (197) Hess, K.; Mahl, H.; Gütter, E. Elektronenmikroskopische Darstellung Großer Längsperioden in Zellulosefasern Und Ihr Vergleich Mit Den Perioden Anderer Faserarten. *Kolloid-Zeitschrift* **1957**, *155* (1), 1–19. <https://doi.org/10.1007/BF01501290>.

- (198) Hearle, J. W. S. The Fine Structure of Fibers and Crystalline Polymers. I. Fringed Fibril Structure. *J Appl Polym Sci* **1963**, *7* (4), 1175–1192. <https://doi.org/10.1002/app.1963.070070401>.
- (199) Iguchi, M.; Yamanaka, S.; Budhiono, A. Bacterial Cellulose - a Masterpiece of Nature's Arts. *J Mater Sci* **2000**, *35* (2), 261–270. <https://doi.org/10.1023/A:1004775229149>.
- (200) Habibi, Y.; Lucia, L. A.; Rojas, O. J. Cellulose Nanocrystals: Chemistry, Self-Assembly, and Applications. *Chem Rev* **2010**, *110* (6), 3479–3500. <https://doi.org/10.1021/cr900339w>.
- (201) Dong, X. M.; Revol, J. F.; Gray, D. G. Effect of Microcrystallite Preparation Conditions on the Formation of Colloid Crystals of Cellulose. *Cellulose* **1998**, *5* (1), 19–32. <https://doi.org/10.1023/A:1009260511939>.
- (202) Zimmermann, T.; Bordeanu, N.; Strub, E. Properties of Nanofibrillated Cellulose from Different Raw Materials and Its Reinforcement Potential. *Carbohydr Polym* **2010**, *79* (4), 1086–1093. <https://doi.org/10.1016/j.carbpol.2009.10.045>.
- (203) Nyström, G.; Mezzenga, R. Liquid Crystalline Filamentous Biological Colloids: Analogies and Differences. *Curr Opin Colloid Interface Sci* **2018**, *38*, 30–44. <https://doi.org/10.1016/J.COCIS.2018.08.004>.
- (204) Van Rie, J.; Thielemans, W. Cellulose–Gold Nanoparticle Hybrid Materials. *Nanoscale* **2017**, *9* (25), 8525–8554. <https://doi.org/10.1039/C7NR00400A>.
- (205) Saito, T.; Hirota, M.; Tamura, N.; Kimura, S.; Fukuzumi, H.; Heux, L.; Isogai, A. Individualization of Nano-Sized Plant Cellulose Fibrils by Direct Surface Carboxylation Using TEMPO Catalyst under Neutral Conditions. *Biomacromolecules* **2009**, *10* (7), 1992–1996. <https://doi.org/10.1021/bm900414t>.
- (206) Xu, T.; Du, H.; Liu, H.; Liu, W.; Zhang, X.; Si, C.; Liu, P.; Zhang, K. Advanced Nanocellulose-Based Composites for Flexible Functional Energy Storage Devices. *Advanced Materials* **2021**, *33* (48), 2101368. <https://doi.org/10.1002/adma.202101368>.
- (207) Gardner, D. J.; Oporto, G. S.; Mills, R.; Samir, M. A. S. A. Adhesion and Surface Issues in Cellulose and Nanocellulose. *J Adhes Sci Technol* **2008**, *22* (5–6), 545–567. <https://doi.org/10.1163/156856108X295509>.
- (208) Beck-Candanedo, S.; Roman, M.; Gray, D. G. Effect of Reaction Conditions on the Properties and Behavior of Wood Cellulose Nanocrystal Suspensions. *Biomacromolecules* **2005**, *6* (2), 1048–1054. <https://doi.org/10.1021/bm049300p>.
- (209) Padalkar, S.; Capadona, J. R.; Rowan, S. J.; Weder, C.; Won, Y.-H.; Stanciu, L. A.; Moon, R. J. Natural Biopolymers: Novel Templates for the Synthesis of Nanostructures. *Langmuir* **2010**, *26* (11), 8497–8502. <https://doi.org/10.1021/la904439p>.
- (210) Spoljaric, S.; Genovese, A.; Shanks, R. A. Polypropylene–Microcrystalline Cellulose Composites with Enhanced Compatibility and Properties. *Compos Part A Appl Sci Manuf* **2009**, *40* (6–7), 791–799. <https://doi.org/10.1016/j.compositesa.2009.03.011>.
- (211) Ljungberg, N.; Bonini, C.; Bortolussi, F.; Boisson, C.; Heux, L.; Cavallé. New Nanocomposite Materials Reinforced with Cellulose Whiskers in Atactic Polypropylene: Effect of Surface and Dispersion Characteristics. *Biomacromolecules* **2005**, *6* (5), 2732–2739. <https://doi.org/10.1021/bm050222v>.
- (212) Siqueira, G.; Bras, J.; Dufresne, A. Cellulose Whiskers versus Microfibrils: Influence of the Nature of the Nanoparticle and Its Surface Functionalization on the Thermal and Mechanical Properties of Nanocomposites. *Biomacromolecules* **2009**, *10* (2), 425–432. <https://doi.org/10.1021/bm801193d>.

- (213) Andresen, M.; Stenstad, P.; Møretrø, T.; Langsrud, S.; Syverud, K.; Johansson, L.-S.; Stenius, P. Nonleaching Antimicrobial Films Prepared from Surface-Modified Microfibrillated Cellulose. *Biomacromolecules* **2007**, *8* (7), 2149–2155. <https://doi.org/10.1021/bm070304e>.
- (214) Fukuzumi, H.; Saito, T.; Iwata, T.; Kumamoto, Y.; Isogai, A. Transparent and High Gas Barrier Films of Cellulose Nanofibers Prepared by TEMPO-Mediated Oxidation. *Biomacromolecules* **2009**, *10* (1), 162–165. <https://doi.org/10.1021/bm801065u>.
- (215) Hubbe, M. A.; Rojas, O. J.; Lucia, L. A.; Sain, M. Cellulosic Nanocomposites, Review. *Bioresources* **2008**, *3* (3), 929–980.
- (216) Lu, P.; Hsieh, Y.-L. Cellulose Nanocrystal-Filled Poly(Acrylic Acid) Nanocomposite Fibrous Membranes. *Nanotechnology* **2009**, *20* (41), 415604. <https://doi.org/10.1088/0957-4484/20/41/415604>.
- (217) Nakagaito, A. N.; Yano, H. The Effect of Fiber Content on the Mechanical and Thermal Expansion Properties of Biocomposites Based on Microfibrillated Cellulose. *Cellulose* **2008**, *15* (4), 555–559. <https://doi.org/10.1007/s10570-008-9212-x>.
- (218) Noishiki, Y.; Nishiyama, Y.; Wada, M.; Kuga, S.; Magoshi, J. Mechanical Properties of Silk Fibroin–Microcrystalline Cellulose Composite Films. *J Appl Polym Sci* **2002**, *86* (13), 3425–3429. <https://doi.org/10.1002/app.11370>.
- (219) Leitner, J.; Hinterstoisser, B.; Wastyn, M.; Keckes, J.; Gindl, W. Sugar Beet Cellulose Nanofibril-Reinforced Composites. *Cellulose* **2007**, *14* (5), 419–425. <https://doi.org/10.1007/s10570-007-9131-2>.
- (220) Svagan, A. J.; Azizi Samir, M. A. S.; Berglund, L. A. Biomimetic Polysaccharide Nanocomposites of High Cellulose Content and High Toughness. *Biomacromolecules* **2007**, *8* (8), 2556–2563. <https://doi.org/10.1021/bm0703160>.
- (221) Chanzy, H.; Henrissat, B.; Vuong, R. Colloidal Gold Labelling of 1,4-β-D-glucan Cellobiohydrolase Adsorbed on Cellulose Substrates. *FEBS Lett* **1984**, *172* (2), 193–197. [https://doi.org/10.1016/0014-5793\(84\)81124-2](https://doi.org/10.1016/0014-5793(84)81124-2).
- (222) Majoinen, J.; Hassinen, J.; Haataja, J. S.; Rekola, H. T.; Kontturi, E.; Kostianen, M. A.; Ras, R. H. A.; Törmä, P.; Ikkala, O. Chiral Plasmonics Using Twisting along Cellulose Nanocrystals as a Template for Gold Nanoparticles. *Advanced Materials* **2016**, *28* (26), 5262–5267. <https://doi.org/10.1002/adma.201600940>.
- (223) Lam, E.; Hrapovic, S.; Majid, E.; Chong, J. H.; Luong, J. H. T. Catalysis Using Gold Nanoparticles Decorated on Nanocrystalline Cellulose. *Nanoscale* **2012**, *4* (3), 997. <https://doi.org/10.1039/c2nr11558a>.
- (224) Qu, D.; Zhang, J.; Chu, G.; Jiang, H.; Wu, C.; Xu, Y. Chiral Fluorescent Films of Gold Nanoclusters and Photonic Cellulose with Modulated Fluorescence Emission. *J Mater Chem C Mater* **2016**, *4* (9), 1764–1768. <https://doi.org/10.1039/C5TC04163E>.
- (225) Guo, J.; Filpponen, I.; Su, P.; Laine, J.; Rojas, O. J. Attachment of Gold Nanoparticles on Cellulose Nanofibrils via Click Reactions and Electrostatic Interactions. *Cellulose* **2016**, *23* (5), 3065–3075. <https://doi.org/10.1007/s10570-016-1042-7>.
- (226) Eskilson, O.; Lindström, S. B.; Sepulveda, B.; Shahjamali, M. M.; Güell-Grau, P.; Sivilér, P.; Skog, M.; Aronsson, C.; Björk, E. M.; Nyberg, N.; Khalaf, H.; Bengtsson, T.; James, J.; Ericson, M. B.; Martinsson, E.; Selegård, R.; Aili, D. Self-Assembly of Mechanoplasmonic Bacterial Cellulose–Metal Nanoparticle Composites. *Adv Funct Mater* **2020**, *30* (40), 2004766. <https://doi.org/10.1002/adfm.202004766>.

- (227) Casado, U.; Mucci, V. L.; Aranguren, M. I. Cellulose Nanocrystals Suspensions: Liquid Crystal Anisotropy, Rheology and Films Iridescence. *Carbohydr Polym* **2021**, *261*, 117848. <https://doi.org/10.1016/j.carbpol.2021.117848>.
- (228) Li, Y.; Prince, E.; Cho, S.; Salari, A.; Mosaddeghian Golestani, Y.; Lavrentovich, O. D.; Kumacheva, E. Periodic Assembly of Nanoparticle Arrays in Disclinations of Cholesteric Liquid Crystals. *Proceedings of the National Academy of Sciences* **2017**, *114* (9), 2137–2142. <https://doi.org/10.1073/pnas.1615006114>.
- (229) Vollick, B.; Kuo, P.-Y.; Thérien-Aubin, H.; Yan, N.; Kumacheva, E. Composite Cholesteric Nanocellulose Films with Enhanced Mechanical Properties. *Chemistry of Materials* **2017**, *29* (2), 789–795. <https://doi.org/10.1021/acs.chemmater.6b04780>.
- (230) Lukach, A.; Thérien-Aubin, H.; Querejeta-Fernández, A.; Pitch, N.; Chauve, G.; Méthot, M.; Bouchard, J.; Kumacheva, E. Coassembly of Gold Nanoparticles and Cellulose Nanocrystals in Composite Films. *Langmuir* **2015**, *31* (18), 5033–5041. <https://doi.org/10.1021/acs.langmuir.5b00728>.
- (231) Querejeta-Fernández, A.; Chauve, G.; Methot, M.; Bouchard, J.; Kumacheva, E. Chiral Plasmonic Films Formed by Gold Nanorods and Cellulose Nanocrystals. *J Am Chem Soc* **2014**, *136* (12), 4788–4793. <https://doi.org/10.1021/ja501642p>.
- (232) Chu, G.; Wang, X.; Yin, H.; Shi, Y.; Jiang, H.; Chen, T.; Gao, J.; Qu, D.; Xu, Y.; Ding, D. Free-Standing Optically Switchable Chiral Plasmonic Photonic Crystal Based on Self-Assembled Cellulose Nanorods and Gold Nanoparticles. *ACS Appl Mater Interfaces* **2015**, *7* (39), 21797–21806. <https://doi.org/10.1021/acsami.5b05645>.
- (233) Garavand, A.; Dadkhah Tehrani, A. New Organic-Inorganic Hybrid Material Based on Functional Cellulose Nanowhisker, Polypseudorotaxane and Au Nanorods. *Carbohydr Polym* **2016**, *152*, 196–206. <https://doi.org/10.1016/j.carbpol.2016.07.038>.
- (234) Ohlendorf, P.; Dulle, M.; Förster, S.; Greiner, A. Supramolecular Nanocomposites: Dual-Functional Cholesteric Hydroxypropyl Cellulose Esters Chemically Linked to Gold Nanoparticles. *ChemNanoMat* **2016**, *2* (4), 290–296. <https://doi.org/10.1002/cnma.201600042>.
- (235) Dong, B. H.; Hinestroza, J. P. Metal Nanoparticles on Natural Cellulose Fibers: Electrostatic Assembly and In Situ Synthesis. *ACS Appl Mater Interfaces* **2009**, *1* (4), 797–803. <https://doi.org/10.1021/am800225j>.
- (236) Yokota, S.; Kitaoka, T.; Opietnik, M.; Rosenau, T.; Wariishi, H. Synthesis of Gold Nanoparticles for In Situ Conjugation with Structural Carbohydrates. *Angewandte Chemie International Edition* **2008**, *47* (51), 9866–9869. <https://doi.org/10.1002/anie.200803922>.
- (237) He, J.; Kunitake, T.; Nakao, A. Facile In Situ Synthesis of Noble Metal Nanoparticles in Porous Cellulose Fibers. *Chemistry of Materials* **2003**, *15* (23), 4401–4406. <https://doi.org/10.1021/cm034720r>.
- (238) Ashraf, S.; Saif-ur-Rehman; Sher, F.; Khalid, Z. M.; Mehmood, M.; Hussain, I. Synthesis of Cellulose–Metal Nanoparticle Composites: Development and Comparison of Different Protocols. *Cellulose* **2014**, *21* (1), 395–405. <https://doi.org/10.1007/s10570-013-0129-7>.
- (239) Koga, H.; Tokunaga, E.; Hidaka, M.; Umemura, Y.; Saito, T.; Isogai, A.; Kitaoka, T. Topochemical Synthesis and Catalysis of Metal Nanoparticles Exposed on Crystalline Cellulose Nanofibers. *Chemical Communications* **2010**, *46* (45), 8567. <https://doi.org/10.1039/c0cc02754e>.
- (240) Carvalho, A. P. G.; Alegria, E. C. B. A.; Fantoni, A.; Ferraria, A. M.; do Rego, A. M. B.; Ribeiro, A. P. C. Effect of Graphene vs. Reduced Graphene Oxide in Gold Nanoparticles for Optical Biosensors—A Comparative Study. *Biosensors (Basel)* **2022**, *12* (3), 163. <https://doi.org/10.3390/bios12030163>.

- (241) Chen, L.; Cao, W.; Quinlan, P. J.; Berry, R. M.; Tam, K. C. Sustainable Catalysts from Gold-Loaded Polyamidoamine Dendrimer-Cellulose Nanocrystals. *ACS Sustain Chem Eng* **2015**, *3* (5), 978–985. <https://doi.org/10.1021/acssuschemeng.5b00110>.
- (242) Yan, W.; Chen, C.; Wang, L.; Zhang, D.; Li, A.-J.; Yao, Z.; Shi, L.-Y. Facile and Green Synthesis of Cellulose Nanocrystal-Supported Gold Nanoparticles with Superior Catalytic Activity. *Carbohydr Polym* **2016**, *140*, 66–73. <https://doi.org/10.1016/j.carbpol.2015.12.049>.
- (243) Zhang, T.; Wang, W.; Zhang, D.; Zhang, X.; Ma, Y.; Zhou, Y.; Qi, L. Biotemplated Synthesis of Gold Nanoparticle–Bacteria Cellulose Nanofiber Nanocomposites and Their Application in Biosensing. *Adv Funct Mater* **2010**, *20* (7), 1152–1160. <https://doi.org/10.1002/adfm.200902104>.
- (244) Li, G.; Sun, K.; Li, D.; Lv, P.; Wang, Q.; Huang, F.; Wei, Q. Biosensor Based on Bacterial Cellulose–Au Nanoparticles Electrode Modified with Laccase for Hydroquinone Detection. *Colloids Surf A Physicochem Eng Asp* **2016**, *509*, 408–414. <https://doi.org/10.1016/j.colsurfa.2016.09.028>.
- (245) Zhang, L.; Li, X.; Ong, L.; Tabor, R. F.; Bowen, B. A.; Fernando, A. I.; Nilghaz, A.; Garnier, G.; Gras, S. L.; Wang, X.; Shen, W. Cellulose Nanofibre Textured SERS Substrate. *Colloids Surf A Physicochem Eng Asp* **2015**, *468*, 309–314. <https://doi.org/10.1016/j.colsurfa.2014.12.056>.
- (246) Ishida, T.; Watanabe, H.; Bebeko, T.; Akita, T.; Haruta, M. Aerobic Oxidation of Glucose over Gold Nanoparticles Deposited on Cellulose. *Appl Catal A Gen* **2010**, *377* (1–2), 42–46. <https://doi.org/10.1016/j.apcata.2010.01.017>.
- (247) Pinto, R. J. B.; Marques, P. A. A. P.; Martins, M. A.; Neto, C. P.; Trindade, T. Electrostatic Assembly and Growth of Gold Nanoparticles in Cellulosic Fibres. *J Colloid Interface Sci* **2007**, *312* (2), 506–512. <https://doi.org/10.1016/j.jcis.2007.03.043>.
- (248) Gruber, S.; Taylor, R. N. K.; Scheel, H.; Greil, P.; Zollfrank, C. Cellulose-Biotemplated Silica Nanowires Coated with a Dense Gold Nanoparticle Layer. *Mater Chem Phys* **2011**, *129* (1–2), 19–22. <https://doi.org/10.1016/j.matchemphys.2011.04.027>.
- (249) Hu, C.; Bai, X.; Wang, Y.; Jin, W.; Zhang, X.; Hu, S. Inkjet Printing of Nanoporous Gold Electrode Arrays on Cellulose Membranes for High-Sensitive Paper-Like Electrochemical Oxygen Sensors Using Ionic Liquid Electrolytes. *Anal Chem* **2012**, *84* (8), 3745–3750. <https://doi.org/10.1021/ac3003243>.
- (250) Han, K.; Kang, K.-S.; Kim, J. Au-Pattern Fabrication on a Cellulose Film Using a Polyurethane Acrylate Mold. *Journal of Micromechanics and Microengineering* **2009**, *19* (3), 035010. <https://doi.org/10.1088/0960-1317/19/3/035010>.
- (251) Ngo, Y. H.; Li, D.; Simon, G. P.; Garnier, G. Gold Nanoparticle–Paper as a Three-Dimensional Surface Enhanced Raman Scattering Substrate. *Langmuir* **2012**, *28* (23), 8782–8790. <https://doi.org/10.1021/la3012734>.
- (252) Bothra, S.; Upadhyay, Y.; Kumar, R.; Ashok Kumar, S. K.; Sahoo, S. K. Chemically Modified Cellulose Strips with Pyridoxal Conjugated Red Fluorescent Gold Nanoclusters for Nanomolar Detection of Mercuric Ions. *Biosens Bioelectron* **2017**, *90*, 329–335. <https://doi.org/10.1016/j.bios.2016.11.066>.
- (253) Wei, H.; Rodriguez, K.; Renneckar, S.; Leng, W.; Vikesland, P. J. Preparation and Evaluation of Nanocellulose–Gold Nanoparticle Nanocomposites for SERS Applications. *Analyst* **2015**, *140* (16), 5640–5649. <https://doi.org/10.1039/C5AN00606F>.
- (254) Park, M.; Chang, H.; Jeong, D. H.; Hyun, J. Spatial Deformation of Nanocellulose Hydrogel Enhances SERS. *Biochip J* **2013**, *7* (3), 234–241. <https://doi.org/10.1007/s13206-013-7306-5>.

- (255) Bumbudsanpharoke, N.; Choi, J.; Park, I.; Ko, S. Facile Biosynthesis and Antioxidant Property of Nanogold-Cellulose Fiber Composite. *J Nanomater* **2015**, *2015*, 1–9. <https://doi.org/10.1155/2015/146460>.
- (256) Johnston, J. H.; Nilsson, T. Nanogold and Nanosilver Composites with Lignin-Containing Cellulose Fibres. *J Mater Sci* **2012**, *47* (3), 1103–1112. <https://doi.org/10.1007/s10853-011-5882-0>.
- (257) You, J.; Zhao, L.; Wang, G.; Zhou, H.; Zhou, J.; Zhang, L. Quaternized Cellulose-Supported Gold Nanoparticles as Capillary Coatings to Enhance Protein Separation by Capillary Electrophoresis. *J Chromatogr A* **2014**, *1343*, 160–166. <https://doi.org/10.1016/j.chroma.2014.03.079>.
- (258) Mahmoud, K. A.; Male, K. B.; Hrapovic, S.; Luong, J. H. T. Cellulose Nanocrystal/Gold Nanoparticle Composite as a Matrix for Enzyme Immobilization. *ACS Appl Mater Interfaces* **2009**, *1* (7), 1383–1386. <https://doi.org/10.1021/am900331d>.
- (259) Chen, M.; Kang, H.; Gong, Y.; Guo, J.; Zhang, H.; Liu, R. Bacterial Cellulose Supported Gold Nanoparticles with Excellent Catalytic Properties. *ACS Appl Mater Interfaces* **2015**, *7* (39), 21717–21726. <https://doi.org/10.1021/acsami.5b07150>.
- (260) Herreros-López, A.; Hadad, C.; Yate, L.; Alshatwi, A. A.; Vicentini, N.; Carofiglio, T.; Prato, M. Synthesis and Catalytic Activity of Gold Nanoparticles Supported on Dendrimeric Nanocellulose Hybrids. *European J Org Chem* **2016**, *2016* (19), 3186–3192. <https://doi.org/10.1002/EJOC.201600148>.
- (261) Mazeau, K.; Vergelati, C. Atomistic Modeling of the Adsorption of Benzophenone onto Cellulosic Surfaces. *Langmuir* **2002**, *18* (5), 1919–1927. <https://doi.org/10.1021/la010792q>.
- (262) Mazeau, K. On the External Morphology of Native Cellulose Microfibrils. *Carbohydr Polym* **2011**, *84* (1), 524–532. <https://doi.org/10.1016/J.CARBPOL.2010.12.016>.
- (263) Larik, S. A.; Khatri, A.; Ali, S.; Kim, S. H. Batchwise Dyeing of Bamboo Cellulose Fabric with Reactive Dye Using Ultrasonic Energy. *Ultrason Sonochem* **2015**, *24*, 178–183. <https://doi.org/10.1016/J.ULTSONCH.2014.12.016>.
- (264) Hokkanen, S.; Repo, E.; Westholm, L. J.; Lou, S.; Sainio, T.; Sillanpää, M. Adsorption of Ni²⁺, Cd²⁺, PO₄³⁻ and NO₃⁻ from Aqueous Solutions by Nanostructured Microfibrillated Cellulose Modified with Carbonated Hydroxyapatite. *Chemical Engineering Journal* **2014**, *252*, 64–74. <https://doi.org/doi.org/10.1016/j.cej.2014.04.101>.
- (265) Hokkanen, S.; Repo, E.; Sillanpää, M. Removal of Heavy Metals from Aqueous Solutions by Succinic Anhydride Modified Mercerized Nanocellulose. *Chemical Engineering Journal* **2013**, *223*, 40–47. <https://doi.org/doi.org/10.1016/j.cej.2013.02.054>.
- (266) Iamazaki, E. T.; Atvars, T. D. Z. Sorption of a Fluorescent Whitening Agent (Tinopal CBS) onto Modified Cellulose Fibers in the Presence of Surfactants and Salt. *Langmuir* **2007**, *23* (26), 12886–12892. <https://doi.org/doi.org/10.1021/la702225h>.
- (267) Iamazaki, E. T.; Atvars, T. D. Z. Role of Surfactants in the Sorption of the Whitening Agent Tinopal CBS onto Viscose Fibers: A Fluorescence Spectroscopy Study. *Langmuir* **2006**, *22* (24), 9866–9873. <https://doi.org/doi.org/10.1021/la061309k>.
- (268) Liu, H.; Shi, H.; Wang, Y.; Wu, W.; Ni, Y. Interactions of Lignin with Optical Brightening Agents and Their Effect on Paper Optical Properties. *Ind Eng Chem Res* **2014**, *53* (8), 3091–3096. <https://doi.org/oi.org/10.1021/ie4032082>.
- (269) Kim, M.; Lee, H.; Kim, M.; Park, Y. C. Coloration and Chromatic Sensing Behavior of Electrospun Cellulose Fibers with Curcumin. *Nanomaterials* **2021**, *Vol. 11*, Page 222 **2021**, *11* (1), 222. <https://doi.org/doi.org/10.3390/nano11010222>.

- (270) Zhou, Y.; Zhang, M.; Hu, X.; Wang, X.; Niu, J.; Ma, T. Adsorption of Cationic Dyes on a Cellulose-Based Multicarboxyl Adsorbent. *J Chem Eng Data* **2013**, *58* (2), 413–421. <https://doi.org/doi.org/10.1021/je301140c>.
- (271) Wang, W.; Zhang, X.; Li, C.; Du, G.; Zhang, H.; Ni, Y. Using Carboxylated Cellulose Nanofibers to Enhance Mechanical and Barrier Properties of Collagen Fiber Film by Electrostatic Interaction. *J Sci Food Agric* **2018**, *98* (8), 3089–3097. <https://doi.org/10.1002/JSFA.8809>.
- (272) Zhang, M.; Ding, C.; Chen, L.; Huang, L. Preparation of Tannin-Immobilized Collagen/Cellulose Bead for Pb(II) Adsorption in Aqueous Solutions. *Bioresources* **2015**, *10* (1), 1773–1789. <https://doi.org/10.15376/BIORES.10.1.1773-1789>.
- (273) Burkinshaw, S. M. The Role of Inorganic Electrolyte (Salt) in Cellulosic Fibre Dyeing: Part 2 Theories of How Inorganic Electrolyte Promotes Dye Uptake. *Coloration Technology* **2021**, *137* (6), 547–586. <https://doi.org/10.1111/COTE.12550>.
- (274) Sun, B.; Hou, Q.; He, Z.; Liu, Z.; Ni, Y. Cellulose Nanocrystals (CNC) as Carriers for a Spirooxazine Dye and Its Effect on Photochromic Efficiency. *Carbohydr Polym* **2014**, *111*, 419–424. <https://doi.org/doi.org/10.1016/j.carbpol.2014.03.051>.
- (275) Araki, J. Dye Adsorption Revisited: Application of the Cationic Dye Adsorption Method for the Quantitative Determination of the Acidic Surface Groups of Nanocellulose Materials. *Cellulose* **2021**, *28* (12), 7707–7715. <https://doi.org/10.1007/s10570-021-04035-x>.
- (276) Bonacchi, S.; Cantelli, A.; Battistelli, G.; Guidetti, G.; Calvaresi, M.; Manzi, J.; Gabrielli, L.; Ramadori, F.; Gambarin, A.; Mancin, F.; Montalti, M. Photoswitchable NIR-Emitting Gold Nanoparticles. *Angewandte Chemie* **2016**, *128* (37), 11230–11234. <https://doi.org/10.1002/ANGE.201604290>.
- (277) Browne, W. R.; Feringa, B. L. Light Switching of Molecules on Surfaces. *Annu. Rev. Phys. Chem.* **2009**, *60*, 407–428. <https://doi.org/10.1146/ANNUREV.PHYSICHEM.040808.090423>.
- (278) Tian, H.; Zhang, J. *Photochromic Materials: Preparation, Properties and Applications*; Wiley, 2016.
- (279) Fritzsche, J. Note Sur Les Carbures d'hydrogène Solides, Tirés Du Goudron de Houille. *CR Acad. Sci* **1867**, *69*, 1035–1037.
- (280) Dürr, H.; Bouas-Laurent, H. *Photochromism: Molecules and Systems*, 1st ed.; Elsevier: Amsterdam, 2003.
- (281) Bouas-Laurent, H.; Dürr, H. Organic Photochromism (IUPAC Technical Report). *Pure and Applied Chemistry* **2001**, *73* (4), 639–665. <https://doi.org/10.1351/pac200173040639>.
- (282) Jerca, F. A.; Jerca, V. V.; Hoogenboom, R. Advances and Opportunities in the Exciting World of Azobenzenes. *Nat Rev Chem* **2021**, *6* (1), 51–69. <https://doi.org/10.1038/s41570-021-00334-w>.
- (283) Cheng, H.; Zhang, S.; Bai, E.; Cao, X.; Wang, J.; Qi, J.; Liu, J.; Zhao, J.; Zhang, L.; Yoon, J. Future-Oriented Advanced Diarylethene Photoswitches: From Molecular Design to Spontaneous Assembly Systems. *Advanced Materials* **2022**, *34* (16), 2108289. <https://doi.org/10.1002/adma.202108289>.
- (284) Teka, T.; Zhang, L.; Ge, X.; Li, Y.; Han, L.; Yan, X. Stilbenes: Source Plants, Chemistry, Biosynthesis, Pharmacology, Application and Problems Related to Their Clinical Application-A Comprehensive Review. *Phytochemistry* **2022**, *197*, 113128. <https://doi.org/10.1016/j.phytochem.2022.113128>.

- (285) Kozlenko, A. S.; Ozhogin, I. V.; Pugachev, A. D.; Lukyanova, M. B.; El-Sewify, I. M.; Lukyanov, B. S. A Modern Look at Spiropyrans: From Single Molecules to Smart Materials. *Top Curr Chem* **2023**, *381* (1), 8. <https://doi.org/10.1007/s41061-022-00417-2>.
- (286) Rogers, J. A.; Bao, Z.; Baldwin, K.; Dodabalapur, A.; Crone, B.; Raju, V. R.; Kuck, V.; Katz, H.; Amundson, K.; Ewing, J.; Drzaic, P. Paper-like Electronic Displays: Large-Area Rubber-Stamped Plastic Sheets of Electronics and Microencapsulated Electrophoretic Inks. *Proceedings of the National Academy of Sciences* **2001**, *98* (9), 4835–4840. <https://doi.org/10.1073/pnas.091588098>.
- (287) Velema, W. A.; Szymanski, W.; Feringa, B. L. Photopharmacology: Beyond Proof of Principle. *J Am Chem Soc* **2014**, *136* (6), 2178–2191. <https://doi.org/10.1021/ja413063e>.
- (288) Russell, T. P. Surface-Responsive Materials. *Science (1979)* **2002**, *297* (5583), 964–967. <https://doi.org/10.1126/science.1075997>.
- (289) Lubbe, A. S.; Szymanski, W.; Feringa, B. L. Recent Developments in Reversible Photoregulation of Oligonucleotide Structure and Function. *Chem Soc Rev* **2017**, *46* (4), 1052–1079. <https://doi.org/10.1039/C6CS00461J>.
- (290) Hartley, G. S. The Cis-Form of Azobenzene. *Nature* **1937**, *140* (3537), 281–281. <https://doi.org/10.1038/140281a0>.
- (291) Bandara, H. M. D.; Burdette, S. C. Photoisomerization in Different Classes of Azobenzene. *Chem Soc Rev* **2012**, *41* (5), 1809–1825. <https://doi.org/10.1039/C1CS15179G>.
- (292) Wu, A.; Talham, D. R. Photoisomerization of Azobenzene Chromophores in Organic/Inorganic Zirconium Phosphonate Thin Films Prepared Using a Combined Langmuir–Blodgett and Self-Assembled Monolayer Deposition. *Langmuir* **2000**, *16* (19), 7449–7456. <https://doi.org/10.1021/la000407h>.
- (293) Yin, R.; Xu, W.; Kondo, M.; Yen, C.-C.; Mamiya, J.; Ikeda, T.; Yu, Y. Can Sunlight Drive the Photoinduced Bending of Polymer Films? *J Mater Chem* **2009**, *19* (20), 3141. <https://doi.org/10.1039/b904973h>.
- (294) Koshima, H.; Ojima, N.; Uchimoto, H. Mechanical Motion of Azobenzene Crystals upon Photoirradiation. *J Am Chem Soc* **2009**, *131* (20), 6890–6891. <https://doi.org/10.1021/ja8098596>.
- (295) Akiyama, H.; Tamada, K.; Nagasawa, J.; Abe, K.; Tamaki, T. Photoreactivity in Self-Assembled Monolayers Formed from Asymmetric Disulfides Having Para-Substituted Azobenzenes. *J Phys Chem B* **2003**, *107* (1), 130–135. <https://doi.org/10.1021/jp026103g>.
- (296) Óvári, L.; Wolf, M.; Tegeder, P. Reversible Changes in the Vibrational Structure of Tetra-*Tert*-Butylazobenzene on a Au(111) Surface Induced by Light and Thermal Activation. *The Journal of Physical Chemistry C* **2007**, *111* (42), 15370–15374. <https://doi.org/10.1021/jp075274o>.
- (297) Murase, T.; Sato, S.; Fujita, M. Switching the Interior Hydrophobicity of a Self-Assembled Spherical Complex through the Photoisomerization of Confined Azobenzene Chromophores. *Angewandte Chemie International Edition* **2007**, *46* (27), 5133–5136. <https://doi.org/10.1002/anie.200700793>.
- (298) Balzani, V.; Credi, A.; Marchioni, F.; Stoddart, J. F. Artificial Molecular-Level Machines. Dethreading–Rethreading of a Pseudorotaxane Powered Exclusively by Light Energy. *Chemical Communications* **2001**, *1* (18), 1860–1861. <https://doi.org/10.1039/b105160c>.
- (299) Liao, X.; Chen, G.; Liu, X.; Chen, W.; Chen, F.; Jiang, M. Photoresponsive Pseudopolyrotaxane Hydrogels Based on Competition of Host–Guest Interactions. *Angewandte Chemie International Edition* **2010**, *49* (26), 4409–4413. <https://doi.org/10.1002/anie.201000141>.

- (300) Dudek, M.; Tarnowicz-Staniak, N.; Deiana, M.; Pokładek, Z.; Samoć, M.; Matczyszyn, K. Two-Photon Absorption and Two-Photon-Induced Isomerization of Azobenzene Compounds. *RSC Adv* **2020**, *10* (66), 40489–40507. <https://doi.org/10.1039/D0RA07693G>.
- (301) Satzger, H.; Spörlein, S.; Root, C.; Wachtveitl, J.; Zinth, W.; Gilch, P. Fluorescence Spectra of Trans- and Cis-Azobenzene – Emission from the Franck–Condon State. *Chem Phys Lett* **2003**, *372* (1–2), 216–223. [https://doi.org/10.1016/S0009-2614\(03\)00364-6](https://doi.org/10.1016/S0009-2614(03)00364-6).
- (302) Yagai, S.; Kitamura, A. Recent Advances in Photoresponsive Supramolecular Self-Assemblies. *Chem Soc Rev* **2008**, *37* (8), 1520. <https://doi.org/10.1039/b703092b>.
- (303) Hansen, M. J.; Lerch, M. M.; Szymanski, W.; Feringa, B. L. Direct and Versatile Synthesis of Red-Shifted Azobenzenes. *Angewandte Chemie International Edition* **2016**, *55* (43), 13514–13518. <https://doi.org/10.1002/ANIE.201607529>.
- (304) Kuntze, K.; Isokuortti, J.; Siiskonen, A.; Durandin, N.; Laaksonen, T.; Priimagi, A. Azobenzene Photoswitching with Near-Infrared Light Mediated by Molecular Oxygen. *J Phys Chem B* **2021**, *125* (45), 12568–12573. <https://doi.org/10.1021/acs.jpcc.1c08012>.
- (305) Dudek, M.; Pokładek, Z.; Deiana, M.; Matczyszyn, K. Molecular Design and Structural Characterization of Photoresponsive Azobenzene-Based Polyamide Units. *Dyes and Pigments* **2020**, *180*, 108501. <https://doi.org/10.1016/j.dyepig.2020.108501>.
- (306) Beharry, A. A.; Sadovski, O.; Woolley, G. A. Azobenzene Photoswitching without Ultraviolet Light. *J Am Chem Soc* **2011**, *133* (49), 19684–19687. <https://doi.org/10.1021/ja209239m>.
- (307) Bléger, D.; Schwarz, J.; Brouwer, A. M.; Hecht, S. *O*-Fluoroazobenzenes as Readily Synthesized Photoswitches Offering Nearly Quantitative Two-Way Isomerization with Visible Light. *J Am Chem Soc* **2012**, *134* (51), 20597–20600. <https://doi.org/10.1021/ja310323y>.
- (308) Agnetta, L.; Bermudez, M.; Riefolo, F.; Matera, C.; Claro, E.; Messerer, R.; Littmann, T.; Wolber, G.; Holzgrabe, U.; Decker, M. Fluorination of Photoswitchable Muscarinic Agonists Tunes Receptor Pharmacology and Photochromic Properties. *J Med Chem* **2019**, *62* (6), 3009–3020. <https://doi.org/10.1021/acs.jmedchem.8b01822>.
- (309) Ulman, A. Formation and Structure of Self-Assembled Monolayers. *Chem Rev* **1996**, *96* (4), 1533–1554. <https://doi.org/10.1021/CR9502357>.
- (310) Love, J. C.; Estroff, L. A.; Kriebel, J. K.; Nuzzo, R. G.; Whitesides, G. M. Self-Assembled Monolayers of Thiolates on Metals as a Form of Nanotechnology. *Chem Rev* **2005**, *105* (4), 1103–1170. <https://doi.org/10.1021/cr0300789>.
- (311) Evans, S. D.; Johnson, S. R.; Ringsdorf, H.; Williams, L. M.; Wolf, H. Photoswitching of Azobenzene Derivatives Formed on Planar and Colloidal Gold Surfaces. *Langmuir* **1998**, *14* (22), 6436–6440. <https://doi.org/10.1021/LA980450T>.
- (312) Caldwell, W. B.; Campbell, D. J.; Chen, K.; Herr, B. R.; Mirkin, C. A.; Malik, A.; Durbin, M. K.; Dutta, P.; Huang, K. G. A Highly Ordered Self-Assembled Monolayer Film of an Azobenzenealkanethiol on Au(111): Electrochemical Properties and Structural Characterization by Synchrotron in-Plane X-Ray Diffraction, Atomic Force Microscopy, and Surface-Enhanced Raman Spectroscopy. *J Am Chem Soc* **1995**, *117* (22), 6071–6082. <https://doi.org/10.1021/ja00127a021>.
- (313) Tamada, K.; Nagasawa, J.; Nakanishi, F.; Abe, K.; Ishida, T.; Hara, M.; Knoll, W. Structure and Growth of Hexyl Azobenzene Thiol SAMs on Au(111). *Langmuir* **1998**, *14* (12), 3264–3271. <https://doi.org/10.1021/la971348j>.
- (314) Müller, M.; Jung, U.; Gusak, V.; Ulrich, S.; Holz, M.; Herges, R.; Langhammer, C.; Magnussen, O. Localized Surface Plasmon Resonance Investigations of Photoswitching in Azobenzene-

- Functionalized Self-Assembled Monolayers on Au. *Langmuir* **2013**, *29* (34), 10693–10699. <https://doi.org/10.1021/la401825f>.
- (315) Lim, H. S.; Han, J. T.; Kwak, D.; Jin, M.; Cho, K. Photoreversibly Switchable Superhydrophobic Surface with Erasable and Rewritable Pattern. *J Am Chem Soc* **2006**, *128* (45), 14458–14459. <https://doi.org/10.1021/ja0655901>.
- (316) Liu, D.; Xie, Y.; Shao, H.; Jiang, X. Using Azobenzene-Embedded Self-Assembled Monolayers To Photochemically Control Cell Adhesion Reversibly. *Angewandte Chemie International Edition* **2009**, *48* (24), 4406–4408. <https://doi.org/10.1002/anie.200901130>.
- (317) Wang, R.; Iyoda, T.; Jiang, L.; Tryk, D. A.; Hashimoto, K.; Fujishima, A. Structural Investigation of Azobenzene-Containing Self-Assembled Monolayer Films. *Journal of Electroanalytical Chemistry* **1997**, *438* (1–2), 213–219. [https://doi.org/10.1016/S0022-0728\(96\)05031-0](https://doi.org/10.1016/S0022-0728(96)05031-0).
- (318) Tamada, K.; Nagasawa, J.; Nakanishi, F.; Abe, K.; Hara, M.; Knoll, W.; Ishida, T.; Fukushima, H.; Miyashita, S.; Usui, T.; Koini, T.; R. Lee, T. Structure of SAMs Generated from Functionalized Thiols on Gold. *Thin Solid Films* **1998**, *327–329* (1–2), 150–155. [https://doi.org/10.1016/S0040-6090\(98\)00618-X](https://doi.org/10.1016/S0040-6090(98)00618-X).
- (319) Victor, J. G.; Torkelson, J. M. On Measuring the Distribution of Local Free Volume in Glassy Polymers by Photochromic and Fluorescence Techniques. *Macromolecules* **1987**, *20* (9), 2241–2250. <https://doi.org/10.1021/ma00175a032>.
- (320) Nakagawa, M.; Watase, R.; Ichimura, K. Preparation of Monolayers of Ion-Paired Macrocyclic Amphiphiles to Estimate a Critical Free Space Required for Azobenzene Photoisomerization. *Chem Lett* **1999**, *28* (11), 1209–1210. <https://doi.org/10.1246/cl.1999.1209>.
- (321) Delamarche, E.; Michel, B.; Gerber, Ch.; Anselmetti, D.; Guentherodt, H.-J.; Wolf, H.; Ringsdorf, H. Real-Space Observation of Nanoscale Molecular Domains in Self-Assembled Monolayers. *Langmuir* **1994**, *10* (9), 2869–2871. <https://doi.org/10.1021/la00021a006>.
- (322) Jaschke, M.; Schönherr, H.; Wolf, H.; Butt, H.-J.; Bamberg, E.; Besocke, M. K.; Ringsdorf, H. Structure of Alkyl and Perfluoroalkyl Disulfide and Azobenzene-thiol Monolayers on Gold(111) Revealed by Atomic Force Microscopy. *J Phys Chem* **1996**, *100* (6), 2290–2301. <https://doi.org/10.1021/jp952355o>.
- (323) Jung, U.; Filinova, O.; Kuhn, S.; Zargarani, D.; Bornholdt, C.; Herges, R.; Magnussen, O. Photoswitching Behavior of Azobenzene-Containing Alkanethiol Self-Assembled Monolayers on Au Surfaces. *Langmuir* **2010**, *26* (17), 13913–13923. <https://doi.org/10.1021/la1015109>.
- (324) Moldt, T.; Przyrembel, D.; Schulze, M.; Bronsch, W.; Boie, L.; Brete, D.; Gahl, C.; Klajn, R.; Tegeder, P.; Weinelt, M. Differing Isomerization Kinetics of Azobenzene-Functionalized Self-Assembled Monolayers in Ambient Air and in Vacuum. *Langmuir* **2016**, *32* (42), 10795–10801. <https://doi.org/10.1021/acs.langmuir.6b01690>.
- (325) Ahonen, P.; Laaksonen, T.; Schiffrin, D. J.; Kontturi, K. Photoswitching Electron Transport Properties of an Azobenzene Containing Thiol-SAM. *Physical Chemistry Chemical Physics* **2007**, *9* (35), 4898–4901. <https://doi.org/10.1039/B709025K>.
- (326) Kumar, A. S.; Ye, T.; Takami, T.; Yu, B.-C.; Flatt, A.K.; Tour, J.M.; Weiss, P. S. Reversible Photo-Switching of Single Azobenzene Molecules in Controlled Nanoscale Environments. *Nano Lett.* **2008**, *8* (6), 1644–1648. <https://doi.org/10.1021/nl080323+>.
- (327) Ito, M.; Wei, T. X.; Chen, P. L.; Akiyama, H.; Matsumoto, M.; Tamada, K.; Yamamoto, Y. A Novel Method for Creation of Free Volume in a One-Component Self-Assembled Monolayer. Dramatic Size Effect of Para-Carborane. *J Mater Chem* **2005**, *15* (4), 478–483. <https://doi.org/10.1039/B411121D>.

- (328) Wan, P.; Jiang, Y.; Wang, Y.; Wang, Z.; Zhang, X. Tuning Surface Wettability through Photocontrolled Reversible Molecular Shuttle. *Chemical Communications* **2008**, No. 44, 5710–5712. <https://doi.org/10.1039/B811729B>.
- (329) Weidner, T.; Bretthauer, F.; Ballav, N.; Motschmann, H.; Orendi, H.; Bruhn, C.; Siemeling, U.; Zharnikov, M. Correlation between the Molecular Structure and Photoresponse in Aliphatic Self-Assembled Monolayers with Azobenzene Tailgroups. *Langmuir* **2008**, *24* (20), 11691–11700. <https://doi.org/10.1021/la802454w>.
- (330) Siemeling, U.; Bruhn, C.; Bretthauer, F.; Borg, M.; Träger, F.; Vogel, F.; Azzam, W.; Badin, M.; Strunskus, T.; Wöll, C. Photoresponsive SAMs on Gold Fabricated from Azobenzene-Functionalised Asparagusic Acid Derivatives. *Dalton Transactions* **2009**, No. 40, 8593–8604. <https://doi.org/10.1039/B905025F>.
- (331) Núñez, R.; Romero, I.; Teixidor, F.; Viñas, C. Icosahedral Boron Clusters: A Perfect Tool for the Enhancement of Polymer Features. *Chem Soc Rev* **2016**, *45* (19), 5147–5173. <https://doi.org/10.1039/C6CS00159A>.
- (332) Tamada, K.; Akiyama, H.; Wei, T. X. Photoisomerization Reaction of Unsymmetrical Azobenzene Disulfide Self-Assembled Monolayers Studied by Surface Plasmon Spectroscopy: Influences of Side Chain Length and Contacting Medium. *Langmuir* **2002**, *18* (13), 5239–5246. <https://doi.org/10.1021/la0157667>.
- (333) Tamada, K.; Akiyama, H.; Wei, T.-X.; Kim, S.-A. Photoisomerization Reaction of Unsymmetrical Azobenzene Disulfide Self-Assembled Monolayers: Modification of Azobenzene Dyes to Improve Thermal Endurance for Photoreaction. *Langmuir* **2003**, *19* (6), 2306–2312. <https://doi.org/10.1021/la0258493>.
- (334) Ah Qune, L. F. N.; Akiyama, H.; Nagahiro, T.; Tamada, K.; Wee, A. T. S. Reversible Work Function Changes Induced by Photoisomerization of Asymmetric Azobenzene Dithiol Self-Assembled Monolayers on Gold. *Appl Phys Lett* **2008**, *93* (8), 083109. <https://doi.org/10.1063/1.2969468>.
- (335) Klajn, R. Immobilized Azobenzenes for the Construction of Photoresponsive Materials. *Pure and Applied Chemistry* **2010**, *82* (12), 2247–2279. <https://doi.org/10.1351/PAC-CON-10-09-04>.
- (336) Shin, K. H.; Eun, J. S. Photoresponsive Azobenzene-Modified Gold Nanoparticle. *Bull Korean Chem Soc* **2008**, *29* (6), 1259–1262. <https://doi.org/10.5012/bkcs.2008.29.6.1259>.
- (337) Klajn, R.; Stoddart, J. F.; Grzybowski, B. A. Nanoparticles Functionalised with Reversible Molecular and Supramolecular Switches. *Chem Soc Rev* **2010**, *39* (6), 2203–2237. <https://doi.org/10.1039/B920377J>.
- (338) Ramírez-Rave, S.; Bernad-Bernad, M. J.; Gracia-Mora, J.; Yatsimirsky, A. K. Recent Advances in Application of Azobenzenes Grafted on Mesoporous Silica Nanoparticles in Controlled Drug Delivery Systems Using Light as External Stimulus. *Mini-Reviews in Medicinal Chemistry* **2020**, *20* (11), 1001–1016. <https://doi.org/10.2174/1389557519666190904145355>.
- (339) Chu, Z.; Han, Y.; Bian, T.; De, S.; Kraí, P.; Klajn, R. Supramolecular Control of Azobenzene Switching on Nanoparticles. *J. Am. Chem. Soc* **2019**, *141*, 1949–1960. <https://doi.org/10.1021/jacs.8b09638>.
- (340) Klajn, R.; Wesson, P. J.; Bishop, K. J. M.; Grzybowski, B. A. Writing Self-Erasing Images Using Metastable Nanoparticle “Inks.” *Angewandte Chemie International Edition* **2009**, *48* (38), 7035–7039. <https://doi.org/10.1002/ANIE.200901119>.
- (341) Lee, J.-W.; Klajn, R. Dual-Responsive Nanoparticles That Aggregate under the Simultaneous Action of Light and CO₂. *Chemical Communications* **2015**, *51* (11), 2036–2039. <https://doi.org/10.1039/C4CC08541H>.

- (342) Krajczewski, J.; Ambroziak, R.; Kudelski, A. Photo-Assembly of Plasmonic Nanoparticles: Methods and Applications. *RSC Adv* **2021**, *11*, 2575–2595. <https://doi.org/10.1039/d0ra09337h>.
- (343) Lysyakova, L.; Lomadze, N.; Neher, D.; Maximova, K.; Kabashin, A. V.; Santer, S. Light-Tunable Plasmonic Nanoarchitectures Using Gold Nanoparticle–Azobenzene-Containing Cationic Surfactant Complexes. *Journal of Physical Chemistry C* **2015**, *119* (7), 3762–3770. <https://doi.org/10.1021/JP511232G>.
- (344) van der Molen, S. J.; Liao, J.; Kudernac, T.; Agustsson, J. S.; Bernard, L.; Calame, M.; van Wees, B. J.; Feringa, B. L.; Schönenberger, C. Light-Controlled Conductance Switching of Ordered Metal–Molecule–Metal Devices. *Nano Lett* **2009**, *9* (1), 76–80. <https://doi.org/10.1021/nl802487j>.
- (345) Zheng, Y. B.; Yang, Y.-W.; Jensen, L.; Fang, L.; Juluri, B. K.; Flood, A. H.; Weiss, P. S.; Stoddart, J. F.; Huang, T. J. Active Molecular Plasmonics: Controlling Plasmon Resonances with Molecular Switches. *Nano Lett* **2009**, *9* (2), 819–825. <https://doi.org/10.1021/nl803539g>.
- (346) Klajn, R.; Fang, L.; Coskun, A.; Olson, M. A.; Wesson, P. J.; Stoddart, J. F.; Grzybowski, B. A. Metal Nanoparticles Functionalized with Molecular and Supramolecular Switches. *J Am Chem Soc* **2009**, *131* (12), 4233–4235. <https://doi.org/10.1021/ja9001585>.
- (347) Yoon, J. H.; Yoon, S. Photoisomerization of Azobenzene Derivatives Confined in Gold Nanoparticle Aggregates. *Physical Chemistry Chemical Physics* **2011**, *13* (28), 12900–12905. <https://doi.org/10.1039/C0CP02588G>.
- (348) Klajn, R.; Bishop, K. J. M.; Grzybowski, B. A. Light-Controlled Self-Assembly of Reversible and Irreversible Nanoparticle Suprastructures. *Proceedings of the National Academy of Sciences* **2007**, *104* (25), 10305–10309. <https://doi.org/10.1073/PNAS.0611371104>.
- (349) Zhao, H.; Sen, S.; Udayabhaskararao, T.; Sawczyk, M. M.; Kučanda, K.; Manna, D.; Kundu, P. K.; Lee, J.-W. W.; Král, P.; Klajn, R. Reversible Trapping and Reaction Acceleration within Dynamically Self-Assembling Nanoflasks. *Nat Nanotechnol* **2016**, *11* (1), 82–88. <https://doi.org/10.1038/nnano.2015.256>.
- (350) Zhang, J.; Whitesell, J. K.; Fox, M. A. Photoreactivity of Self-Assembled Monolayers of Azobenzene or Stilbene Derivatives Capped on Colloidal Gold Clusters. *Chemistry of Materials* **2001**, *13* (7), 2323–2331. <https://doi.org/10.1021/cm000752s>.
- (351) Manna, A.; Chen, P.-L.; Akiyama, H.; Wei, T.-X.; Tamada, K.; Knoll, W. Optimized Photoisomerization on Gold Nanoparticles Capped by Unsymmetrical Azobenzene Disulfides. *Chemistry of Materials* **2003**, *15* (1), 20–28. <https://doi.org/10.1021/cm0207696>.
- (352) Hallett-Tapley, G. L.; D’Alfonso, C.; Pacioni, N. L.; McTiernan, C. D.; González-Béjar, M.; Lanzalunga, O.; Alarcon, E. I.; Scaiano, J. C. Gold Nanoparticle Catalysis of the Cis–Trans Isomerization of Azobenzene. *Chemical Communications* **2013**, *49* (86), 10073. <https://doi.org/10.1039/c3cc41669k>.
- (353) Tarnowicz-Staniak, N.; Vázquez-Díaz, S.; Pavlov, V.; Matczyszyn, K.; Grzelczak, M. Cellulose as an Inert Scaffold in Plasmon-Assisted Photoregeneration of Cofactor Molecules. *ACS Appl Mater Interfaces* **2020**, *12* (17), 19377–19383. <https://doi.org/10.1021/acsami.9b21556>.
- (354) Liu, L.; Ouyang, S.; Ye, J. Gold-Nanorod-Photosensitized Titanium Dioxide with Wide-Range Visible-Light Harvesting Based on Localized Surface Plasmon Resonance. *Angewandte Chemie International Edition* **2013**, *52* (26), 6689–6693. <https://doi.org/10.1002/anie.201300239>.
- (355) Zheng, Z.; Tachikawa, T.; Majima, T. Single-Particle Study of Pt-Modified Au Nanorods for Plasmon-Enhanced Hydrogen Generation in Visible to Near-Infrared Region. *J Am Chem Soc* **2014**, *136* (19), 6870–6873. <https://doi.org/10.1021/ja502704n>.

- (356) Kumar, D.; Lee, A.; Lee, T.; Lim, M.; Lim, D.-K. Ultrafast and Efficient Transport of Hot Plasmonic Electrons by Graphene for Pt Free, Highly Efficient Visible-Light Responsive Photocatalyst. *Nano Lett* **2016**, *16* (3), 1760–1767. <https://doi.org/10.1021/acs.nanolett.5b04764>.
- (357) Sánchez-Iglesias, A.; Chuvilin, A.; Grzelczak, M. Plasmon-Driven Photoregeneration of Cofactor Molecules. *Chemical Communications* **2015**, *51* (25), 5330–5333. <https://doi.org/10.1039/C4CC07829B>.
- (358) Sánchez-Iglesias, A.; Barroso, J.; Solís, D. M.; Taboada, J. M.; Obelleiro, F.; Pavlov, V.; Chuvilin, A.; Grzelczak, M. Plasmonic Substrates Comprising Gold Nanostars Efficiently Regenerate Cofactor Molecules. *J Mater Chem A Mater* **2016**, *4* (18), 7045–7052.
- (359) Zhang, P.; Fujitsuka, M.; Majima, T. Hot Electron-Driven Hydrogen Evolution Using Anisotropic Gold Nanostructure Assembled Monolayer MoS₂. *Nanoscale* **2017**, *9* (4), 1520–1526. <https://doi.org/10.1039/C6NR07740D>.
- (360) An, X.; Wen, Y.; Almuji, A.; Cheng, D.; Li, J.; Jia, X.; Zou, J.; Ni, Y. Nano-Fibrillated Cellulose (NFC) as Versatile Carriers of TiO₂ Nanoparticles (TNPs) for Photocatalytic Hydrogen Generation. *RSC Adv* **2016**, *6* (92), 89457–89466. <https://doi.org/10.1039/C6RA21042B>.
- (361) Anirudhan, T. S.; Deepa, J. R. Nano-Zinc Oxide Incorporated Graphene Oxide/Nanocellulose Composite for the Adsorption and Photo Catalytic Degradation of Ciprofloxacin Hydrochloride from Aqueous Solutions. *J Colloid Interface Sci* **2017**, *490*, 343–356. <https://doi.org/10.1016/j.jcis.2016.11.042>.
- (362) Tu, K.; Wang, Q.; Lu, A.; Zhang, L. Portable Visible-Light Photocatalysts Constructed from Cu₂O Nanoparticles and Graphene Oxide in Cellulose Matrix. *The Journal of Physical Chemistry C* **2014**, *118* (13), 7202–7210. <https://doi.org/10.1021/jp412802h>.
- (363) Uppada, V.; Bhaduri, S.; Noronha, S. B. Cofactor Regeneration – an Important Aspect of Biocatalysis. *Curr Sci* **2014**, *106* (7), 946–957.
- (364) Berg, J. M.; Tymoczko, J. L.; Stryer, L. *Biochemistry*, 5th ed.; W.H. Freeman: New York, 2002.
- (365) Pollak, N.; Dölle, C.; Ziegler, M. The Power to Reduce: Pyridine Nucleotides – Small Molecules with a Multitude of Functions. *Biochemical Journal* **2007**, *402* (2), 205–218. <https://doi.org/10.1042/BJ20061638>.
- (366) Chenault, H. K.; Whitesides, G. M. Regeneration of Nicotinamide Cofactors for Use in Organic Synthesis. *Appl Biochem Biotechnol* **1987**, *14* (2), 147–197. <https://doi.org/10.1007/BF02798431>.
- (367) Liu, J.; Cazelles, R.; Chen, Z. P.; Zhou, H.; Galarneau, A.; Antonietti, M. The Bioinspired Construction of an Ordered Carbon Nitride Array for Photocatalytic Mediated Enzymatic Reduction. *Phys. Chem. Chem. Phys.* **2014**, *16* (28), 14699–14705. <https://doi.org/10.1039/C4CP01348D>.
- (368) Jones, J. B.; Sneddon, D. W.; Higgins, W.; Lewis, A. J. Preparative-Scale Reductions of Cyclic Ketones and Aldehyde Substrates of Horse Liver Alcohol Dehydrogenase with in Situ Sodium Dithionite Recycling of Catalytic Amounts of NAD. *J Chem Soc Chem Commun* **1972**, *0* (15), 856. <https://doi.org/10.1039/c39720000856>.
- (369) Taylor, K. E.; Jones, J. B. Nicotinamide Coenzyme Regeneration by Dihydropyridine and Pyridinium Compounds. *J Am Chem Soc* **1976**, *98* (18), 5689–5694. <https://doi.org/10.1021/ja00434a047>.
- (370) Ali, I.; Khan, T.; Omanovic, S. Direct Electrochemical Regeneration of the Cofactor NADH on Bare Ti, Ni, Co and Cd Electrodes: The Influence of Electrode Potential and Electrode Material. *J Mol Catal A Chem* **2014**, *387*, 86–91. <https://doi.org/10.1016/j.molcata.2014.02.029>.

- (371) Wienkamp, R.; Steckhan, E. Selective Generation of NADH by Visible Light. *Angewandte Chemie International Edition in English* **1983**, *22* (6), 497–497. <https://doi.org/10.1002/anie.198304971>.
- (372) Liu, J.; Antonietti, M. Bio-Inspired NADH Regeneration by Carbon Nitride Photocatalysis Using Diatom Templates. *Energy Environ Sci* **2013**, *6* (5), 1486. <https://doi.org/10.1039/c3ee40696b>.
- (373) Wang, X.; Saba, T.; Yiu, H. H. P.; Howe, R. F.; Anderson, J. A.; Shi, J. Cofactor NAD(P)H Regeneration Inspired by Heterogeneous Pathways. *Chem* **2017**, *2* (5), 621–654. <https://doi.org/10.1016/j.chempr.2017.04.009>.
- (374) Wang, X.; Meng, Q.; Gao, L.; Jin, Z.; Ge, J.; Liu, C.; Xing, W. Recent Progress in Hydrogen Production from Formic Acid Decomposition. *Int J Hydrogen Energy* **2018**, *43* (14), 7055–7071. <https://doi.org/10.1016/j.ijhydene.2018.02.146>.
- (375) Cai, Y.; Li, X.; Zhang, Y.; Wei, X.; Wang, K.; Chen, J. Highly Efficient Dehydrogenation of Formic Acid over a Palladium-Nanoparticle-Based Mott–Schottky Photocatalyst. *Angewandte Chemie International Edition* **2013**, *52* (45), 11822–11825. <https://doi.org/10.1002/anie.201304652>.
- (376) Kuehnel, M. F.; Wakerley, D. W.; Orchard, K. L.; Reisner, E. Photocatalytic Formic Acid Conversion on CdS Nanocrystals with Controllable Selectivity for H₂ or CO. *Angewandte Chemie International Edition* **2015**, *54* (33), 9627–9631. <https://doi.org/10.1002/anie.201502773>.
- (377) Zheng, Z.; Tachikawa, T.; Majima, T. Plasmon-Enhanced Formic Acid Dehydrogenation Using Anisotropic Pd–Au Nanorods Studied at the Single-Particle Level. *J Am Chem Soc* **2015**, *137* (2), 948–957. <https://doi.org/10.1021/ja511719g>.
- (378) Wu, B.; Lee, J.; Mubeen, S.; Jun, Y.-S.; Stucky, G. D.; Moskovits, M. Plasmon-Mediated Photocatalytic Decomposition of Formic Acid on Palladium Nanostructures. *Adv Opt Mater* **2016**, *4* (7), 1041–1046. <https://doi.org/10.1002/ADOM.201600055>.
- (379) Ferry, J. G. Formate Dehydrogenase. *FEMS Microbiol Lett* **1990**, *87* (3–4), 377–382. <https://doi.org/10.1111/j.1574-6968.1990.tb04940.x>.
- (380) Hendel, T.; Wuithschick, M.; Kettemann, F.; Birnbaum, A.; Rademann, K.; Polte, J. In Situ Determination of Colloidal Gold Concentrations with UV–Vis Spectroscopy: Limitations and Perspectives. *Anal Chem* **2014**, *86* (22), 11115–11124. <https://doi.org/10.1021/ac502053s>.
- (381) Khlebtsov, N. G.; Khlebtsov, B. N.; Kryuchkova, E. V.; Zarkov, S. V.; Burov, A. M. Universal Determination of Gold Concentration in Colloids with UV–Vis Spectroscopy. *The Journal of Physical Chemistry C* **2022**, *126* (45), 19268–19276. <https://doi.org/10.1021/acs.jpcc.2c05843>.
- (382) Tardy, B. L.; Yokota, S.; Ago, M.; Xiang, W.; Kondo, T.; Bordes, R.; Rojas, O. J. Nanocellulose–Surfactant Interactions. *Curr Opin Colloid Interface Sci* **2017**, *29*, 57–67. <https://doi.org/10.1016/j.cocis.2017.02.004>.
- (383) Halas, N. J.; Lal, S.; Chang, W.-S.; Link, S.; Nordlander, P. Plasmons in Strongly Coupled Metallic Nanostructures. *Chem Rev* **2011**, *111* (6), 3913–3961. <https://doi.org/10.1021/cr200061k>.
- (384) Grzelczak, M.; Pérez-Juste, J.; García de Abajo, F. J.; Liz-Marzán, L. M. Optical Properties of Platinum-Coated Gold Nanorods. *The Journal of Physical Chemistry C* **2007**, *111* (17), 6183–6188. <https://doi.org/10.1021/jp0671502>.
- (385) Joo, J.; Uchida, T.; Cuesta, A.; Koper, M. T. M.; Osawa, M. The Effect of PH on the Electrocatalytic Oxidation of Formic Acid/Formate on Platinum: A Mechanistic Study by Surface-Enhanced Infrared Spectroscopy Coupled with Cyclic Voltammetry. *Electrochim Acta* **2014**, *129*, 127–136. <https://doi.org/10.1016/j.electacta.2014.02.040>.

- (386) Hartland, G. V. Optical Studies of Dynamics in Noble Metal Nanostructures. *Chem Rev* **2011**, *111* (6), 3858–3887. <https://doi.org/10.1021/cr1002547>.
- (387) Wu, J. T.; Wu, L. H.; Knight, J. A. Stability of NADPH: Effect of Various Factors on the Kinetics of Degradation. *Clin Chem* **1986**, *32* (2), 314–319. <https://doi.org/10.1093/clinchem/32.2.314>.
- (388) Tarnowicz-Staniak, N.; Staniak, M.; Dudek, M.; Grzelczak, M.; Matczyszyn, K.; Tarnowicz-Staniak, N.; Dudek, M.; Matczyszyn, K.; Staniak, M.; Grzelczak, M. Gold Nanorods Grant an ON-OFF Control over the Kinetics of the Z-E Isomerization of Azobenzene-Based Photoswitch via Thermoplasmonic Effect. **2024**. <https://doi.org/10.26434/CHEMRXIV-2024-VNJ32>.
- (389) Bian, T.; Chu, Z.; Klajn, R.; Bian, T.; Chu, Z.; Klajn, R. The Many Ways to Assemble Nanoparticles Using Light. *Advanced Materials* **2020**, *32* (20), 1905866. <https://doi.org/10.1002/ADMA.201905866>.
- (390) Khanal, B. P.; Zubarev, E. R. Rings of Nanorods. *Angewandte Chemie International Edition* **2007**, *46* (13), 2195–2198. <https://doi.org/10.1002/anie.200604889>.
- (391) Dai, Q.; Coutts, J.; Zou, J.; Huo, Q. Surface Modification of Gold Nanorods through a Place Exchange Reaction inside an Ionic Exchange Resin. *Chemical Communications* **2008**, No. 25, 2858. <https://doi.org/10.1039/b804797a>.
- (392) El Khoury, J. M.; Zhou, X.; Qu, L.; Dai, L.; Urbas, A.; Li, Q. Organo-Soluble Photoresponsive Azo Thiol Monolayer-Protected Gold Nanorods. *Chemical Communications* **2009**, No. 16, 2109. <https://doi.org/10.1039/b901826c>.
- (393) Wang, Q.; Li, D.; Xiao, J.; Guo, F.; Qi, L. Reversible Self-Assembly of Gold Nanorods Mediated by Photoswitchable Molecular Adsorption. *Nano Res* **2019**, *12* (7), 1563–1569. <https://doi.org/10.1007/s12274-019-2393-9>.
- (394) Dong, L.; Chen, Y.; Zhai, F.; Tang, L.; Gao, W.; Tang, J.; Feng, Y.; Feng, W. Azobenzene-Based Solar Thermal Energy Storage Enhanced by Gold Nanoparticles for Rapid, Optically-Triggered Heat Release at Room Temperature. *J Mater Chem A Mater* **2020**, *8* (36), 18668–18676. <https://doi.org/10.1039/D0TA06913B>.
- (395) Kunfi, A.; Vlocskó, R. B.; Keresztes, Z.; Mohai, M.; Bertóti, I.; Ábrahám, Á.; Kiss, É.; London, G. Photoswitchable Macroscopic Solid Surfaces Based On Azobenzene-Functionalized Polydopamine/Gold Nanoparticle Composite Materials: Formation, Isomerization and Ligand Exchange. *Chempluschem* **2020**, *85* (5), 797–805. <https://doi.org/10.1002/CPLU.201900674>.
- (396) Kunfi, A.; Ábrahám, Á.; Gyulai, G.; Kiss, É.; London, G. Light-Induced and Thermal Isomerization of Azobenzenes on Immobilized Gold Nanoparticle Aggregates. *Chempluschem* **2022**, *87* (7), e202200153. <https://doi.org/10.1002/cplu.202200153>.
- (397) Dai, Z.; Lo, P. K. Photo-Switchable Patterning of Gold Nanoparticles along 3D DNA Nanotubes. *Nanoscale* **2018**, *10* (12), 5431–5435. <https://doi.org/10.1039/C7NR09650J>.
- (398) Wang, Z.; Li, Z.; Liu, Z. Photostimulated Reversible Attachment of Gold Nanoparticles on Multiwalled Carbon Nanotubes. *The Journal of Physical Chemistry C* **2009**, *113* (10), 3899–3902. <https://doi.org/10.1021/jp900055z>.
- (399) Sánchez-Iglesias, A.; Claes, N.; Solís, D. M.; Taboada, J. M.; Bals, S.; Liz-Marzán, L. M.; Grzelczak, M. Reversible Clustering of Gold Nanoparticles under Confinement. *Angewandte Chemie International Edition* **2018**, *57* (12), 3183–3186. <https://doi.org/10.1002/anie.201800736>.
- (400) Chang, H.-H.; Murphy, C. J. Mini Gold Nanorods with Tunable Plasmonic Peaks beyond 1000 Nm. *Chemistry of Materials* **2018**, *30* (4), 1427–1435. <https://doi.org/10.1021/acs.chemmater.7b05310>.

- (401) Samanta, D.; Klajn, R. Aqueous Light-Controlled Self-Assembly of Nanoparticles. *Adv Opt Mater* **2016**, *4* (9), 1373–1377. <https://doi.org/10.1002/ADOM.201600364>.
- (402) Rao, P.; Doremus, R. Kinetics of Growth of Nanosized Gold Clusters in Glass. *J Non Cryst Solids* **1996**, *203*, 202–205. [https://doi.org/10.1016/0022-3093\(96\)00483-8](https://doi.org/10.1016/0022-3093(96)00483-8).
- (403) Rodríguez-Fernández, J.; Pérez-Juste, J.; Mulvaney, P.; Liz-Marzán, L. M. Spatially-Directed Oxidation of Gold Nanoparticles by Au(III)–CTAB Complexes. *J Phys Chem B* **2005**, *109* (30), 14257–14261. <https://doi.org/10.1021/jp052516g>.
- (404) Huang, R.; Wen, Y. H.; Shao, G. F.; Zhu, Z. Z.; Sun, S. G. Single-Crystalline and Multiple-Twinned Gold Nanoparticles: An Atomistic Perspective on Structural and Thermal Stabilities. *RSC Adv* **2014**, *4* (15), 7528–7537. <https://doi.org/10.1039/C3RA46631K>.
- (405) Sau, T. K.; Murphy, C. J. Seeded High Yield Synthesis of Short Au Nanorods in Aqueous Solution. *Langmuir* **2004**, *20* (15), 6414–6420. <https://doi.org/10.1021/la049463z>.
- (406) Carbó-Argibay, E.; Rodríguez-González, B.; Gómez-Graña, S.; Guerrero-Martínez, A.; Pastoriza-Santos, I.; Pérez-Juste, J.; Liz-Marzán, L. M. The Crystalline Structure of Gold Nanorods Revisited: Evidence for Higher-Index Lateral Facets. *Angewandte Chemie International Edition* **2010**, *49* (49), 9397–9400. <https://doi.org/10.1002/ANIE.201004910>.
- (407) Li, W.; Zhang, M.; Zhang, J.; Han, Y. Self-Assembly of Cetyl Trimethylammonium Bromide in Ethanol-Water Mixtures. *Frontiers of Chemistry in China 2006 1:4* **2006**, *1* (4), 438–442. <https://doi.org/10.1007/S11458-006-0069-Y>.
- (408) Misra, P. K.; Mishra, B. K.; Behera, G. B. Micellization of Ionic Surfactants in Tetrahydrofuran-Water and Acetonitrile-Water Mixed-Solvent Systems. *Colloids and Surfaces* **1991**, *57* (1), 1–10. [https://doi.org/10.1016/0166-6622\(91\)80175-N](https://doi.org/10.1016/0166-6622(91)80175-N).
- (409) Rahmanzadeh, M.; Rezakhani, N.; Khosharay, S. Z.; Danalou, F.; Rostami, S.; Mahsa, R.; Naser, R.; Sima, Z. D.; Farzan, R.; Shahin, K.; Zeinali Danalou, S.; Rostami, F.; Khosharay, S. Z. Interfacial Behavior of Aqueous Solutions of Cetyltrimethylammonium Bromide (CTAB), Additives and Their Mixtures: The Experimental and Modeling Study. *Iran. J. Chem. Chem. Eng.* **2022**, *40* (2), 568–578. <https://doi.org/https://dx.doi.org/10.30492/ijcce.2021.131116.4237>.
- (410) Ghosh, K. K.; Roy, S. Thermodynamics of Micelle Formation of Some Cationic Surfactants as a Function of Temperature and Solvent. *Indian J Chem* **1998**, *37B*, 875–880.
- (411) Jiang, Z.; Zhao, P.; Li, J.; Liu, X.; Hu, C. Effect of Tetrahydrofuran on the Solubilization and Depolymerization of Cellulose in a Biphasic System. *ChemSusChem* **2018**, *11* (2), 397–405. <https://doi.org/10.1002/CSSC.201701861>.
- (412) Wang, S.; Ren, J.; Li, W.; Sun, R.; Liu, S. Properties of Polyvinyl Alcohol/Xylan Composite Films with Citric Acid. *Carbohydr Polym* **2014**, *103* (1), 94–99. <https://doi.org/10.1016/J.CARBPOL.2013.12.030>.
- (413) Shang, Z.; An, X.; Seta, F. T.; Ma, M.; Shen, M.; Dai, L.; Liu, H.; Ni, Y. Improving Dispersion Stability of Hydrochloric Acid Hydrolyzed Cellulose Nano-Crystals. *Carbohydr Polym* **2019**, *222*, 115037. <https://doi.org/10.1016/J.CARBPOL.2019.115037>.
- (414) Abitbol, T.; Marway, H.; Cranston, E. D. Surface Modification of Cellulose Nanocrystals with Cetyltrimethylammonium Bromide. *Nord Pulp Paper Res J* **2014**, *29* (1), 46–57. <https://doi.org/10.3183/NPPRJ-2014-29-01-P046-057>.
- (415) Salajková, M.; Berglund, L. A.; Zhou, Q. Hydrophobic Cellulose Nanocrystals Modified with Quaternary Ammonium Salts. *J Mater Chem* **2012**, *22* (37), 19798–19805. <https://doi.org/10.1039/C2JM34355J>.

- (416) del Caño, R.; Gisbert-González, J. M.; González-Rodríguez, J.; Sánchez-Obrero, G.; Madueño, R.; Blázquez, M.; Pineda, T. Effective Replacement of Cetyltrimethylammonium Bromide (CTAB) by Mercaptoalkanoic Acids on Gold Nanorod (AuNR) Surfaces in Aqueous Solutions. *Nanoscale* **2020**, *12* (2), 658–668. <https://doi.org/10.1039/C9NR09137H>.
- (417) Moreno, J.; Gerecke, M.; Grubert, L.; Kovalenko, S. A.; Hecht, S. Sensitized Two-NIR-Photon Z→E Isomerization of a Visible-Light-Addressable Bistable Azobenzene Derivative. *Angewandte Chemie International Edition* **2016**, *55* (4), 1544–1547. <https://doi.org/10.1002/ANIE.201509111>.
- (418) Jones, L. B.; Hammond, G. S. Mechanisms of Photochemical Reactions in Solution. XXX.1 Photosensitized Isomerization of Azobenzene. *J Am Chem Soc* **1965**, *87* (18), 4219–4220. <https://doi.org/10.1021/JA01096A059>.
- (419) Wang, L.; Zhou, Y.; Ma, S.; Zhang, H. Reprocessable and Healable Room Temperature Photoactuators Based on a Main-Chain Azobenzene Liquid Crystalline Poly(Ester-Urea). *J Mater Chem C Mater* **2021**, *9* (38), 13255–13265. <https://doi.org/10.1039/D1TC03064G>.
- (420) Meng, L.; Xin, N.; Hu, C.; Wang, J.; Gui, B.; Shi, J.; Wang, C.; Shen, C.; Zhang, G.; Guo, H.; Meng, S.; Guo, X. Side-Group Chemical Gating via Reversible Optical and Electric Control in a Single Molecule Transistor. *Nat Commun* **2019**, *10* (1), 1–8. <https://doi.org/10.1038/s41467-019-09120-1>.
- (421) Szymański, W.; Beierle, J. M.; Kistemaker, H. A. V.; Velema, W. A.; Feringa, B. L. Reversible Photocontrol of Biological Systems by the Incorporation of Molecular Photoswitches. *Chem Rev* **2013**, *113* (8), 6114–6178. <https://doi.org/10.1021/cr300179f>.
- (422) Dudek, M.; Deiana, M.; Pokladek, Z.; Mlynarz, P.; Samoc, M.; Matczyszyn, K. Light-Driven Chiroptical Photoswitchable DNA Assemblies Mediated by Bioinspired Photoresponsive Molecules. *Nanoscale* **2018**, *10* (24), 11302–11306. <https://doi.org/10.1039/C8NR01784K>.
- (423) Sobczak, G.; Sashuk, V. Photoswitchable Catalysis Mediated by Nanoparticles. *ChemCatChem* **2021**, *13* (2), 506–513. <https://doi.org/10.1002/CCTC.202001598>.
- (424) Chen, J.; Chen, K. Y.; Carroll, G. T.; Feringa, B. L. Facile Assembly of Light-Driven Molecular Motors onto a Solid Surface. *Chemical Communications* **2014**, *50* (84), 12641–12644. <https://doi.org/10.1039/C4CC04440A>.
- (425) Giles, L. W.; Faul, C. F. J.; Tabor, R. F. Azobenzene Isomerization in Condensed Matter: Lessons for the Design of Efficient Light-Responsive Soft-Matter Systems. *Mater Adv* **2021**, *2* (13), 4152–4164. <https://doi.org/10.1039/D1MA00340B>.
- (426) Bléger, D.; Hecht, S. Visible-Light-Activated Molecular Switches. *Angewandte Chemie International Edition* **2015**, *54* (39), 11338–11349. <https://doi.org/10.1002/ANIE.201500628>.
- (427) Fuchter, M. J. On the Promise of Photopharmacology Using Photoswitches: A Medicinal Chemist's Perspective. *J Med Chem* **2020**, *63* (20), 11436–11447. <https://doi.org/10.1021/acs.jmedchem.0c00629>.
- (428) Goulet-Hanssens, A.; Utecht, M.; Mutruc, D.; Titov, E.; Schwarz, J.; Grubert, L.; Bléger, D.; Saalfrank, P.; Hecht, S. Electrocatalytic Z → E Isomerization of Azobenzenes. *J Am Chem Soc* **2017**, *139* (1), 335–341. <https://doi.org/10.1021/jacs.6b10822>.
- (429) Goulet-Hanssens, A.; Rietze, C.; Titov, E.; Abdullahu, L.; Grubert, L.; Saalfrank, P.; Hecht, S. Hole Catalysis as a General Mechanism for Efficient and Wavelength-Independent Z → E Azobenzene Isomerization. *Chem* **2018**, *4* (7), 1740–1755. <https://doi.org/10.1016/j.chempr.2018.06.002>.
- (430) Chechik, V. Reduced Reactivity of Aged Au Nanoparticles in Ligand Exchange Reactions. *J Am Chem Soc* **2004**, *126* (25), 7780–7781. <https://doi.org/10.1021/ja048879w>.

- (431) França, R.; Zhang, X.-F.; Veres, T.; Yahia, L.; Sacher, E. Core–Shell Nanoparticles as Prodrugs: Possible Cytotoxicological and Biomedical Impacts of Batch-to-Batch Inconsistencies. *J Colloid Interface Sci* **2013**, *389* (1), 292–297. <https://doi.org/10.1016/j.jcis.2012.08.065>.
- (432) Titov, E.; Lysyakova, L.; Lomadze, N.; Kabashin, A. V.; Saalfrank, P.; Santer, S. Thermal Cis-to-Trans Isomerization of Azobenzene-Containing Molecules Enhanced by Gold Nanoparticles: An Experimental and Theoretical Study. *The Journal of Physical Chemistry C* **2015**, *119* (30), 17369–17377. <https://doi.org/10.1021/acs.jpcc.5b02473>.
- (433) Simoncelli, S.; Aramendía, P. F. Mechanistic Insight into the Z–E Isomerization Catalysis of Azobenzenes Mediated by Bare and Core–Shell Gold Nanoparticles. *Catal. Sci. Technol.* **2015**, *5* (4), 2110–2116. <https://doi.org/10.1039/C4CY01442A>.
- (434) Gemen, J.; Klajn, R. Electron Catalysis Expands the Supramolecular Chemist’s Toolbox. *Chem* **2022**, *8* (5), 1183–1186. <https://doi.org/10.1016/J.CHEMPR.2022.04.022>.
- (435) Al-Zubeidi, A.; Wang, Y.; Lin, J.; Flatebo, C.; Landes, C. F.; Ren, H.; Link, S. D-Band Holes React at the Tips of Gold Nanorods. *J Phys Chem Lett* **2023**, *14* (23), 5297–5304. <https://doi.org/10.1021/ACS.JPCLETT.3C00997>.
- (436) Novo, C.; Funston, A. M.; Mulvaney, P. Direct Observation of Chemical Reactions on Single Gold Nanocrystals Using Surface Plasmon Spectroscopy. *Nat Nanotechnol* **2008**, *3* (10), 598–602. <https://doi.org/10.1038/nnano.2008.246>.
- (437) Novo, C.; Funston, A. M.; Gooding, A. K.; Mulvaney, P. Electrochemical Charging of Single Gold Nanorods. *J Am Chem Soc* **2009**, *131* (41), 14664–14666. <https://doi.org/10.1021/ja905216h>.
- (438) Göstl, R.; Senf, A.; Hecht, S. Remote-Controlling Chemical Reactions by Light: Towards Chemistry with High Spatio-Temporal Resolution. *Chem Soc Rev* **2014**, *43* (6), 1982–1996. <https://doi.org/10.1039/C3CS60383K>.
- (439) Piella, J.; Merkoçi, F.; Genç, A.; Arbiol, J.; Bastús, N. G.; Puntès, V. Probing the Surface Reactivity of Nanocrystals by the Catalytic Degradation of Organic Dyes: The Effect of Size, Surface Chemistry and Composition. *J Mater Chem A Mater* **2017**, *5* (23), 11917–11929. <https://doi.org/10.1039/c7ta01328k>.
- (440) Grommet, A. B.; Lee, L. M.; Klajn, R. Molecular Photoswitching in Confined Spaces. *Acc. Chem. Res.* **2020**, *53* (11), 2600–2610. <https://doi.org/10.1021/acs.accounts.0c00434>.
- (441) Dong, M.; Babalhavaeji, A.; Samanta, S.; Beharry, A. A.; Woolley, G. A. Red-Shifting Azobenzene Photoswitches for in Vivo Use. *Acc Chem Res* **2015**, *48* (10), 2662–2670. <https://doi.org/10.1021/acs.accounts.5b00270>.
- (442) Hammerich, M.; Schütt, C.; Stähler, C.; Lentès, P.; Röhricht, F.; Höppner, R.; Herges, R. Heterodiazocines: Synthesis and Photochromic Properties, Trans to Cis Switching within the Bio-Optical Window. *J Am Chem Soc* **2016**, *138* (40), 13111–13114. <https://doi.org/10.1021/jacs.6b05846>.
- (443) Dong, M.; Babalhavaeji, A.; Collins, C. V.; Jarrah, K.; Sadovski, O.; Dai, Q.; Woolley, G. A. Near-Infrared Photoswitching of Azobenzenes under Physiological Conditions. *J Am Chem Soc* **2017**, *139* (38), 13483–13486. <https://doi.org/10.1021/jacs.7b06471>.
- (444) Velema, W. A.; Van Der Berg, J. P.; Hansen, M. J.; Szymanski, W.; Driessen, A. J. M.; Feringa, B. L. Optical Control of Antibacterial Activity. *Nat Chem* **2013**, *5* (11), 924–928. <https://doi.org/10.1038/NCHEM.1750>.
- (445) Fehrentz, T.; Schönberger, M.; Trauner, D. Optochemical Genetics. *Angewandte Chemie - International Edition* **2011**, *50* (51), 12156–12182. <https://doi.org/10.1002/ANIE.201103236>.

- (446) Dudek, M.; Deiana, M.; Pokladek, Z.; Pawlik, K.; Matczyszyn, K. Reversible Photocontrol of DNA Melting by Visible-Light-Responsive F4-Coordinated Azobenzene Compounds. *Chemistry – A European Journal* **2018**, *24* (71), 18963–18970. <https://doi.org/10.1002/CHEM.201803529>.
- (447) Dong, M.; Babalhavaeji, A.; Hansen, M. J.; Kálmán, L.; Woolley, G. A. Red, Far-Red, and near Infrared Photoswitches Based on Azonium Ions. *Chemical Communications* **2015**, *51* (65), 12981–12984. <https://doi.org/10.1039/C5CC02804C>.
- (448) Lentès, P.; Stadler, E.; Röhricht, F.; Brahm, A.; Gröbner, J.; Sönnichsen, F. D.; Geschiedt, G.; Herges, R. Nitrogen Bridged Diazocines: Photochromes Switching within the Near-Infrared Region with High Quantum Yields in Organic Solvents and in Water. *J Am Chem Soc* **2019**, *141* (34), 13592–13600. <https://doi.org/10.1021/jacs.9b06104>.
- (449) Konrad, D. B.; Savasci, G.; Allmendinger, L.; Trauner, D.; Ochsenfeld, C.; Ali, A. M. Computational Design and Synthesis of a Deeply Red-Shifted and Bistable Azobenzene. *J Am Chem Soc* **2020**, *142* (14), 6538–6547. <https://doi.org/10.1021/jacs.9b10430>.
- (450) Samanta, S.; Babalhavaeji, A.; Dong, M. X.; Woolley, G. A. Photoswitching of Ortho-Substituted Azonium Ions by Red Light in Whole Blood. *Angewandte Chemie International Edition* **2013**, *52* (52), 14127–14130. <https://doi.org/10.1002/ANIE.201306352>.
- (451) Kennedy, A. D. W.; Sandler, I.; Andréasson, J.; Ho, J.; Beves, J. E. Visible-Light Photoswitching by Azobenzazoles. *Chemistry – A European Journal* **2020**, *26* (5), 1103–1110. <https://doi.org/10.1002/CHEM.201904309>.
- (452) Croissant, J.; Maynadier, M.; Gallud, A.; Peindy N'Dongo, H.; Nyalosaso, J. L.; Derrien, G.; Charnay, C.; Durand, J. O.; Raehm, L.; Serein-Spirau, F.; Cheminet, N.; Jarrosson, T.; Mongin, O.; Blanchard-Desce, M.; Gary-Bobo, M.; Garcia, M.; Lu, J.; Tamanoi, F.; Tarn, D.; Guardado-Alvarez, T. M.; Zink, J. I. Two-Photon-Triggered Drug Delivery in Cancer Cells Using Nanoimpellers. *Angew Chem Int Ed Engl* **2013**, *52* (51), 13813. <https://doi.org/10.1002/ANIE.201308647>.
- (453) Izquierdo-Serra, M.; Gascón-Moya, M.; Hirtz, J. J.; Pittolo, S.; Poskanzer, K. E.; Ferrer, È.; Alibés, R.; Busqué, F.; Yuste, R.; Hernando, J.; Gorostiza, P. Two-Photon Neuronal and Astrocytic Stimulation with Azobenzene-Based Photoswitches. *J Am Chem Soc* **2014**, *136* (24), 8693–8701. <https://doi.org/10.1021/ja5026326>.
- (454) Boyer, J.-C.; Carling, C.-J.; Gates, B. D.; Branda, N. R. Two-Way Photoswitching Using One Type of Near-Infrared Light, Upconverting Nanoparticles, and Changing Only the Light Intensity. *J Am Chem Soc* **2010**, *132* (44), 15766–15772. <https://doi.org/10.1021/ja107184z>.
- (455) Wang, L.; Dong, H.; Li, Y.; Xue, C.; Sun, L.-D.; Yan, C.-H.; Li, Q. Reversible Near-Infrared Light Directed Reflection in a Self-Organized Helical Superstructure Loaded with Upconversion Nanoparticles. *J Am Chem Soc* **2014**, *136* (12), 4480–4483. <https://doi.org/10.1021/ja500933h>.
- (456) Mandl, G. A.; Rojas-Gutierrez, P. A.; Capobianco, J. A. A NIR-Responsive Azobenzene-Based Supramolecular Hydrogel Using Upconverting Nanoparticles. *Chemical Communications* **2018**, *54* (46), 5847–5850. <https://doi.org/10.1039/C8CC03101K>.
- (457) Lim, C. K.; Li, X.; Li, Y.; Drew, K. L. M.; Palafox-Hernandez, J. P.; Tang, Z.; Baev, A.; Kuzmin, A. N.; Knecht, M. R.; Walsh, T. R.; Swihart, M. T.; Ågren, H.; Prasad, P. N. Plasmon-Enhanced Two-Photon-Induced Isomerization for Highly-Localized Light-Based Actuation of Inorganic/Organic Interfaces. *Nanoscale* **2016**, *8* (7), 4194–4202. <https://doi.org/10.1039/C5NR07973J>.
- (458) Bortolus, P.; Monti, S. Cis-Trans Photoisomerization of Azobenzene. Solvent and Triplet Donors Effects. *Journal of Physical Chemistry* **1979**, *83* (6), 648–652. <https://doi.org/10.1021/J100469A002>.

- (459) Cembran, A.; Bernardi, F.; Garavelli, M.; Gagliardi, L.; Orlandi, G. On the Mechanism of the Cis–trans Isomerization in the Lowest Electronic States of Azobenzene: S_0 , S_1 , and T_1 . *J Am Chem Soc* **2004**, *126* (10), 3234–3243. <https://doi.org/10.1021/ja038327y>.
- (460) Isokuortti, J.; Kuntze, K.; Virkki, M.; Ahmed, Z.; Vuorimaa-Laukkanen, E.; Filatov, M. A.; Turshatov, A.; Laaksonen, T.; Priimagi, A.; Durandin, N. A. Expanding Excitation Wavelengths for Azobenzene Photoswitching into the Near-Infrared Range via Endothermic Triplet Energy Transfer. *Chem Sci* **2021**, *12* (21), 7504–7509. <https://doi.org/10.1039/D1SC01717A>.
- (461) Jiang, Z.; Xu, M.; Li, F.; Yu, Y. Red-Light-Controllable Liquid-Crystal Soft Actuators via Low-Power Excited Upconversion Based on Triplet–Triplet Annihilation. *J Am Chem Soc* **2013**, *135* (44), 16446–16453. <https://doi.org/10.1021/ja406020r>.
- (462) Kurihara, M.; Hirooka, A.; Kume, S.; Sugimoto, M.; Nishihara, H. Redox-Conjugated Reversible Isomerization of Ferrocenylazobenzene with a Single Green Light. *Journal of American Chemical Society* **2002**, *124*, 8800–8801. <https://doi.org/10.1021/JA026625>.
- (463) Liu, Z. F.; Hashimoto, K.; Fujishima, A. Photoelectrochemical Information Storage Using an Azobenzene Derivative. *Nature* **1990**, *347* (6294), 658–660. <https://doi.org/10.1038/347658a0>.
- (464) Nishi, H.; Asahi, T.; Kobatake, S. Plasmonic Enhancement of Gold Nanoparticles on Photocycloreversion Reaction of Diarylethene Derivatives Depending on Particle Size, Distance from the Particle Surface, and Irradiation Wavelength. *Physical Chemistry Chemical Physics* **2012**, *14* (14), 4898–4905. <https://doi.org/10.1039/C2CP23820A>.
- (465) Nishi, H.; Asahi, T.; Kobatake, S. Plasmonic Enhancement of a Photocycloreversion Reaction of a Diarylethene Derivative Using Individually Dispersed Silver Nanoparticles. *ChemPhysChem* **2012**, *13* (16), 3616–3621. <https://doi.org/10.1002/cphc.201200442>.
- (466) Tsuboi, Y.; Shimizu, R.; Shoji, T.; Kitamura, N. Near-Infrared Continuous-Wave Light Driving a Two-Photon Photochromic Reaction with the Assistance of Localized Surface Plasmon. *J Am Chem Soc* **2009**, *131* (35), 12623–12627. <https://doi.org/10.1021/ja9016655>.
- (467) Padilla, M.; Peccati, F.; Bourdelande, J. L.; Solans-Monfort, X.; Guirado, G.; Sodupe, M.; Hernando, J. Enhanced Photocatalytic Activity of Gold Nanoparticles Driven by Supramolecular Host–Guest Chemistry. *Chemical Communications* **2017**, *53* (13), 2126–2129. <https://doi.org/10.1039/C6CC09600J>.
- (468) Ho, M.-L.; Chi, B.-J.; Hung, T.-Y.; Liao, H.-Y.; Wang, J.-C.; Wang, T.-Y.; Shyue, J.-J. Enhanced Photochromism of Chromen-Based Colorants near Silver Nanorods in Sol–Gel Matrix. *CrystEngComm* **2013**, *15* (30), 5969. <https://doi.org/10.1039/c3ce40293b>.
- (469) Stiévenard, D.; Guérin, D.; Lenfant, S.; Lévêque, G.; Nijhuis, C. A.; Vuillaume, D. Electrical Detection of Plasmon-Induced Isomerization in Molecule–Nanoparticle Network Devices. *Nanoscale* **2018**, *10* (48), 23122–23130. <https://doi.org/10.1039/C8NR07603K>.
- (470) Schaffer, A. L.; Dobbins, T. A.; Pearson, S.-A. Interrupted Time Series Analysis Using Autoregressive Integrated Moving Average (ARIMA) Models: A Guide for Evaluating Large-Scale Health Interventions. *BMC Med Res Methodol* **2021**, *21* (1), 58. <https://doi.org/10.1186/s12874-021-01235-8>.
- (471) Hyndman, R. J.; Khandakar, Y. Automatic Time Series Forecasting: The Forecast Package for R. *J Stat Softw* **2008**, *27* (3 SE-Articles), 1–22. <https://doi.org/10.18637/jss.v027.i03>.
- (472) R Core Team. R: A Language and Environment for Statistical Computing. R Foundation for Statistical Computing: Vienna, Austria 2022. <https://www.r-project.org/>.
- (473) Benjamini, Y.; Hochberg, Y. Controlling the False Discovery Rate: A Practical and Powerful Approach to Multiple Testing. *Journal of the Royal Statistical Society. Series B (Methodological)* **1995**, *57* (1), 289–300.

- (474) Gille, K.; Knoll, H.; Quitzsch, K. Rate Constants of the Thermal Cis-Trans Isomerization of Azobenzene Dyes in Solvents, Acetone/Water Mixtures, and in Microheterogeneous Surfactant Solutions. *Int J Chem Kinet* **1999**, *31*, 337–350. [https://doi.org/10.1002/\(SICI\)1097-4601\(1999\)31:5](https://doi.org/10.1002/(SICI)1097-4601(1999)31:5).
- (475) Bernal, J. L.; Cummins, S.; Gasparini, A. Interrupted Time Series Regression for the Evaluation of Public Health Interventions: A Tutorial. *Int J Epidemiol* **2017**, *46* (1), 348–355. <https://doi.org/10.1093/IJE/DYW098>.